metals

Special Issue Reprint

Numerical Simulation of Solidification Processes

Edited by
Mohsen Eshraghi

mdpi.com/journal/metals

MDPI

Numerical Simulation of Solidification Processes

Numerical Simulation of Solidification Processes

Editor

Mohsen Eshraghi

MDPI

Basel • Beijing • Wuhan • Barcelona • Belgrade • Novi Sad • Cluj • Manchester

Editor
Mohsen Eshraghi
California State University,
Los Angeles
Los Angeles, CA, USA

Editorial Office
MDPI
St. Alban-Anlage 66
4052 Basel, Switzerland

This is a reprint of articles from the Special Issue published online in the open access journal *Metals* (ISSN 2075-4701) (available at: https://www.mdpi.com/journal/metals/special_issues/simu_solidif).

For citation purposes, cite each article independently as indicated on the article page online and as indicated below:

Lastname, A.A.; Lastname, B.B. Article Title. *Journal Name* **Year**, *Volume Number*, Page Range.

ISBN 978-3-0365-8600-7 (Hbk)
ISBN 978-3-0365-8601-4 (PDF)
doi.org/10.3390/books978-3-0365-8601-4

Cover image courtesy of Mohsen Eshraghi

Contents

About the Editor

Mohsen Eshraghi

Mohsen Eshraghi is a Professor of Mechanical Engineering and Director of the Materials Science and Engineering program at California State University, Los Angeles. His research interests are in the areas of Computational Materials Science, Solidification, and Additive Manufacturing. As the founding director of the Advanced Materials and Manufacturing Laboratory (AM^2L), he has served as the PI, co-PI, and senior personnel on multiple NASA and NSF projects, studying microstructural evolution during solidification of alloys under microgravity and terrestrial conditions.

Preface

This Special Issue aims to explore the numerical simulation of solidification processes, combining computational physics, numerical models, systematic experiments, and advanced manufacturing techniques. By delving into the complexities of solidification phenomena, these simulations enable researchers to understand the macroscopic and microscopic aspects of the process, while providing engineers with predictive capabilities to enhance material properties through process parameter modifications. The eleven high-quality papers presented here are authored by distinguished researchers, covering a broad array of solidification modeling studies. As the Guest Editor, I hope that the rich array of research presented here will contribute to the advancement of scientific knowledge and engineering practices in solidification processes. I extend my appreciation to the esteemed authors, reviewers, and the editorial staff of Metals for their valuable contributions and support in bringing this Special Issue to fruition.

Mohsen Eshraghi
Editor

metals

MDPI

Editorial

Numerical Simulation of Solidification Processes

Mohsen Eshraghi

Department of Mechanical Engineering, California State University, Los Angeles, 5151 State University Drive, Los Angeles, CA 90032, USA; mohsen.eshraghi@calstatela.edu

1. Introduction and Scope

Solidification is a critical step for many manufacturing processes, including casting, welding, and additive manufacturing. While solidification happens during the processing of all types of materials, the solidification of metallic alloys has been of utmost importance to scientists and engineers. This importance comes from the fact that the solidification microstructure has a significant influence on the properties of the solidified materials. The kinetics of solidification also determines the distribution of solute atoms, which eventually leads to micro-segregation, secondary phases, and the formation of various defects, which exert enormous influence on mechanical properties. By combining the bedrock computational physics and informatics with systematic experiments and advanced manufacturing, we can reduce the cost, risk, and cycle time for new product development. Numerical simulation of solidification processes can help scientists gain a better understanding of the kinetics governing the macroscopic, as well as microscopic, features of the solidification process. From an industrial point of view, solidification modeling enables engineers to predict the properties of the material and subsequently modify the process parameters to produce materials of higher quality. Several physical phenomena are involved during solidification processes that, in turn, make the simulations very complex. In the wake of promising progress in the area of solidification modeling, this Special Issue embraces studies on the numerical simulation of solidification phenomena for a variety of applications and processes.

2. Contributions

In this Special Issue, eleven high-quality papers from distinguished researchers are published that cover a wide range of solidification modeling studies including steel casting and solidification, permeability, segregation, cracking and thermal distortion, dendrite growth and grain morphology, welding, and additive manufacturing.

Two of the papers covered topics related to the additive manufacturing of nickel and titanium alloys with studies on 3D modeling of the solidification structure evolution of superalloys in powder bed fusion additive manufacturing processes [1] and in situ X-ray radiography and computational modeling to predict grain morphology in β-Titanium during simulated additive manufacturing [2].

Three of the papers were focused on phase-field modeling of dendritic microstructure evolution and presented studies on permeability measurements of 3D microstructures generated by phase-field simulation of the solidification of an Al-Si alloy during chill casting [3]; a phase-field study on the interaction between grains during columnar-to-equiaxed transition in laser welding [4]; and a two-dimensional phase-field investigation of unidirectionally solidified tip-splitting microstructures [5].

Five papers focused on the casting and solidification of steel, which presented investigations on the optimization of heavy reduction processes on continuous-casting bloom [6]; the effects of alloying elements on solidification structures and macro-segregation in slabs [7]; the prediction of thermal distortion during steel solidification [8]; an analysis of micro-segregation of solute elements on the central cracking of continuously cast

Citation: Eshraghi, M. Numerical Simulation of Solidification Processes. *Metals* **2023**, *13*, 1303. https://doi.org/10.3390/met13071303

Received: 26 June 2023
Revised: 5 July 2023
Accepted: 5 July 2023
Published: 21 July 2023

bloom [9]; and numerical simulation of macro-segregation formation in a 2.45 ton steel ingot using a three-phase equiaxed solidification model [10].

Finally, we provided a review of large-scale simulations of microstructural evolution during alloy solidification [11] featuring the framework and methodologies for achieving scalability in solidification microstructure simulations while highlighting the areas of focus that need more attention.

As Guest Editor of this Special Issue, I hope that the papers included in this collection will be beneficial to scientists and engineering in advancing their research and development endeavors.

3. Conclusions and Outlook

The progression of the numerical models and computational techniques for the simulation of solidification processes has shown that the factors for realistic results are constantly improving. In prediction analysis, the complexity has grown with respect to technological advances. The combination of improved physics models and computational algorithms with thermodynamical databases would enable the calculation of multicomponent phase equilibria, allowing for more reliable simulations for real-world industrial applications. Several manufacturing and material processing applications can take advantage of the prediction capabilities offered by solidification simulations, which include casting, welding, and additive manufacturing processes. The modeling approaches still have many improvements to innovate upon, with promising developments in novel numerical techniques, machine learning, and computing power.

Acknowledgments: As the Guest Editor, I appreciate the invaluable contributions of the distinguished authors, and the time and effort of the reviewers, editors, and the editorial staff of *Metals*.

Conflicts of Interest: The author declares no conflict of interest.

References

1. Nastac, L. 3D Modeling of the Solidification Structure Evolution of Superalloys in Powder Bed Fusion Additive Manufacturing Processes. *Metals* **2021**, *11*, 1995. [CrossRef]
2. Jasien, C.; Saville, A.; Becker, C.; Klemm-Toole, J.; Fezzaa, K.; Sun, T.; Pollock, T.; Clarke, A. In Situ X-ray Radiography and Computational Modeling to Predict Grain Morphology in β-Titanium during Simulated Additive Manufacturing. *Metals* **2022**, *12*, 1217. [CrossRef]
3. Berger, R.; Apel, M.; Laschet, G.; Jessen, W.; Schröder, W.; Wipperfürth, J.; Austermann, J.; Hopmann, C. Permeability Measurements of 3D Microstructures Generated by Phase Field Simulation of the Solidification of an Al-Si Alloy during Chill Casting. *Metals* **2021**, *11*, 1895. [CrossRef]
4. Xiong, L.; Wang, C.; Wang, Z.; Jiang, P. The Interaction between Grains during Columnar-to-Equiaxed Transition in Laser Welding: A Phase-Field Study. *Metals* **2020**, *10*, 1647. [CrossRef]
5. Laxmipathy, V.; Wang, F.; Selzer, M.; Nestler, B. A Two-Dimensional Phase-Field Investigation on Unidirectionally Solidified Tip-Splitting Microstructures. *Metals* **2022**, *12*, 376. [CrossRef]
6. Yang, B.; Wang, M.; Zhang, H.; Liu, S.; Wang, G.; Wang, X. Optimization of Heavy Reduction Process on Continuous-Casting Bloom. *Metals* **2022**, *12*, 1873. [CrossRef]
7. Zhang, P.; Wang, M.; Shi, P.; Xu, L. Effects of Alloying Elements on Solidification Structures and Macrosegregation in Slabs. *Metals* **2022**, *12*, 1826. [CrossRef]
8. Azizi, G.; Thomas, B.; Asle Zaeem, M. Prediction of Thermal Distortion during Steel Solidification. *Metals* **2022**, *12*, 1807. [CrossRef]
9. Zeng, Q.; Xiao, C.; Li, J. Analysis of Micro-Segregation of Solute Elements on the Central Cracking of Continuously Cast Bloom. *Metals* **2021**, *11*, 382. [CrossRef]
10. Wang, T.; Wang, E.; Delannoy, Y.; Fautrelle, Y.; Budenkova, O. Numerical Simulation of Macrosegregation Formation in a 2.45 ton Steel Ingot Using a Three-Phase Equiaxed Solidification Model. *Metals* **2021**, *11*, 262. [CrossRef]
11. Cusato, N.; Nabavizadeh, S.; Eshraghi, M. A Review of Large-Scale Simulations of Microstructural Evolution during Alloy Solidification. *Metals* **2023**, *13*, 1169. [CrossRef]

metals

MDPI

Article

3D Modeling of the Solidification Structure Evolution of Superalloys in Powder Bed Fusion Additive Manufacturing Processes

Laurentiu Nastac

Department of Metallurgical and Materials Engineering, The University of Alabama, P.O. Box 870202, Tuscaloosa, AL 35487, USA; lnastac@eng.ua.edu; Tel.: +1-205-348-4844

Abstract: Recently, a few computational methodologies and algorithms have been developed to simulate the microstructure evolution in powder bed fusion (PBF) additive manufacturing (AM) processes. However, none of these have attempted to simulate the grain structure evolution in multitrack, multilayer AM components in a fully 3D transient mode and for the entire AM geometry. In this work, a multiscale model, which consists of coupling a transient, discrete-source 3D AM process model with a 3D stochastic solidification structure model, was applied to quickly, efficiently, and accurately predict the grain structure evolution of IN625 alloys during Laser Powder Bed Fusion (LPBF). The capabilities of this model include studying the effects of process parameters and part geometry on solidification conditions and their impact on the grain structure formation within multicomponent alloy parts processed via AM. Validation was accomplished based on single-layer LPBF IN625 benchmark experiments, previously performed and analyzed at the National Institute of Standards and Technology (NIST), USA. This modeling approach can also be used to quantitatively predict the solidification structure of Ti-6Al-4V alloys in electron beam AM processes.

Keywords: modeling of additive manufacturing processes; Laser Powder Bed Fusion; rapid solidification; grain structure evolution; texture and grain morphology; superalloys; IN625

Citation: Nastac, L. 3D Modeling of the Solidification Structure Evolution of Superalloys in Powder Bed Fusion Additive Manufacturing Processes. *Metals* **2021**, *11*, 1995. https://doi.org/10.3390/met11121995

Academic Editors: Babak Shalchi Amirkhiz and Mohsen Eshraghi

Received: 17 October 2021
Accepted: 7 December 2021
Published: 10 December 2021

1. Introduction

The main aim of this study is to validate a multiscale mesoscopic modeling approach to predict the microstructure evolution of alloys during powder bed fusion processes (e.g., Electron Beam Additive Manufacturing (EBAM) and selective laser melting (SLM) processes [1,2]). A review of the effects of the major process parameters on the quality of the Laser Powder Bed Fusion (LPBF) products, including the rapid solidification microstructure of IN718, is presented in [3]. It is well-known [3,4] that solidification maps can serve as a guide for estimating microstructures with respect to temperature gradient (G) and solidification rate (R) parameters. However, due to the complexity of the AM process, solidification maps are not accurate enough to predict the formation of microstructures. Thus, an accurate predictive microstructure model would be an extremely useful tool for assisting in AM product quality control.

The multiscale model used in this study consists of coupling a fully transient 3D Computational Fluid Dynamics (CFD) macro-model with a 3D solidification structure micromodel [4–8]. Figure 1 presents the coupling methodology between the CFD macro-code and the solidification structure evolution stochastic mesoscopic code. The solidification structure model was adapted to SLM process conditions (e.g., rapid solidification regime [8,9]).

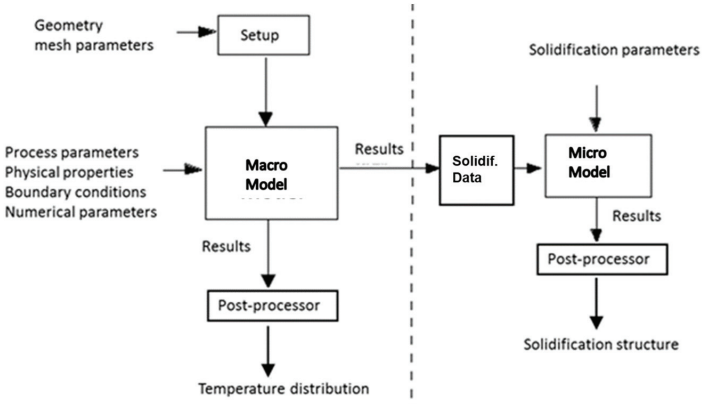

Figure 1. Diagram showing the coupling between the CFD macro-code and the solidification structure evolution stochastic mesoscopic code.

SLM single-layer IN625 benchmark experiments using LPBF equipment were performed and analyzed at the National Institute of Standards and Technology (NIST), USA [10]. These experimental results were used to validate the 3D coupled macro-micro model. It is considered in the coupled model that the complex combination of crystallographic requirements, isomorphism, epitaxy, and the changing direction of melt pool motion and thermal gradient direction produced the observed texture and grain morphology. In addition, the entire AM geometry is simulated with this 3D fully transient model; therefore, there are no limitations/assumptions in accounting for rapid solidification kinetics, remelting, epitaxy, isomorphism, etc., as there could be in other recently proposed AM models [11–13]. Thus, having a 3D modeling tool would be very useful for interpreting these phenomena. This model can be applied to predict experimental observations then further applied to determine the influence of various process parameters, including the scan path, on the formation of texture and grain morphology in multitrack, multilayer AM components.

2. The Modeling Approach

2.1. The Macro-Model Description

A fully implicit, control-volume method was employed to describe the 3D transient macro-transport phenomena in solidifying AM products. The macro-model accounts for energy transport within the AM product by conduction and to the surroundings by conduction, convection, and thermal radiation. A time-dependent, volumetric heat flux moving source was assumed to account for the SLM process. The evaporation of the alloying elements is ignored in the current model.

In the absence of convective transport, the governing heat conduction equation for a 3D geometry is as follows:

$$\begin{array}{l} \frac{\partial}{\partial t}(\rho T) = \frac{\partial}{\partial x}\left(\frac{K}{c_p}\frac{\partial T}{\partial x}\right) + \frac{\partial}{\partial y}\left(\frac{K}{c_p}\frac{\partial T}{\partial y}\right) + \frac{\partial}{\partial z}\left(\frac{K}{c_p}\frac{\partial T}{\partial z}\right) + S_T + S_L \text{ for } 0 \le z \le Z(t) \\ \text{with } S_L = \frac{1}{c_p}\frac{A\,P}{\sqrt{2\pi^{3/2}\sigma^3}}\,\exp\left(-\frac{\left(x^2+y^2+1.35z^2\right)}{2\sigma^2}\right) \quad S_T = \frac{L}{c_p}\frac{\partial}{\partial t}\left(\rho\, f_S\right) \text{ and } f_S = \frac{T_L - T}{T_L - T_S} \end{array} \quad (1)$$

where T is the temperature; t is time; ρ is the density; K is the thermal conductivity; c_p is the specific heat; S_L is the source term associated with the laser power; A is the absorption coefficient; P is the laser power; σ is the laser beam radius; 1.35 is the value of the oblate spheroid parameter in z direction; S_T is the source term associated with the change of phases, which describes the rates of latent heat evolution during the liquid/solid transformation; L is the latent heat of solidification; f_S is the solid fraction; T_L is the liquidus temperature; T_S is the solidus temperature; and $Z(t)$ is the expanding domain height up to the maximum AM product height.

For conventional PBF processes such as SLM and EBAM, there is a single continuously scanning energy source (S_L), which is deposited during a time scale Δt. Δt must be sufficiently small with respect to the elapsed time required for the source to traverse a distance equal to its 4σ beam diameter. The implementation of this energy source is described in more detail in [2].

As shown in Equation (1), the solid fraction is linearly dependent on the temperature in the mushy region. The source term linearization technique described in [14] was used to implement the S_T. Although more sophisticated models [4,15] can be used to describe AM product solidification, the current approach not only describes both columnar and equiaxed solidification, but also accounts for remelting phenomena.

The continuum thermo-physical properties (K, c_p, and ρ) are weighted by the solid fraction and liquid fraction (f_L) as follows:

$$c_p = f_S\, c_{p_S} + f_L\, c_{p_L} \quad K = f_S\, K_S + f_L\, K_L \quad \text{and} \quad \rho = g_S\, \rho_S + g_L\, \rho_L \quad \text{with} \quad f_S = \frac{g_S\, \rho_S}{\rho} \quad \text{and} \quad f_L = \frac{g_L\, \rho_L}{\rho} \tag{2}$$

For a 3D geometry, the appropriate heat transfer boundary conditions (BCs) for the AM processes are: heat losses by conduction, convection, and radiation at the geometry top, edge and bottom, and AM process-specific BCs at the top of the geometry to account for the heat input due to the moving/scanning volumetric source.

2.2. The Micromodel Description

The present stochastic approach differs from the classical "Cellular Automata" technique [4] in that it uses thermal history results from the deterministic model described in the previous section. The development of the stochastic model for grain structure evolution is described in more detail in [4,5]. This description includes nucleation and growth kinetics, as well as the growth anisotropy and grain selection mechanisms. The required input data for stochastic calculations are provided by the macroscopic model and include: (i) local cooling rates calculated at the liquidus and solidus temperatures, (ii) time-dependent temperature gradients in the mushy zone, also calculated at the liquidus and solidus temperatures, and (iii) local solidification start time and end time. Local cooling rates calculated at the liquidus temperature are used to compute the nucleation parameters. Local average cooling rates, and time-dependent temperature gradients in the mushy zone are used to compute the grain growth parameters.

During the solidification of AM processed products, at least three grain morphologies can be encountered: equiaxed grains, columnar grains solidified under a variable G/V ratio, and columnar grains solidified under a relatively constant G/V ratio, where G and V are the local temperature gradient and solid–liquid (S/L) interface velocity of the mushy region, respectively. All aforementioned morphologies, as well as the columnar-to-equiaxed transition, are driven by more or less the same solidification mechanism, that is, the nucleation and growth competition of various phases in the mushy region.

The stochastic models for equiaxed and columnar grains solidified under a variable G/V ratio are presented in [4,5]. The columnar structure solidified under a relatively constant G/V ratio, which is perhaps the most common morphology encountered during AM, is described below.

2.2.1. Description of the Columnar Interface Tracking

Tracking of the columnar front assumes that, at the columnar front, the growth velocity is equal to the interface velocity of the dendrite tip at the same location. For a 3D domain, the position of the columnar front (X_c, Y_c, Z_c) at time $t + \delta t$ can be iteratively computed by

$$X_c^{t+\partial t} = X_c^t + \frac{1}{cos\theta} V_c^t\, \frac{G_x}{G_T}\, \partial t \quad Y_c^{t+\partial t} = Y_c^t + \frac{1}{cos\theta} V_c^t\, \frac{G_y}{G_T}\, \partial t \quad \text{and} \quad Z_c^{t+\partial t} = Z_c^t + \frac{1}{cos\theta} V_c^t\, \frac{G_z}{G_T}\, \partial t \quad \text{with } G_T = \sqrt{G_X^2 + G_y^2 + G_z^2} \tag{3}$$

where V_c is the solidification velocity of the columnar front; G_T is the local temperature gradient in the mushy zone; G_x, G_y and G_z are the temperature gradients in the x, y, and z directions, respectively; and θ is the angle between the normal to the solidification front, and the preferred [*hkl*] crystallographic growth direction. The crystallographic growth direction of the columnar grains is randomly chosen during the modeling of the surface nucleation event. The methodology for accounting for the preferential crystallographic growth of cubic crystals in the [100] direction is described in detail in [4,16,17].

The solidification kinetics velocity of the columnar front, V_c, is computed based on growth kinetics as [4]:

$$V_C = \frac{D_L}{\pi^2 \Gamma\, k_e\, \Delta T_{LS}} (\Delta T^*)^2 \qquad \text{with} \quad \Delta T^* = a\, G_T \tag{4}$$

where D_L is the liquid diffusivity, Γ is the Gibbs–Thomson coefficient, k_e is the equilibrium partition coefficient, ΔT_{LS} is the solidification interval, ΔT^* is the S/L interface undercooling, and a is the mesh size.

The stochastic model described above has to be adapted for rapid solidification conditions, which are encountered in AM processing. At normal cooling rates, the tip radius of the dendrite decreases as the solidification velocity increases. However, as the cooling rate increases in the rapid solidification range, the tip radius increases, which is accompanied by a decrease in branching, and the morphology of the grain changing from dendritic to cellular. To account for the rapid solidification conditions (where solidification velocities typically exceed 0.01 m/s) in Equation (4), the partition coefficient (k^*) and liquidus slope (m_L^*) of each alloying element need be corrected using Aziz [8], and Baker and Kahn [9] equations, respectively:

$$k^*(V) = \frac{k_e + \delta_i\, V/D_i}{1 + \delta_i\, V/D_i} \qquad m_L^*(V) = \frac{m_L}{1 - k_e}\left[1 - k^*\left(1 - \ln\frac{k^*}{k_e}\right)\right] \tag{5}$$

where V is the S/L interface velocity, D_i is the interfacial diffusivity, δ_i is the atomic boundary layer thickness, and m_L is the equilibrium liquidus slope.

2.2.2. Computational Aspects for 3D Modeling of AM Products

Following are some important computational aspects related to the stochastic modeling of microstructures in AM products:

The time step, δt, used in computations is determined by the Courant criterion:

$$\partial t = \frac{a}{2V_c} \tag{6}$$

where a is the mesh size, and V_c is the S/L interface velocity.

Physically, Equation (6) uses the same principle as is applied in free surface fluid flow computations, i.e., growth is not allowed to take place for more than one half of the mesh size during each time step calculation. Note that, as shown in Equation (6), the time step is linearly dependent on the mesh size.

It was determined that the mesh size should be about 2 μm for simulating the solidification structure in AM products. For this mesh size, the simulation results converged and matched experimental observations [10].

The computer memory and CPU time requirements of the current stochastic model are summarized below:

- The GPU (CUDA) and CPU (C++) were utilized to compile the 3D micromodel code;
- The CUDA 3D-Micro simulator is at least one order of magnitude faster than the CPU Micro-3D simulator using the Intel Skylake AL supercomputer;
- The CPU 3D-Micro simulator is fairly fast, typically taking about 8 h for a multilayer, multitrack simulation using a 2 μm mesh size (33 million cells, RAM 6 GB);

- The CPU 3D-Micro simulator can run 2.75 trillion cells on the Intel Skylake AL supercomputer (RAM 500 GB), which is equivalent of a 1.4 mm^3 geometry using a 2 μm mesh size.

3. Results and Discussion

Table 1 shows the thermo-physical and material kinetics properties of IN625 used in the current simulation. A pseudo-phase diagram IN625-Nb is assumed. The isopleth section of the Ni-Cr-Nb-Fe-Mo phase diagram with 21 wt. % Cr, 5 wt. % Fe, 9 wt. % Mo, and 0.8 wt. % Co is shown in Figure 1 in [18]. The Nb composition of IN625 is 4.1 wt. %. The nucleation density of the columnar grains (N_0) is also given in Table 1.

Table 1. Themo-physical and material kinetics properties of IN625 [4,10,18].

Property	Value	Unit
ρ	7620	kg/m^3
c_p	720	J/kg/K
K	30.1	W/m/K
L	2.95×10^5	J/kg
m_L	−12.0	K/wt. %
Γ	1.0×10^{-7}	K/m
D_L	3.0×10^{-9}	m^2/s
k_e	0.5	
T_L	1622	K
ΔT_{LS}	49.2	K
N_0	1.0×10^{10}	m^{-2}
a	1.0	μm

The process conditions used in the NIST experiment and in the current simulation, such as the laser power (P), and the laser scanning speed (V_s) (see Table 2), create cooling rates in the range of 10^5–10^6 K/s, and temperature gradients in the range of 10^5–10^7 K/m.

Table 2. Process and material parameters used in the current simulation [10,19].

Parameter	Value	Unit
P	195	W
V_s	0.8	m/s
σ	50	μm
A	0.3	-
Δt	5.0×10^{-5}	s
Substrate material	IN625	-
Initial temperature	298.15	K

The mesh size used in the current simulation is 2 μm for the macro-model and 1 μm for the micromodel. Additional details regarding the geometry and the process conditions are presented in [10].

Figure 2 presents a comparison between the experiments [10] and the simulation results for the IN625 LPBF single-layer case. The legend in Figure 2 shows the preferential

crystallographic orientation angle of the columnar grains as 65535 color indices (*CI*). The orientation angles can be extracted from the legend using Equation (7):

$$\theta = \frac{\pi}{2}\frac{CI}{65535} - \frac{\pi}{4} \quad (7)$$

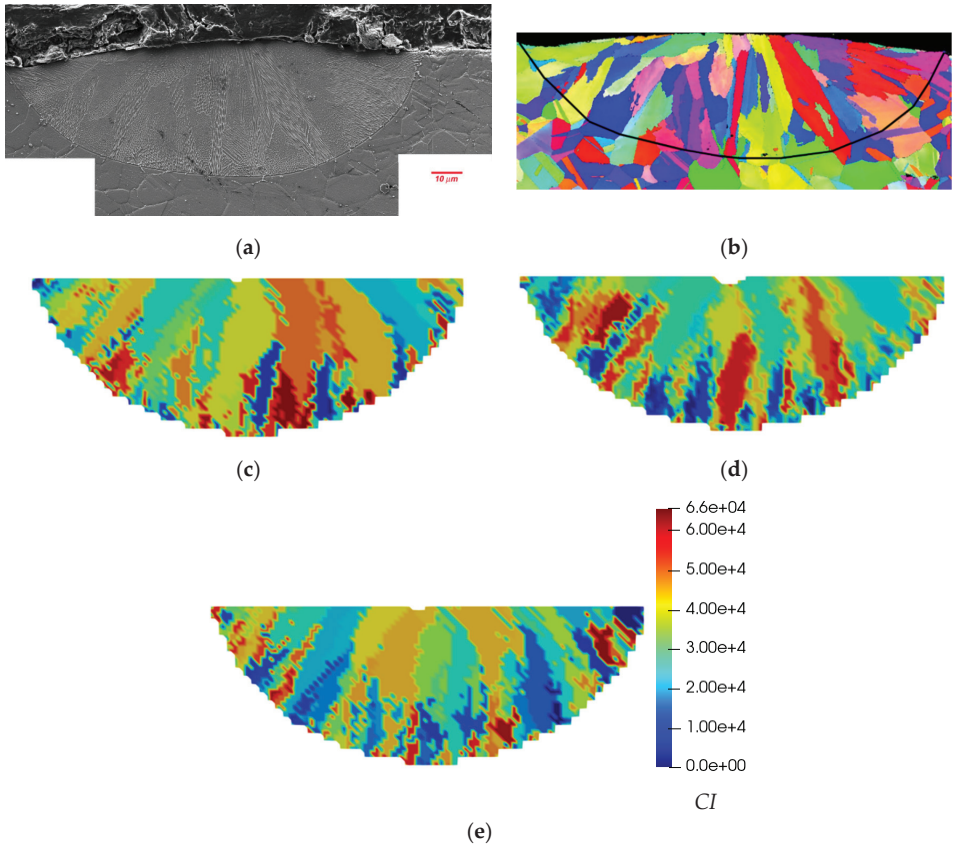

Figure 2. Comparison between experiment [10] (**a**,**b**) and simulations (3 different YK planes—(**c**–**e**)). The black line in (**b**) shows the location of the melt pool boundary.

Thus, when $CI/65535$ ratio varies from 0 to 1, θ ranges from $-\pi/4$ to $\pi/4$.

A favorable comparison between the experiment and the simulation results in terms of melt pool dimensions and solidification grain structure can be seen in Figure 2. The height and diameter of the experimental melt pool, as shown in Figure 2a,b, are about 40 μm and 130 μm, respectively. The predicted height and diameter of the melt pool shown in Figure 2c–e are about 44 μm and 128 μm, respectively. The experimental average columnar grain size at the top of the pool in Figure 2b is about 10 μm. The predicted average columnar grain size at the top of the pool in Figure 2c–e is about 11 μm. In addition, the predicted and experimental grain orientations in Figure 2 match quite well. The comparison of the predicted and experimental grain selection mechanism is also remarkable. Figure 2 shows that there are 28 predicted grains and 27 experimental grains at the bottom of the pool and only 14 predicted grains and 13 experimental grains at the top of the pool.

Additional 2D and 3D plots for different planes of the same modeling case are presented in Figures 3 and 4. The best-oriented grains (CIs in the middle of the CI legends in

Figures 2–4) with respect to the temperature gradient will typically grow to the top of the pool surface, while the worst-oriented grains will normally disappear.

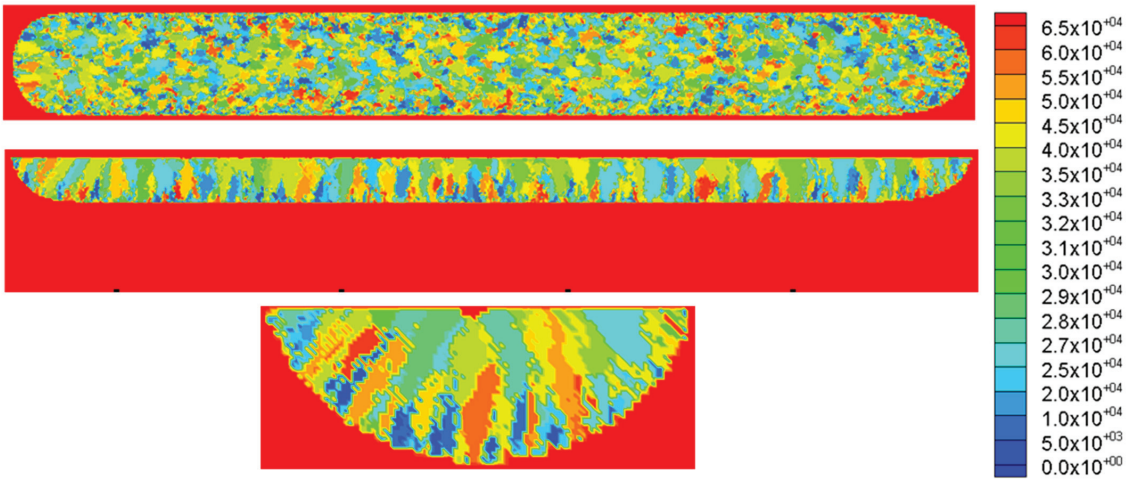

Figure 3. 3D grain structure simulation results: (middle XY, XK, and YK planes).

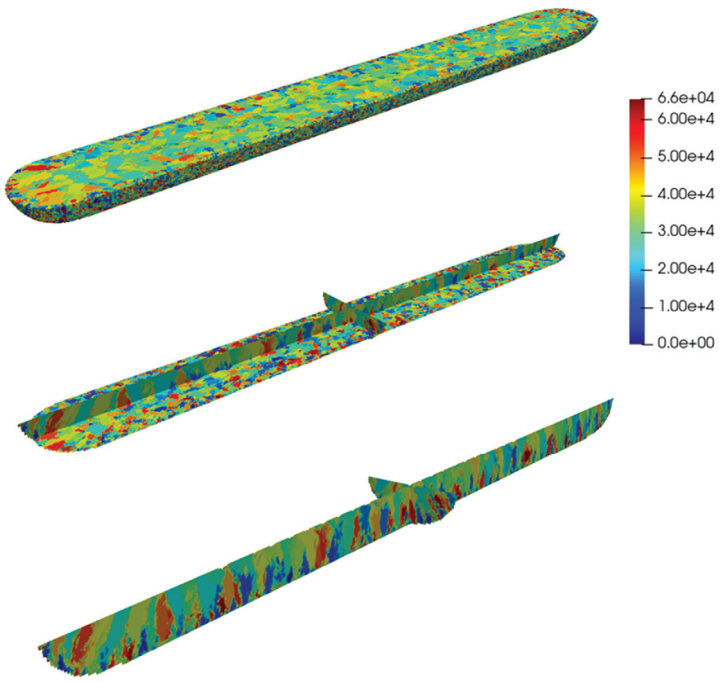

Figure 4. 3D grain structure simulation results (2D and 3D plots).

4. Conclusions

An integrated multiscale transient 3D modeling tool, which consists of coupling a fully transient 3D macro-model with a 3D micromodel, was applied to simulate the 3D microstructure evolution during LPBF solidification of IN625. The coupled multiscale model was successfully validated against the benchmark experiments performed by NIST,

regarding the melt pool dimensions and the columnar grain size and orientation. The CPU time for the studied simulation is about 1 h on the Intel Skylake AL supercomputer. Notably, the current CPU 3D-Micro simulator can run approximately 2.75 trillion cells on the Intel Skylake AL supercomputer (RAM 500 GB), which is equivalent to a 1.4 mm^3 geometry using a mesh size of 2 μm.

Funding: This research was not supported by external funding.

Data Availability Statement: Not applicable.

Acknowledgments: The Alabama Supercomputer Authority (www.asc.edu) (accessed on 4 October 2021) is acknowledged for providing the computing resources to run the simulation presented in this paper.

Conflicts of Interest: The author declares no conflict of interest.

References

1. Liu, S.; Shin, Y.C. Additive manufacturing of Ti6Al4V alloy: A review. *Mater. Des.* **2019**, *164*, 107552. [CrossRef]
2. Schwalbach, E.J.; Donegan, S.P.; Chapman, M.G.; Chaput, K.J.; Groeber, M.A. A discrete source model of powder bed fusion additive manufacturing thermal history. *Addit. Manuf.* **2019**, *25*, 485–498. [CrossRef]
3. Oliveira, J.P.; LaLonde, A.; Ma, J. Processing parameters in laser powder bed fusion metal additive manufacturing. *Mater. Des.* **2020**, *193*, 108762. [CrossRef]
4. Nastac, L. *Modeling and Simulation of Microstructure Evolution in Solidifying Alloys, a Monograph*; Springer: New York, NY, USA, 2004. [CrossRef]
5. Nastac, L. A Multiscale Transient Modeling Approach for Predicting the Solidification Structure in VAR-Processed Alloy 718 Ingots. *Met. Mater. Trans. A* **2014**, *45*, 44–50. [CrossRef]
6. Nastac, L.; Valencia, J.J.; Tims, M.L.; Dax, F.R. Advances in Solidification of IN718 and RS5 Alloys. In Proceedings of the Fifth International Special Emphasis Symposium on Superalloy 718, 625, 706, and Derivatives, Pittsburgh, PA, USA, 17–20 June 2001.
7. Stefanescu, D.M. *Science and Engineering of Casting Solidification*; Springer: New York, NY, USA, 2009.
8. Aziz, M.J. Model for solute redistribution during rapid solidification. *J. Appl. Phys.* **1982**, *53*, 1158–1168. [CrossRef]
9. Baker, J.C.; Cahn, J.W. *Thermodynamics of Solidification, Solidification*; American Society of Metals: Metals Park, OH, USA, 1971; p. 23.
10. 2018 AM-Bench Test Descriptions for AMB2018-02, NIST. Available online: https://www.nist.gov/ambench/amb2018-02-description (accessed on 30 November 2021).
11. Rolchigo, M.; Stump, B.; Belak, J.F.; Plotkowski, A. Sparse thermal data for cellular automata modeling of grain structure in additive manufacturing. *Model. Simul. Mater. Sci. Eng.* **2020**, *28*, 065003. [CrossRef]
12. Koepf, J.A.; Gotterbarm, M.R.; Markl, M.; Körner, C. 3D multi-layer grain structure simulation of powder bed fusion additive manufacturing. *Acta Mater.* **2018**, *152*, 119–126. [CrossRef]
13. Rodgers, T.; Madison, J.D.; Tikare, V. Simulation of metal additive manufacturing microstructures using kinetic Monte Carlo. *Comput. Mater. Sci.* **2017**, *135*, 78–89. [CrossRef]
14. Patankar, S.V. *Numerical Heat Transfer and Fluid Flow*; Hemisphere Publishing Corporation: New York, NY, USA, 1980.
15. Nastac, L.; Sundarraj, S.; Yu, K.O.; Pang, Y. The Stochastic Modeling of Solidification Structures in Alloy 718 Remelt Ingots: Research Summary. *J. Metals* **1998**, *50*, 30–35.
16. Wei, H.; Mazumder, J.; Debroy, T. Evolution of solidification texture during additive manufacturing. *Sci. Rep.* **2015**, *5*, 16446. [CrossRef] [PubMed]
17. Nastac, L. A 3D stochastic mesoscopic model for prediction of microstructure evolution during solidification of dendritic alloys. *Met. Res. Technol.* **2014**, *111*, 311–319. [CrossRef]
18. Mohammadpour, P.; Phillion, A.B. Solidification microstructure selection maps for laser powder bed fusion of multicomponent alloys. *IOP Conf. Ser. Mater. Sci. Eng.* **2020**, *861*, 012005. [CrossRef]
19. Khorasani, M.; Ghasemi, A.; Leary, M.; O'Neil, W.; Gibson, I.; Cordova, L.; Rolfe, B. Numerical and analytical investigation on meltpool temperature of laser-based powder bed fusion of IN718. *Int. J. Heat Mass Transf.* **2021**, *177*, 121477. [CrossRef]

metals

MDPI

Article

In Situ X-ray Radiography and Computational Modeling to Predict Grain Morphology in β-Titanium during Simulated Additive Manufacturing

Chris Jasien [1,*], Alec Saville [1], Chandler Gus Becker [1], Jonah Klemm-Toole [1], Kamel Fezzaa [2], Tao Sun [3], Tresa Pollock [4] and Amy J. Clarke [1]

[1] George S. Ansell Department of Metallurgical and Materials Engineering, Colorado School of Mines, Golden, CO 80401, USA; asaville@mines.edu (A.S.); chbecker@mines.edu (C.G.B.); jklemmto@mines.edu (J.K.-T.); amyclarke@mines.edu (A.J.C.)
[2] Advanced Photon Source, Argonne National Laboratory, Lemont, IL 60439, USA; fezzaa@anl.gov
[3] Materials Science and Engineering, University of Virginia, Charlottesville, VA 22904, USA; ts7qw@virginia.edu
[4] Materials Department, University of California Santa Barbara, Santa Barbara, CA 93106, USA; pollock@engineering.ucsb.edu
* Correspondence: jasien@mines.edu

Abstract: The continued development of metal additive manufacturing (AM) has expanded the engineering metallic alloys for which these processes may be applied, including beta-titanium alloys with desirable strength-to-density ratios. To understand the response of beta-titanium alloys to AM processing, solidification and microstructure evolution needs to be investigated. In particular, thermal gradients (Gs) and solidification velocities (Vs) experienced during AM are needed to link processing to microstructure development, including the columnar-to-equiaxed transition (CET). In this work, in situ synchrotron X-ray radiography of the beta-titanium alloy Ti-10V-2Fe-3Al (wt.%) (Ti-1023) during simulated laser-powder bed fusion (L-PBF) was performed at the Advanced Photon Source at Argonne National Laboratory, allowing for direct determination of Vs. Two different computational modeling tools, SYSWELD and FLOW-3D, were utilized to investigate the solidification conditions of spot and raster melt scenarios. The predicted Vs obtained from both pieces of computational software exhibited good agreement with those obtained from in situ synchrotron X-ray radiography measurements. The model that accounted for fluid flow also showed the ability to predict trends unobservable in the in situ synchrotron X-ray radiography, but are known to occur during rapid solidification. A CET model for Ti-1023 was also developed using the Kurz–Giovanola–Trivedi model, which allowed modeled Gs and Vs to be compared in the context of predicted grain morphologies. Both pieces of software were in agreement for morphology predictions of spot-melts, but drastically differed for raster predictions. The discrepancy is attributable to the difference in accounting for fluid flow, resulting in magnitude-different values of Gs for similar Vs.

Keywords: in situ radiography; additive manufacturing; solidification modeling; beta-titanium; CET modeling

Citation: Jasien, C.; Saville, A.; Becker, C.G.; Klemm-Toole, J.; Fezzaa, K.; Sun, T.; Pollock, T.; Clarke, A.J. In Situ X-ray Radiography and Computational Modeling to Predict Grain Morphology in β-Titanium during Simulated Additive Manufacturing. *Metals* **2022**, *12*, 1217. https://doi.org/10.3390/met12071217

Academic Editors: Mohsen Eshraghi and Eric Hug

Received: 1 June 2022
Accepted: 2 July 2022
Published: 19 July 2022

1. Introduction

The continued development of metal additive manufacturing (AM) over the past couple of decades has expanded the applications and material classes in which these processes can be used. Titanium (Ti) alloys have been at the center of this development, due to their superior properties, particularly for aerospace and defense applications. Although Ti-6Al-4V (Ti-64) has typically dominated in terms of use and research pertaining to metal AM processes, metastable β-Ti alloys have begun to find increased use over Ti-64 (an $\alpha + \beta$ alloy), due to their increased strength-to-density ratios, among other properties [1]. These

metastable β-Ti alloys differ from other classifications of Ti in that the high-temperature β-phase may be retained upon quenching to room temperature, which is of relevance to AM processes [2,3]. The ability to maintain this metastable β-phase is a result of sufficient additions of β-phase stabilizing elements, such as vanadium (V) or molybdenum (Mo). Although sufficient amounts of β-phase stabilizing elements can be added to create stable β-Ti alloys, where the β-phase is retained even at slow cooling rates, they are of more limited use for engineering applications. Throughout the rest of this paper, metastable β-Ti alloys will be referred to as simply β-Ti alloys.

AM technology has allowed for an increased amount of applications in which AM can add value, however many metal-AM processes create parts with anisotropy. This is primarily due to the large columnar grains that can grow along the build height. For this reason, there has been a desire to develop ways to break up these grains to produce ones that are more equiaxed and much smaller in size. These equiaxed grains yield more isotropic mechanical properties that are typically more favorable for structural applications. Approaches such as melt-pool manipulation, modification of alloy composition, and alteration of processing parameters have proven to be successful in increasing regions of equiaxed grains [4–7]. Of the aforementioned techniques, parameter alteration has been the dominant research focus, because it does not add any significant cost or complexity to the process that other approaches might. This has led to widespread investigation of microstructure–processing links in AM alloys [8–10]. For Ti-alloys, this has primarily been conducted for Ti-64 [11–15], where a thorough understanding of the microstructure–processing link has allowed for the use of AM-produced Ti-64 parts in aircraft [16]. Meanwhile, work in the realm of β-Ti alloys has been mostly limited to the "printability" of the material and resulting mechanical properties [17,18].

In order to advance this alloy field for AM, correlations between microstructures and processing parameters, similar to those for Ti-64, are needed. This allows not only for an increased chance of a successful build, but also for the ability to create site-specific microstructures and properties within a single part [19,20], an impossibility with other manufacturing processes. To do this, an alloy-specific solidification map and an understanding of where scan strategies typically fall within this map are needed. A solidification map relates thermal gradients (Gs) and solid–liquid interface velocities (Vs) during solidification to resultant grain morphologies. These predicted maps are typically available in the literature for ubiquitous engineering alloys, but not for β-Ti alloys. Kobyrn et al. used Hunt-criterion boundary lines to classify columnar, mixed, or equiaxed regions based on experimental observations of grain morphologies in Ti-64 for a variety of processes [21]. Their solidification map has widely been accepted and used to predict grain morphologies in AM of Ti-64 [15,22,23]. To create a map for β-Ti alloys using a similar technique, knowledge of resulting Gs and Vs is required. The small size of L-PBF melt pools makes it difficult to obtain accurate Vs using commercial data-collection equipment. For this reason, high-spatial-resolution experiments at national user facilities can be used to determine Vs under L-PBF conditions [24]. Local Gs, on the other hand, are impossible to obtain using almost any experimental setup. For this reason, simulation tools are typically required to predict Gs at all points on the solid–liquid interface [25]. The combinations of Gs and Vs, coupled with an alloy-specific solidification map, then provide the necessary information needed to draw conclusions on the effect of processing parameters on as-built microstructures.

In this study, in situ synchrotron X-ray radiography of simulated L-PBF of the β-Ti alloy Ti-10V-2Fe-3Al (wt.%) (Ti-1023) was used to determine solidification velocities as a function of time and location within the melt pool. Conduction of these experiments at the Advanced Photon Source (APS) at Argonne National Laboratory (ANL) provided the desired spatial and temporal resolutions needed to quantify solidification velocities as a function of position and time within the micron-sized melt-pools characteristic of L-PBF. The corresponding widths and depths of the melt pools were used to calibrate models from two pieces of computational software, SYSWELD and FLOW-3D. The predicted Vs from these tools were compared to those obtained from the in situ synchrotron X-ray

radiography to assess the ability of each software to model the complexity of solidification events occurring within the simulated L-PBF melt pools. Additionally, the combinations of Gs and Vs from the models were compared to each other in the context of predicted grain morphologies from a developed CET model for Ti-1023.

2. Experimental Setup

2.1. APS L-PBF Simulator and In Situ X-ray Radiography

In order to obtain Vs at locations along the melt-pool, laser powder bed fusion (L-PBF) simulator experiments were performed at the Sector 32-ID-B beamline at the Advanced Photon Source (APS) at Argonne National Laboratory (ANL), similar to those conducted by Zhao et al. [24]. A schematic of the experimental setup is shown below in Figure 1. Images of the experiments were collected using 80,000 frames/s. In order to purely study the rapid solidification of the alloy under L-PBF conditions, approximately 200 μm thick Ti-1023 substrates were used, instead of powder. Spot-melts were performed using powers of 82 W, 139 W, and 197 W and constant 1 ms dwell times, while 1.5 mm length rasters were completed at powers ranging from 54 W to 512 W and travel speeds of 0.25–2.00 m/s. A wide set of parameters were selected to achieve a variety of solidification conditions and grain morphologies within the samples. Additionally, all experiments were conducted at room temperature and in an inert atmosphere of argon gas.

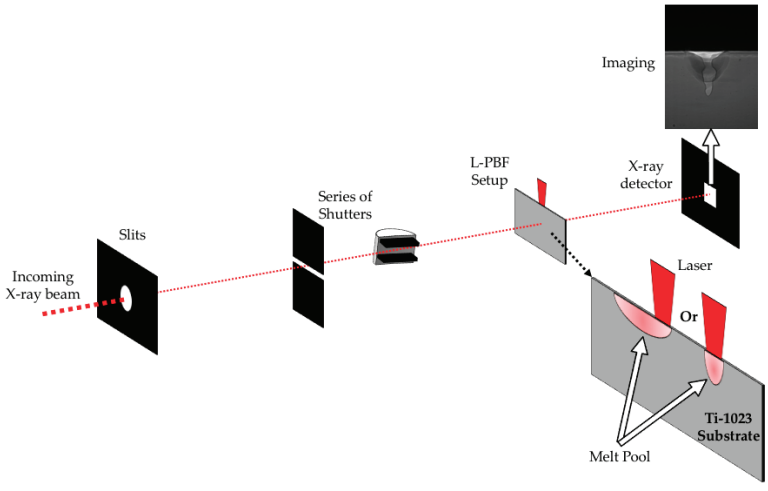

Figure 1. Schematic of the X-ray imaging L-PBF simulator experiments on the Sector 32-ID-B beamline at the APS at ANL. Note: distances between components not to scale.

The resulting imaging of each experiment was used to determine the observed solid–liquid interface velocity as a function of position in the melt pool. This was done using an *ImageJ* macro, where the solid–liquid interface was identified through a manual selection of points for each frame. Data were then compiled and converted into a set of points that described the evolution of the melt pool as a function of time. A *Python* script was then utilized to fit a polynomial to each melt pool and to calculate the change in position as a function of time for a specified direction of interest, i.e., across the top of the melt pool, or from the bottom to the top of the melt pool. The in situ radiography was also used to provide maximum depth measurements of the melt pools, while postmortem, top-down secondary electron imaging (SEI) using a Tescan S8252G scanning electron microscope provided the maximum widths, which together, helped to calibrate the final simulations in the modeling work.

2.2. Model Setup and Inputs

Initial modeling of the APS experiments described above was conducted using a conduction-only commercial software tool called SYSWELD. Although SYSWELD is intended for fusion welding applications, the APS experiments resembled simple laser welding and were assumed to fit within the capabilities of the software. To begin the modeling of these experiments, thermophysical material properties of Ti-1023 were needed. The testing and development of material property databases are notoriously lacking and only exist for a select number of engineering alloys. For Ti, these properties are only widely available for pure Ti and Ti-64 [26]. Due to Ti-64 being an $\alpha + \beta$ alloy and Ti-1023 being a β alloy, Ti-64 properties were not used as approximations for Ti-1023. With no extensive research on the thermophysical properties of β-Ti, thermodynamic prediction software was used to predict these properties for Ti-1023 whenever possible. Density and specific heat as a function of temperature were obtained using Thermo-Calc TCTI/Ti-alloys database version 3 [27]. Although the database was not robust enough to directly calculate these values, simple relationships were used. For instance, enthalpy is a direct output of the software, but to obtain specific heat, the derivative of enthalpy with respect to temperature was taken to approximate specific heat. Thermal conductivity is another important property; however, the Ti database used in this work was not mature enough to predict this quantity. Taking into account the approximate beta-transition temperature predicted by Thermo-Calc, the thermal conductivity as a function of temperature for Ti-64 from Mills [26] was modified to reflect an approximate set of values for Ti-1023. These estimated thermophysical properties were used as material property input for the following models and are shown in Figure 2.

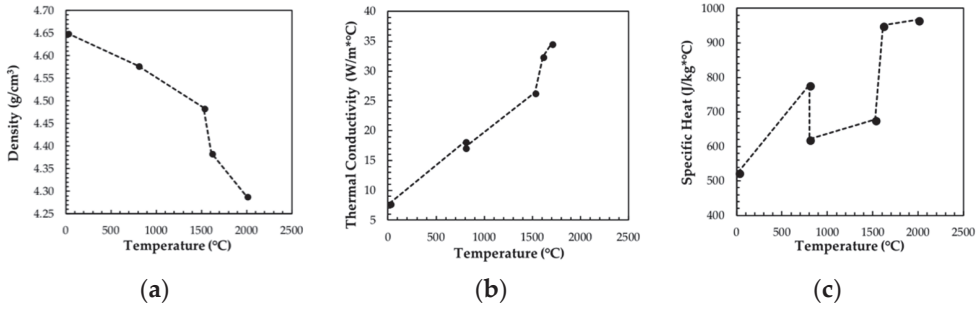

Figure 2. Graphs of estimated (**a**) density, (**b**) thermal conductivity, and (**c**) specific heat as a function of temperature for Ti-1023.

The specific geometry used within SYSWELD to simulate the various experimental spot-melt and raster conditions is presented in Figure 3. In the melt region of the model, the mesh size was 10 μm × 10 μm × 10 μm and progressively coarsened to decrease the computational time of the simulation. The size of this mesh was limited by the capabilities of SYSWELD, due to problems encountered performing simulations with smaller mesh sizes. The specific experiments simulated within SYSWELD are presented in Table 1. For each condition, the simulation needed to be calibrated using an iterative process of manipulating the dimensions of the Gaussian heat source and efficiency term, until the simulated melt pool dimensions agreed with those obtained from experiments. Additionally, the initial temperature of the substrate for these models was 293 K.

Another commercial software tool, FLOW-3D, was used to simulate the same L-PBF conditions modeled within SYSWELD. FLOW-3D is a computational fluid dynamics (CFD) software and is significantly more computationally intensive than SYSWELD. It accounts for more complicated melt pool dynamics, such as evaporation, surface tension, and convective heat transfer. As a result of this complexity, additional material properties were required to fully capture the complexity of the melt pools. Similar to the reasons discussed above for density, thermal conductivity, and specific heat, many of these properties are not readily

available for Ti-1023. In addition, current thermodynamic calculation software is unable to predict them, as was performed for density and specific heat. For this reason, values reported for Ti-64 were used when necessary. All the relevant material properties are listed in Table 2. Additionally, when the in situ imaging of an experiment exhibited keyholing, multiple reflections and Fresnel absorption were activated within the model.

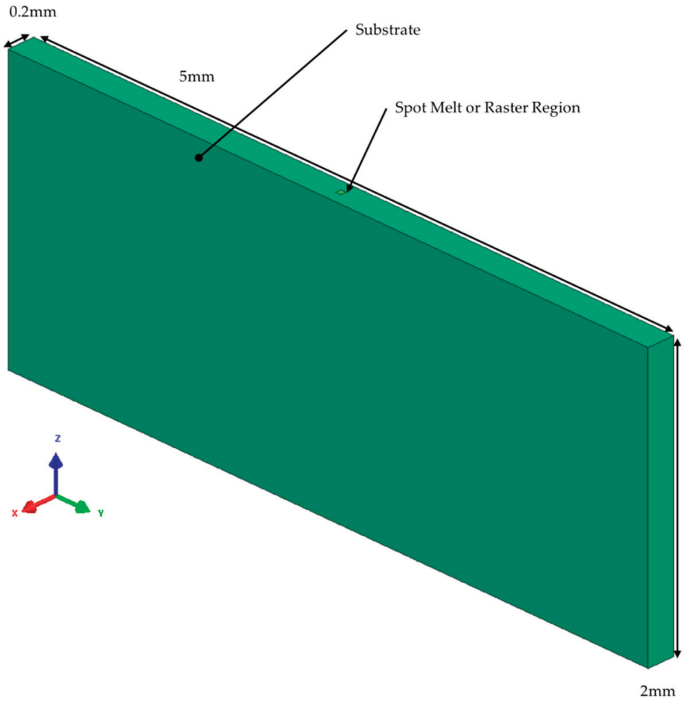

Figure 3. Dimensioned computer-aided design (CAD) model used within SYSWELD for all spot-melt and raster scenarios.

Table 1. Process parameters of the modeled spot-melt and raster experiments.

Experiment	Power (W)	Travel Speed (m/s) or Dwell Time (ms)	Energy Input (J/m)
Spot-melt	82	1	-
Spot-melt	139	1	-
Spot-melt	197	1	-
Raster	53.5	0.25	214
Raster	82	0.50	164
Raster	139	0.50	278

Table 2. Material property inputs for FLOW-3D.

Property	Value	Reference
Surface Tension Coefficient	1.5 N/m	[28]
Surface Tension Temperature Dependence	-2.6×10^{-4} N/m/K	
Solidus Temperature	1798 K	[27]
Liquidus Temperature	1883 K	
Vaporization Temperature	3315 K	[28]
Latent Heat of Melting	0.286 MJ/kg	
Latent Heat of Vaporization	9.7 MJ/kg	

The same substrate dimensions modeled using SYSWELD were used to simulate the experiments within FLOW-3D, although additional boundary conditions and space for fluid flow were added (Figure 4). Mesh size was again smallest in the melt region and coarsened moving away from the melt region; however, the mesh was initially finer, 5 µm × 5 µm × 5 µm, in the FLOW-3D models. Additionally, only half of the model was simulated to reduce the required computational time.

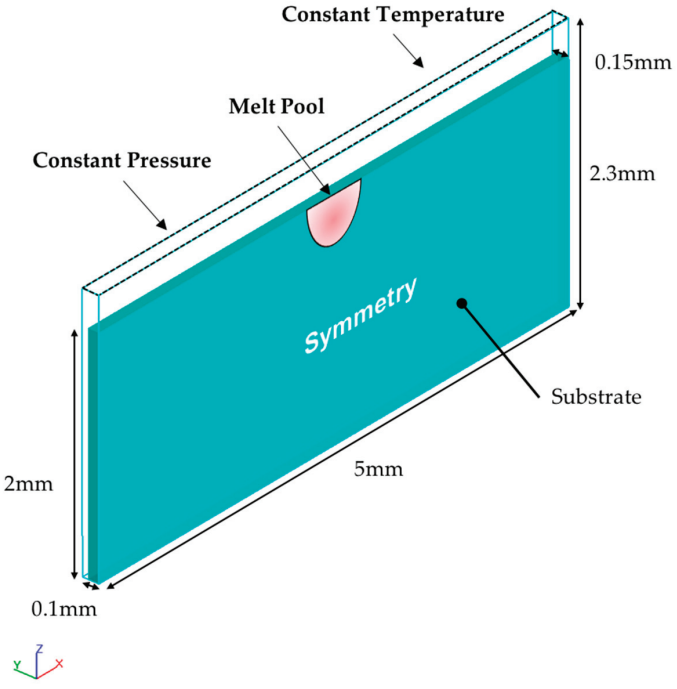

Figure 4. Dimensioned CAD model used within FLOW-3D with labeled boundary conditions for all spot-melt and raster scenarios.

2.3. Columnar-to-Equiaxed Transition Model

In order to relate the G-V predictions from the models directly to microstructure, a prediction of the columnar-to-equiaxed transition (CET) for Ti-1023 was developed using a modified version of the Kurz–Giovanola–Trivedi (KGT) model proposed by Gäuman et al. [29,30]. This modification neglected nucleation undercooling at high Gs, and the equation is presented below:

$$\left(\frac{G^n}{V}\right) = a\left\{\left(\frac{-4\pi N_o}{3\ln(1-\phi)}\right)^{\frac{1}{3}} \cdot \frac{1}{n+1}\right\}^n \quad (1)$$

where G is thermal gradient, V is solidification velocity, N_o is nucleation density, ϕ is volume fraction of equiaxed grains, and n and a are constants relative to the alloy. Thermo-Calc software was utilized to calculate equilibrium solute liquidus slopes (m) and partition coefficients determined at the liquidus temperature (k) for V, iron (Fe), and aluminum (Al), while other modified KGT model inputs were obtained from the literature. The exact model parameters used in this CET model are presented below in Table 3.

Table 3. Modified KGT model inputs to predict CET in Ti-1023.

Model Input		Value	Reference
Solute Diffusivity		7.9×10^{-9} m/s^2	[31]
Gibbs–Thomson Coefficient		5×10^{-7} m·K	[32]
Nucleation Undercooling		5 K	
Nucleation Density		1×10^{15} nuclei/m^3	
m	Vanadium	−4.744 K/wt.%	[27]
	Iron	−12.841 K/wt.%	
	Aluminum	−5.932 K/wt.%	
k	Vanadium	0.756	[27]
	Iron	0.317	
	Aluminum	0.894	
$\phi_{columnar}$		0.0066	[33]
$\phi_{equiaxed}$		0.66	

3. Results and Discussion

3.1. APS Experiment Melt Pool Tracking

A representative solid–liquid interface evolution during solidification and resulting solidification velocities are presented in Figure 5a,b, respectively. The approximate melt pool outlines in Figure 5a were obtained by manually plotting points along the perimeter of the observed solid–liquid interface from the in situ synchrotron X-ray radiography for a series of time steps. With this solid–liquid interface progression, velocities in any direction could be determined with those for the horizontal and vertical directions, as shown in Figure 5b. These velocities were compared to those predicted by the simulations and used to assess how well the models correlated to the experiments. Additionally, Figure 6a–c illustrates how the maximum width and depth of the melt pools were obtained from postmortem microscopy and in situ radiography of the simulated L-PBF spot-melts and rasters. These values were used to calibrate the models presented in the next section.

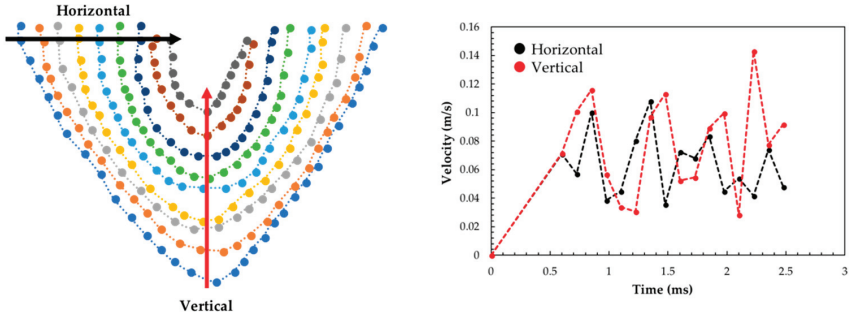

(**a**) (**b**)

Figure 5. (**a**) Progression of the solid–liquid interface of a spot-melt for a series of 0.25 ms time-steps with labeled directions of velocity extraction; (**b**) solidification velocities as a function of time in the horizontal and vertical directions of the spot-melt presented in (**a**).

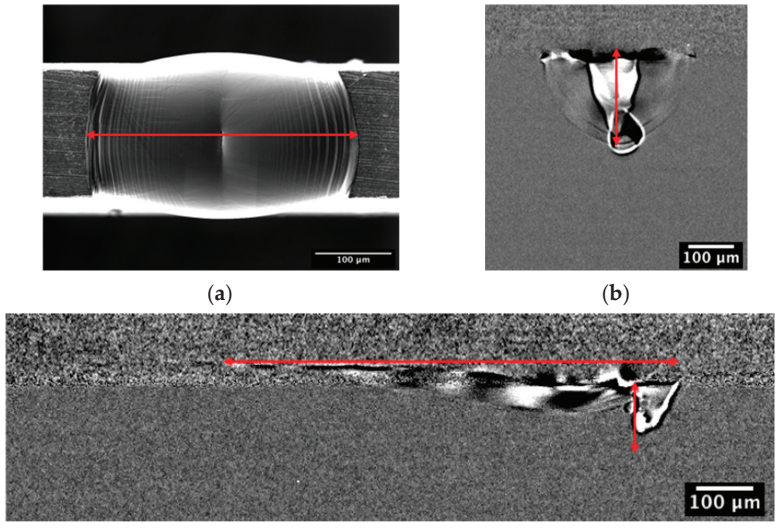

(**a**) (**b**)

(**c**)

Figure 6. Methods of obtaining melt pool dimensions for calibration of model for (**a**) maximum width of a spot-melt using top-down, postmortem secondary electron imaging (SEI), (**b**) maximum depth of a spot-melt using in situ imaging, and (**c**) width and depth of a raster using in situ imaging.

3.2. Melt-Pool Modeling

All spot-melt and raster scenarios were successfully modeled within SYSWELD. A representative simulation is presented below in Figure 7. The resulting dimensions of the simulated melt pools matched the experiments well, with no more than 10% error observed.

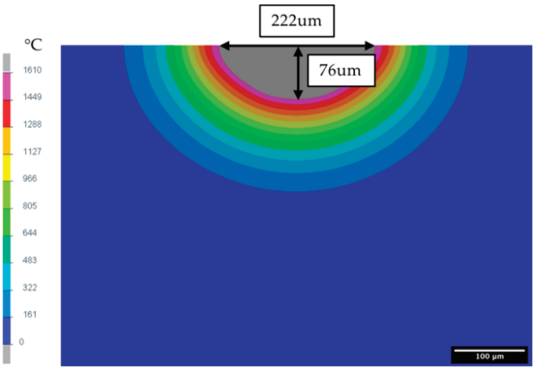

Figure 7. Cross-section of 82 W spot-melt scenario, showing maximum temperature contours predicted by SYSWELD and resulting maximum melt pool depth and width. Note: grey area shows predicted area that is above 1610 °C, the approximate liquidus temperature.

From these simulations, predicted solidification velocities were obtained horizontally at the top of the melt pool and compared to those calculated from the APS in situ radiography for the selected spot-melt and raster scenarios. Similar in situ spot-melt experiments performed by Zhao et al. on thin Ti-64 plates yielded similar velocity profiles to those presented in Figure 8a–c [24]. After the laser is shut off, no initial solidification is detected until hundreds of microseconds later. Upon the initial measurable solidification, subsequent solid–liquid interface velocities remained relatively constant throughout much of the solidification. In some instances, the velocity appears to slightly decrease, which was

also noted by Zhao et al. and hypothesized to be a result of recalescence. The measured velocities in this work do not reach as high of values as reported by Zhao et al. (~0.1 m/s vs. ~0.5 m/s); however, this is likely due to slight differences in experimental conditions.

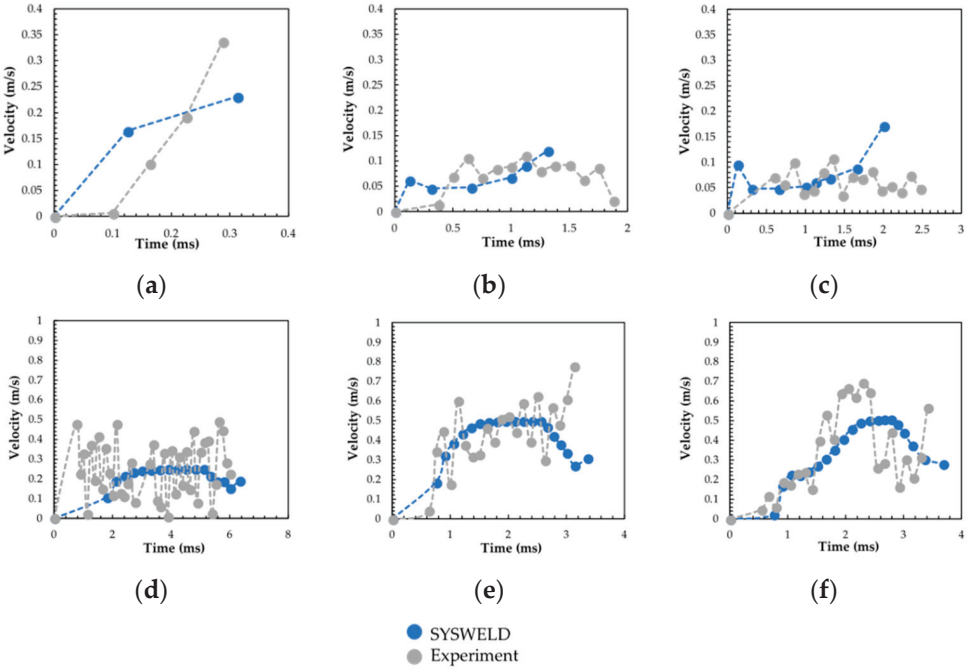

Figure 8. Plots of predicted solidification velocity at the top of the melt pool for (**a**) 82 W, (**b**) 139 W, and (**c**) 197 W spot-melts and (**d**) 53.5 W and 0.25 m/s, (**e**) 82 W and 0.5 m/s, and (**f**) 139 W and 0.5 m/s rasters using SYSWELD and values obtained from X-ray in situ radiography. Note: time = 0 for (**a**–**c**) refers to the moment the laser was turned off and time = 0 for (**d**–**f**) refers to the moment the laser was turned on and began rastering.

Directly comparing the experimental and simulated velocities, the first discrepancy between the solidification velocities from SYSWELD and the APS experiments is that the simulations output data at relatively coarse time-steps. This results in the simulations are unable to completely convey the solidification trends for each set of process parameters. For example, in Figure 8a, only two SYSWELD velocity measurements could be obtained, which does not allow for an accurate prediction of solidification conditions. Additionally, in some scenarios, SYSWELD predicts the melt pool is fully solidified approximately 0.5 ms before that observed in the experimental data set, as seen in Figure 8b,c. For the rasters in Figure 8d–f, the Vs obtained directly from the APS experiments reach higher values as compared to what the model predicts. These Vs are also less continuous and "jump" up or down quickly, which is likely due to the limitations of the frame rate of the camera used in the experiments and difficulty in tracking low-power melt pools. If these velocities were averaged, they would better match the expected steady-state velocities.

Although limited in some prediction capabilities, many of the simulations are able to predict the general solidification of rasters, but not spot-melts. From in situ experiments conducted using a dynamic transmission electron microscope (DTEM), Mckeown et al. showed that as the solidification front progresses in a spot-melt, it does so with a relatively constant acceleration [34]. In all three spot-melt scenarios, the predicted velocities from SYSWELD do not exhibit this linear increase. Rather, there appears to be a change from a decreasing to increasing acceleration as the laser power is increased. This suggests that the

simulation is not able to capture this phenomenon. For the rasters in Figure 8d–f, a better correlation is observed, where the velocity initially increases until it reaches a steady state, where this velocity is approximately the laser travel speed. It then slightly decreases when the laser is turned off, until the velocity sharply increases again during the final stages of solidification. Once the laser is turned off, the melt pool is essentially a spot-melt and exhibits the same constant acceleration of the solid–liquid interface, as discussed above.

SYSWELD does not allow for the direct calculation of thermal gradients (Gs), so they were determined using the following relationship:

$$G = \frac{1}{V}\dot{T} \tag{2}$$

where V is the solidification velocity and $\dot{T}$ is the cooling rate. From Figure 9a, the G-V conditions during solidification of a 139 W spot-melt transition from higher thermal gradients and lower velocities to lower thermal gradients and higher velocities as solidification progresses. An opposite relationship is observed in Figure 9b for a 53.5 W and 0.25 m/s raster during the progression of solidification, where low Vs and Gs are initially predicted until steady-state conditions are achieved and the G-V conditions then become approximately constant. When the laser is turned off, the raster melt-pool should exhibit conditions similar to a spot-melt; however, the thermal gradient increases rather than decreases, as in the spot-melt. This inconsistency may be a result of the very low power of the raster, and the melt pool created as a result. Applying these observations to predicted grain morphologies, the solidification conditions of the spot-melt correspond to an initially fully columnar structure that transforms into a mixed structure as solidification progresses. The different G-V conditions in the raster result in an equiaxed structure that transforms to mixed morphology during the final stages of solidification.

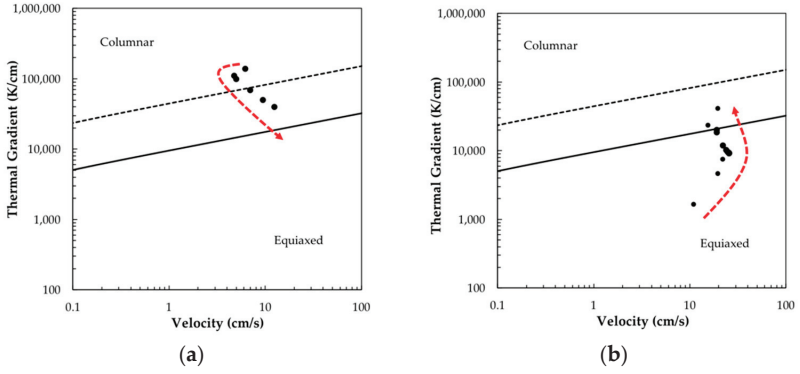

Figure 9. Predicted SYSWELD G-V conditions from the edge to the center of a melt pool or beginning to end of a raster overlaid onto the Ti-1023 CET for (**a**) 139 W spot-melt and (**b**) 53.5 W and 0.25 m/s raster. Note: arrows in (**a**,**b**) show progression of solidification.

All spot-melt and raster scenarios were successfully modeled within FLOW-3D; a representative simulation is presented below in Figure 10. The resulting dimensions of the simulated melt pools were more difficult to match to the experiments than SYSWELD, but no more than 15% error was observed. The increased complexity of FLOW-3D allowed for data output at finer time-steps, and the predicted Vs better matched the solidification characteristics of the melt pool. For the spot-melt in Figure 11a, both FLOW-3D and SYSWELD datasets agree with the experimental Vs and maintain a constant velocity of ~0.05 m/s. However, SYSWELD predicts final solidification occurs 0.5 ms before experimentally observed, while FLOW-3D better matches. At the end of solidification, FLOW-3D predicts a large increase in velocity that was not captured in the experimental dataset. This final increase was predicted in every performed FLOW-3D simulation, while if observed in the

experimental data, was not to the extent of FLOW-3D. However, other rapid solidification experiments have reported this acceleration during the final stages of solidification [26,35]. Zhao et al. attributed it to the maximum local thermal gradients better aligning with the easy growth directions as the grains approach the center of the melt pool [24]. Therefore, it is likely this phenomenon did occur in the melt pool, but the limited spatial and temporal resolution of the experimental in situ imaging was unable to capture it. These results are also in good agreement with other simulation work that has examined solidification velocities of spot-melts for AM and traditional laser welding [25,36,37]. For the raster presented in Figure 11b, similar observations are seen between the three datasets. In much of the steady-state region, both FLOW-3D and SYSWELD predict an approximately constant velocity of 0.25 m/s that matches with the experimental data. There are many variations in the experimental data, but they are approximately centered around the travel speed, 0.25 m/s. These jumps are likely due to the difficulty in seeing this low-power raster, and therefore manually tracking the melt pool. Although the two predicted datasets align during the steady state, the transient conditions deviate. SYSWELD does not predict a steady state occurring until around 2 ms, where both FLOW-3D and experimental data show that it occurs earlier at 1 ms.

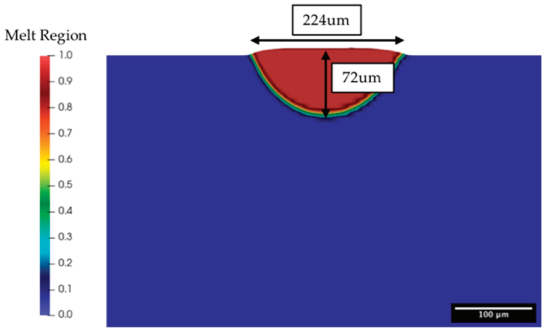

Figure 10. Cross-section of 82 W spot-melt scenario, showing maximum melt region predicted by FLOW-3D and the resulting melt pool depth and width.

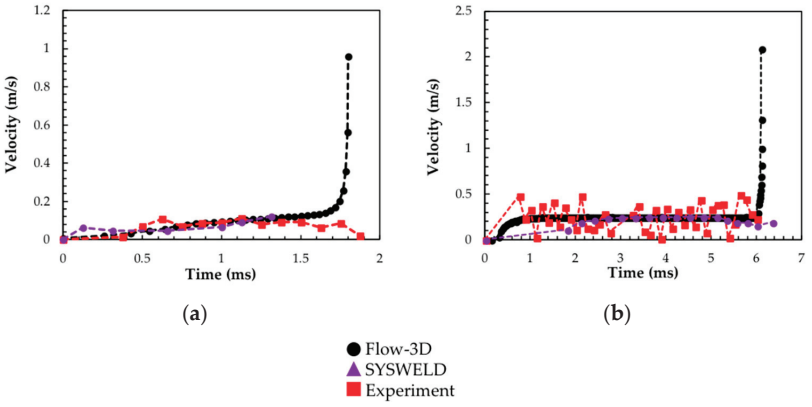

Figure 11. Comparison of solidification velocity at the top of the melt pool predicted by FLOW-3D and SYSWELD and observed in the experiment for (**a**) 139 W spot-melt and (**b**) 53.5 W and 0.25 m/s raster. Note: time = 0 for (**a**) refers to the moment the laser was turned off and time = 0 for (**b**) refers to the moment the laser was turned on and began rastering. Additionally, the laser was turned off at 6 ms in (**b**).

Predicted G-V conditions from FLOW-3D are compared to SYSWELD for the same spot-melt and raster scenario below in Figure 12. The initial solidification conditions of the spot-melt in Figure 12a deviate between the two pieces of software, where FLOW-3D predicts a much lower solidification velocity for a similar thermal gradient. Despite this difference, the same columnar grain morphology is expected using the overlaid CET. However, previous spot-melt simulation work has shown that as solidification progresses, velocity continually increases, while thermal gradients decrease [25,36,37]. These observations better align with the predictions of FLOW-3D compared to SYSWELD. As solidification progresses, the G-V conditions predicted by the two pieces of software begin to align, until the premature solidification prediction of the SYSWELD model. The acceleration of the solid/liquid interface at the final stages of solidification with FLOW-3D results in the prediction of a greater chance of forming a fully equiaxed region in the spot-melt. Raghavan et al. performed similar G-V mapping for Inconel 718 spot-melts and also found that at the later stages of solidification, the decreasing Gs and increasing Vs resulted in a greater likelihood of transitioning from columnar to equiaxed grains [25]. This change in grain morphology is also commonly observed during fusion welding [38].

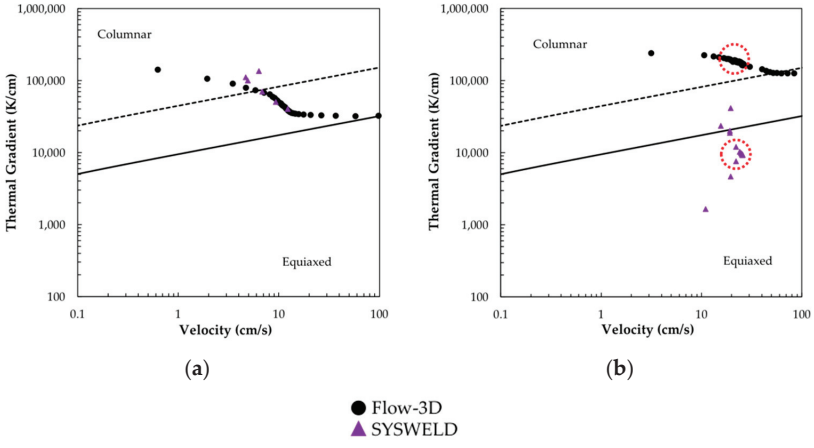

Figure 12. Predicted FLOW-3D and SYSWELD G-V conditions at the top of the melt pool overlaid onto the Ti-1023 CET for (**a**) 139 W spot-melt and (**b**) 53.5 W and 0.25 m/s raster. Note: circles in (**b**) show the steady-state regions.

Unlike the spot-melt scenario, Figure 12b shows a significant deviation between FLOW-3D and SYSWELD for predicted G-V conditions of a raster. The thermal gradients at the initial solidification of the melt pool differ by orders of magnitude. This results in a predicted columnar morphology for FLOW-3D and equiaxed for SYSWELD. The discrepancy is likely a result of FLOW-3D accounting for Marangoni flow and recoil pressure in the melt pool. Khairallah et al. showed that activating these two effects resulted in lower amounts of residual heat compared to more simplistic models that neglect those phenomena [39]. The reason for this is that Marangoni flow and recoil pressure effectively alter the cooling conditions, due to the formation of a melt pool with increased surface area, where evaporative and radiative surface cooling can then aid in increasing the cooling rate of the melt pool. As discussed previously, SYSWELD does not directly output a thermal gradient, and Equation (2) was used to indirectly obtain it from solidification velocity and cooling rate. If more simplistic models such as SYSWELD predict larger amounts of stored heat for the same process parameters, this results in slower cooling rates than those of more complicated models. This explains why SYSWELD predicts smaller thermal gradients as compared to FLOW-3D for similar velocities. As a steady state is approached within the system, both models continue to exhibit dissimilar trends. For FLOW-3D, the thermal gradient decreases before remaining relatively constant during the steady state,

while the thermal gradient increases in SYSWELD. In similar modeling work conducted by Polonsky et al., the addition of fluid flow was shown to not alter the G-V trends during solidification [40]. However, this is not true in this work, although this discrepancy may be a result of how Gs were indirectly calculated, rather than directly outputted. Lastly, when the laser is turned off and solidification begins to resemble that of a spot-melt rather than a raster, FLOW-3D follows the G-V trend predicted by both models in Figure 12a, where the velocity increases as the thermal gradient slightly decreases. SYSWELD predicts the complete opposite trend and does not even match up with its own spot-melt prediction. However, this is likely due to the combination of a small melt-pool and the inability of SYSWELD to output sufficiently fine time-steps, rather than discrepancies in the same software for spot-melts and rasters. Although the final solidification conditions of the two models both predict a mixed structure, the evolution from start to finish is completely different. FLOW-3D is columnar where SYSWELD is equiaxed for much of the raster, until both transition to mixed during the final stages of solidification.

4. Conclusions

Two different simulation tools, SYSWELD and FLOW-3D, were used to model simulated L-PBF spot-melt and raster experiments performed at the APS at ANL. These experiments were used to calibrate the models and compare the accuracy of their solidification velocity predictions. From this work, drawn conclusions are as follows:

(1) For spot-melts, model predictions from more simplistic tools such as SYSWELD are able to match velocity profiles obtained from specialized AM-simulated experiments. However, the relatively coarse time-steps make it difficult to fully capture the initial, intermediate, and final stages of melt-pool solidification.
(2) Final solidification phenomena known to occur in rapid solidification experiments, such as rapid acceleration of the solid–liquid interface, were undetectable with the utilized in situ synchrtoron x-ray imaging, but were predicted by FLOW-3D. This capability shows that high-fidelity models are able to provide insights into melt-pool solidification conditions that may not be detectable with some experimental setups.
(3) G-V predictions of spot-melts from SYSWELD and FLOW-3D align with each other and experimental observations from other work. This is not true of raster simulations, where SYSWELD predicts G-V trends different from those of FLOW-3D and basic knowledge of melt-pool solidification. This presents a limitation of SYSWELD for predicting as-built grain morphologies using solidification maps.

Without knowledge of the actual grain morphologies of these experiments, it is difficult to determine the accuracy of the G-V predictions. The use of electron backscatter diffraction (EBSD) would provide insights and validate or invalidate grain morphology predictions of the models. If validated, this approach provides a method for the determination of parameter regimes that produce desired grain morphologies. This methodology can also be applied to understand the effect of other processing parameters, such as scan strategy or preheat temperature.

Although direct comparison to as-solidified grain morphologies is still needed to validate the predictions of these models, FLOW-3D better predicts solidification conditions during L-PBF and can be utilized to advance our understanding of alloys' response to a range of AM-like conditions.

Author Contributions: Conceptualization, C.J., A.S. and A.J.C.; methodology, C.J., A.S., C.G.B., K.F., T.S. and A.J.C.; validation, C.J., C.G.B. and J.K.-T.; formal analysis, C.J.; investigation, C.J., A.S., J.K.-T., K.F., T.S. and A.J.C.; writing—original draft preparation, C.J.; writing—review and editing, C.J., A.J.C. and T.P.; visualization, C.J.; supervision, A.J.C.; project administration, A.J.C.; funding acquisition, A.J.C. All authors have read and agreed to the published version of the manuscript.

Funding: This work was supported by the Department of the Navy, USA, Office of Naval Research, USA, under ONR award number N00014-18-1-2794. Any opinions, findings, and conclusions or recommendations expressed in this material are those of the author(s) and do not necessarily reflect

the views of the Office of Naval Research. This research used resources of the Advanced Photon Source, a U.S. Department of Energy (DOE) Office of Science user facility operated for the DOE Office of Science by Argonne National Laboratory under Contract No. DE-AC02-06CH11357.

Data Availability Statement: Not applicable.

Acknowledgments: The authors gratefully acknowledge ATI (Allegheny Technologies Incorporated), a member of the Center for Advanced Non-Ferrous Structural Alloys (CANFSA), a National Science Foundation Industry/University Cooperative Research Center (I/UCRC) (Award No. 2137243) at the Colorado School of Mines, for providing the studied material.

Conflicts of Interest: The authors declare no conflict of interest.

References

1. Duerig, T.W.; Terlinde, G.T.; Williams, J.C. Phase transformations and tensile properties of Ti-10V-2Fe-3AI. *Met. Mater. Trans. A* **1980**, *11*, 1987–1998. [CrossRef]
2. Duerig, T.W.; Williams, J.C. *Beta Titanium Alloys in the 80s: Proceedings of the Symposium*; Metallurgical Society of AIME: Englewood, CO, USA, 1984; pp. 19–67.
3. Lütjering, G.; Williams, J.C. *Titanium*, 2nd ed.; Springer: Berlin/Heidelberg, Germany; New York, NY, USA, 2007.
4. Bermingham, M.; StJohn, D.; Krynen, J.; Tedman-Jones, S.; Dargusch, M. Promoting the columnar to equiaxed transition and grain refinement of titanium alloys during additive manufacturing. *Acta Mater.* **2019**, *168*, 261–274. [CrossRef]
5. Roehling, T.T.; Shi, R.; Khairallah, S.A.; Roehling, J.D.; Guss, G.M.; McKeown, J.T.; Matthews, M.J. Controlling grain nucleation and morphology by laser beam shaping in metal additive manufacturing. *Mater. Des.* **2020**, *195*, 109071. [CrossRef]
6. Qiu, C.; Ravi, G.; Attallah, M.M. Microstructural control during direct laser deposition of a β-titanium alloy. *Mater. Des.* **2015**, *81*, 21–30. [CrossRef]
7. Zhu, Y.-Y.; Tang, H.-B.; Li, Z.; Xu, C.; He, B. Solidification behavior and grain morphology of laser additive manufacturing titanium alloys. *J. Alloy. Compd.* **2018**, *777*, 712–716. [CrossRef]
8. Balla, V.K.; Das, M.; Mohammad, A.; Al-Ahmari, A.M. Additive Manufacturing of γ-TiAl: Processing, Microstructure, and Properties: Additive Manufacturing of γ-TiAl: Processing. *Adv. Eng. Mater.* **2016**, *18*, 1208–1215. [CrossRef]
9. Kurzynowski, T.; Gruber, K.; Stopyra, W.; Kuźnicka, B.; Chlebus, E. Correlation between process parameters, microstructure and properties of 316 L stainless steel processed by selective laser melting. *Mater. Sci. Eng. A* **2018**, *718*, 64–73. [CrossRef]
10. Liang, Y.-J.; Cheng, X.; Li, J.; Wang, H.-M. Microstructural control during laser additive manufacturing of single-crystal nickel-base superalloys: New processing–microstructure maps involving powder feeding. *Mater. Des.* **2017**, *130*, 197–207. [CrossRef]
11. Yang, J.; Yu, H.; Yin, J.; Gao, M.; Wang, Z.; Zeng, X. Formation and control of martensite in Ti-6Al-4V alloy produced by selective laser melting. *Mater. Des.* **2016**, *108*, 308–318. [CrossRef]
12. Zhai, Y.; Galarraga, H.; Lados, D.A. Microstructure, static properties, and fatigue crack growth mechanisms in Ti-6Al-4V fabricated by additive manufacturing: LENS and EBM. *Eng. Fail. Anal.* **2016**, *69*, 3–14. [CrossRef]
13. Thijs, L.; Verhaeghe, F.; Craeghs, T.; Van Humbeeck, J.; Kruth, J.-P. A study of the microstructural evolution during selective laser melting of Ti–6Al–4V. *Acta Mater.* **2010**, *58*, 3303–3312. [CrossRef]
14. Levkulich, N.; Semiatin, S.; Gockel, J.; Middendorf, J.; DeWald, A.; Klingbeil, N. The effect of process parameters on residual stress evolution and distortion in the laser powder bed fusion of Ti-6Al-4V. *Addit. Manuf.* **2019**, *28*, 475–484. [CrossRef]
15. Saville, A.I.; Vogel, S.C.; Creuziger, A.; Benzing, J.T.; Pilchak, A.L.; Nandwana, P.; Klemm-Toole, J.; Clarke, K.D.; Semiatin, S.L.; Clarke, A.J. Texture evolution as a function of scan strategy and build height in electron beam melted Ti-6Al-4V. *Addit. Manuf.* **2021**, *46*, 102118. [CrossRef]
16. Norsk Titanium Delivers First FAA-Certified, Additive Manufactured Ti64 Structural Aviation Components. Available online: http://www.norsktitanium.com/media/press/norsk-titanium-delivers-first-faacertified-additive-manufactured-ti64-structural-aviation-components (accessed on 20 October 2021).
17. Zopp, C.; Blümer, S.; Schubert, F.; Kroll, L. Processing of a metastable titanium alloy (Ti-5553) by selective laser melting. *Ain Shams Eng. J.* **2017**, *8*, 475–479. [CrossRef]
18. Schwab, H.; Palm, F.; Kühn, U.; Eckert, J. Microstructure and mechanical properties of the near-beta titanium alloy Ti-5553 processed by selective laser melting. *Mater. Des.* **2016**, *105*, 75–80. [CrossRef]
19. Dehoff, R.; Kirka, M.M.; Sames, W.J.; Bilheux, H.; Tremsin, A.; Lowe, L.E.; Babu, S. Site specific control of crystallographic grain orientation through electron beam additive manufacturing. *Mater. Sci. Technol.* **2014**, *31*, 931–938. [CrossRef]
20. Plotkowski, A.; Ferguson, J.; Stump, B.; Halsey, W.; Paquit, V.; Joslin, C.; Babu, S.; Rossy, A.M.; Kirka, M.; Dehoff, R. A stochastic scan strategy for grain structure control in complex geometries using electron beam powder bed fusion. *Addit. Manuf.* **2021**, *46*, 102092. [CrossRef]
21. Kobryn, P.; Semiatin, S. Microstructure and texture evolution during solidification processing of Ti–6Al–4V. *J. Mater. Process. Technol.* **2003**, *135*, 330–339. [CrossRef]
22. DebRoy, T.; Wei, H.L.; Zuback, J.S.; Mukherjee, T.; Elmer, J.W.; Milewski, J.O.; Beese, A.M.; Wilson-Heid, A.; De, A.; Zhang, W. Additive manufacturing of metallic components–Process, structure and properties. *Prog. Mater. Sci.* **2018**, *92*, 112–224. [CrossRef]

23. Al-Bermani, S.S.; Blackmore, M.L.; Zhang, W.; Todd, I. The Origin of Microstructural Diversity, Texture, and Mechanical Properties in Electron Beam Melted Ti-6Al-4V. *Met. Mater. Trans. A* **2010**, *41*, 3422–3434. [CrossRef]
24. Zhao, C.; Fezzaa, K.; Cunningham, R.W.; Wen, H.; De Carlo, F.; Chen, L.; Rollett, A.D.; Sun, T. Real-time monitoring of laser powder bed fusion process using high-speed X-ray imaging and diffraction. *Sci. Rep.* **2017**, *7*, 3602. [CrossRef] [PubMed]
25. Raghavan, N.; Dehoff, R.; Pannala, S.; Simunovic, S.; Kirka, M.; Turner, J.; Carlson, N.; Babu, S.S. Numerical modeling of heat-transfer and the influence of process parameters on tailoring the grain morphology of IN718 in electron beam additive manufacturing. *Acta Mater.* **2016**, *112*, 303–314. [CrossRef]
26. Mills, K.C. *Recommended Values of Thermophysical Properties for Selected Commercial Alloys*; Woodhead: Cambridge, UK, 2002. [CrossRef]
27. Thermo-Calc Software TCTI/Ti-Alloys Database Version 3.
28. Bayat, M.; Thanki, A.; Mohanty, S.; Witvrouw, A.; Yang, S.; Thorborg, J.; Tiedje, N.S.; Hattel, J. Keyhole-induced porosities in Laser-based Powder Bed Fusion (L-PBF) of Ti6Al4V: High-fidelity modelling and experimental validation. *Addit. Manuf.* **2019**, *30*, 100835. [CrossRef]
29. Kurz, W.; Giovanola, B.; Trivedi, R. Theory of microstructural development during rapid solidification. *Acta Met.* **1986**, *34*, 823–830. [CrossRef]
30. Gäumann, M.; Bezençon, C.; Canalis, P.; Kurz, W. Single-crystal laser deposition of superalloys: Processing–microstructure maps. *Acta Mater.* **2001**, *49*, 1051–1062. [CrossRef]
31. Liu, D.; Wang, Y. Mesoscale multi-physics simulation of rapid solidification of Ti-6Al-4V alloy. *Addit. Manuf.* **2018**, *25*, 551–562. [CrossRef]
32. Rolchigo, M.; LeSar, R. Modeling of binary alloy solidification under conditions representative of Additive Manufacturing. *Comput. Mater. Sci.* **2018**, *150*, 535–545. [CrossRef]
33. Hunt, J. Steady state columnar and equiaxed growth of dendrites and eutectic. *Mater. Sci. Eng.* **1984**, *65*, 75–83. [CrossRef]
34. McKeown, J.T.; Zweiacker, K.; Liu, C.; Coughlin, D.R.; Clarke, A.J.; Baldwin, J.K.; Gibbs, J.; Roehling, J.D.; Imhoff, S.D.; Gibbs, P.J.; et al. Time-Resolved In Situ Measurements During Rapid Alloy Solidification: Experimental Insight for Additive Manufacturing. *JOM* **2016**, *68*, 985–999. [CrossRef]
35. McKeown, J.T.; Kulovits, A.K.; Liu, C.; Zweiacker, K.; Reed, B.W.; LaGrange, T.; Wiezorek, J.M.; Campbell, G.H. In situ transmission electron microscopy of crystal growth-mode transitions during rapid solidification of a hypoeutectic Al–Cu alloy. *Acta Mater.* **2014**, *65*, 56–68. [CrossRef]
36. He, X.; Fuerschbach, P.W.; DebRoy, T. Heat transfer and fluid flow during laser spot welding of 304 stainless steel. *J. Phys. D Appl. Phys.* **2003**, *36*, 1388–1398. [CrossRef]
37. He, X.; Elmer, J.W.; DebRoy, T. Heat transfer and fluid flow in laser microwelding. *J. Appl. Phys.* **2005**, *97*, 084909. [CrossRef]
38. Lienert, T.; Siewert, T.; Babu, S.; Acoff, V. (Eds.) Fundamentals of Weld Solidification. In *Welding Fundamentals and Processes*; ASM International: Almere, The Netherlands, 2011; pp. 96–114. [CrossRef]
39. Khairallah, S.A.; Anderson, A.T.; Rubenchik, A.; King, W.E. Laser powder-bed fusion additive manufacturing: Physics of complex melt flow and formation mechanisms of pores, spatter, and denudation zones. *Acta Mater.* **2016**, *108*, 36–45. [CrossRef]
40. Polonsky, A.T.; Raghavan, N.; Echlin, M.P.; Kirka, M.M.; Dehoff, R.R.; Pollock, T.M. 3D Characterization of the Columnar-to-Equiaxed Transition in Additively Manufactured Inconel 718. In *Superalloys 2020*; Tin, S., Hardy, M., Clews, J., Cormier, J., Feng, Q., Marcin, J., O'Brien, C., Suzuki, A., Eds.; Springer International Publishing: Cham, Switzerland, 2020; pp. 990–1002. [CrossRef]

metals

MDPI

Article

Permeability Measurements of 3D Microstructures Generated by Phase Field Simulation of the Solidification of an Al-Si Alloy during Chill Casting

Ralf Berger [1,*], Markus Apel [1], Gottfried Laschet [1], Wilhelm Jessen [2], Wolfgang Schröder [2], Jens Wipperfürth [3], Johannes Austermann [3] and Christian Hopmann [3]

[1] ACCESS e.V, Intzestrasse 5, D-52072 Aachen, Germany; m.apel@access-technology.de (M.A.); g.laschet@access-technology.de (G.L.)
[2] Institut of Aerodynamics (AIA), RWTH Aachen University, Wüllnerstrasse 5a, D-52062 Aachen, Germany; W.Jessen@aia.rwth-aachen.de (W.J.); office@aia.rwth-aachen.de (W.S.)
[3] Institute of Plastics Processing (IKV), RWTH Aachen University, Seffenter Weg 201, D-52064 Aachen, Germany; jens.wipperfuerth@ikv.rwth-aachen.de (J.W.); johannes.austermann@ikv.rwth-aachen.de (J.A.); office@ikv.rwth-aachen.de (C.H.)
* Correspondence: r.berger@access-technology.de

Abstract: The permeability of the semi-solid state is important for the compensation of volume shrinkage during solidification, since insufficient melt feeding can cause casting defects such as hot cracks or pores. Direct measurement of permeability during the dynamical evolution of solidification structures is almost impossible, and numerical simulations are the best way to obtain quantitative values. Equiaxed solidification of the Al-Si-Mg alloy A356 was simulated on the microscopic scale using the phase field method. Simulated 3D solidification structures for different stages along the solidification path were digitally processed and scaled up to generate 3D models by additive manufacturing via fused filament fabrication (FFF). The Darcy permeability of these models was determined by measuring the flow rate and the pressure drop using glycerol as a model fluid. The main focus of this work is a comparison of the measured permeability to results from computational fluid flow simulations in the phase field framework. In particular, the effect of the geometrical constraint due to isolated domain walls in a unit cell with a periodic microstructure is discussed. A novel method to minimize this effect is presented. For permeability values varying by more than two orders of magnitude, the largest deviation between measured and simulated permeabilities is less than a factor of two.

Keywords: solidification; permeability; phase field; additive manufacturing; measurement; scaled model

Citation: Berger, R.; Apel, M.; Laschet, G.; Jessen, W.; Schröder, W.; Wipperfürth, J.; Austermann, J.; Hopmann, C. Permeability Measurements of 3D Microstructures Generated by Phase Field Simulation of the Solidification of an Al-Si Alloy during Chill Casting. *Metals* **2021**, *11*, 1895. https://doi.org/10.3390/met11121895

Academic Editor: Noé Cheung

Received: 26 October 2021
Accepted: 22 November 2021
Published: 25 November 2021

1. Introduction

In casting processes, the formation of defects such as shrinkage porosity [1] or hot tears [2,3] depend on melt flow through the mushy zone, and hence on its permeability. Due to the small scale of length of the melt-filled structures, the Reynolds number is typically very low. The Reynolds number describes the ratio of the inertial forces over the viscous forces in a flow, therefore, for a very low Reynolds number the contribution of the inertial term in the Navier–Stokes equations can be considered negligible. Omitting this term leads to the Stokes equations, which, for an incompressible fluid and a steady state solution, take the form:

$$\mu \nabla^2 \boldsymbol{u} - \nabla p + \boldsymbol{f} = 0$$

$$\nabla \cdot \boldsymbol{u} = 0$$

where $\boldsymbol{u}$ stands for the vector field of the velocity, $\boldsymbol{f}$ for that of external forces, and p for the scalar field of the pressure. The Stokes equations describe creeping flows and, for an incompressible fluid, constitute a linear differential equation system. Since solutions $(\boldsymbol{u}, p)$

of the associated homogeneous system can be superimposed linearly, this implies a linear correlation between the averaged pressure gradient $\overline{\nabla p}$ and the averaged flow velocity $\overline{u}$ (the superficial velocity) for a region. This linear correlation is described by Darcy's law:

$$\overline{u} = -\frac{K}{\mu} \cdot \overline{\nabla p}$$

Here, K is the Darcy permeability, which in the case of anisotropy must be expressed as a tensor. This tensor allows for a homogenized description of the permeability of the mushy zone on a mesoscopic scale.

In this research paper, permeabilities resulting from CFD simulations on different microstructures are compared to measurements performed on scaled models of the same microstructures. In this case, the microstructures were generated by the multi-phase-field simulation [4] of the equiaxed solidification of a hypoeutectic Al-Si alloy during chill casting. For four different selected time steps, the generated phase field data were digitalized and written as an STL file. Scaled models were built from the STL data by additive manufacturing. Permeability measurements were performed on these models.

The results of these measurements are compared with results from CFD simulations on the same unscaled melt-filled dendrite networks.

Related Works

Several approaches have been used to directly measure the Darcy permeability of the mushy zone, e.g., by measuring the flow of eutectic melt in carefully temperature-controlled samples or by removing the melt during solidification and forcing water through the remaining porous microstructure [5,6].

In other approaches, the microstructure at some stage of solidification was preserved, either by quenching, or by removal of melt, then analysed by metallographic methods including serial sectioning [7] and microtomography [8] to generate virtual 2D [9] or 3D [7,8,10] models which were then investigated aided by CFD simulations to determine the permeability.

Microstructures generated, e.g., by phase field simulations, offer the opportunity to take virtual snapshots of the same structure at several stages of the solidification progress with clearly defined regions of solid and liquid. The permeability of such structures was also investigated in CFD simulations [10–12].

Takaki et al. [13] performed a succession of phase field and lattice Boltzmann flow large scale simulations in order to predict the permeability of melt flow normal to directionally solidified columnar dendrite structure. Li et al. [14] achieved 3D phase field simulation of the solidification of the hot tear sensitive Al-Cu 4.5% alloy. At selected fraction solids, they extracted 300 2D slices of the predicted equiaxed microstructure in order to reconstruct a 3D model suitable for the subsequent fluid flow analysis and permeability prediction. Recently, Zhang et al. [15] studied the influence of the forced flow on the permeability of dendritic networks by using a combined phase field lattice Boltzmann method. They saw that for columnar dendrite networks, the permeability decreases exponentially to the incoming velocity due to impingement or interlocking of secondary arms; whereas for equiaxed networks, their permeability tensors become more anisotropic with increasing melt velocity, and their networks tend to become columnar. Khajeh and Maijer [16] generated 3D models of microstructures by X-ray microtomography and compared permeabilities resulting from Kozeny–Carman, CFD simulations and flow measurements on scaled models. James et al. [17] compared CFD results with permeability measurements for a structure constructed of layered, slotted plates. Moreover, Bodaghi et al. [18] recently compared three additive manufacturing techniques (fused deposition method, stereolithography (SLA) and multi jet fusion) to produce referenced porous media for permeability measurements and show that the SLA process yields the highest integrity in the printed samples with tolerances well below 2% of nominal thickness.

2. Materials and Methods

2.1. Phase Field Model

The phase field simulation started from a pure melt of Al, 7% Si, 0.3% Mg and 0.1% Cu. The latter chemical element was added to mimic the effect of trace elements in a technical A356 casting alloy. The solidification was simulated at a resolution of 0.5 µm, using the finite difference method implemented in MICRESS [19]. This resolution was chosen to adequately represent features such as narrow channels and tip radii of dendrites, with feature sizes in the range of several micrometers. To represent a statistically homogeneous, isotropic mushy zone in an adequate manner [20], it was desirable to choose a large RVE (representative volume element) that included multiple grains, but processing power and memory size of the available computational hardware limited the feasible RVE dimensions. Since it is statistically unlikely to find grains with the same orientation next to each other in an equiaxially solidified region, then a grain that has another representation of itself as a direct neighbour under periodic boundary conditions should also be avoided. This avoids artificial contributions to the anisotropy of the permeability.

For the aforementioned reasons, an RVE size of 150 × 150 × 150 µm^3 was chosen and for primary solidification, six fcc-Al nuclei were placed randomly in the RVE, corresponding to an average grain diameter of 83 µm. The multi-phase-field approach used in MICRESS assigns a phase field to each grain, allowing different anisotropy functions for the solid–liquid interface corresponding to different grain orientations, as well as material properties such as diffusivities and individual concentration fields depending on the physical phase [21]. The aluminium based thermodynamic database from Thermo–Calc [22,23] was linked to account for the thermodynamics of phase transitions.

To represent solidification conditions in the bulk of a part produced by chill casting, periodic boundary conditions together with a superimposed heat extraction rate of 240 W/cm^3 were chosen. The temperature evolution was derived from the energy balance, taking into account enthalpy, heat capacity and the heat extraction. In the RVE, a uniform temperature was assumed. Then, the simulation resulted in a cooling rate of 15 K/s during primary solidification, close to cooling curves measured in a chill cast axisymmetric A356 bowl [24].

At a solid fraction of f_S = 0.50 eutectic solidification was started by additional solidification of silicon in diamond structure from silicon nuclei, which were allowed to nucleate at 4 K undercooling in the melt or at 10 K undercooling at the interface between melt and the fcc-Al-phase. While the resolution of the simulation was insufficient to fully resolve fine silicon lamellae growing during eutectic solidification due to computational limitations, it was sufficient to simulate the effect of eutectic growth on the solid–liquid interface, and hence the permeability of the microstructure.

The eutectic solidification resulted in a strong recalescence, as shown in Figure 1. This was due to the assumption of a constant heat extraction rate in the simulation. The effect could have been avoided, e.g., by a multiscale approach [25,26], which would better reflect the thermal conditions during this phase of solidification, whereby the increased latent heat released from eutectic solidification in the region adjacent to the RVE would reduce the cooling rate and hence the temperature gradient, which locally would lead to a reduced heat extraction rate.

During solidification, a snapshot of the phase field φ was generated at regular intervals to observe the evolving microstructure and analyse the change of its permeability. Additional details of the simulation scenario and analysis of the permeability are described in [4]. Four of these microstructures were chosen for the additive manufacturing of scaled physical samples for which the permeability was measured experimentally.

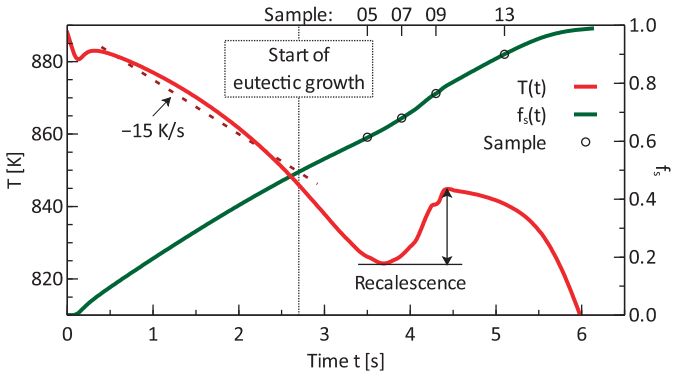

Figure 1. Temperature and solid fraction over time during solidification.

2.2. Digital Filtering

Several issues emerge when phase field simulation data are used as direct input for the generation of a physical model for an experimental study, as discussed below. An important advantage when determining the permeability of periodic structures in CFD simulations is the ability to also apply periodic boundary conditions to the flow, so that the RVE can be regarded as embedded in a larger mushy region with similar permeability conditions. The flow across "side" boundaries with a normal perpendicular to the pressure gradient can significantly contribute to the permeability in the direction of the gradient. The periodic boundary conditions of the CFD simulation also allow for a net flow across those "side" boundaries from which off diagonal elements of the permeability tensor can be deduced, so the eigenvalues and -vectors of the complete tensor can be determined. These periodic flow conditions cannot be reproduced in experimental measurements, where these boundaries are blocked by an enclosing container, not permitting any flow across the sides of the RVE. To minimize the effect of such limitations, a filtering process was applied to the microstructure phase field data from which the models were generated:

(1) To minimize the effect due to blocked flow at the "sides", an RVE of the periodic structure was chosen by a translation, such that the flow resulting from CFD simulations was minimal across the RVE boundaries parallel to the pressure gradient. As a criterion, the absolute flow across planes parallel to the boundaries was integrated and new boundary planes chosen, for which this quantity is small;
(2) A supporting structure was added to keep grains in place. This structure consisted of 1.5 mm wide struts along the edges of the cubic RVE;
(3) Completely encapsulated liquid, which does not contribute to the permeability, was removed (classified as solid region) to enhance structural stability of the models;
(4) Isolated solid regions unconnected to the supported structure were removed.

The filtering process is illustrated in Figure 2. The differences between solid fractions due to filtering were small ($\Delta f_S < 0.01$), figures for f_S given below were those of the original structures. From the resulting phase field data, an iso-surface at $\varphi = 0.5$ of the phase field variable φ was saved in an STL format. Between the simulation domain of extension $150 \times 150 \times 150$ μm^3 and the corresponding thermoplastic sample of 5 cm side length, a scale factor of $\alpha = 10^3/3$ was adopted. This scale factor was chosen so that the minimum feature size of the samples was within the resolution of the used additive manufacturing techniques.

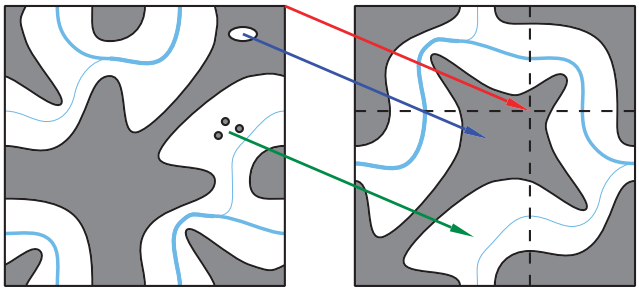

Figure 2. Illustration of the filtering process. Red arrow: a unit cell of the periodic structure is chosen so that obstruction of fluid flow (light blue for a horizontal gradient) at side boundaries is minimized. Blue arrow: enclosed liquid is removed. Green arrow: Small solid particles are removed.

Additional Navier–Stokes simulations were performed on the microstructures that resulted from the filtering process, using no slip boundary conditions on boundaries parallel to the pressure gradient and fixed pressure and orthogonal in- and outflow on boundaries perpendicular to the pressure gradient. As for the CFD simulations using periodic boundary conditions, low pressure gradients were applied, resulting in creeping flows with Reynolds numbers $Re < 10^{-5}$. For more details concerning the CFD simulations see [4].

2.3. Additive Manufacturing

The prepared samples were manufactured additively via fused filament fabrication (FFF). FFF is an extrusion-based process in which strands of molten thermoplastic material are layer-wise deposited to build up a 3D-part [27].

The layer-wise manufacturing principle of FFF allows for the realization of highly complex structures not otherwise possible to manufacture, as represented by the dendritic grain microstructure [28–30]. However, technology-specific limitations must be considered. These include the necessity of support structures during manufacturing and their removal [31]. Support structures are additional geometries separate from the part that provides a base for areas of the part which would otherwise not be supported by previous layers [32]. After the manufacturing process, the support structures are removed. In FFF, support structures are required in areas of the part in which newly deposited beads are not otherwise supported by previous layers. Unsupported strands would otherwise sag, resulting in low geometric part quality or part defects. When manufacturing complex structures, as presented in this work, the mechanical removal of support structures might not be possible due to inaccessibility. However, by using a soluble FFF material for support structures, they can be removed from otherwise inaccessible areas by rinsing in solvent. Based on this assessment, FFF is suitable for the manufacturing of scaled grain microstructure specimens.

For FFF, the X1000 from German RepRap GmbH (Feldkirchen, Germany) was used with a X500 high temperature dual extruder. The dual extrusion set-up enabled the possibility to simultaneously use multiple materials, such as a main material to build up the part in addition to a support material which was required for the complex internal structures. The diameter of the nozzle was 0.4 mm and thus led to a high accuracy and quality of the part. A layer height of 0.2 mm was chosen. For slicing, the Software Simplify3D developed by Simplify3D, Cincinnati, OH, USA, was used. The FFF processing parameters are listed in Table 1. To manufacture the specimens, Polyamide 6 (PA6) was utilized, as it shows good media resistance against a wide range of media, such as glycerol. For the support structures, polyvinyl alcohol (PVA) was used. PVA is water-soluble, therefore the support structures could be removed after manufacturing by soaking and rinsing in water.

Table 1. FFF process parameters for specimen manufacturing.

Setting	PA6	PVA
Nozzle temperature [°C]	260	220
Build plate temperature [°C]	80	
Nozzle diameter [mm]	0.4	0.4
Layer height [mm]	0.2	
Extrusion width [mm]	0.5	
Printing speed [mm/s]	30	
Infill density [%]	100	n/a

During the solidification progress, four equiaxed microstructures, corresponding to fraction solid (f_S) varying from 0.61 up to 0.91, were selected, and scaled 3D samples were printed with a side length of $5 \times 5 \times 5$ cm^3. Seven polyamide samples (see Figure 3) for 4 equiaxed morphologies were produced by a fused filament deposition process.

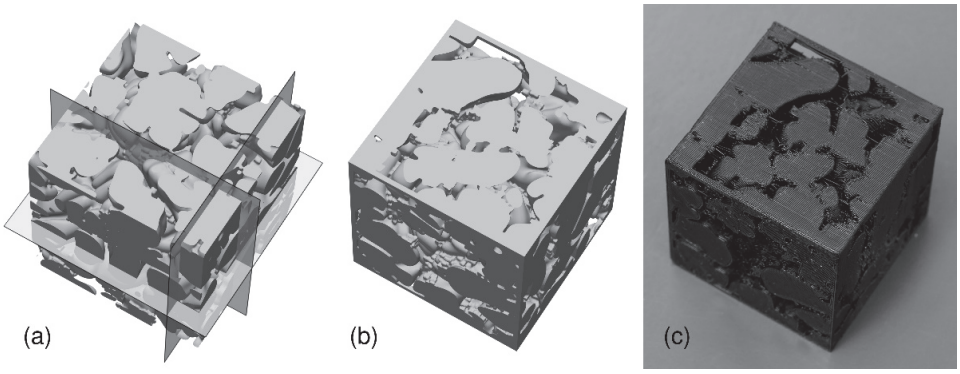

Figure 3. Microstructure geometry with an RVE edge length of 150 µm before (**a**) and after (**b**) filtering, and scaled, additively manufactured microstructure sample (**c**) with an edge length of 5 cm. The structure has a solid fraction f_S = 68.1%. The transparent planes in (**a**) indicate the new boundaries chosen for the filtering process.

2.4. Permeability Measurements

Measurements of the permeability were performed by using a fluid with similar characteristics to a molten metal. The flow rate and pressure drop through the scaled porous samples Δp were measured using an experimental set-up that was built according to the set-up described by Khajeh and Maijer [33].

To achieve similarity to the flow conditions occurring in a solidifying alloy ($Re < 1$), it was necessary to use a liquid with a high viscosity. Therefore, pure glycerol was chosen for these measurements.

According to Darcy's law [33]:

$$\frac{m/t\rho}{A} = \frac{Q}{A} = \frac{K}{\mu}\left(\frac{\Delta p}{L}\right),$$

the permeability K is calculated, where A is the cross-section area of the sample, L is the length of the sample, Q is the volumetric flow rate, ρ is the density of the fluid, and μ is the viscosity of the fluid. Since the fluid properties ρ and μ exhibit temperature dependence, the temperature of the fluid was measured after each test. The properties of glycerol were obtained via interpolation from literature values [34,35].

The experimental set up shown in Figure 4 consisted of a pressurized tank, a vacuum pump, a sample holder, and a pipe configuration with different valves. The 24 L pressurized tank equipped with an external pressure source was used as fluid reservoir. The cube-shaped samples (see Figure 3) were mounted into a sample holder and the measurements were conducted in each axis direction by sequentially reorienting the sample in the holder, while each sample orientation was measured twice. After a vacuum pump was used to evacuate the air from the pores, the fluid was forced through the sample by generating a positive pressure difference of 0.2 bar, which was kept constant during each measurement.

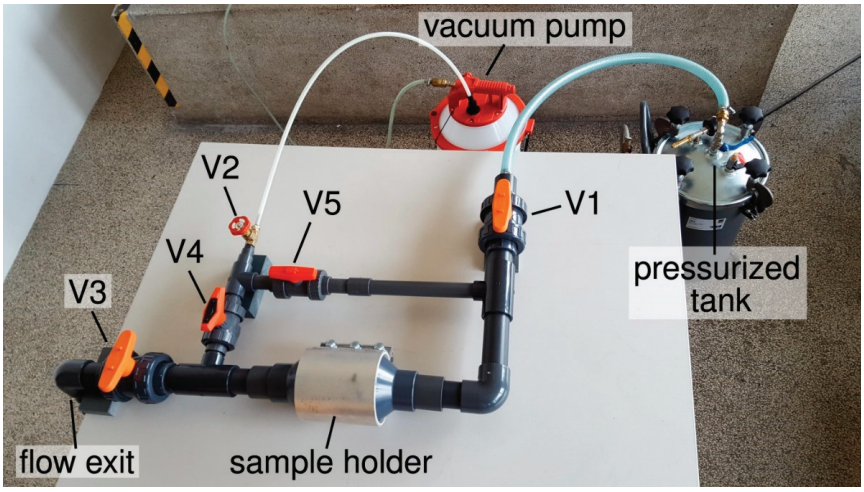

Figure 4. Experimental set-up of the permeability measurements. The scaled sample is installed in different orientations in the sample holder.

The measurement procedure is described as follows: First, the air was evacuated on both sides of the sample through valve V2 using the connected vacuum pump while the valves V1 and V3 remained closed. In the second step, valve V2 was closed, valve V1 was opened, and the glycerol entered the evacuated pipe system including the sample holder. Then, the valves V4 and V5 were closed. In the last step, valve V3 was opened and the glycerol flowed through the flow exit into a measuring vessel. After steady-flow conditions were reached, the mass m of the glycerol pushed through the sample was measured over a period of time t.

Using the Reynolds number:

$$Re = \frac{\rho\sqrt{K}Q}{\mu A},$$

the validity of the flow conditions ($Re < 1$) was finally calculated. In all experiments, the Reynolds number varied between 0.001 and 0.008.

3. Results

Since the permeability scales proportional to the square of the feature size, the measured results were multiplied by a factor of α^{-2}, to represent the permeability of the original microstructures.

As shown in Figure 5, on a logarithmic scale, a good correlation between experimental and calculated permeabilities was obtained, nevertheless, the periodic boundary of the model cannot be imposed in the experimental set-up, and slightly smaller permeabilities were expected.

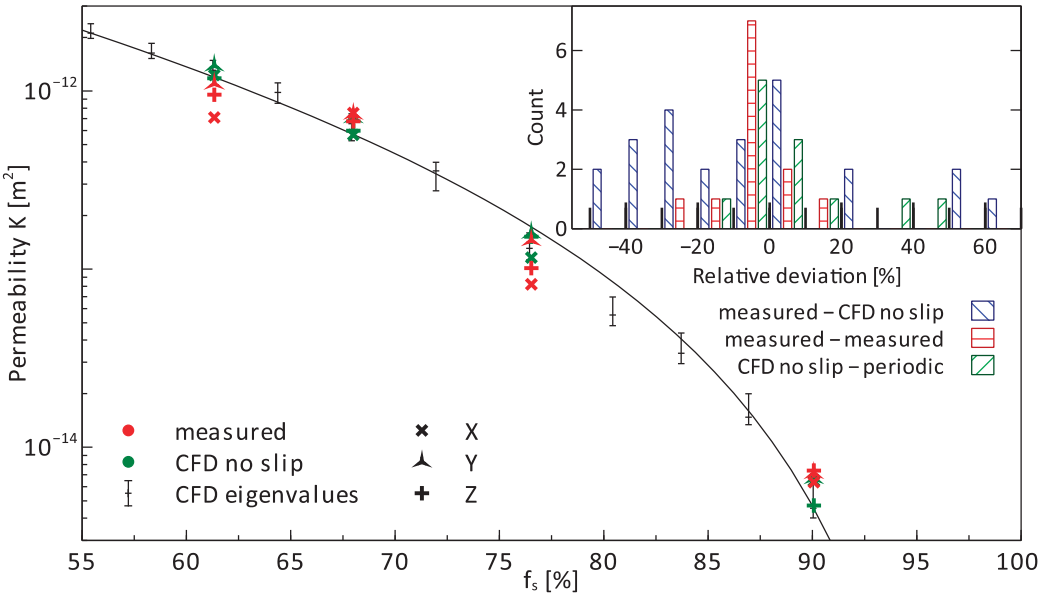

Figure 5. Comparison of predicted and simulated permeabilities of equiaxed dendritic microstructures at selected fraction solids. Inset: bar plot of relative differences between permeability results (first cited is the reference for relative deviation).

Table 2 shows the results for permeabilities resulting from CFD simulations for the original structures with periodic boundary conditions (abbreviated as 'p' in the table) discussed in more detail in [4], for the filtered structures with no slip boundary conditions (abbreviated as 'ns'), and from two measurements performed on the additively manufactured structures.

Table 2. Permeability results [m^2].

Sample	f_S [%]	Permeability Measured, Scaled			BC	Permeability CFD		
		K_X	K_Y	K_Z		K_X	K_Y	K_Z
05	61.4	7.04×10^{-13}	1.09×10^{-12}	9.83×10^{-13}	ns	1.23×10^{-12}	1.39×10^{-12}	1.18×10^{-12}
		7.16×10^{-13}	1.11×10^{-12}	9.23×10^{-13}	p	1.28×10^{-12}	1.44×10^{-12}	1.27×10^{-12}
07	68.1	7.13×10^{-13}	7.31×10^{-13}	7.27×10^{-13}	ns	5.67×10^{-13}	7.12×10^{-13}	5.99×10^{-13}
		8.92×10^{-13}	7.59×10^{-13}	6.26×10^{-13}	p	6.11×10^{-13}	7.28×10^{-13}	5.86×10^{-13}
09	76.8	8.38×10^{-14}	1.32×10^{-13}	9.97×10^{-14}	ns	1.16×10^{-13}	1.60×10^{-13}	1.52×10^{-13}
		8.06×10^{-14}	1.58×10^{-13}	1.03×10^{-13}	p	1.30×10^{-13}	1.56×10^{-13}	1.16×10^{-13}
13	90.7	6.35×10^{-15}	7.14×10^{-15}	7.12×10^{-15}	ns	6.46×10^{-15}	6.71×10^{-15}	4.71×10^{-15}
		6.37×10^{-15}	7.18×10^{-15}	7.67×10^{-15}	p	4.37×10^{-15}	6.00×10^{-15}	4.56×10^{-15}

The inset in Figure 5 shows the relative differences between the permeabilities resulting from the two different CFD simulations and from two measurements performed for each structure. For the periodic simulations, the diagonal terms of the permeability tensor aligned to the X-, Y- and Z-coordinates were used in this comparison. The average permeability resulting from measurements was compared with that resulting from CFD simulations with no slip boundary conditions.

4. Discussion

Due to the limited size of the RVE, an anisotropy of the permeability was observed in the CFD simulations as well as in the measurements. In CFD simulations with periodic

boundary conditions, this anisotropy showed up as different eigenvalues, in simulations with no slip boundary conditions and in measurements as different permeabilities in X-, Y- and Z-directions. Measurement and simulation both showed a higher permeability in the Y-direction for the microstructure samples. As can be seen, in most cases the differences between the two CFD simulations were less than 10%. The differences between the two measurements of the same permeability were also below 10% in most cases, while the differences between measured and computed permeabilities spanned a much wider range.

Possible sources for the observed differences between measured permeabilities and those derived from CFD simulations can be separated into three categories:

- Inaccurate CFD simulations;
- Structural differences between the physical models and the geometries used in CFD-simulations;
- Errors in the measurement process.

4.1. Accuracy of CFD Simulations

In tests using structures with known permeabilities the deviations between reference value and calculated permeability were found to be below 2% for the software used in the CFD simulations. To estimate if convergence to a steady state was reached, the change in magnitude of the superficial velocity during the final 1/10th of simulation time was observed and found to be below 2.4% in all cases. The filtering process did not affect the difference between measured and simulated permeability, since the permeabilities of structures after filtering were compared with the measured permeabilities.

4.2. Accuracy of Physical Models

The layer height in the FFF process of 0.2 mm was an order of magnitude smaller than structural length scales such as channel diameters, therefore the accuracy of the process was considered to be sufficiently accurate. Other possible sources of structural differences between digital and physical models may have resulted from deformations of the model that could have occurred, e.g., during the removal of support structures, but also during the measurement process, when the structure was subjected to a force of $\Delta p \cdot A = 50$ N. Other structural differences could have resulted from obstacles such as loose filament strands becoming lodged in narrow channels.

Structural differences due to elastoplastic deformation and obstacles lodged in narrow channels could explain the observed larger deviations between measured and computed permeabilities. Unless obstacles become stuck or unstuck during or between measurements, such deviations would also be consistent for multiple measurements under very similar conditions.

4.3. Accuracy of Measurements

The comparison of multiple measurements gave an estimate of statistical errors of the permeability measurements. A systematic error may have resulted from the pressure drop in the pipes connecting the sample holder to the pressurized tank and the flow exit. Since the diameter of the pipes was about an order of magnitude larger than the diameter of channels in the measured structure, and the pressure drop for flow through a pipe of length l and diameter d is $\Delta p \sim l/d^4$ according to the Hagen–Poiseuille equation, this error could be estimated to be about two to three orders of magnitude smaller than the measured pressure drop, even when the length of the pipes is taken into account.

5. Conclusions

The Darcy permeability of microstructures resulting from a phase field simulation of a solidifying A356 alloy was determined by CFD simulations and by measurements of glycerol passing through scaled models of the microstructure. To the authors' knowledge this is the first work investigating permeability measurements of scaled models of periodic structures resulting from phase field simulations.

A novel filtering method was developed for the microstructures to minimize the effect of known limitations of the physical measurement of the permeability of periodic structures. CFD simulations with the filtered structures, and no slip boundary conditions better reproducing the measurement, showed the differences introduced by the filtering method to be below 10% in most cases. Differences between two measurements of the same permeability fell in the same range.

The comparison between the measurement of the permeability of the 3D-printed samples and the simulations showed a wider range of differences, but was still in good agreement, considering that the permeability varied over several orders of magnitude during the solidification.

The agreement was improved when the experimental data were compared to CFD simulations performed on the filtered structures with boundary conditions more closely matching the experimental conditions, although neither the digital filtering process, nor statistical measurement errors could completely explain the observed deviations between simulated and measured permeabilities.

Outlook

In this work periodic structures were used to represent semi-solid regions that are statistically homogeneous over larger scales. In future research, the impact of gradients in microstructure features such as length scales might be investigated. Such structures can result from different cooling conditions in nearby regions of a cast part.

Author Contributions: Conceptualization, R.B., G.L., M.A., W.J. and J.W.; methodology, R.B., M.A., W.J. and J.A.; software, R.B.; validation, R.B., M.A. and W.J.; formal analysis, R.B. and W.J.; investigation, W.J., J.W. and J.A.; data curation, R.B., W.J. and J.A.; writing—original draft preparation, R.B., G.L., W.J. and J.W.; writing—review and editing, R.B., M.A., G.L., W.J., W.S., J.W., J.A. and C.H.; visualization, R.B. and W.J.; supervision, M.A., W.J. and J.W.; project administration, M.A., W.S. and J.W.; funding acquisition, M.A., W.S., J.W. and C.H. All authors have read and agreed to the published version of the manuscript.

Funding: This research was funded by the German Research Foundation (DFG) in the framework of the Collaborative Research Center SFB-1120–236616214 Precision Melt Engineering.

Institutional Review Board Statement: Not applicable.

Informed Consent Statement: Not applicable.

Conflicts of Interest: The authors declare no conflict of interest. The funders had no role in the design of the study; in the collection, analyses, or interpretation of data; in the writing of the manuscript, or in the decision to publish the results.

References

1. Dantzig, J.A.; Rappaz, M. *Solidification*; EPFL Press: Lausanne, Switzerland, 2009.
2. Rappaz, M.; Drezet, J.-M.; Gremaud, M. A new hot-tearing criterion. *Metall. Mater. Trans. A* **1999**, *30*, 449–455. [CrossRef]
3. Böttger, B.; Apel, M.; Santillana, B.; Eskin, D.G. Relationship Between Solidification Microstructure and Hot Cracking Susceptibility for Continuous Casting of Low-Carbon and High-Strength Low-Alloyed Steels: A Phase-Field Study. *Metall. Mater. Trans. A* **2013**, *44*, 3765–3777. [CrossRef]
4. Berger, R.; Apel, M.; Laschet, G. An analysis of the melt flow permeability for evolving hypoeutectic Al-Si mushy zone microstructures by phase field simulations. *Materialia* **2021**, *15*, 100966. [CrossRef]
5. Khajeh, E.; Mirbagheri, S.M.H.; Davami, P. Modeling of permeability with the aid of 3D interdendritic flow simulation for equiaxed dendritic structures. *Mater. Sci. Eng. A* **2008**, *475*, 355–364. [CrossRef]
6. Mirbagheri, S.M.H.; Khajeh, E. Modelling and simulation of equiaxed dendritic structures permeability for Pb–Sn alloys. *Mater. Sci. Technol.* **2008**, *24*, 1444–1451. [CrossRef]
7. Madison, J.; Spowart, J.E.; Rowenhorst, D.J.; Aagesen, L.K.; Thornton, K.; Pollock, T.M. Fluid flow and defect formation in the three-dimensional dendritic structure of nickel-based single crystals. *Metall. Mater. Trans. A Phys. Metall. Mater. Sci.* **2012**, *43*, 369–380. [CrossRef]
8. Khajeh, E.; Maijer, D.M. Numerical determination of permeability of Al-Cu alloys using 3D geometry from X-ray microtomography. *Mater. Sci. Technol.* **2010**, *26*, 1469–1476. [CrossRef]

9. Bhat, M.S.; Poirier, D.R.; Heinrich, J.C. Permeability for cross flow through columnar-dendritic alloys. *Metall. Mater. Trans. B* **1995**, *26*, 1049–1056. [CrossRef]
10. Ludwig, A.; Kharicha, A.; Hölzl, C.; Domitner, J.; Wu, M.; Pusztai, T. 3D Lattice Boltzmann flow simulations through dendritic mushy zones. *Eng. Anal. Bound. Elem.* **2014**, *45*, 29–35. [CrossRef]
11. Böttger, B.; Haberstroh, C.; Giesselmann, N. Cross-Permeability of the Semisolid Region in Directional Solidification: A Combined Phase-Field and Lattice-Boltzmann Simulation Approach. *JOM* **2016**, *68*, 27–36. [CrossRef]
12. Mitsuyama, Y.; Takaki, T.; Sakane, S.; Shibuta, Y.; Ohno, M. Permeability tensor for columnar dendritic structures: Phase-field and lattice Boltzmann study. *Acta Mater.* **2020**, *188*, 282–287. [CrossRef]
13. Takaki, T.; Sakane, S.; Ohno, M.; Shibuta, Y.; Aoki, T. Permeability prediction for flow normal to columnar solidification structures by large–scale simulations of phase–field and lattice Boltzmann methods. *Acta Mater.* **2019**, *164*, 237–249. [CrossRef]
14. Li, L.; Zhang, R.; Hu, S.; Zhang, D.; Yang, S.; Wang, C.; Jiang, H. Prediction of mushy zone permeability of Al–4.5 wt% Cu alloy during solidification by phase field model and CFD simulation. *China Foundry* **2019**, *16*, 313–318. [CrossRef]
15. Zhang, X.; Kang, J.; Guo, Z.; Han, Q. Effect of the forced flow on the permeability of dendritic networks: A study using phase-field-lattice Boltzmann method. *Int. J. Heat Mass Transf.* **2019**, *131*, 196–205. [CrossRef]
16. Khajeh, E.; Maijer, D.M. Permeability evolution during equiaxed dendritic solidification of Al–4.5 wt%Cu. *Model. Simul. Mater. Sci. Eng.* **2012**, *20*, 035004. [CrossRef]
17. James, J.D.; Brown, S.G.R.; Spittle, J.A.; Lavery, N.P. Experimental apparatus for validation of computer models of the permeability of metallic alloys in the mushy zone. In Proceedings of the Modeling of Casting, Welding and Advanced Solidification Processes—XI, Opio, France, 28 May–2 June 2006; pp. 1189–1196.
18. Bodaghi, M.; Ban, D.; Mobin, M.; Park, C.H.; Lomov, S.V.; Nikzad, M. Additively manufactured three dimensional reference porous media for the calibration of permeability measurement set-ups. *Compos. Part A Appl. Sci. Manuf.* **2020**, *139*, 106119. [CrossRef]
19. MICRESS®, the Microstructure Evolution Simulation Software. Available online: www.micress.de (accessed on 1 August 2017).
20. Torquato, S. *Random Heterogeneous Materials*; Interdisciplinary Applied Mathematics; Springer: New York, NY, USA, 2002; Volume 16.
21. Eiken, J. *A Phase-Field Model for Technical Alloy Solidification*; Shaker Verlag: Herzogenrath, Germany, 2009.
22. Aluminium-Based Alloys Databases. Available online: https://thermocalc.com/products/databases/aluminum-based-alloys/ (accessed on 23 November 2021).
23. Thermocalc Software. Available online: www.thermocalc.com (accessed on 1 August 2017).
24. Laschet, G.; Vossel, T.; Wolff, N.; Apel, M.; Bührig-Polaczek, A. Multiscale Solidification Simulation of an Axisymmetric A356 Component in Die Casting. In Proceedings of the 6th Decennial International Conference on Solidification Processing, Old Windsor, UK, 25–28 July 2017; pp. 576–580.
25. Böttger, B.; Eiken, J.; Apel, M. Phase-field simulation of microstructure formation in technical castings—A self-consistent homoenthalpic approach to the micro–macro problem. *J. Comput. Phys.* **2009**, *228*, 6784–6795. [CrossRef]
26. Zhou, B.; Laschet, G.; Eiken, J.; Behnken, H.; Apel, M. Multiscale solidification simulation of Sr-modified Al-Si-Mg alloy in die casting. *IOP Conf. Ser. Mater. Sci. Eng.* **2020**, *861*, 012034. [CrossRef]
27. Osswald, T.A. *Understanding Polymer Processing: Processes and Governing Equations*, 2nd ed.; Carl Hanser Verlag GmbH & Co. KG: München, Germany, 2017.
28. Dizon, J.R.C.; Espera, A.H.; Chen, Q.; Advincula, R.C. Mechanical characterization of 3D-printed polymers. *Addit. Manuf.* **2018**, *20*, 44–67. [CrossRef]
29. Dey, A.; Yodo, N. A Systematic Survey of FDM Process Parameter Optimization and Their Influence on Part Characteristics. *J. Manuf. Mater. Process.* **2019**, *3*, 64. [CrossRef]
30. Oliveira, J.P.; LaLonde, A.D.; Ma, J. Processing parameters in laser powder bed fusion metal additive manufacturing. *Mater. Des.* **2020**, *193*, 108762. [CrossRef]
31. Gebhardt, A.; Kessler, J.; Thurn, L. *3D Printing: Understanding Additive Manufacturing*; Carl Hanser Verlag GmbH & Co. KG: München, Germany, 2018.
32. *DIN EN ISO/ASTM 52900: Additive Fertigung—Grundlagen—Terminologie*; Beuth Verlag GmbH: Berlin, Germany, 2018.
33. Khajeh, E.; Maijer, D.M. Physical and numerical characterization of the near-eutectic permeability of aluminum–copper alloys. *Acta Mater.* **2010**, *58*, 6334–6344. [CrossRef]
34. Bosart, L.W.; Snoddy, A.O. New Glycerol Tables. *Ind. Eng. Chem.* **1927**, *19*, 506–510. [CrossRef]
35. Segur, J.B.; Oberstar, H.E. Viscosity of Glycerol and Its Aqueous Solutions. *Ind. Eng. Chem.* **1951**, *43*, 2117–2120. [CrossRef]

metals

MDPI

Article

The Interaction between Grains during Columnar-to-Equiaxed Transition in Laser Welding: A Phase-Field Study

Lingda Xiong [1], Chunming Wang [2], Zhimin Wang [1,*] and Ping Jiang [1]

[1] School of Mechanical Science and Engineering, Huazhong University of Science and Technology, Wuhan 430074, China; d201677183@hust.edu.cn (L.X.); jiangping@hust.edu.cn (P.J.)

[2] State Key Lab of Material Processing and Die & Mould Technology, Huazhong University of Science and Technology, Wuhan 430074, China; cmwang@hust.edu.cn

* Correspondence: d201677150@hust.edu.cn; Tel.: +86-139-1079-2774

Received: 21 September 2020; Accepted: 27 November 2020; Published: 7 December 2020

Abstract: A phase-field model was applied to study CET (columnar-to-equiaxed transition) during laser welding of an Al-Cu model alloy. A parametric study was performed to investigate the effects of nucleation undercooling for the equiaxed grains, nucleation density and location of the first nucleation seed ahead of the columnar front on the microstructure of the fusion zone. The numerical results indicated that nucleation undercooling significantly influenced the occurrence and the time of CET. Nucleation density affected the occurrence of CET and the size of equiaxed grains. The dendrite growth behavior was analyzed to reveal the mechanism of the CET. The interactions between different grains were studied. Once the seeds ahead of the columnar dendrites nucleated and grew, the columnar dendrite tip velocity began to fluctuate around a value. It did not decrease until the columnar dendrite got rather close to the equiaxed grains. The undercooling and solute segregation profile evolutions of the columnar dendrite tip with the CET and without the CET had no significant difference before the CET occurred. Mechanical blocking was the major blocking mechanism for the CET. The equiaxed grains formed first were larger than the equiaxed grains formed later due to the decreasing of undercooling. The size of equiaxed grain decreased from fusion line to center line. The numerical results were basically consistent with the experimental results obtained by laser welding of a 2A12 Al-alloy.

Keywords: phase-field model; columnar-to-equiaxed transition; laser welding; interaction

1. Introduction

CET (columnar-to-equiaxed transition) occurs when the growth path of columnar grains is blocked by the equiaxed grains form ahead of the columnar front. CET significantly changes the morphology and size of microstructure [1]. It is observed that CET often happens during the solidification process in the molten pool after welding. The microstructure in the fusion zone determines the mechanical properties of welding joints [2]. Therefore, a better understanding of the CET is of great importance to obtain weld joints with high quality.

Numerous experiments have been made to reveal the nucleation mechanism and the factors that affect the CET during solidification process. Gandin et al. conducted a directional solidification experiment with Al–Si alloy. The experimental results showed that nuclei of equiaxed grains may come from heterogeneous nucleation or dendrite arm detachment/fragmentation [3]. Nguyen-Thi et al. observed the dynamic phenomena of the CET during Al-Ni alloy directional solidification by X-ray radiography. They found that the nucleation undercooling of the equiaxed grain depended on the heterogeneous particle size: larger heterogeneous particles needed lower undercooling than smaller

heterogeneous particles [4]. Villafuerte et al. studied the effect of alloy composition on CET in ferritic stainless-steel tungsten inert gas (TIG) welding. It was found that the CET was ascribed to heterogeneous nucleation of ferritic on Ti-rich cuboidal inclusions [5]. Geng et al. adopted an overlap welding procedure to identify the nucleation mechanism in laser welds of aluminum alloys. The result indicated that the nucleation mechanism in laser welding was heterogeneous nucleation, rather than grain detachment and dendrite fragmentation [6].

Modeling has been developed into an important method to study the CET over decades. CET models can be classified into two types: deterministic models and stochastic models. Deterministic models rely on averaged quantities and equations that are solved on a macroscopic scale whereas stochastic models follow the nucleation and growth of each individual grain [7]. Hunt established an analytical model to predict CET in directional solidification [8]. The model has been improved by Kurz et al. to predict the microstructure in welding or other processes involving rapid solidification [9]. Badillo et al. applied the phase-field model to study CET in alloy directional solidification. They found that high pulling velocity and low temperature gradient promote equiaxed growth [1]. Martorano et al. applied a multiphase/multiscale model to study the solutal interaction mechanism for CET in alloy solidification. When the solute rejected from the equiaxed grains was sufficient to dissipate the undercooling at the columnar front, the CET would occur. [10]. Li et al. used the phase-field model to study the CET in alloy solidification. The results indicated that the columnar zone length and the equiaxed grain size increased with the decrease of cooling rate [11]. Viardin et al. conducted the first 3D phase-field simulation of CET and the numerical results were consistent with the experiment [12]. Dong et al. applied a CA-FE (cellular automaton-finite difference) model to study the influence of crystallographic orientation of the columnar dendrites on CET. The simulation indicated that crystallographic orientation had little effect on CET [13]. Biscuola et al. adopted two deterministic model (a model developed by Martorano and a modified Hunt's model) and one stochastic model (CA (cellular automation) model) to study the CET in Al–Si alloy directional solidification. The results indicated that the mechanical blocking occurred in the stochastic model by adopting a blocking fraction of 0.2, rather than 0.49 used in Hunt model [14]. With the development of numerical simulation, several researchers successfully applied multi-phase-field model and CA-FE model to predict CET which occurs in the solidification process in molten pool during metallic welding and additive manufacturing [15–19]. Han et al. used a CA-FE model to predict the CET in the welded pool. They found that the undercooled zone width and the maximum undercooling in front of columnar grains increased with the decrease of the distance to weld center [20]. The above work has greatly improved understanding about the blocking mechanism and influence factors of CET. However, the details of the grain growth and the interactions between different grains during the CET in laser welding have not been studied yet.

In the present work, a phase-field model was used to study the influence of nucleation undercooling, nucleation density and location of first nucleation seed on the CET during laser welding. The dendrite tip behavior and undercooling distribution were analyzed to illustrate the growth of dendrites and equiaxed grains. The blocking mechanisms for CET were discussed. Finally, the experiment was conducted to verify the numerical result.

2. Models and Experiments

2.1. Macroscopic Model

Zheng et al. proposed a transient condition macroscopic model to obtain the time dependent pulling velocity V_p and thermal gradient G [21]. This model is applied in the present work. The shape of the molten pool is composed of two half ellipsoids, as shown in Figure 1. The temperature at the molten pool edge T_l is equilibrium liquidus temperature. The solidification process occurs in the rear ellipsoid area.

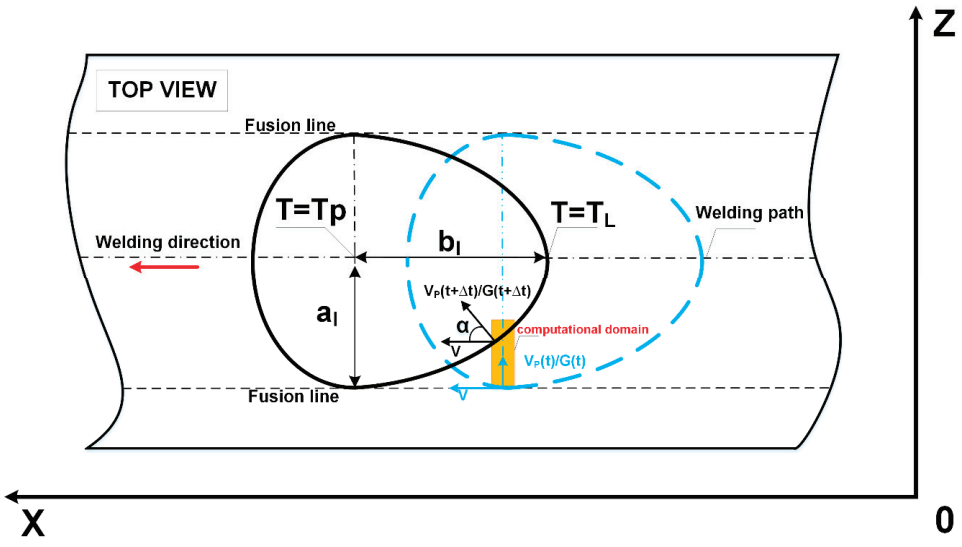

Figure 1. Macrograph of the molten pool.

In Figure 1, a_l and b_l are the depth and rear length of the solidification area, respectively. T_p is the highest temperature at the center of molten pool. V is the welding velocity of laser welding. α is the angle between S/L (solid/liquid) interface pulling velocity and welding velocity. The yellow area is the computational domain. $V_p(t)$ is the S/L interface pulling velocity. $G(t)$ is the temperature gradient. Hence, $V_p(t)$ and $G(t)$ in the computational domain can be expressed as:

$$V_p(t) = \frac{a_l V^2 t}{\sqrt{V^2 t^2 (a_l{}^2 - b_l{}^2) + b_l{}^4}} \tag{1}$$

$$G(t) = \frac{T_p - T_l}{\sqrt{V^2 t^2 + a_l{}^2 \frac{1 - V^2 t^2}{b_l{}^2}}} \tag{2}$$

2.2. Phase-Field Modeling

The phase-field model developed by Zheng was applied to simulate the microstructure evolution during solidification process [21]. The 'frozen temperature approximation' was adopted.

$$T(z,t) = T_0 + G(t)(z - \int_0^t V_p(t\prime)dt\prime) \tag{3}$$

where $T_0 = T(z_0,t)$ is a reference temperature, and $G(t)$ is the temperature gradient along pulling direction, the integrand term $\int_0^t V_p(t\prime)dt\prime$ is the pulling distance of S/L interface.

A scalar field φ is introduced into the phase-field model to indicate the phase state at every point. In solid phase, $\varphi = 1$. In the liquid phase, $\varphi = -1$. At the S/L interface, φ continuously changes from -1 to 1. A dimensionless supersaturation field U is introduced to characterize the solute concentration.

$$U = \frac{1}{1-k}\left(\frac{2kc/c_\infty}{1-\varphi+k(1+\varphi)} - 1\right) \tag{4}$$

where k is equilibrium partition coefficient, c is the solute concentration and c_∞ is the global sample composition.

The governing equations of the phase-field model in two-dimensions can be expressed as the following:

$$\tau_0 a(\widehat{n})^2[1-(1-k)\frac{z-\int_0^t V_p(t\prime)d(t\prime)}{l_T}]\frac{\partial\varphi}{\partial t} = W^2\vec{\nabla}[a(\widehat{n})^2\vec{\nabla}\varphi]+\varphi-\varphi^3-\lambda(1-\varphi^2)^2[U+\frac{z-\int_0^t V_p(t\prime)d(t\prime)}{l_T}] \quad (5)$$

$$(\tfrac{1+k}{2}-\tfrac{1-k}{2}\varphi)\frac{\partial U}{\partial t} = \vec{\nabla}\left(D_L\tfrac{1-\varphi}{2}\vec{\nabla}U+\tfrac{1}{2\sqrt{2}}W[1+(1-k)U]\frac{\partial\varphi}{\partial t}\frac{\vec{\nabla}\varphi}{\left|\vec{\nabla}\varphi\right|}\right)+\tfrac{1}{2}[1+(1-k)U]\frac{\partial\varphi}{\partial t} \quad (6)$$

where W is the interface width (length scale) and τ_0 is the relaxation time (time scale) respectively, $a(\widehat{n})$ is the anisotropy of the surface tension, λ is a coupling constant, l_T is the dimensionless thermal length.

$$W = d_0\lambda/a_1 \quad (7)$$

$$\tau_0 = a_2\lambda W/D_L \quad (8)$$

$$a(\widehat{n}) = 1+\varepsilon\cos 4\theta \quad (9)$$

$$d_0 = \Gamma/(|m|(1-k)c_l^0) \quad (10)$$

$$l_T = \frac{|m|(1-k)c_l^0}{G(t)} \quad (11)$$

$$c_l^0 = c_\infty/k \quad (12)$$

where $a_1 = 0.88839$ and $a_2 = 0.6267$, D_L is the solute diffusion coefficient in the liquid region, θ is the angle between the interface normal and pulling direction, ε is the anisotropy strength, d_0 is the capillarity length, m is the liquid slope of alloy, Γ is the Gibbs-Thomson coefficient, c_l^0 is the equilibrium solute concentration on the liquid side of S/L interface.

2.3. Computational Details

The length and width of 2-D computational domain used in the simulations were 3000 Δz and 2000 Δx respectively. $\Delta x = \Delta z = 0.8W = 2.72\times10^{-8}$ m. Therefore, the actual size of computational domain was 8.16×10^{-5} m $\times$ 5.44×10^{-5} m. The initial condition is shown in Figure 2. The temperature at S/L interface was 922.6 K. The simulations in the present work were initialized with a thin solid layer (whose width is 100 Δx) at the left wall. The S/L interface was planar. The reference temperature T_0 of S/L interface at the beginning was equilibrium liquidus temperature. The solute was distributed uniformly in the liquid (i.e., solute concentration in the liquid is 4 wt %). The values of parameters involved in phase-field modeling is shown in Table 1.

Wang et al. studied the microstructure evolution during solidification of welding molten pool. They found that the columnar dendrite growth during welding can be divided into four stages: linear growth stage, nonlinear growth stage, competitive growth stage and relatively steady growth stage [22]. In our early stage works, the variation of maximum undercooling ahead of planar S/L interface with time at linear growth stage is shown in Figure 3. We found that the maximum of undercooling ahead of S/L interface during linear growth stage was so large (>17 K) that if the seeds for nucleation were set at the beginning of the simulation, CET would occur before S/L underwent a Mullins–Sekerka instability and columnar dendrites grew when nucleation undercooling was smaller than 17 K. In this circumstance, there would be no columnar dendrites in the fusion zone. This phenomenon was not consistent with what we have observed in the experiment. Therefore, the seeds for nucleation were set in front of the solid layer in the simulations. However, only after entering the relatively steady growth stage (i.e., after 7.0×10^5 time steps—35% of the overall simulation time), the seeds in the liquid begin to translate into nuclei when the local undercooling (=T_1 (C) − T) at the seeds exceeds

the nucleation undercooling, as shown in Figure 4. The seeds for nucleation were distributed in a rectangular array. The horizontal and vertical distances between all adjacent seeds were equal. The radius of heterogeneous nuclei was 2 Δx.

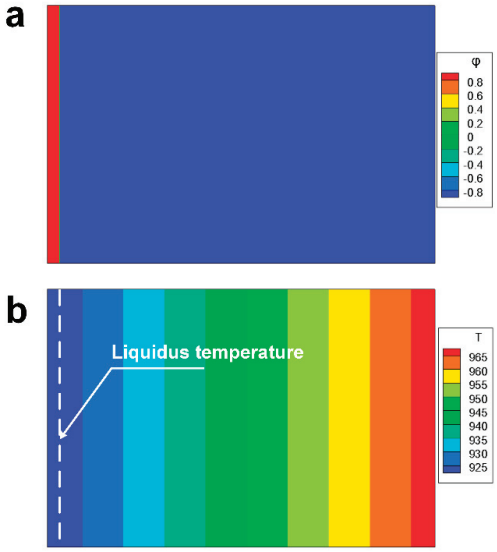

Figure 2. The initial condition of simulation: (**a**) the scalar field φ; (**b**) the temperature distribution.

Table 1. The values of parameters involved in phase-field modeling.

Parameter	Value	Unit
Coupling parameter: λ	8.0	-
Alloy composition: c_∞	4	wt %
Capillary length: d_0	3.8×10^{-9}	m
Interface width: W	3.4×10^{-8}	m
Partition coefficient: k	0.14	-
Liquidus slope: m	−2.6	K/wt %
Diffusion coefficient: D_L	3.0×10^{-9}	m^2/s
The anisotropy strength: ε	0.01	-
Gibbs–Thomson coefficient: Γ	2.4×10^{-7}	K × m

One of the aims of the present work was to study effects of nucleation undercooling for the equiaxed grains, nucleation density and location of first nucleation seed on CET. Various sets of nucleation undercooling for the equiaxed grains, nucleation density and location of first nucleation seed have been applied in the simulations as shown in Table 2.

Moving-domain technology was applied in the simulations for decreasing simulation time cost. When the temperature of the left wall was higher than 892 K, all fields were shifted by one grid point to the left. The maximum temperature at the right wall was always above the equilibrium liquidus temperature (922.6 K). The upper and lower boundaries were set periodic boundary condition. The zero-Neumann boundary conditions were applied to the other boundaries. The governing equations were discretized by finite difference method. A time step size of $\Delta t = 0.02 \times \tau_0$ $(0.02 < \Delta x^2/4D_L) = 3.88 \times 10^{-8}$ s was chosen to applied in the computation. The evolution of the phase and solute concentration fields were obtained by calculating the governing Equations (5) and (6). The total number of iterations is 2.0×10^7 (100% of the simulation time), corresponding to actual time 0.0772 s for the solidification process. The self-developed code was

programed by C. Finite difference method with CUDA 9.2 (CUDA Version 9.2.88, NVIDIA Corporation, Santa Clara, CA, USA) parallelization was used to solve the governing equations.

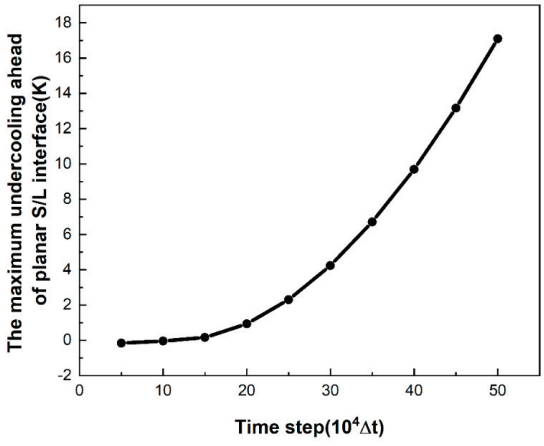

Figure 3. The variation of maximum undercooling ahead of planar S/L interface with time.

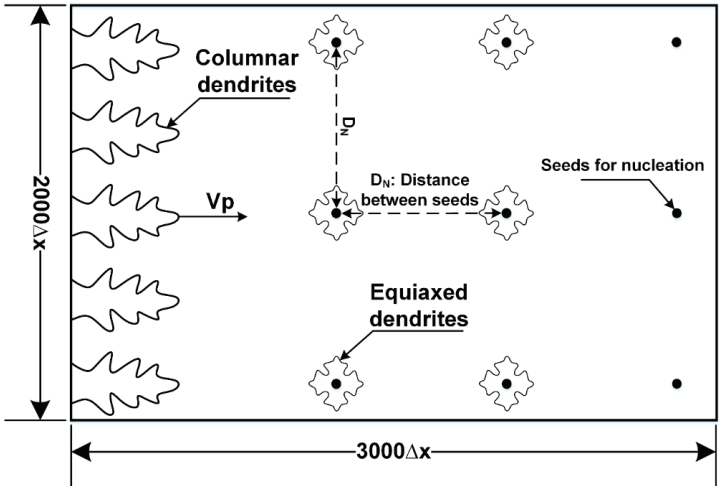

Figure 4. The setting of heterogeneous nuclei in the computational domain.

Table 2. The growth condition of heterogeneous nuclei.

Case Number	U_n: Nucleation Undercooling (K)	D_n: Distance between Nuclei (Δx)	X_f: Location of First Seed at X Coordinate Axis (Δx)	The Relative Distance between the Initial Planar Front and the First Seeds
1	11	200	200	1578
2	16	200	200	1578
3	21	200	200	1578
4	11	400	200	1578
5	11	500	200	1578
6	11	1000	200	1578
7	11	200	100	1678
8	11	200	300	1878

2.4. Experiment Design and Material Properties

In order to verify the numerical results, laser welding experiments were conducted. Al-4 wt % Cu alloy 2A12 was used as welded material. Cu is the main component of 2A12 Al-alloy. The content of Cu is 4 wt %. The contents of other chemical elements in 2A12 Al-alloy are very low. The solidification structure of 2A12 Al-alloy can be maintained after the molten pool cool to room temperature. Therefore, the 2A12 Al-alloy can be considered representative for a binary Al-Cu alloy, as used in the simulation. The thickness of the sample was 4 mm. Chemical composition of the material was detected by EDS. It is shown in Table 3. The laser welding equipment was an IPG YLR-4000 fiber laser (IPG Photonics Corporation, Oxford, MA, USA) with a peak power of 4.0 kW and an ABB IRB4400 robot as shown in Figure 5. Pure argon at a flow rate of 2.0 m^3/h was used for top surface shielding. The defocusing distance was 0 mm. The laser power was 2.5 kW and the welding velocity was 1.8 m/min. After laser welding, the microstructure at top surface of welded joint was observed by Scanning Electron Microscopy (SEM, Carl Zeiss, Oberkochen, Germany). The size of equiaxed grains at different areas were measured by electron back-scattered diffraction (EBSD, Carl Zeiss, Oberkochen, Germany).

Table 3. The chemical composition of 2A12 in wt %.

Element	Al	Cu	Mg	Mn
wt %	94.38	3.92	1.08	0.62

Figure 5. Welding devices: (**a**) IPG YLR-4000 fiber laser; (**b**) ABB IRB4400 robot.

The characteristic parameters of the molten pool are listed in Table 4.

Table 4. The characteristic parameters of the molten pool.

Symbol	Value	Unit
$T_p - T_l$	742	K
a_l	1.2844×10^{-3}	m
b_l	2.0825×10^{-3}	m

3. Results and Discussion

The microstructure evolution in the molten pool in Case 1 as a typical example is shown in Figure 6. Figure 6a shows the well-developed columnar dendrites just before the CET occurs. The primary dendrite arm spacing was 117.6 Δx. In Figure 6b, the growth path of columnar dendrites was blocked by the equiaxed grains and columnar dendrites stopped growing. The CET occurred. Figure 6c–h shows the equiaxed grain growth after the CET. It was found that the length of equiaxed grains that nucleated at the end of simulation (in Figure 6h) were smaller than the length of equiaxed grains that formed at the beginning of relatively steady growth stage (in Figure 6c) (i.e., The size of equiaxed grain decreased from fusion line to center line).

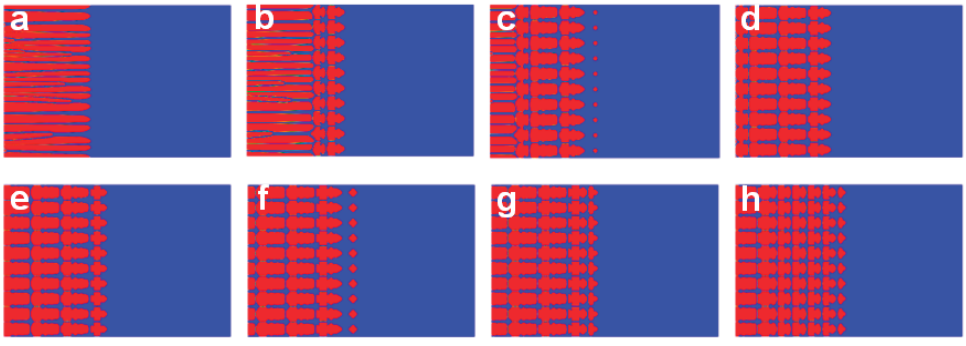

Figure 6. The microstructure evolution at different time step: (**a**) 7.0×10^5 (35.0% of the total simulation time); (**b**) 7.3×10^5 (36.5% of the total simulation time); (**c**) 7.8×10^5 (39.0% of the total simulation time); (**d**) 8.1×10^5 (40.5% of the total simulation time); (**e**) 8.6×10^5 (43.0% of the total simulation time); (**f**) 9.1×10^5 (45.5% of the total simulation time); (**g**) 9.6×10^5 (48.0% of the total simulation time); (**h**) 1.01×10^6 (50.5% of the total simulation time).

The effects of nucleation undercooling for the equiaxed grains, nucleation density and location of first nucleation seed on the CET were discussed in the following section. In order to illustrate the blocking mechanism for CET and the behaviors of the equiaxed grains after the CET, the variation of dendrite tip velocity, undercooling in front of dendrite tips and the solute segregation at dendrite tips were analyzed to characterize the interactions between columnar grains and equiaxed grains and the interactions between equiaxed grains at neighboring columns.

3.1. The Effects of Heterogeneous Nucleation Parameters on Microstructure

Figure 7 shows the microstructures for Case 1–3, where the applied nucleation undercoolings are 11 K, 16 K and 21 K, respectively. It can be seen that when nucleation undercooling was 21 K, no equiaxed grain formed and no CET occurred. When nucleation undercooling was 11 K or 16 K, the CET occurred. However, the equiaxed grains with 16 K nucleation undercooling were bigger than that with 11 K nucleation undercooling. The CET with 16 K nucleation undercooling occurred later

(at 1.32×10^6 Δt—66.0% of the total simulation time) than that (at 7.1×10^5 Δt—35.5% of the total simulation time) with 11 K nucleation undercooling.

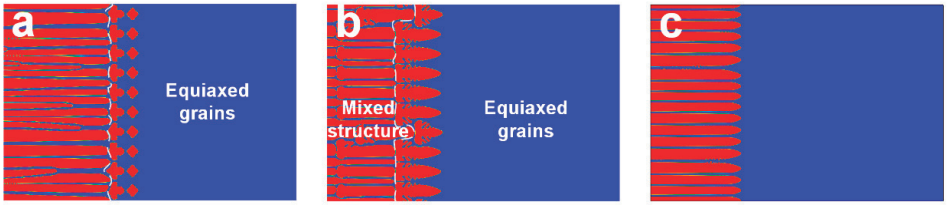

Figure 7. Effects of the nucleation undercooling on the CET for D_n = 200 Δx and X_f = 200 Δx: (**a**) U_n = 11 K; (**b**) U_n = 16 K; (**c**) U_n = 21 K.

According to research by Badillo et al., the maximum undercooling along the symmetry line between columnar dendrites was generally larger than that ahead of dendrite tip in directional solidification [1]. The comparison between the maximum undercooling along the symmetry line between columnar dendrites and the maximum undercooling ahead of dendrite tip when no CET occurs in laser welding is shown in Figure 8. It was found that the maximum undercooling along the symmetry line between columnar dendrites was only a little bit larger than that ahead of dendrite tip. Both undercoolings increased monotonically after entering relatively steady growth stage. Therefore, in the following section, the undercooling ahead of dendrite tip was applied to analyze. However, the undercoolings did not exceed 21 K at the end of simulations when time step = 2.0×10^6 Δt. Therefore, CET did not happen with 21 K nucleation undercooling. And the CET with 16 K nucleation undercooling happened later (at 1.32×10^6 Δt) than that (at 7.1×10^5 Δt) with 11 K nucleation undercooling. The time for the second column of seed to reach nucleation undercooling required more time when nucleation undercooling was 16 K. In this circumstance, the first column of equiaxed grain had more time to grow and become bigger compared to that with 11 K nucleation undercooling.

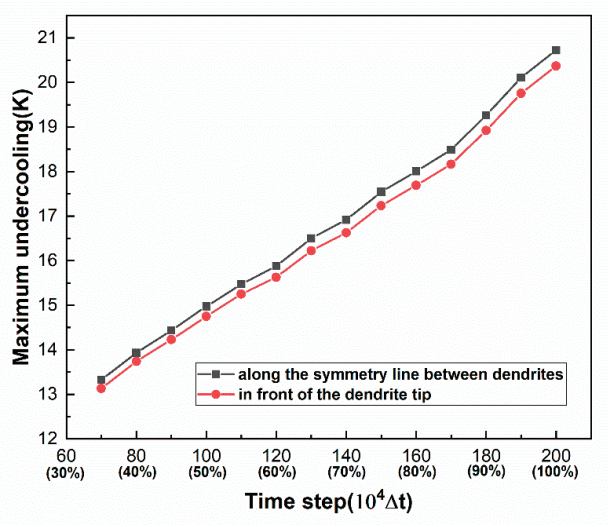

Figure 8. The comparison between the maximum undercooling along the symmetry line between columnar dendrites and the maximum undercooling ahead of dendrite tip.

Figure 9 shows the microstructures for Case 1 and 4–6, where D_n (the distance between seeds) are 200 Δx, 400 Δx, 500 Δx and 1000 Δx, respectively. It can be seen that when D_n was less than 1000 Δx,

the CET occurred. The size of equiaxed grains increased with the increasing of distance between seeds. When D_n was 1000 Δx, no CET occurred and the elongated equiaxed grains and columnar dendrites coexisted in the computational domain. In Figure 9a (D_n = 200 Δx), the equiaxed grains were elongated while the grains were not elongated in Figure 9b (D_n = 400 Δx) and Figure 9c (D_n = 500 Δx). The sidebranchings were well-developed in Figure 9b (D_n = 400 Δx) and Figure 9c (D_n = 500 Δx). In Figure 9d, the dendrite arms of elongated equiaxed grains which were vertical to thermal gradient grew along its dendrite direction imposed crystallographic orientation. However, the columnar dendrites next to these dendrite arms always grew so fast that they blocked the growth path of the equiaxed dendrites arms vertical to thermal gradient direction. Therefore, no CET occurred and the final microstructure was a mixed structure (elongated equiaxed grains and columnar dendrites).

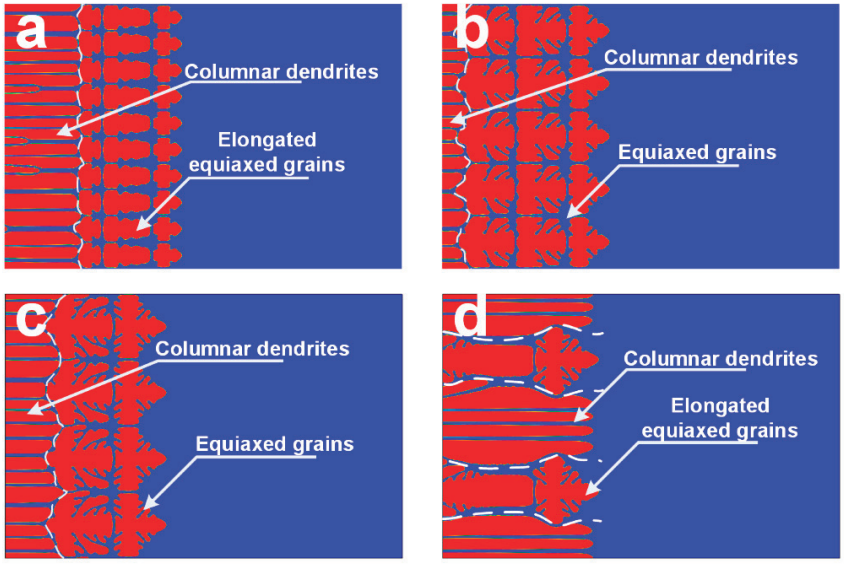

Figure 9. Effects of the nucleation density on the CET for U_n = 11 K and X_f = 200 Δx: (**a**) D_n = 200 Δx; (**b**) D_n = 400 Δx; (**c**) D_n = 500 Δx; (**d**) D_n = 1000 Δx.

To investigate the effects of the location of first seed on the CET, 100 Δx, 200 Δx and 300 Δx were selected with D_n was 200 Δx. Figure 10 shows the morphologies of equiaxed grains for Case 1, 7 and 8. It was found that the location of first seed significantly influenced the morphology of equiaxed grain microstructure at first column. In Figure 10a, there was only one equiaxed grain. It grew between two columnar dendrites. In Figure 10b, the equiaxed grains at first column grew and blocked the growth path of columnar dendrites. In Figure 10c, the equiaxed grains at first column did not only block the growth path of columnar dendrites but also were elongated. Figure 11 shows the undercooling distribution along the line x = 300 Δx where nuclei formed. It was found that in the liquid ahead of the columnar dendrite, with the distance to the dendrite tips increasing, the undercooling increased very slowly at first. Then it increased rapidly to the maximum value. Finally, the undercooling gradually decreased. Figure 11b shows the locations of first emerging nuclei in Case 1, 7 and 8 at 7.0×10^5 Δt—35% of the overall simulation time. It was found that in Case 7 (Figure 10a, D_n = 100 Δx), two columns of nuclei (location: 1122 Δx and 1322 Δx) formed at the same time. In Case 1 (Figure 10b, D_n = 200 Δx) and 8 (Figure 10c, D_n = 300 Δx), only one column of nuclei formed since the undercooling at the next column of seeds was below 11 K. The size of equiaxed grains at first column depended on the location where first column of nuclei formed. The closer the distance from the location where first row of nuclei form to point A where the undercooling firstly exceeded 11 K in the liquid, the earlier the

second column of seeds formed. In this circumstance, the time left for equiaxed grains at first column to grow and the space ahead of first column of nuclei decreased. Therefore, the size of the first column of equiaxed grains decreased.

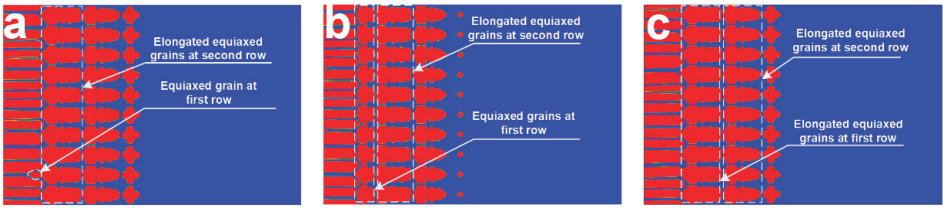

Figure 10. Effects of the location of first seed on the CET for U_n = 11 K and D_n = 200 Δx: (**a**) X_f = 100 Δx; (**b**) X_f = 200 Δx; (**c**) X_f = 300 Δx.

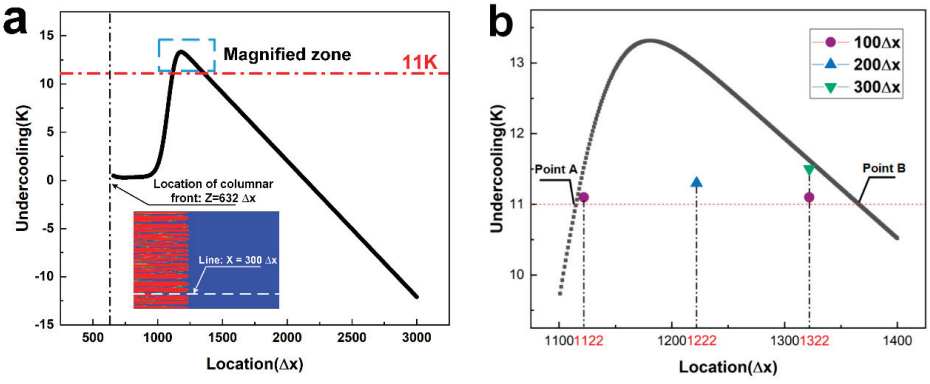

Figure 11. (**a**) The undercooling distribution along the line y = 300 Δx at the 7.0 × 10^5 Δt; (**b**) The undercooling distribution in magnified zone.

3.2. Interaction between Different Grains

To investigate the mechanism of the CET for laser welding, the interaction between different grains were studied. The velocities of columnar dendrite arm and equiaxed grain arm as shown in Figure 12 were selected to study the interaction between grains.

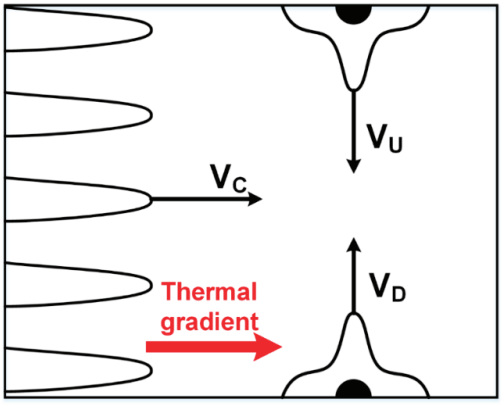

Figure 12. The growth of columnar and equiaxed grains.

A dimensionless dendrite tip velocity can be obtained by the following equation:

$$v = -\frac{1}{|\nabla\varphi|} * \frac{\partial\varphi}{\partial t} \tag{13}$$

The actual dendrite tip velocity divided by (W/τ_0) is the dimensionless dendrite tip velocity, W/τ_0 was equal to 1.75×10^{-2} m/s.

Without CET, the columnar dendrite tip velocity increased slowly after entering relatively steady growth stage as shown in Figure 13. In Case 1, 4 and 5, the CET occurred when the distance between nuclei increased from 200 Δx to 500 Δx. Figure 14a–c shows the dimensionless velocity and undercooling variations of the columnar dendrite tip until the CET occurs in Case 1, 4 and 5. The selected columnar dendrites analyzed in Figure 14 lied on the line y = 116 Δx in case 1, line y = 188 Δx in case 4 and line y = 242 Δx in case 5, respectively. Figure 14d–f shows the dimensionless velocity and solute segregation variations of the columnar dendrite tip until the CET occurs in Case 1, 4 and 5. As shown in Figure 14a–c, the columnar dendrite tip velocity fluctuated around a value at first. Then the velocity decreased and the columnar dendrite stopped advancing into the liquid after the columnar dendrites got rather close to the equiaxed grains. However, compared to undercooling, the columnar dendrite tip velocity was more related with solute concentration. When the solute segregation at columnar dendrite tip finally increased rapidly, the columnar dendrite tip velocity decreased quickly at the same time. It suggested that the constitutional undercooling played a more important role on the decreasing of columnar dendrite tip velocity. The blue pans in Figure 14d–f show the time step when the solute layers of columnar dendrites and equiaxed grains contacted with each other. It was interesting that the columnar dendrite tip velocity did not decrease until the solute layers of columnar dendrites and equiaxed grains have interacted with each other for some time, but not immediately after the solute layers of these dendrites interact with each other. As mentioned above, the columnar dendrite tip velocity increased continuously after entering relatively steady growth stage without CET. Therefore, the contact of solute layers of columnar dendrites and equiaxed grains firstly prevented the columnar dendrite tip velocity from increasing. The columnar dendrite tip velocity fluctuated around a value. After the solute in front of the columnar dendrite tip accumulated for some time, the columnar dendrite tip velocity started to decrease.

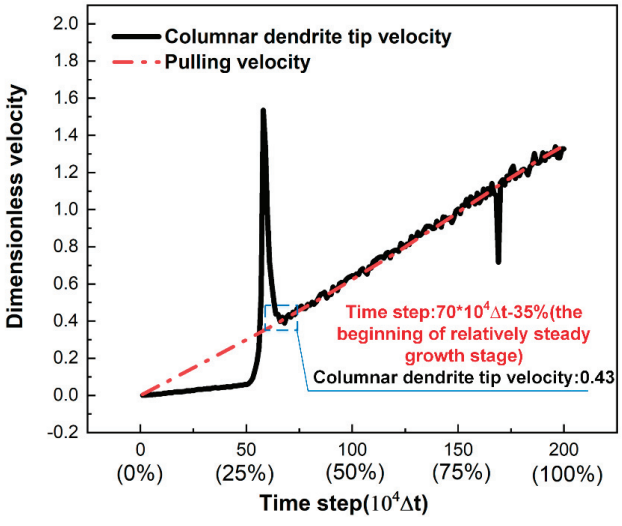

Figure 13. Columnar dendrite tip velocity evolution without CET.

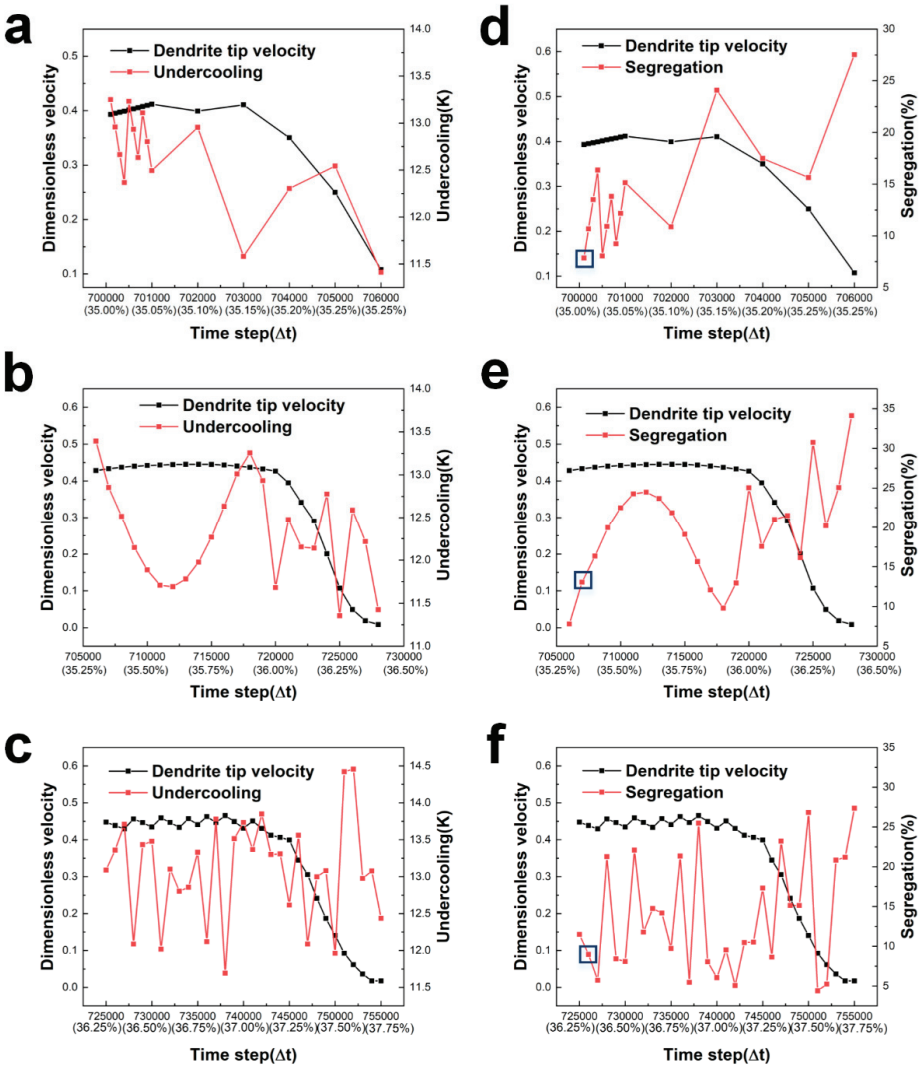

Figure 14. The velocity and undercooling variations of columnar dendrite tip with time for U_n = 11 K and X_f = 200 Δx: (**a**) D_n = 200 Δx; (**b**) D_n = 400 Δx; (**c**) D_n = 500 Δx. The velocity and solute segregation variations of columnar dendrite tip with time for U_n = 11 K and X_f = 200 Δx: (**d**) D_n = 200 Δx; (**e**) D_n = 400 Δx; (**f**) D_n = 500 Δx.

Figure 15 shows the dimensionless velocity, undercooling and solute segregation variations of the dendrite arm tip of equiaxed grains vertical to thermal gradient until the CET occurs in Case 1, 4 and 5. It was found that the dendrite tip velocity was very high soon after the seed nucleated and grew. Then the velocity decreased rapidly to around the value 0.4. After that, the velocity fluctuated around 0.4. Finally, the dendrite arms met together and the tip velocity decreased to 0. The undercooling of dendrite arm tip mainly kept increasing before the dendrite arms got too close. It began to decrease with the final increase of the solute segregation at the dendrite arm tip. The solute segregation at the dendrite arm tip kept increasing when the equiaxed grain dendrite arm grew.

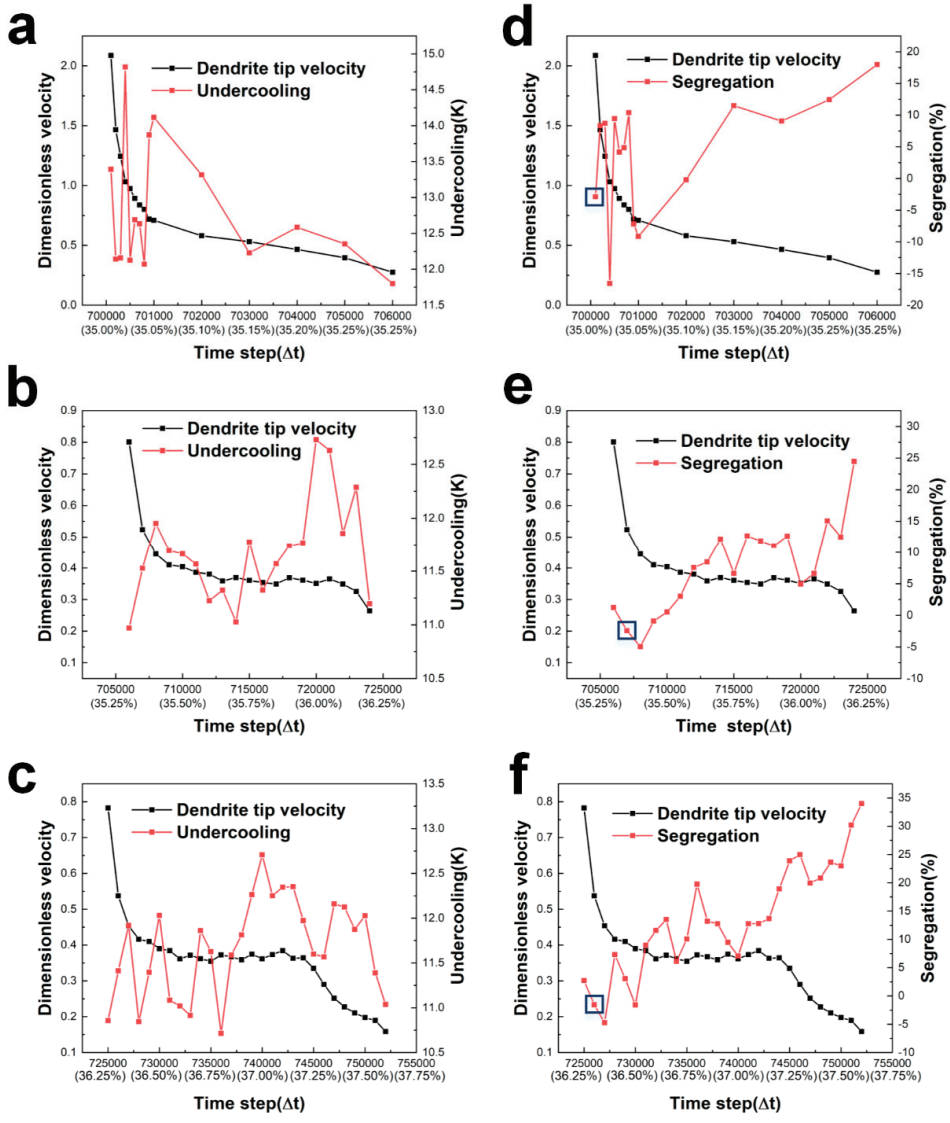

Figure 15. The dimensionless velocity and undercooling variations of equiaxed dendrite tip with time for U_n = 11 K and X_f = 200 Δx: (**a**) D_n = 200 Δx; (**b**) D_n = 400 Δx; (**c**) D_n = 500 Δx. The velocity and solute segregation variations of columnar dendrite tip with time for U_n = 11 K and X_f = 200 Δx: (**d**) D_n = 200 Δx; (**e**) D_n = 400 Δx; (**f**) D_n = 500 Δx.

Figure 16 shows the comparison of dimensionless columnar dendrite tip velocity, undercooling and solute segregation between Case 5 (U_n = 11 K, X_f = 200 Δx and D_n = 500 Δx) in which the CET occurs and Case 6 (U_n = 11 K, X_f = 200 Δx and D_n = 1000 Δx) in which no CET occurs. It was found that no significant difference existed between the undercoolings and solute segregations of Case 5 and 6. However, the CET occurred when the columnar grains and equiaxed grains got rather close to each other. No space was available for columnar dendrite growth. Therefore, it was concluded that the CET was mainly caused by mechanical blocking but not thermal nor solute blocking.

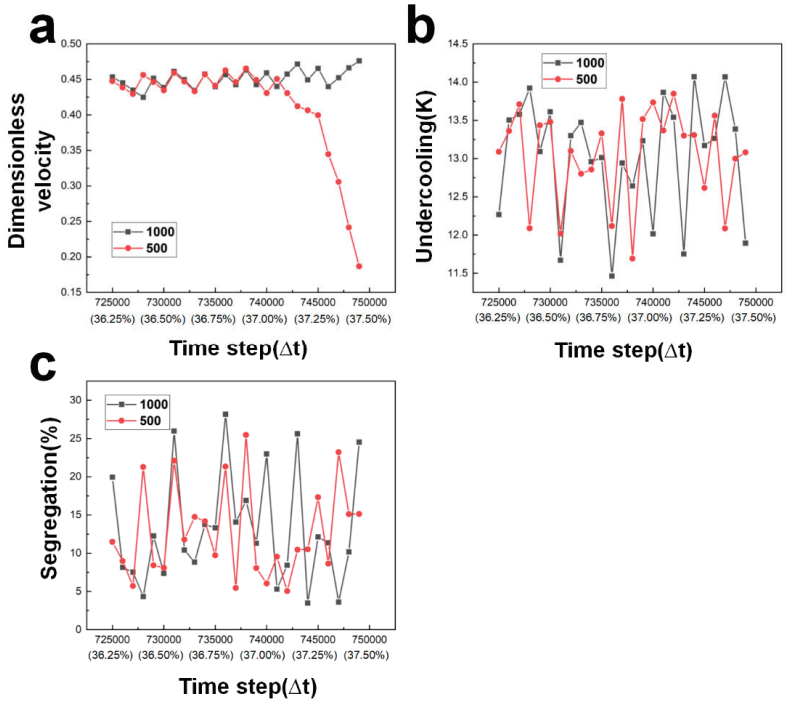

Figure 16. The comparisons of: (**a**) columnar dendrite tip velocity; (**b**) undercooling of dendrite tip; (**c**) solute segregation between case 5 and 6.

In Case 1 (U_n = 11 K, X_f = 200 Δx and D_n = 200 Δx), equiaxed grains that nucleated later were smaller than equiaxed grains that nucleated at the beginning of relatively steady growth stage after the CET occurred. This phenomenon indicated that the growing behaviors of equiaxed grains nucleating at different times were different. In order to illustrate this phenomenon, the microstructure evolution after CET was analyzed.

Until the first nucleation occurred at 7.0×10^5 Δt, the frontier of columnar dendrite had accumulated amount of solute. To ensure the reliability of the analysis, the second column of nuclei were used to study the growth behaviors of equiaxed-grain dendrite arm parallel to thermal gradient as shown in Figure 17 to avoid the effect of solute layer ahead of columnar dendrites.

Figure 18 shows the evolution of dimensionless dendrite tip velocity, undercooling and solute segregation. It was found that the solute segregation at dendrite tip was small (less than 1%). The overall solute segregation decreased. The decrease of solute concentration increased the undercooling of dendrite tip. Therefore, the overall undercooling increased. These factors promoted the increasing of dendrite tip velocity. However, the dendrite tip velocity was very high at the beginning. Then it decreased very fast to 0.25 and fluctuated. Finally, the dendrite tip was stopped by the third column of nuclei.

To illustrate the reason for change of equiaxed grain size with time, it was essential to study the undercooling distribution ahead of the equiaxed grain in the liquid and the undercooling evolution with time. As shown in Figure 19a, the undercooling in liquid increased at first, then decreased continuously with the increasing of distance to the equiaxed grains. Furthermore, the value of the maximum undercooling and its distance to the equiaxed grains increased with time as shown in Figure 19b.

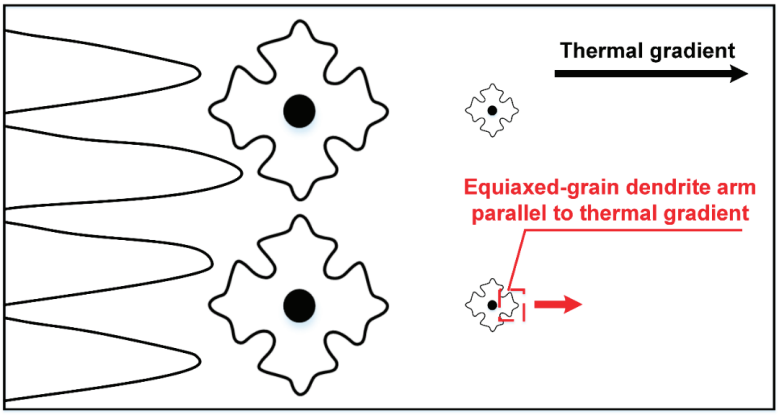

Figure 17. The diagram of second row of nuclei.

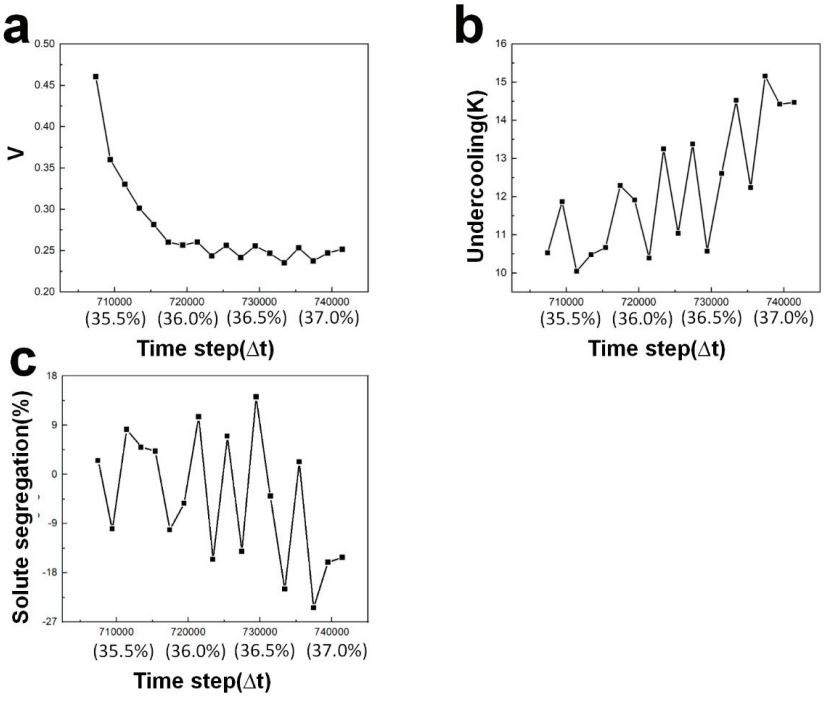

Figure 18. The evolution of (**a**) dendrite tip velocity; (**b**) undercooling; (**c**) segregation.

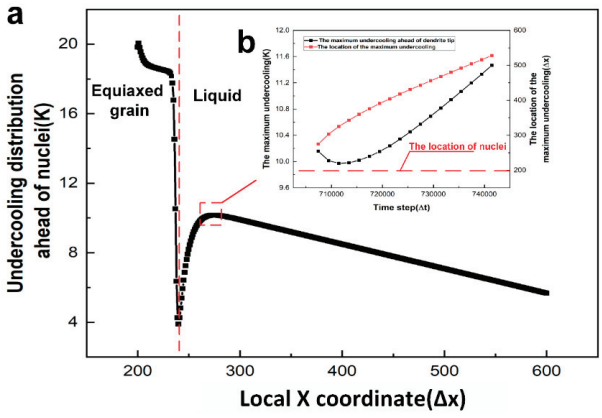

Figure 19. (**a**) The undercooling distribution ahead of nuclei; (**b**) The value and location variations of maximum undercooling in the liquid in Figure 17a with time.

The time interval of each column of equiaxed-grain formation (i.e., the growing time for equiaxed grains in the front column) is shown in Figure 20. Except for the first column of equiaxed-grain formation which were affected by columnar dendrite growth, the growing time for 2nd–7th columns of equiaxed grains was significantly longer than the following columns of equiaxed grain. Therefore, the 2nd–7th columns of equiaxed grains were elongated. The undercooling distributions ahead of nucleated seeds when the nuclei were formed at 705,430 Δt (2nd column) and 1,990,720 Δt (134th column) are shown in Figure 20b. At the location of nuclei, the undercooling ahead of nuclei in the liquid at 705,430 Δt (2nd) and 1,990,720 Δt (last column) were calculated by following expression.

$$U_n = T_0 - mc_n - (T_1 + GD_n) \quad (14)$$

$$U = T_0 - mc - (T_1 + GD) \quad (15)$$

where U is undercooling of selected point ahead of the nuclei, U_n is the undercooling at seed position just before nucleation i.e., 11 K, T_0 is the melting point of pure Al, T_1 is the temperature of reference point, D is the distance from selected point to reference point, D_n is the distance from nuclei to reference point. Therefore, the relationship between U and U_n is shown as Equation (16) (Equations (14) and (15)):

$$U = U_0 + m \times (C_0 - C) - G \times D_s \quad (16)$$

where D_s is the distance from the selected point to nuclei.

When a nucleus formed, the solute around the nucleus did not diffuse for a long distance. Therefore, it can be assumed that the solute concentration ahead of the nucleus in the liquid was not affected by the nucleation. In this condition, the undercooling of selected point was mainly affected by the temperature gradient. As shown in Figure 20c, the temperature gradient decreased with time. Therefore, the undercooling ahead of nuclei in the liquid at 705,430 Δt (the 2nd column) was smaller than that at 1,990,720 Δt (the 134th column). The undercooling at the position where the 3rd column of nuclei set at 705,430 Δt was lower than that at the position where the 135th column of nuclei set at 1,990,720 Δt. The 3rd column of nuclei needed more time to form than the 135th column of nuclei. As a result, the 2nd–7th columns of equiaxed grains had more time to grow. Therefore, the size of equiaxed grain decreased from fusion line to center line.

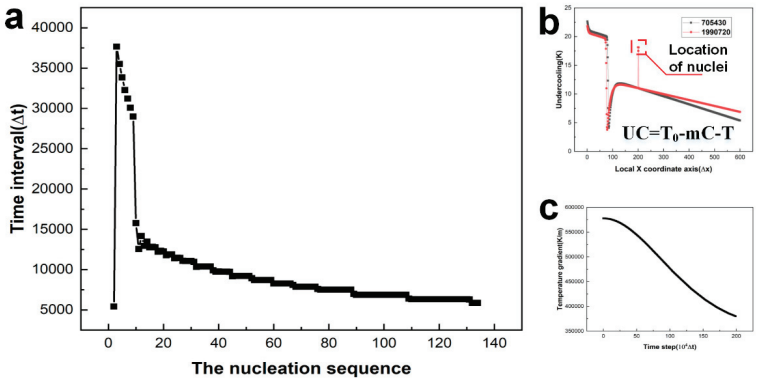

Figure 20. (**a**) The time interval of each row of equiaxed-grain formation; (**b**) undercooling distribution when seeds nucleate; (**c**) temperature gradient variation with time.

3.3. Experimental Results

Figure 21 shows the microstructure at the top surface of the fusion zone. It was found that the fusion zone was consisted of 3 zones: (a) columnar grain zone; (b) mixed microstructure zone; (c) Equiaxed grain zone. The grain size of equiaxed grains was measured. As shown in Figure 22, it was found that the size of equiaxed grain decreased from fusion line to center line, corresponding to the numerical result.

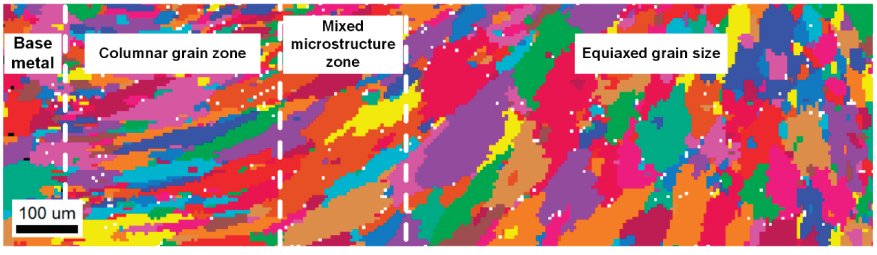

Figure 21. The microstructure of fusion zone.

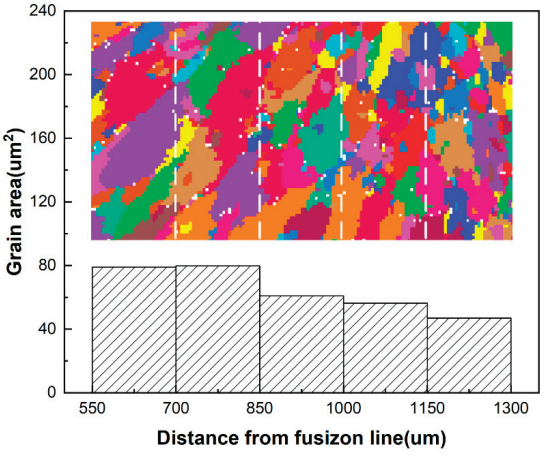

Figure 22. The size distribution of equiaxed grain in the fusion zone.

4. Conclusions

The CET during laser welding was investigated using a 2-D phase-field model. Experiments were conducted to verify the numerical result. The conclusion are as follows:

(1) Nucleation undercooling significantly influenced the occurrence and the time of CET. Nucleation density affected the occurrence of CET and the size of equiaxed grains.
(2) The contact of solute layers of columnar dendrites and equiaxed grains firstly prevented the columnar dendrite tip velocity from increasing. The solute blocking decreased the dendrite tip velocity of columnar grains before the CET happened. The mechanical blocking was the major mechanism for the CET.
(3) The decrease of the temperature gradient during solidification of the laser welding molten pool led to the decreasing of size of equiaxed grain from the fusion line to the center line.

It should be noted, however, that the microstructure evolution in real 3-D space during welding is more complex than a 2-D phase-field numerical simulation can predict. Nonetheless, 2D phase-field models have been applied to simulate CET during solidification for decades [1,11,18]. The results have shown a reasonable quantitative agreement between simulations and the analytical model for CET. However, a 2D model assumes an in-depth homogeneity of the system, a condition that prohibits modeling of fully-realistic 3D microstructural features. In a 2D model, Pe or the direction of crystalline orientations are limited to a smaller range than in a 3D model [23]. The solute diffusion during solidification can be completely blocked by the dendrite arms in 2D simulations, while it can bypass the 3D arms [24]. Interactions between crystals in the solidification process in real 3D physical space are more likely to appear between different layers. This effect cannot be simulated by a 2D model [25,26]. When the fluid flow is taken into consideration, the differences in the flow pattern in front of dendrite tips lead to the differences of dendrite growth behavior between 2D and 3D simulations [27]. All the above differences produce different distributions of solute, growth kinetics, and dendrite morphology between a 2D model and the 3D reality, limiting the accuracy of a 2D model for real 3D dendrite growth behaviors [23,27–30].

In principle it would have been interesting to compare our simulation results with Hunt's model. In Hunt's model, it is assumed that the columnar front is blocked, causing the CET, when the equiaxed grain fraction at the front is equal to or larger than a predetermined blocking fraction. Hunt's model can be applied for CET prediction in the solidification of laser welding molten pool if the temperature distribution and variation are known. However, in our present work, we focused on the interaction between the columnar grains and equiaxed grains and the computational domain was very small (81.6 × 54.4 um) compared to the whole columnar grain front in Hunt's model. The computational domain in our work can thus not represent the whole columnar grain front in Hunt's model. A comparison between our simulations and Hunt's model therefore lacks comparability, and, any comparison with Hunt's model has therefore not been in the present work. However, in the future, we plan to predict the whole microstructure of the laser welding fusion zone by phase-field modeling using multi-graphics processing units (GPUs) parallel computing. In this case, it will be very useful and meaningful to compare the results of our future work with Hunt's model.

Author Contributions: Conceptualization, Z.W.; methodology, L.X.; software, Z.W.; validation, L.X.; formal analysis, L.X.; investigation, L.X.; resources, P.J.; data curation, L.X.; writing—original draft preparation, L.X.; writing—review and editing, Z.W.; visualization, L.X.; supervision, Z.W.; project administration, C.W.; funding acquisition, C.W. All authors have read and agreed to the published version of the manuscript.

Funding: This research was funded by the National Natural Science Foundation of China, grant number 51861165202, the National Natural Science Foundation of China, grant number 51705173 and Science and Technology Planning Project of Guangdong Province, grant number 2017B090913001. The APC was funded by the National Natural Science Foundation of China, grant number 51705173.

Acknowledgments: The authors are grateful to the Analysis and Test Center of HUST (Huazhong University of Science and Technology) and the State Key Laboratory of Material Processing and Die & Mould Technology of HUST, for their friendly cooperation.

Conflicts of Interest: The authors declare no conflict of interest.

References

1. Badillo, A.; Beckermann, C. Phase-field simulation of the columnar-to-equiaxed transition in alloy solidification. *Acta Mater.* **2006**, *54*, 2015–2026. [CrossRef]
2. Kou, S. *Welding Metallurgy*; Wiley: Hoboken, NJ, USA, 2003.
3. Gandin, C.A. Experimental study of the transition from constrained to unconstrained growth during directional solidification. *ISIJ Int.* **2000**, *40*, 971–979. [CrossRef]
4. Nguyen-Thi, H.; Reinhart, G.; Mangelinck-Noël, N.; Jung, H.; Billia, B.; Schenk, T.; Gastaldi, J.; Härtwig, J.; Baruchel, J. In-situ and real-time investigation of columnar-to-equiaxed transition in metallic alloy. *Metall. Mater. Trans. A* **2007**, *38*, 1458–1464. [CrossRef]
5. Villafuerte, J.C.; Pardo, E.; Kerr, H.W. The effect of alloy composition and welding conditions on columnar-equiaxed transitions in ferritic stainless steel gas-tungsten arc welds. *Metall. Trans. A* **1990**, *21*, 2009. [CrossRef]
6. Geng, S.; Jiang, P.; Shao, X.; Guo, L.; Mi, G.; Wu, H.; Wang, C.; Han, C.; Gao, S. Identification of nucleation mechanism in laser welds of aluminum alloy. *Appl. Phys. A* **2019**, *125*, 396. [CrossRef]
7. Spittle, J.A. Columnar to equiaxed grain transition in as solidified alloys. *Int. Mater. Rev.* **2006**, *51*, 247–269. [CrossRef]
8. Hunt, J.D. Steady state columnar and equiaxed growth of dendrites and eutectic. *Mater. Sci. Eng.* **1984**, *65*, 75–83. [CrossRef]
9. Gaumann, M.; Trivedi, R.; Kurz, W. Nucleation ahead of the advancing interface in directional solidification. *Mater. Sci. Eng. A Struct. Mater. Prop. Microstruct. Process.* **1997**, *226*, 763–769. [CrossRef]
10. Martorano, M.A.; Beckermann, C.; Gandin, C.-A. A solutal interaction mechanism for the columnar-to-equiaxed transition in alloy solidification. *Metall. Mater. Trans. A* **2003**, *34*, 1657–1674. [CrossRef]
11. Li, J.; Wang, J.; Yang, G. Phase-field simulation of microstructure development involving nucleation and crystallographic orientations in alloy solidification. *J. Cryst. Growth* **2007**, *309*, 65–69. [CrossRef]
12. Viardin, A.; Sturz, L.; Zimmermann, G.; Apel, M. Phase-field modeling of the columnar-to-equiaxed transition in neopentylglycol-camphor alloy solidification. In *International Symposium on Physical Sciences in Space*; Meyer, A., Egry, I., Eds.; IOP Publishing Ltd.: Bonn, Germany, 2011.
13. Dong, H.B.; Lee, P.D. Simulation of the columnar-to-equiaxed transition in directionally solidified Al–Cu alloys. *Acta Mater.* **2005**, *53*, 659–668. [CrossRef]
14. Biscuola, V.B.; Martorano, M.A. Mechanical blocking mechanism for the columnar to equiaxed transition. *Metall. Mater. Trans. A* **2008**, *39*, 2885–2895. [CrossRef]
15. Chen, R.; Xu, Q.; Liu, B. A Modified cellular automaton model for the quantitative prediction of equiaxed and columnar dendritic growth. *J. Mater. Sci. Technol.* **2014**, *30*, 1311–1320. [CrossRef]
16. Liu, P.W.; Ji, Y.Z.; Wang, Z.; Qiu, C.L.; Antonysamy, A.A.; Chen, L.Q.; Cui, X.Y.; Chen, L. Investigation on evolution mechanisms of site-specific grain structures during metal additive manufacturing. *J. Mater. Process. Technol.* **2018**, *257*, 191–202. [CrossRef]
17. Zhan, X.; Lin, X.; Gao, Z.; Qi, C.; Zhou, J.; Gu, D. Modeling and simulation of the columnar-to-equiaxed transition during laser melting deposition of Invar alloy. *J. Alloys Compd.* **2018**, *755*, 123–134. [CrossRef]
18. Montiel, D.; Liu, L.; Xiao, L.; Zhou, Y.; Provatas, N. Microstructure analysis of AZ31 magnesium alloy welds using phase-field models. *Acta Mater.* **2012**, *60*, 5925–5932. [CrossRef]
19. Liu, P.; Wang, Z.; Xiao, Y.; Horstemeyer, M.F.; Cui, X.; Chen, L. Insight into the mechanisms of columnar to equiaxed grain transition during metallic additive manufacturing. *Addit. Manuf.* **2019**, *26*, 22–29. [CrossRef]
20. Han, R.; Lu, S.; Dong, W.; Li, D.; Li, Y. Multi-scale Simulation for the Columnar to Equiaxed Transition in the Weld Pool. *ISIJ Int.* **2016**, *56*, 1003–1012. [CrossRef]
21. Zheng, W.; Dong, Z.; Wei, Y.; Song, K. Onset of the initial instability during the solidification of welding pool of aluminum alloy under transient conditions. *J. Cryst. Growth* **2014**, *402*, 203–209. [CrossRef]

22. Wang, L.; Wei, Y.; Zhan, X.; Yu, F. A phase field investigation of dendrite morphology and solute distributions under transient conditions in an Al-Cu welding molten pool. *Sci. Technol. Weld. Join.* **2016**, *21*, 446–451. [CrossRef]
23. Ghmadh, J.; Debierre, J.-M.; Deschamps, J.; Georgelin, M.; Guerin, R.; Pocheau, A. Directional solidification of inclined structures in thin samples. *Acta Mater.* **2014**, *74*, 255–267. [CrossRef]
24. Eshraghi, M.; Hashemi, M.; Jelinek, B.; Felicelli, S.D. Three-Dimensional Lattice Boltzmann Modeling of Dendritic Solidification under Forced and Natural Convection. *Metals* **2017**, *7*, 474. [CrossRef]
25. Feng, L.; Gao, Y.L.; Lu, N.N.; Zhu, C.S.; An, G.S.; Zhong, J.H. Phase-field simulation of competitive growth of grains in a binary alloy during directional solidification. *China Foundry* **2018**, *15*, 333–342. [CrossRef]
26. Guo, C.; Li, J.; Wang, Z.; Wang, J. Non-uniplanar competitive growth of columnar dendritic grains during directional solidification in quasi-2D and 3D configurations. *Mater. Des.* **2018**, *151*, 141–153. [CrossRef]
27. Takaki, T.; Sakane, S.; Ohno, M.; Shibuta, Y.; Aoki, T. Large-scale phase-field lattice Boltzmann study on the effects of natural convection on dendrite morphology formed during directional solidification of a binary alloy. *Comput. Mater. Sci.* **2020**, *171*, 313–320. [CrossRef]
28. Sakane, S.; Takaki, T.; Rojas, R.; Ohno, M.; Shibuta, Y.; Shimokawabe, T.; Aoki, T. Multi-GPUs parallel computation of dendrite growth in forced convection using the phase-field-lattice Boltzmann model. *J. Cryst. Growth* **2017**, *474*, 154–159. [CrossRef]
29. Wesner, E.; Choudhury, A.; August, A.; Berghoff, M.; Nestler, B. A phase-field study of large-scale dendrite fragmentation in Al-Cu. *J. Cryst. Growth* **2012**, *359*, 107–121. [CrossRef]
30. Nastac, L. An Efficient 3D Stochastic Model for Predicting the Columnar-to-Equiaxed Transition in Alloy 718. *IOP Conf. Ser. Mater. Sci. Eng.* **2015**, *84*, 012089. [CrossRef]

metals

MDPI

Article

A Two-Dimensional Phase-Field Investigation on Unidirectionally Solidified Tip-Splitting Microstructures

V. Pavan Laxmipathy [1,*], Fei Wang [1], Michael Selzer [1,2] and Britta Nestler [1,2]

[1] Institute of Applied Materials, Karlsruhe Institute of Technology (KIT), Strasse am Forum 7, 76131 Karlsruhe, Germany; fei.wang@kit.edu (F.W.); michael.selzer@kit.edu (M.S.); britta.nestler@kit.edu (B.N.)
[2] Institute of Digital Materials Science, Karlsruhe University of Applied Sciences, Moltkestr. 30, 76133 Karlsruhe, Germany
* Correspondence: pavan.veluvali2@kit.edu

Abstract: The onset of morphological instabilities along a solidifying interface has a tendency to influence the microstructural characteristics of cast alloys. In the present study, the initiation as well as the mechanism of microstructural pattern formation is investigated by a quantitative phase-field approach. For energetically isotropic interfaces, we show that the presence of grain boundary grooves promotes the initiation of morphological instabilities, and with progressive solidification, they subsequently amplify into tip-splitting microstructures. We also demonstrate that the grain boundary groove shape influences the amplification of the ridge-shaped instability near the pit region. The structural transition of tip splitting to dendritic microstructures is showcased through the effect of interfacial anisotropy. In addition, the prediction of the tip-splitting position is discussed through an analytical criterion, wherein the sign of the surface Laplacian of interfacial curvature dictates the formation of crest and trough positions in a tip-splitting pattern. In complete agreement with the sharp-interface theory, our phase-field simulations validate the analytically obtained tip-splitting position and suggest that the two tips evolve symmetrically on either side of the hindered concave region. Furthermore, the role of lattice anisotropy on the tip-splitting phenomenon is also discussed in detail.

Keywords: pattern formation; tip splitting; phase-field model; grain boundary groove; microstructure formation

Citation: Laxmipathy, V.P.; Wang, F.; Selzer, M.; Nestler, B. A Two-Dimensional Phase-Field Investigation on Unidirectionally Solidified Tip-Splitting Microstructures. *Metals* **2022**, *12*, 376. https://doi.org/10.3390/met12030376

Academic Editor: Mohsen Eshraghi

Received: 18 January 2022
Accepted: 20 February 2022
Published: 22 February 2022

1. Introduction

Over the last few decades, the selection of microstructural patterns has been a long-standing fundamental interest in scientific and technological advancements. In the presence of high supercoolings [1], pressure gradients [2–4], and low magnetic fields [5], complex microstructural patterns systematically evolve in simulated environments. In unidirectional solidification, the crystal–melt interface generally consists of imperfections in the form of grain boundaries, impurities, and distortions. When morphological instabilities are triggered along a planar front by thermal or constitutional undercooling, these crystal imperfections act as preferred locations for the initiation of interfacial instabilities. Especially, in the presence of grain boundaries, the solid–liquid interfaces become unstable by passing through a different, slightly more complicated, sequence of morphological changes [6]. Schaefer and Glicksman [7] performed seminal experiments and recorded the temporal evolution of morphological instabilities in a polycrystalline sample. Originated near the grain boundary grooves, it was concluded that the protuberances amplified into liquid melt in the form of dendritic branches.

After successful experiments, the stability of a dendritic pattern was first quantitatively evaluated by Mullins and Sekerka [8,9]. It was concluded that an advancing interface splits if the tip radius ρ_i is larger than the critical wavelength λ_i. For example, the tip radius

becomes unstable at the smallest wavelength and results in the formation of symmetrically broken fingers. Later, based on this theory, several investigators [7,10,11] carried out experiments on succinonitrile-based transparent alloys to demonstrate the lateral spreading of the instabilities. For example, Noël et al. [10] performed in situ experiments to study the emergence of non-planar patterns, and they analyzed the cellular interfaces in a transparent binary alloy. It was confirmed that the initiation and the formation of a grain boundary groove lead to the propagation of ridges and depressions along a planar front. In addition, as the solidification velocity was increased beyond the critical velocity of a planar interface, the initial instability occurred at the two slightly convex ridges, which later coarsened and dominated the growth competition among cellular microstructures. Furthermore, at high growth rates, the progressive development of low-amplitude ripples via the formation of ramified patterns was also noticed. Several directional solidification studies [12–14] have shown the emergence of complex tip-splitting microstructures in the absence of interfacial anisotropy. A split tip defines a disordered pattern, whereas the presence of interfacial anisotropy energy brings in a steady and a directionally dependent tip with side branches. Over the last few decades, the structural transition of a solidifying interface into an unidirectionally solidified microstructure has been of considerable interest in cast binary alloys. Therefore, it is important to characterize and control such shapes resulting from solidification.

Apart from the aforementioned literature, various experiments [13,15,16] and theoretical findings [17] have attempted to justify and elucidate the underlying mechanism of branching. While Martin et al. [17] presented the side branching in a dendrite through the disturbances in the mean curvature, Nittman et al. [13] illustrated the tip-splitting phenomenon as a relation with the imposed numerical noise in the bulk. Similarly, Devachelle et al. [18] provided an optimization principle in order to describe the dynamics of a diffusion-limited finger. Moreover, another classical way to study the pattern genesis is through the Hele–Shaw cell [4]. Confined in-between two parallelly separated plates, this method describes the generation of Saffman–Taylor cells, as a result of an unstable interface between the two viscous fluids. Likewise, Suekane et al. [19] studied the three-dimensional characteristics of viscous fingers, where the flow instabilities events were described as a combination of frequent tip splitting, shielding, and coalescence.

More recently, Glicksman [16] proposed a deterministic side-branching mechanism for anisotropic dendrites. According to this theory, the rotation points near the dendritic tip developed a wrinkle, which later grew into a side branch. The local analysis was proved to be successful in kinematically determining the rotation points for branching, wherein the crystal experienced an accelerated growth depending upon the sign of the surface Laplacian of the interfacial curvature $\nabla_s^2\kappa$. Later, several phase-field simulations [20–22] subsequently confirmed the role of capillary-mediated fluxes in an anisotropic dendrite. In particular, Mullis [20] re-evaluated the findings in Ref. [16] and reported that the above criterion is a useful tool for understanding the branching mechanism. However, in light of the above-mentioned literature, the determination of tip-splitting positions for an energetically isotropic microstructure has been less understood. For example, although previous studies [23,24] have addressed the tip-splitting phenomenon, a quantitative study, whereby the dynamic comparison of the sharp-interface criterion, as well as the role of numerical effects, such as grid anisotropy and numerical noise, is still elusive. Additionally, it needs to be established if the theoretical criterion previously deduced to explain the behavior of secondary branches can be extended to accurately predict the tip-splitting positions. In this regard, the present work intends to fill the gap in our understanding, and it reports a two-dimensional phase-field investigation to elucidate the formation and the behavior of unidirectionally solidified tip-splitting microstructures.

The rest of the manuscript is organized as follows: in the following section, we briefly describe our phase-field model through the evolution equations for the phase and the concentration fields. In the Results and Discussion section, we first simulate the two-dimensional tip-splitting microstructures from a bicrystal specimen. Initiated at the

grain boundary grooves, we illustrate that the morphological instabilities amplify into tip-splitting microstructures due to the presence of isotropic interfacial energy. Next, the role of groove shape as well as the strength of interfacial anisotropy is discussed in detail. Furthermore, the underlying mechanism of tip instability is discussed in detail, wherein, based on the sharp-interface analytical criterion, the splitting region is showcased. Later, we perform phase-field simulations to demonstrate and validate the analytically derived branching region. In addition, a comparative study between simulations and a sharp-interface theory reveals the effect of the underlying grid on our numerical results. Finally, we put forward the conclusions from the present work.

2. Model Description

Over the last two decades, the phase-field approach is gaining popularity as a method of choice to model complex microstructures in solidification, precipitation, and strain-induced transformation studies [25]. In the present work, the phase-field model employed is based on the grand potential formulation by Choudhury and Nestler [26] where the evolution of phases is determined by the minimization of the modified functional $d\Omega/dt \leqslant 0$, given by

$$\Omega(T, \boldsymbol{\mu}, \boldsymbol{\phi}) = \int_{\Omega} \left[\Psi(T, \boldsymbol{\mu}, \boldsymbol{\phi}) + \left(\epsilon a(\boldsymbol{\phi}, \nabla \boldsymbol{\phi}) + \frac{1}{\epsilon} w(\boldsymbol{\phi}) \right) \right] d\Omega, \tag{1}$$

where T is the temperature, $\boldsymbol{\mu} = (\mu_1, \ldots, \mu_i, \ldots, \mu_{K-1})$ is a vector consisting of $K-1$ chemical potentials of the system at a given temperature, and $\boldsymbol{\phi} = (\phi_1, \ldots, \phi_\alpha, \ldots, \phi_N)$ describes the phase index vector, where ϕ_α represents the local volume fraction of the α phase. In addition, ϵ is a length scale related to the thickness of the diffuse interface. The terms $\epsilon a(\boldsymbol{\phi}, \nabla \boldsymbol{\phi})$ and $\frac{1}{\epsilon} w(\boldsymbol{\phi})$ are the gradient and obstacle-type energy densities, which take the thermodynamics of the interface into account [25]. In the present work, the mole fractions of component B in the solid and liquid are set as $c_B^{s,eq} = 0.8$ and $c_B^{l,eq} = 0.2$, respectively. Similar to our previous studies [27,28], we consider a binary alloy model system, and we also would like to reiterate that the temporal evolution of tip-splitting microstructures is not affected by the selected mole fractions. Rather, the evolution of the microstructure depends on the imposed melt supersaturation, expressed as $\Delta = (c_B^{l,eq} - c_B^l)/(c_B^{l,eq} - c_B^{s,eq})$, where c_B^l is the initial concentration in liquid phase. Lastly, all the parameters used in our numerical simulations are given in Table 1.

Table 1. Dimensionless parameters for the present study.

Description	Parameter	Value
Partition coefficient	k	0.25
Discretized grid space	$\Delta x = \Delta y$	1.0×10^{-7} m
Domain size	$Nx \times Ny$	1000×1000
Interface width	ϵ	4.0×10^{-7} m
Melt supersaturation	$\Delta = \left(\frac{c_B^{l,eq} - c_B^l}{c_B^{l,eq} - c_B^{s,eq}} \right)$	0.50

The evolution equations for the phase-field is given as

$$\tau \epsilon \frac{\partial \phi_\alpha}{\partial t} = \epsilon \left(\nabla \cdot \frac{\partial a(\boldsymbol{\phi}, \nabla \boldsymbol{\phi})}{\partial \nabla \phi_\alpha} - \frac{\partial a(\boldsymbol{\phi}, \nabla \boldsymbol{\phi})}{\partial \phi_\alpha} \right) - \frac{1}{\epsilon} \frac{\partial w(\boldsymbol{\phi})}{\partial \phi_\alpha} - \frac{\partial \Psi(T, \boldsymbol{\mu}, \boldsymbol{\phi})}{\partial \phi_\alpha} - \lambda, \tag{2}$$

where λ is a Lagrange multiplier so that the local constraint $\sum_{\alpha=1}^{N} \phi_\alpha = 1$ is fulfilled. The gradient energy term reads as,

$$\epsilon a(\boldsymbol{\phi}, \nabla \boldsymbol{\phi}) = \epsilon \sum_{\alpha,\beta=1}^{N,N} \gamma_{\alpha\beta} [a_c(\boldsymbol{q}_{\boldsymbol{\alpha\beta}})]^2 |\boldsymbol{q}_{\boldsymbol{\alpha\beta}}|^2, \tag{3}$$

where $\boldsymbol{q_{\alpha\beta}}$ models the surface energy of the evolving phase boundary and $\gamma_{\alpha\beta}$ is the interfacial energy per unit area of the α/β interface. Here, to simulate a tip-splitting microstructure, an isotropic interfacial energy is imposed using $a_c(\boldsymbol{q_{\alpha\beta}}) = 1$. Interfaces with finite interfacial anisotropy and having an underlying four-fold cubic symmetry are modeled by the expression

$$a_c(\boldsymbol{q}_{\alpha\beta}) = 1 - \delta_{\alpha\beta}\left(3 \mp 4\frac{|\boldsymbol{q}_{\alpha\beta}|_4^4}{|\boldsymbol{q}_{\alpha\beta}|^4}\right), \tag{4}$$

where $|\boldsymbol{q}_{\alpha\beta}|_4^4 = \sum_{i=1}^{d}(q_i^4)$ and $|\boldsymbol{q}_{\alpha\beta}|^4 = [\sum_{i=1}^{d}(q_i^2)]^2$. The strength of the anisotropy of the $\alpha - \beta$ phase or grain boundary is given by the parameter $\delta_{\alpha\beta}$. In general, phase transformation in alloy solidification is driven by both heat and mass transport. However, since these processes occur at significantly different time scales, for the present study, the conduction of heat in the system is treated as isothermal, wherein the domain temperature T in Equation (2) is assumed to be constant throughout the system and thereby plays no role in the temporal evolution of the microstructures. The term $w(\phi)$ represents the multiobstacle potential. Now, the evolution equation for the chemical potentials can be expressed as

$$\frac{\partial \mu}{\partial t} = \left[\sum_{\alpha=1}^{N} h(\phi_\alpha)\frac{\partial c(\boldsymbol{\mu})}{\partial \mu}\right]^{-1} \times \left\{\nabla \cdot \left(M(\boldsymbol{\phi})\nabla\mu - \boldsymbol{J_{at}} - \boldsymbol{q}\right) - c^{\alpha}(\boldsymbol{\mu})h^{'}(\phi_\alpha)\frac{\partial \phi}{\partial t}\right\}. \tag{5}$$

In the above equation, the mass flux on the right-hand side has contributions from diffusion due to the gradient in the chemical potential and the interface mobility $M_{ij}(\boldsymbol{\phi})$. Additionally, with an imposed magnitude of 0.06, the term $\boldsymbol{q}$ represents the conserved noise in the bulk liquid phase, and the anti-trapping current $\boldsymbol{J_{at}}$ compensates the solute-trapping effect due to an enlarged interface in our phase-field model. This effect can be negated through the anti-trapping current; see Choudhury and Nestler [26] for more details. All terms in Equations (2) and (5) are explicitly defined by Choudhury and Nestler [25,26]. Lastly, while Equations (2) and (5) are numerically solved in space via a finite difference discretization, the time derivative follows an explicit Euler scheme. Finally, the current numerical algorithm is parallelized via message passing interface (MPI) to distribute the computing task on multicore high-performance architectures.

3. Results and Discussion

3.1. Tip-Splitting Microstructures

Initiated at the grain boundary, we first investigate the temporal evolution of a morphological pattern, wherein the planar solidification front transforms into a ramified tip-splitting microstructure in a supersaturated melt under isothermal conditions; see Figure 1. Here, we perform the numerical simulations in a two-dimensional domain of 1000×1000 numerical cells, with the space discretization $\Delta x = 1.0 \times 10^{-7}$ m. In addition, the interface width is given as $\epsilon = 4 \times \Delta x$, such that the equilibrium diffuse-interface profile encompasses eight grid points in the numerical domain. Furthermore, on the left and right side of the domain walls, the periodic boundary condition is imposed for the phase and concentration fields. At the top boundary, the Neumann boundary condition is applied for both the fields.

In a supersaturated melt of composition $\Delta = 0.50$, and during the initial stages, the interface remains planar and advances slowly toward the liquid region. As shown in Figure 1, with the accumulation of solutal fields ahead of the solid–liquid interface at the groove pit, the planar interface loses its stability and undergoes the well-known Mullins–Sekerka instability [8], which states that the stability of a solid–liquid interface is governed by the critical wavelength and the extent of constitutional supercooling in the bulk. When compared with the grain centers, the instabilities at the grain boundary amplify at a faster rate into primary ridges. We also notice that parts of the grain centers not immediately

adjacent to the grain boundary remain featureless and undistorted. Afterwards, while the shape of the instability across the domain depends on whether it decays or grows, the initial morphological instability from a liquid groove always coarsens. As a ridge is developed near a grain boundary, the solute is laterally rejected outwards, leading to the formation of secondary depressions. Nevertheless, these primary ridges evolve into a periodic array of hills and later transform into a ramified dendritic network, depending upon the anisotropy in the solid–liquid interfacial energy. Analogous to the present observation, the correlation between grain boundaries and the formation of cellular arrays was reported in the experimental work of Noël et al. [10]. It was suggested that the surface undulations and cell alignment along the grain boundary, typically observed during the initial stages, give way to a flat, regular arrangement of cells. Moreover, in the present scenario and as depicted in Figure 1, the dynamic evolution of the interface instabilities is simulated with isotropic solid–liquid energy such that random tip-splitting structures are observed. The simulated non-planar tip-splitting microstructures are widely known as seaweed structures, which were originally observed in several experimental and phase-field investigations [1,2,12,13,29]. While the columnar dendrites are directionally dependent with a steady-state dendritic shape, the ramified microstructures in Figure 1 are considered as solidification patterns without any orientational order. Only from a morphological point of view these tip-splitting microstructures look like the degenerate tips in a directionally solidified dendrite [30].

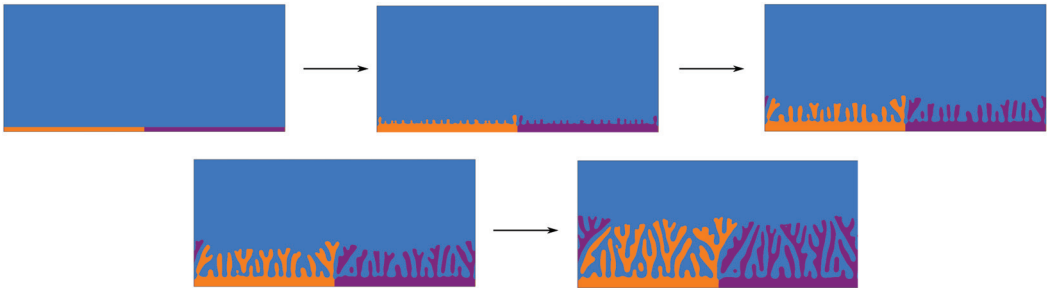

Figure 1. Temporal evolution of a tip-splitting microstructure in a supersaturated melt of composition $\Delta = 0.50$. The primary ridges developed at the grain boundary groove amplify into split structures along with the propagation of hillocks across the two solid grains. The combined influence of constitutionally supercooled alloy melt near the solid–liquid interface and isotropic interfacial energy promote the formation of a tip-splitting morphology. Here, the magenta and orange colors refer to the two distinct solid grains, and blue color represents the liquid phase, respectively.

Depicted in Figure 2a–c, it is important to note that the fundamental and repeating characteristic of a seaweed structure is the successive and continuous splitting of the tips. Herein, a local competition between the preferred crystal growth direction and the presence of strong concentration gradients results in the repeated splitting of the leading tip into two parts. In Figure 2a, when growth conditions are imposed for which a planar interface just becomes unstable, a zone of supercooled liquid exists ahead of the planar interface, which causes the interface to become unstable and to form a perturbed shape. As the threshold value of the interface velocity is exceeded, the lateral diffusion of solute reduces the solute concentration at the cell tip. Subsequently, with progressive solidification, this sequential process is repeated, and thereafter, a complex fractal-like dense microstructure is generated. Similar to the diffusion-limited growth of isotropic crystals [2,12,13], the formation of seaweed patterns is inherently related to the low anisotropic properties of the solid–liquid interface. Nevertheless, the absence of anisotropy promotes an uninhibited, omnidirectional growth via irregular branching and splittings of an evolving interface [24].

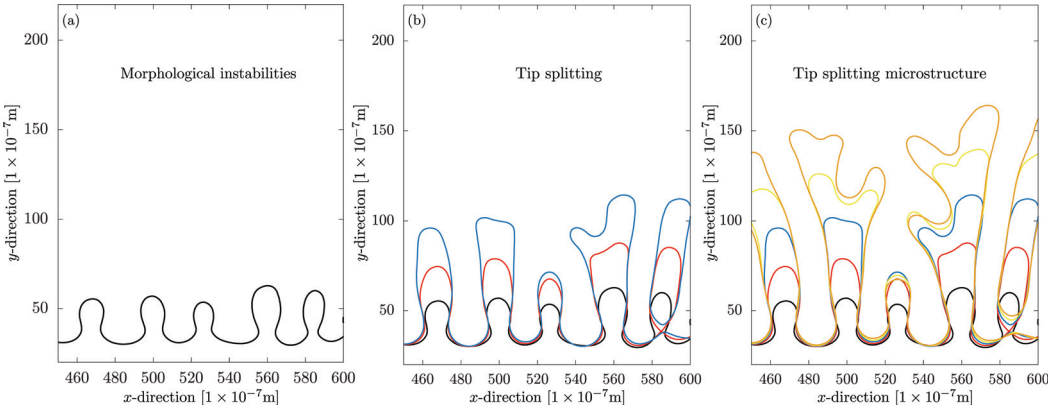

Figure 2. (**a**–**c**) Phase-field isolines illustrating the development of a tip-splitting microstructure from a unidirectionally solidified solid–liquid interface. Morphological instabilities evolve with time to undergo successive branching at the tip. Sequential steps to generate a seaweed microstructure: Initial morphological instabilities → amplification of tips → tip-splitting event. Isolines with various colors represent different simulation timesteps.

3.2. Effect of Groove Shape

Grain boundary grooves develop along a solidification front whenever bicrystal or polycrystal grains are in close contact with an alloy melt. Since the grain boundary groove region initiates pattern formation, in this section, we study the role of groove shapes on the morphological development of instabilities during alloy solidification. Figure 3 depicts the temporal inception of a ridge-shaped instability near a groove pit for different R_0, where R_0 is the ratio between solid–solid γ_{gb} and solid–liquid interfacial energies γ_{sl}. As shown in Figure 3, we observe that an increase in the ratio R_0 amplifies the growth of the instability adjacent to the grain boundary groove region. As the solidification of the solid–liquid interface commences from an initial configuration, the imposed surface energy modifies the groove shape, which in turn assists in the temporal development of ridges into tip-splitting microstructures. With increasing solid–liquid interfacial energy contribution, i.e., for decreasing R_0 , and as shown via Figure 4, we also notice that a shallow groove shape promotes the constrained growth of humps such that the instability height decreases as a function of simulation time. This behavior qualitatively agrees with previous experimental and phase-field studies [7,31], where the role of a grain boundary groove on the initiation of morphological instabilities during alloy solidification was discussed in detail. Furthermore, the stability analysis by Coriell et al. [32] also provided a theoretical background. It was reported that the groove pit depth determines the transient amplification of the ridges, and the main role of a grain boundary is to provide an initial perturbation based on the local concentration gradients at the pit region. Therefore, the formation of an instability near the grain boundary groove and the initiation of perturbations across the solid grains is largely controlled and influenced by the chosen surface energies at the trijunction. Nonetheless, for the limiting case $R_0 \to 0$, as the grain boundary energy contribution diminishes, we expect the development of an instability to be completely inhibited.

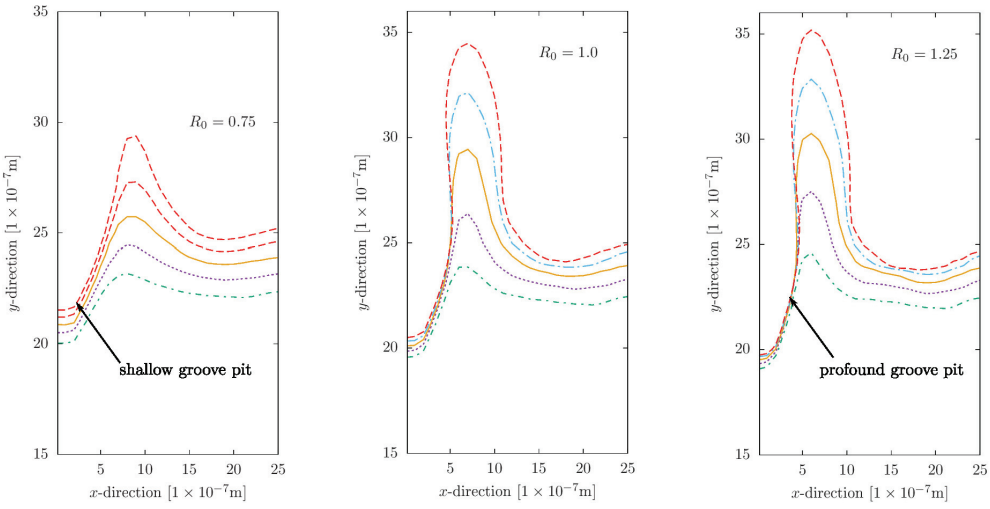

Figure 3. Effect of groove shape on the morphological development of primary ridges near a grain boundary. An increase in the ratio R_0, where R_0 is the ratio between solid–solid γ_{gb} to solid–liquid interfacial energies γ_{sl} increases the local amplification of the ridge shaped instability. In contrast, a shallow groove due to an increase in the solid–liquid interfacial energy contribution (decreasing R_0) hinders the growth of the instability near the groove pit region. Various colored isolines represent different simulation timesteps.

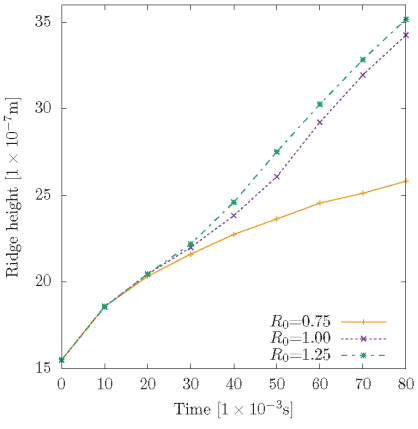

Figure 4. Ridge height as a function of simulation time for different groove shapes (different R_0). An increase in the ratio R_0 assists the morphological development of ridge-shaped instability near the grain boundary groove region.

3.3. Effect of Interfacial Anisotropy

In this section, we briefly study the role of interfacial anisotropy on pattern formation, and the various morphologies that arise from an unidirectionally solidified interfacial front are depicted in Figure 5. Here, we impose a four-fold interfacial anisotropy in solid–liquid energy formulation such that the strength of anisotropy of an α/β interface is given by the parameter $\delta_{\alpha\beta}$; for expression and implementation, see Ref. [25]. As shown in Figure 5, we observe that the imposed strength of anisotropy controls the direction as well as the morphology of the microstructure. While $\delta_{\alpha\beta} = 0.0$ generates a disoriented tip-splitting structure, an increase in the anisotropic strength $\delta_{\alpha\beta}$ promotes the formation of steady-

state columnar dendrites. In general, the local competition of bulk and interfacial forces determines the transition of a planar interface into a ramified pattern. Due to the presence of significant surface energy anisotropy, the absence of frequent tip splitting is noticed for $\delta_{\alpha\beta} > 0.01$. As reported in our previous study [28], the presence of a grain boundary promotes an inter-dendritic growth competition among converging dendritic networks, which in turn influences the texture as well as the structural stability of single-crystal alloys in high-temperature applications.

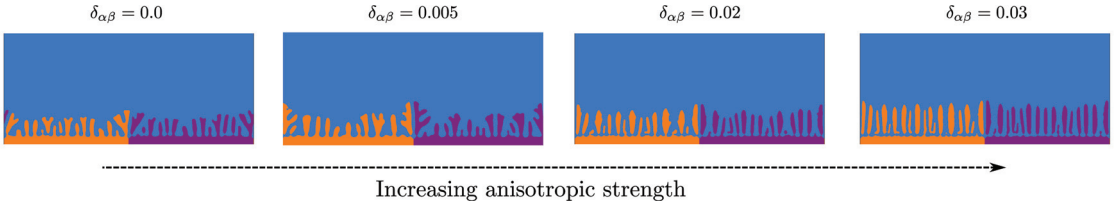

Figure 5. Reconstructed simulation screenshots illustrating the role of interfacial anisotropy on pattern formation. With an increase in the anisotropic strength $\delta_{\alpha\beta}$, the tip-splitting microstructure translates into an array of columnar dendrites.

3.4. Analytical Criterion for Tip Splitting

From the aforementioned simulations, it is evident that for a tip-splitting morphology, the stability ranges exist over a wide range of growth conditions, and the solidification patterns evolve into dendrites or seaweeds depending upon the imposed interfacial anisotropy [33]. However, one of the major drawbacks in the literature is that such a study shows no clarity on the tip-splitting position. Recently, Glicksman [16] proposed an analytical criterion for the branching mechanism through the Gibbs–Thomson temperature distribution as an active interfacial energy. According to this theory, the sign of the surface Laplacian of interfacial curvature $\nabla_s^2\kappa$, where κ is the interfacial curvature, predicts whether the interface moves toward the melt or the crystal. It was reported that a positive $\nabla_s^2\kappa$ represented the growth of the interface, whereas a negative $\nabla_s^2\kappa$ promoted a hindered growth of the interface [16]. Thereupon, the local analysis was proved to be successful in kinematically determining the rotation points for branching, where the crystal experienced an accelerated growth. The present section builds on this theory and addresses the fundamental tip-splitting behavior in seaweed microstructures. In the forthcoming segments, the expressions for the sharp-interface analytical criterion for a convex profile in two dimensions is derived and subsequently compared with two-dimensional phase-field simulations.

Since the main objective of this section is to demonstrate and predict the tip-splitting phenomenon, similar to the instabilities observed in the Figure 2a, the interface shape is chosen to be convex and symmetric in order to avoid any mathematical complexity. To begin with, the analytical criterion for a two-dimensional surface is determined in the following manner. Let $f(x)$ be the equation of a parabola in a two-dimensional domain, given as

$$f(x) = -\alpha(x - h)^2 + p, \tag{6}$$

where $\alpha, h,$ and p are the scaled dimensionless parameters controlling the width and the position of the parabola. In the present study, $h = 500$ and $p = 250$, and α is taken as 0.02. Let us begin the calculation of the analytical criterion $\nabla_s^2\kappa$, starting with the expression of interfacial curvature $\kappa(x)$, for a two-dimensional convex interface,

$$\kappa(x) = \frac{f''(x)}{(1 + f'(x)^2)^{\frac{3}{2}}}. \tag{7}$$

Now, the gradient of the interfacial curvature along the arc length s can be written as

$$\frac{\partial \kappa}{\partial s} = \frac{\partial \kappa}{\partial x}\frac{\partial x}{\partial s}, \tag{8}$$

$$\frac{\partial \kappa}{\partial s} = \frac{1}{\sqrt{1+(\frac{\partial y}{\partial x})^2}}\frac{\partial \kappa}{\partial x}. \tag{9}$$

Let the above equation be termed as $g(x)$; thus,

$$g(x) = \frac{1}{\sqrt{1+(\frac{\partial y}{\partial x})^2}}\frac{\partial \kappa}{\partial x}. \tag{10}$$

Finally, in order to calculate the surface Laplace, the surface divergence of the gradient along the arc length is taken. Using Equation (10), we obtain

$$\nabla_s^2 \kappa = \frac{\partial g(x)}{\partial x}\frac{\partial x}{\partial s} = \frac{1}{\sqrt{1+(\frac{\partial y}{\partial x})^2}}\frac{\partial g(x)}{\partial x}. \tag{11}$$

The above derivation can be rewritten by substituting $f(x)$ from Equation (6) into Equation (7) as

$$\nabla_s^2 \kappa = \frac{\frac{576\alpha^5(x-h)^2}{(1+4\alpha^2(x-h)^2)^4} - \frac{24\alpha^3}{(1+4\alpha^2(x-h)^2)^3}}{\sqrt{1+4\alpha^2(x-h)^2}}. \tag{12}$$

The positions along the x-direction for which the analytical criterion is exactly zero are given by

$$x = \frac{2h\alpha \pm \frac{\sqrt{5}}{5}}{2\alpha}. \tag{13}$$

As shown in Figure 6, Equation (12) represents the analytically predicted tip-splitting position for a convex crystal–melt interface. Herein, we observe that the sharp-interface criterion $\nabla_s^2\kappa$ for $\alpha = 0.02$ has two positive regions at $x < 490 \times 10^{-7}$ m and $x > 510 \times 10^{-7}$ m, whereas the negative region lies in between 490×10^{-7} m $< x < 510 \times 10^{-7}$ m. During solidification, and as represented with a red dot in Figure 6, the minimum at $\nabla_s^2\kappa = -0.000191$ starts to evolve toward the solid in a hindered manner. In contrast, we notice that the two maxima at $\nabla_s^2\kappa = 4.6 \times 10^{-5}$ (black dots in Figure 6) shall accelerate toward the opposite direction in order to generate the foremost point. Therefore, the tip-splitting region is predicted where the interface undergoes a hindered growth, and it begins when the analytical criterion passes through zero. The form of the plot in Figure 6 is a direct comparison with the normal flux reported by Glicksman [16], where the solid–liquid interface evolved accordingly to undergo systematic branching. Nonetheless, having derived the analytical positions for a tip-splitting event, in the next section, we systematically compare with our phase-field results.

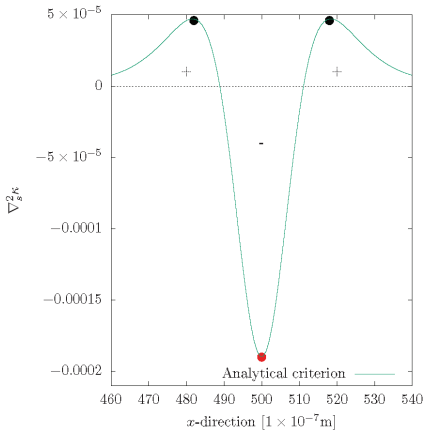

Figure 6. Calculated sharp-interface analytical criterion for $\alpha = 0.02$ as a function of the grid position. The positive and negative regions indicate the crest and the trough positions during a tip-splitting event. The forked region lies between the $\nabla_s^2\kappa < 0$ region, whereas the two tips start to evolve at the $\nabla_s^2\kappa > 0$ positions.

3.5. Comparison between Sharp-Interface Analytical Criterion and Phase-Field Simulation

In the present section, two-dimensional phase-field simulations are performed to comprehend and subsequently validate the analytically derived tip-splitting position. As shown earlier and in previous studies [29,33], crystal–melt interfaces with weak anisotropies evolve into tip-splitting microstructures in a unidirectionally solidification setup. Similar to previous sections, the domain size as well as the boundary conditions are considered to be the same; i.e., on the left and right side domain walls, the periodic boundary condition is imposed for the phase and concentration fields. At the top boundary, the Neumann boundary condition is applied for both the fields. In order to have a direct comparison with the sharp-interface criterion, the initial condition is a convex crystal–melt interface profile with $\delta_{\alpha\beta} = 0.005$ as given by Equation (6), and the temporal evolution of the solid–liquid interface is shown in Figure 7 via the red isolines. At $t = 130 \times 10^{-3}$ s, the red isoline in Figure 7 depicts the formation of a crest and trough, which in turn indicates that the evolving crystal–melt interface has undergone tip splitting. The projection of Figure 6 (dashed blue line) in Figure 7 (solid red line) further reveals that the interface evolves into a crest where the analytical criterion is positive, while the negative $\nabla_s^2\kappa$ corresponds to a hindered forked region. In Figure 7, it can be seen that this segment now proceeds in the opposite direction toward the crystal, compared with the two hillocks developed on either side, when $\nabla_s^2\kappa$ passes through zero. Such positions are known as Laplace or rotation points; i.e., the sign of the analytical criterion $\nabla_s^2\kappa$ reverses [24]. As derived earlier, the interface positions where the analytical criterion is exactly zero are given by Equation (13), and a direct comparison with the phase-field result also shows a convincing agreement with the splitting positions in Figure 7. Further comparisons with different α are included in the supplemental material. The present analysis agrees in spirit with Kesseler, Koplik, and Levine [34,35], where a geometrical approach successfully proved that the interfacial curvature at the tip decreases with time, and finally, a tip-splitting event is initiated once the interfacial curvature at the tip passes through zero. Additionally, a sharp-interface criterion for side branching in anisotropic dendrites was reported with similar remarks [17]. Here, the evolution of a convex instability was tracked, wherein the difference between the time-dependent curvature and the curvature of a steady-state crystal was plotted to present different scenarios for the generation of side branches.

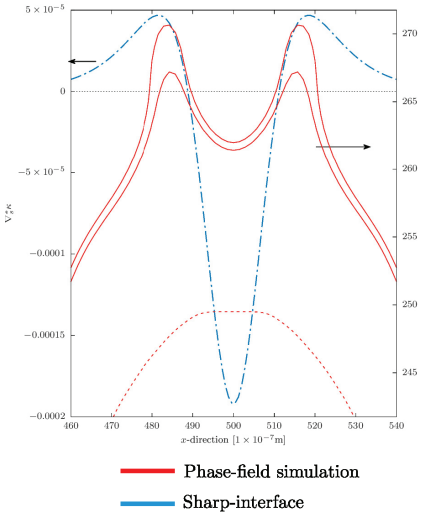

Figure 7. The temporal formation of crests, at $x = 490 \times 10^{-7}$ m, $x = 510 \times 10^{-7}$ m, and the formation of a trough at 490×10^{-7} m $< x < 510 \times 10^{-7}$ m exhibit the tip-splitting phenomenon from a two-dimensional phase-field simulation (red isolines). The initial interface profile in accordance with Equation (6) is also illustrated. A direct comparison with the analytically obtained positions (blue dashed lines) reveal that both tips are generated in the positive regions of Figure 6, whereas the split region is determined by the negative region of the interface. The left and right arrows respectively indicate the $\nabla_s^2\kappa$ and the grid positions.

In general, the magnitude of fluxes plays an important role in the formation of tip-splitting microstructures. A recent study by Mullis [20] found the magnitude of tangential flux and location of the first perturbation to be consistent at high undercoolings. For a solid–liquid interface profile, where the interfacial curvature varies non-linearly with its arc length, the gradients developed parallel to the interface contribute toward the generation of an inflection point, especially at the tip region. However, as these fluxes are proportional to the interfacial curvature, they recede significantly away from the tip, where the bulk fluxes are dominant. The surface accelerates due to cooling and retards by virtue of heating; a combination of such effects creates the development of an inhibited interface at the negative $\nabla_s^2\kappa$ region, facilitating the branching process at the predicted position. In other words, the initiation of the cusped region transpires when $\nabla_s^2\kappa$ turns negative. The concave portion of the interface in Figure 7 also indicates some sort of solutal sink along the U-shaped interface. Finally, the two tips that are triggered by means of strong fluxes multiply into several tip-splitting events during the later stages of the simulation and produce a classic seaweed microstructure.

While we have discussed the initiation and the mechanism of a tip-splitting event, the absence of such instabilities is also observed when a sphere is considered as an initial condition; see Figure 8. For a sphere with an isotropic interfacial energy, the curvature-dependent analytical criterion is defined by the absence of crest and trough regions. Likewise, with such an initial condition, the sphere evolves consistently without any tip-splitting events, and the simulated isotropic spherical seed in Figure 8 is in excellent agreement with the sharp-interface theory. Lastly, while the role of lattice anisotropy is investigated in the upcoming section, the role of discretization spacing is discussed in detail in the supplementary material.

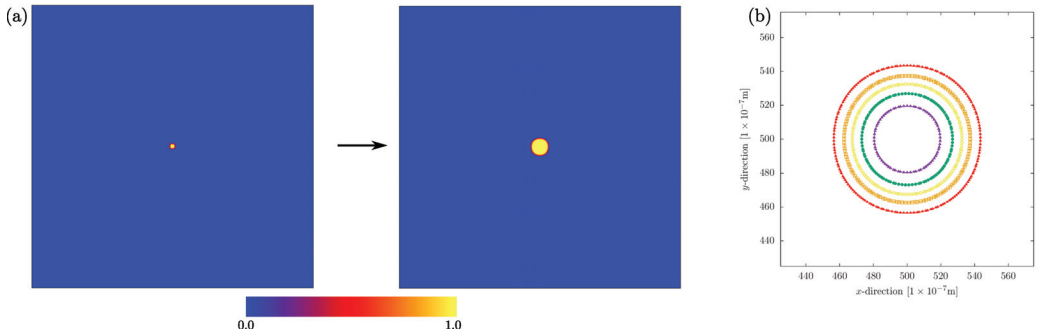

Figure 8. (**a**,**b**) Simulation screenshots and phase-field isolines for an isotropic spherical seed. As the interfacial curvature varies linearly with its arc length, the absence of tip splitting is also captured. This phenomenon is in complete accordance with the sharp-interface analytical prediction, which is defined by the absence of crest and trough regions. The color bar illustrates the phase-field according to the legend embedded below the simulation snapshots. Left to right simulation frames, as well as the phase-field isolines, indicate the evolution of the spherical seed with time.

3.6. Effect of Lattice Anisotropy

In the present section, the effect of lattice anisotropy on our numerical results is discussed in detail. In order to accurately analyze the tip-splitting phenomenon and minimize the pinning effect of the underlying lattice on the solid–liquid interface, we systematically compare the equilibrium shapes of a spherical crystal seed from the phase-field simulation with its corresponding shape in the sharp-interface theory [36,37], which is expressed in the Cartesian coordinates as

$$x = r_0\left[f(\theta,\varphi)\sin(\theta)\cos(\varphi) + \frac{\partial f(\theta,\varphi)}{\partial\theta}\cos(\theta)\cos(\varphi) - \frac{\partial f(\theta,\varphi)}{\partial\varphi}\sin(\varphi)/\sin(\theta)\right], \quad (14)$$

$$y = r_0\left[f(\theta,\varphi)\sin(\theta)\sin(\varphi) + \frac{\partial f(\theta,\varphi)}{\partial\theta}\cos(\theta)\sin(\varphi) + \frac{\partial f(\theta,\varphi)}{\partial\varphi}\cos(\varphi)/\sin(\theta)\right], \quad (15)$$

$$z = r_0\left[f(\theta,\varphi)\cos(\theta) - \frac{\partial f(\theta,\varphi)}{\partial\theta}\sin(\theta)\right], \quad (16)$$

and,

$$f(\theta,\varphi) = 1 + \frac{4\delta^e_{\alpha\beta}}{1-3\delta^e_{\alpha\beta}}\left[\cos^4(\theta) + \sin^4(\theta)(1-2\sin^2(\varphi)\cos^2(\varphi))\right]. \quad (17)$$

Here, (θ,φ) are the spherical angles along the normal direction to the solid–liquid interface. Since our study is focused on two-dimensional simulations, we restrict ourselves by comparing the equilibrium shapes along the $x-y$ plane only. Furthermore, in the above equation, $\delta^e_{\alpha\beta}$ represents the effective anisotropic strength of the solid–liquid interface, given as $\delta^e_{\alpha\beta} = \frac{r_{10}/r_{11}-1}{r_{10}/r_{11}+1}$, where r_{10} and r_{11} are the radial distances from the origin to the solid–liquid interface along the y axis, and along the $x = y$ line, respectively, from the phase-field simulation.

Next, the equilibrium shape obtained from our phase-field study is first initialized with a two-dimensional seed of radius $r_0 = 45 \times 10^{-7}$ m. In addition, the melt supersaturation $\Delta = 0.8$ is selected such that the bulk phases are in equilibrium, and the solid phase would neither shrink nor grow with time. As shown in the earlier section, the tip-splitting microstructures are widely observed for $\delta_{\alpha\beta} < 0.01$, and thereby, we have considered two different anisotropic strengths, $\delta_{\alpha\beta} = 0$ for the isotropic case, and $\delta_{\alpha\beta} = 0.005$ for weakly anisotropic interfaces. Figures 9 and 10 depict the equilibrium shapes from the phase-field simulations, and an excellent agreement with the obtained sharp-interface profiles for

two different cases is observed. Henceforth, from the the above analysis, we emphasize that the grid or lattice anisotropy has a minimal effect on the crystal–melt shapes, which quantitatively illustrates the accuracy of our phase-field results. Nevertheless, for the sake of further investigating the role of lattice anisotropy, direct comparisons for simulations with strong anisotropic strengths and different crystal radii have been discussed in detail in the supplementary material.

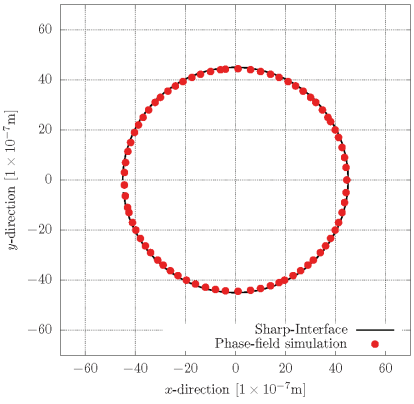

Figure 9. For an energetically isotropic interface $\delta_{\alpha\beta} = 0$, the simulated solid phase with radius $r_0 = 45 \times 10^{-7}$ m shows a complete agreement with the sharp-interface theory. Here, the obtained effective anisotropy $\delta^e_{\alpha\beta} = 0.0001$ shows negligible effect from the underlying lattice on our simulated crystal shape.

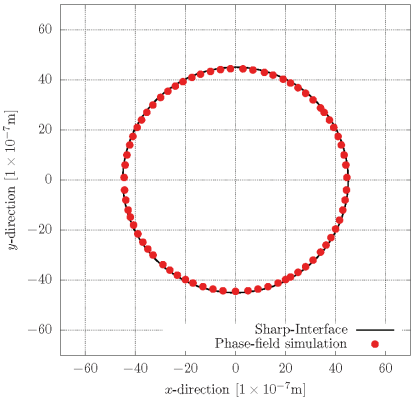

Figure 10. For a weak anisotropic solid–liquid interface, $\delta_{\alpha\beta} = 0.005$, a direct comparison with the sharp-interface equilibrium shape shows excellent agreement, and the obtained effective anisotropy $\delta^e_{\alpha\beta} = 0.0045$ shows a minute variation when compared with the imposed value.

4. Conclusions

In the present work, we have extensively discussed the unidirectional solidification of tip-splitting microstructures through the phase-field modeling approach. Here, the formation as well as the temporal evolution of morphological instabilities along a solidifying interface as a result of constitutional supercooling near the solid–liquid interface is simulated. At first, we have shown that the presence of grain boundaries in bicrystal alloys promotes ridge-shaped morphological instabilities near the grain boundary grooves. The convex instabilities across the solidification front consequently amplify and develop

into a tip-splitting microstructure for energetically isotropic interfaces. With an increase in the ratio R_0, the role of the groove shape on the amplification of ridge-shaped instabilities near a grain boundary is demonstrated to be qualitatively in agreement with previous studies. Next, we have studied the tip-splitting phenomenon in a microstructural pattern, whereby the sharp-interface analytical criterion operates as the focal point for analyzing and predicting the tip-splitting position. The tip-splitting phenomenon builds upon the previous experimental and theoretical studies, and it successfully provides the regions for tip splitting for the first time.

The analytically obtained tip-splitting position is dynamically validated via performing two-dimensional phase-field simulations. Furthermore, the advancing interface tries to split in the same region as evaluated analytically. As a consequence of heating and cooling, the interface starts to evolve via forking between the positions, i.e., where the $\nabla_s^2\kappa$ passes through zero. The solidifying interface amplifies into the melt as a crest where $\nabla_s^2\kappa > 0$, and it concurrently evolves as a trough where $\nabla_s^2\kappa < 0$. Moreover, since the present mechanism is curvature dependent, the absence of tip-splitting events is also illustrated for a sphere, where the interfacial curvature varies linearly with its arc length. The effect of lattice anisotropy on the crystal–melt interfaces is also investigated, where we have successfully compared the equilibrium shapes from the phase-field simulations with its corresponding shape in the sharp-interface theory. In the end, through various numerical simulations and validation studies, we conclude by suggesting that through the present analytical criterion, a tip-splitting phenomenon is deterministic and predictable vis-á-vis the local interfacial curvature of the crystal, which should vary non-linearly with its arc length.

Supplementary Materials: The following supporting information can be downloaded at: https://www.mdpi.com/article/10.3390/met12030376/s1.

Author Contributions: Conceptualization, V.P.L., F.W.; Methodology, V.P.L., F.W.; Validation, V.P.L., F.W.; Investigation, V.P.L., F.W.; Software, V.P.L., F.W., M.S.; Visualization, V.P.L.; Writing—original draft preparation, V.P.L.; Writing—review and editing, V.P.L., F.W., M.S., B.N.; Supervision, B.N. All authors have read and agreed to the published version of the manuscript.

Funding: This research was funded by the cooperative graduate school "Gefügestrukturanalyse und Prozessbewertung" funded by the ministry of the state of Baden-Württemberg (MWK), Germany.

Institutional Review Board Statement: Not applicable.

Informed Consent Statement: Not applicable.

Data Availability Statement: The data presented in this study are available on request from the authors.

Acknowledgments: We would like to acknowledge financial support through the Gottfried-Wilhelm-Leibniz prize NE 822/31-1 of the research work by the German Research Foundation (DFG): Contributions to the classification of the tip-splitting events are provided by the programmes: Virtual Materials Design (VirtMat), project no. 9 (P3 MSE, 43.31.02), and Renewable 383 Energies (MTET 38.04.04) funded by the Helmholtz association. The authors also acknowledge the computing time from the high-performance clusters provided by the state of Baden-Württemberg through bwHPC.

Conflicts of Interest: The authors declare no conflict of interest.

References

1. Ihle, T.; Müller-Krumbhaar, H. Fractal and compact growth morphologies in phase transitions with diffusion transport. *Phys. Rev. E* **1994**, *49*, 2972. [CrossRef]
2. Ben-Jacob, E.; Deutscher, G.; Garik, P.; Goldenfeld, N.D.; Lareah, Y. Formation of a dense branching morphology in interfacial growth. *Phys. Rev. Lett* **1986**, *57*, 1903. [CrossRef]
3. Ben-Jacob, E.; Cohen, I.; Levine, H. Cooperative self-organization of microorganisms. *Adv. Phys.* **2000**, *49*, 395–554. [CrossRef]
4. Saffman, P.G.; Taylor, G. The penetration of a fluid into a porous medium or Hele-Shaw cell containing a more viscous liquid. Proceedings of the Royal Society of London A: Mathematical, Physical and Engineering Sciences. *R. Soc.* **1958**, *245*, 312–329.

5. Assadi, H.; Oghabi, M.; Herlach, D.M. Influence of ordering kinetics on dendritic growth morphology. *Acta Mater.* **2009**, *57*, 1639–1647. [CrossRef]
6. Glicksman, M.E. *Principles of Solidification: An Introduction to Modern Casting and Crystal Growth Concepts*; Springer Science & Business Media: Berlin/Heidelberg, Germany, 2010.
7. Schaefer, R.; Glicksman, M. Initiation of dendrites by crystal imperfections. *Metall. Trans.* **1970**, *1*, 1973–1978. [CrossRef]
8. Mullins, W.W.; Sekerka, R. Stability of a planar interface during solidification of a dilute binary alloy. *J. Appl. Phys.* **1964**, *35*, 444–451. [CrossRef]
9. Mullins, W.W.; Sekerka, R.F. Morphological stability of a particle growing by diffusion or heat flow. *J. Appl. Phys.* **1963**, *34*, 323–329. [CrossRef]
10. Noël, N.; Jamgotchian, H.; Billia, B. In situ and real-time observation of the formation and dynamics of a cellular interface in a succinonitrile-0.5 wt% acetone alloy directionally solidified in a cylinder. *J. Cryst. Growth* **1997**, *181*, 117–132. [CrossRef]
11. Morris, L.; Winegard, W. The development of cells during the solidification of a dilute Pb-Sb alloy. *J. Cryst. Growth* **1969**, *5*, 361–375. [CrossRef]
12. Utter, B.; Ragnarsson, R.; Bodenschatz, E. Alternating tip splitting in directional solidification. *Phys. Rev. Lett.* **2001**, *86*, 4604–4607. [CrossRef]
13. Nittmann, J.; Stanley, H.E. Tip splitting without interfacial tension and dendritic growth patterns. *Nonlinear Phys. Beginners Fractals Chaos Solitons Pattern Form. Cell. Autom. Complex Syst.* **1998**, *321*, 166.
14. Akamatsu, S.; Faivre, G.; Ihle, T. Symmetry-broken double fingers and seaweed patterns in thin-film directional solidification of a nonfaceted cubic crystal. *Phys. Rev. E* **1995**, *51*, 4751. [CrossRef]
15. Šebestíková, L.; D'Hernoncourt, J.; Hauser, M.; Müller, S.; De Wit, A. Flow-field development during finger splitting at an exothermic chemical reaction front. *Phys. Rev. E* **2007**, *75*, 026309. [CrossRef]
16. Glicksman, M.E. Mechanism of dendritic branching. *Metall. Mater. Trans. A* **2012**, *43*, 391–404. [CrossRef]
17. Martin, O.; Goldenfeld, N. Origin of sidebranching in dendritic growth. *Phys. Rev. A* **1987**, *35*, 1382. [CrossRef]
18. Devauchelle, O.; Szymczak, P.; Pecelerowicz, M.; Cohen, Y.; Seybold, H.J.; Rothman, D.H. Laplacian networks: Growth, local symmetry, and shape optimization. *Phys. Rev. E* **2017**, *95*, 033113. [CrossRef]
19. Suekane, T.; Ono, J.; Hyodo, A.; Nagatsu, Y. Three-dimensional viscous fingering of miscible fluids in porous media. *Phys. Rev. Fluids* **2017**, *2*, 103902. [CrossRef]
20. Mullis, A.M. Spontaneous deterministic side-branching behavior in phase-field simulations of equiaxed dendritic growth. *J. Appl. Phys.* **2015**, *117*, 114305. [CrossRef]
21. Shang, S.; Guo, Z.; Han, Z. On the kinetics of dendritic sidebranching: A three dimensional phase field study. *J. Appl. Phys.* **2016**, *119*, 164305, [CrossRef]
22. Wang, Z.; Wang, J.; Yang, G. Phase-field investigation of effects of surface-tension anisotropy on deterministic sidebranching in solutal dendritic growth. *Phys. Rev. E* **2008**, *78*, 042601. [CrossRef] [PubMed]
23. Jia-Xue, Y.; Zhi-Jun, W.; Jun-Jie, L.; Jin-Cheng, W. Tip-splitting instability in directional solidification based on bias field method. *Chin. Phys. B* **2015**, *24*, 078107.
24. Glicksman, M.E. Capillary-mediated interface perturbations: Deterministic pattern formation. *J. Cryst. Growth* **2016**, *450*, 119–139. [CrossRef]
25. Nestler, B.; Garcke, H.; Stinner, B. Multicomponent alloy solidification: phase-field modeling and simulations. *Phys. Rev. E* **2005**, *71*, 041609. [CrossRef]
26. Choudhury, A.; Nestler, B. Grand-potential formulation for multicomponent phase transformations combined with thin-interface asymptotics of the double-obstacle potential. *Phys. Rev. E* **2012**, *85*, 021602. [CrossRef]
27. Laxmipathy, V.P.; Wang, F.; Selzer, M.; Nestler, B. Phase-field simulations of grain boundary grooving under diffusive-convective conditions. *Acta Mater.* **2021**, *204*, 116497. [CrossRef]
28. Laxmipathy, V.P.; Wang, F.; Selzer, M.; Nestler, B. A two-dimensional phase-field study on dendritic growth competition under convective conditions. *Comput. Mater. Sci.* **2021**, *186*, 109964. [CrossRef]
29. Provatas, N.; Wang, Q.; Haataja, M.; Grant, M. Seaweed to dendrite transition in directional solidification. *Phys. Rev. Lett.* **2003**, *91*, 155502. [CrossRef]
30. Utter, B.; Bodenschatz, E. Dynamics of low anisotropy morphologies in directional solidification. *Phys. Rev. E* **2002**, *66*, 051604, [CrossRef]
31. Laxmipathy, V.P.; Wang, F.; Selzer, M.; Nestler, B.; Ankit, K. Influence of melt convection on the morphological evolution of seaweed structures: Insights from phase-field simulations. *Comput. Mater. Sci.* **2019**, *170*, 109196. [CrossRef]
32. Coriell, S.; Sekerka, R. Morphological stability near a grain boundary groove in a solid-liquid interface during solidification of a binary alloy. *J. Cryst. Growth* **1973**, *19*, 285–293. [CrossRef]
33. Dantzig, J.; Di Napoli, P.; Friedli, J.; Rappaz, M. Dendritic growth morphologies in Al-Zn alloys—Part II: Phase-field computations. *Metall. Mater. Trans. A* **2013**, *44*, 5532–5543. [CrossRef]
34. Kessler, D.A.; Koplik, J.; Levine, H. Geometrical models of interface evolution. II. Numerical simulation. *Phys. Rev. A* **1984**, *30*, 3161. [CrossRef]
35. Brower, R.C.; Kessler, D.A.; Koplik, J.; Levine, H. Geometrical models of interface evolution. *Phys. Rev. A* **1984**, *29*, 1335–1342. [CrossRef]

36. Voorhees, P.; Coriell, S.; McFadden, G.; Sekerka, R. The effect of anisotropic crystal-melt surface tension on grain boundary groove morphology. *J. Cryst. Growth* **1984**, *67*, 425–440. [CrossRef]
37. Cahn, J.; Hoffman, D. A vector thermodynamics for anisotropic surfaces—II. Curved and faceted surfaces. *Acta Metall.* **1974**, *22*, 1205–1214. [CrossRef]

metals

MDPI

Article

Optimization of Heavy Reduction Process on Continuous-Casting Bloom

Bao Yang [1], Minglin Wang [1,*], Hui Zhang [1,*], Shuai Liu [1,2], Guobin Wang [1,3] and Xuebing Wang [1,4]

[1] National Engineering and Research Center for Continuous Casting Technology, Central Iron and Steel Research Institute, Beijing 100081, China
[2] School of Metallurgical and Ecological Engineering, University of Science and Technology Beijing, Beijing 100083, China
[3] Department of Chemistry and Chemical Engineering, Lvliang University, Lvliang 033001, China
[4] Material Digital R&D Center, China Iron & Steel Research Institute Group, Beijing 100081, China
* Correspondence: wangminglin2005@sina.com (M.W.); zhangh@cisri.com.cn (H.Z.)

Abstract: Heavy reduction (HR) is an effective technique to control V segregation in continuous casting bloom, but the effect of segregation improvement is limited by the parameters such as reduction position and reduction amounts. In order to improve the macrosegregation of bloom, numerical simulation and plant experiments are adopted in this research. A heat transfer model and a reduction model with comprehensive thermo-physical parameters were established. The two models were verified by comparing the measured surface temperature and the theoretical strain at the solidification front. It is determined that the position of the HR of the bearing steel bloom is 20.82 m~24.97 m from the meniscus, and the solid fraction in the center of the bloom is 0.6~1. The total reduction of the HR is set to 30 mm, and the reduction of each roller in the reduction range is set to 4 mm, 5 mm, 9 mm, 7 mm, and 5 mm, respectively, to prevent the formation of internal cracks. Plant trials were conducted to verify the effect of the optimized HR. The results show that the carbon segregation degree on the V channel and non-channel of the bloom decreases from 1.2 to 1.16 and increases from 0.93 to 0.95, respectively, and the central carbon segregation degree decreases from 1.17 to 1.15. Meanwhile, the internal crack was not found in the bloom.

Keywords: heavy reduction; V segregation; bearing steel bloom; reduction parameters; crack

Citation: Yang, B.; Wang, M.; Zhang, H.; Liu, S.; Wang, G.; Wang, X. Optimization of Heavy Reduction Process on Continuous-Casting Bloom. *Metals* **2022**, *12*, 1873. https://doi.org/10.3390/met12111873

Academic Editor: Mohsen Eshraghi

Received: 30 September 2022
Accepted: 29 October 2022
Published: 2 November 2022

1. Introduction

Bearing steel is the basic steel of the advanced manufacturing industry. With the transformation and upgrading of the manufacturing industry, higher requirements are put forward for the quality of bearing steel [1]. Bearing steel is mostly produced by bloom continuous casting. Due to its high carbon content, macrosegregation occurs easily in the continuous casting process [2,3]. However, is difficult to eliminate or greatly improve segregation in subsequent rolling and heat treatment [4]. Therefore, macrosegregation has greatly affected the quality of products.

Low superheat pouring technology [5], electromagnetic stirring technology [6,7], and billet reduction technology [8,9] are considered effective in improving the macrosegregation of the billet. Low superheat casting technology can improve the equiaxed crystal rate of the billet, but whether it can reduce the equiaxed crystal size has not been determined. In addition, the size of equiaxed grains is directly related to the point segregation, and the relationship between superheat and the size, shape, distribution, and solute enrichment of point segregation in continuous casting billet is the theoretical basis for formulating control measures, but there are few reports [10]. Therefore, it is still difficult to improve the macroscopic point segregation by adjusting the superheat.

Oh K S et al.studied the effect of different electromagnetic stirring modes on V segregation in 250 mm × 300 mm bloom, and the results showed that S-EMS had the best effect

on regulating V segregation [11]. According to the formation theory of V segregation, the effects of M-EMS and S-EMS on segregation are embodied in solidification structure and molten steel fluidity. The conclusions of different scholars are contradictory as to whether or not it can regulate the size and area ratio of V segregation [10].

In the above technologies, billet reduction technology includes mechanical soft/heavy reduction [12–15], thermal soft reduction [16–21], and hot core heavy reduction technology. Among them, the hot core reduction technology is mainly used for welding the shrinkage of the casting blank, the hot reduction technology is to rely on the end surface cooling to achieve a rapid temperature drop of the billet surface corresponding to the center of the billet, thereby compensating for the solidification shrinkage of the central area and inhibiting the flow of the enriched liquid to the center of the billet [17]. Mechanical soft reduction is generally implemented in the solid phase ratio of 0.6~0.8 range, the amount of reduction is generally not more than 10 mm [22].

With the improvement and upgrading of the continuous casting machine, the section of the billet is becoming larger and larger. The single hot reduction technology and soft reduction technology obviously cannot meet the requirements of improving the macrosegregation of the bloom. Heavy reduction (HR) technology of the final Solidifying End is considered to be an effective means to improve the macrosegregation of bloom [23]. Macrosegregation mainly includes central segregation and V segregation. The formation of central segregation can be attributed to the flow of enriched molten steel in the two-phase region during the final solidification process [24–27], which can be caused by many factors, such as bulging, roll offset, solidification and heat shrinkage during continuous casting. Many scholars have proposed mechanical soft or heavy reduction [12–15] and thermal soft reduction [16–20] to improve central segregation and achieved remarkable results.

Different scholars have different views on the causes of V segregation. Tomono believes that V segregation is due to the fact that the enriched liquid between the equiaxed crystals is sucked in and flows downwards, and that the enriched liquid accumulates along certain planes as the accumulated equiaxed crystals forcefully move toward the center of the bloom [28]. Abbott [29] believed that V segregation is caused by the erosion and thermal tearing of the solid by the flowing enrichment liquid. Li et al. believe that V segregation is caused by solidification shrinkage tearing cracks in the equiaxed dendritic network [30]. Therefore, the reasons for the formation of bloom V segregation remain to be further explored, from the principle of control V segregation has not yet formed a unified view.

At present, the research on reducing spot segregation and V segregation by roller soft reduction has been widely reported [22,31,32]. However, the casting machine, steel, casting speed, and production environment have a certain degree of difference, so the use of HR control V segregation still needs a separate analysis. In this paper, the 380 mm × 450 mm bearing steel bloom was studied. This production line is newly built, the initial production of bloom specifications 380 mm × 450 mm, and there are problems such as macrosegregation in the bloom. In order to determine the solid phase rate at the solidification end of the bloom, a solidification heat transfer model was established. Then a reasonable reduction interval was determined. At the same time, a series of reduction parameters was proposed based on the thermal-mechanical coupling model, which theoretically controlled the generation of internal cracks. Finally, plant experiments were carried out to verify the improvement effect of the optimized HR parameters on V segregation.

2. Model Description

A circular-arc caster with a curved mold was studied. The caster has five strands and mainly produces the bloom with a section size of 250 mm × 250 mm and 380 mm × 450 mm. Its arc radius is 14 m. The schematic diagram of the bloom caster is shown in Figure 1. The effective lengths of the mold and the secondary cooling zone are 0.8 m and 3.43 m, respectively. Mold electromagnetic stirring (M-EMS), final electromagnetic stirring (F-EMS), and a casting and rolling system of solidification end are applied to improve the

quality of the bloom. In the secondary cooling zone, air-mist nozzles are used to ensure uniform cooling. The distance from the roll-casting system of the solidification end to the meniscus is 18.67 m~27.17 m, mainly including six pairs of soft reduction(SR) rollers and three pairs of heavy reduction rollers. Among them, the first six pairs of reduction rollers are soft reduction equipment, which is installed in the arc section. The last three pairs of reduction rollers are heavy reduction equipment, which is installed in the horizontal section. The diameter of all reduction rollers is 500 mm. In the solidification end, HR is applied to improve the inner quality of the bloom, while its technical parameters are underdetermined.

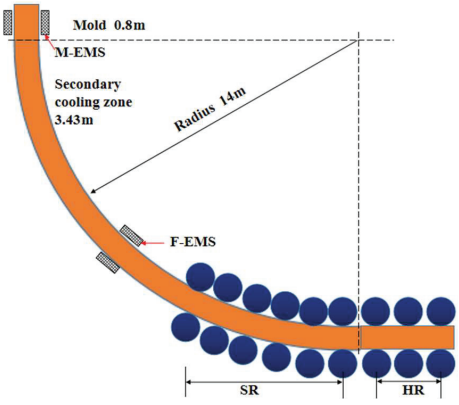

Figure 1. Schematic diagram of the bloom continuous caster.

2.1. Model Establishment

A slice-moving method was applied to the heat transfer model. Figure 2a shows the coordinate system and geometric model of the slice. To simplify the calculation, the geometric model adopted half of the transverse section of the bloom with a thickness of 10 mm, namely with a dimension of 225 mm × 380 mm × 10 mm. The geometric model also considered the round corner according to the final bloom size. The radius of the round corner was 10 mm. During the simulation, it was assumed the slice moved from the mold to the secondary cooling zone and the air-cooling zone. Figure 2b shows the reduction finite element of the bloom, including the reduction roller, support roller, and bloom. The reduction roller and support roller are rigid materials, while the bloom is an elastic material. Considering the symmetry of the width direction of the bloom, the geometric size of the bloom in the model is 225 mm × 380 mm × 1000 mm. The radius, thickness, and length of the two rollers are 300 mm, 50 mm, and 300 mm. The total number of model grids is 72,000.

2.1.1. Assumption

Under the premise of ensuring calculation accuracy, the following assumptions are made for the heat transfer model and the reduction model, respectively:

(1) The heat transfer was neglected in the casting direction and the meniscus.
(2) The convective heat transfer was equivalent to conductive heat transfer.
(3) Deformation at the solidification end of the bloom conforms to the small deformation theory.
(4) The influence of ferrostatic pressure and bending straightening force in casting direction on bloom deformation was ignored.
(5) The high-temperature creep of the bloom is neglected and the reduction process is steady-state process.

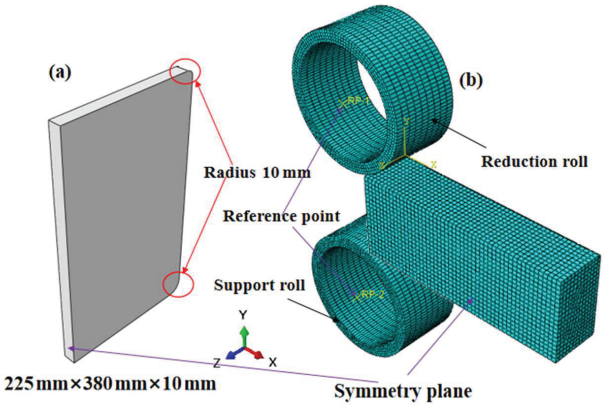

Figure 2. Solidification heat transfer model and cast-rolling model: (**a**) Geometric model of the slice, (**b**) Reduction finite-element of the bloom.

2.1.2. Governing Equation

Based on the above assumptions, a two-dimensional unsteady state heat transfer equation was expressed as follows. The equivalent specific heat method is used to express the effect of solidification latent heat on the solidification process, referring to Reference [22].

$$\rho c \frac{\partial T}{\partial t} = \frac{\partial}{\partial x}\left(k\frac{\partial T}{\partial x}\right) + \frac{\partial}{\partial y}\left(k\frac{\partial T}{\partial y}\right) \quad (1)$$

where, ρ is density, kg/m^2; c is the specific heat capacity, J/(kg·°C); k is the thermal conductivity, w/(m·°C); T is temperature, °C; and x and y are the distance in the width direction of the bloom transverse section, m.

The total deformation of bloom during reduction consists of thermal deformation, elastic deformation increment, and plastic deformation increment.

$$d\varepsilon = [\alpha]dT + [D_e]^2 d\sigma + dk\frac{\partial \varphi}{\partial \sigma} \quad (2)$$

where, $d\varepsilon$ is the total deformation; $[\alpha]$ is thermal expansion coefficient matrix; T is temperature, °C; $[D_e]$ is an elastic matrix, σ is stress, Pa; k is a constant, φ is Mises yield function.

2.1.3. Boundary Conditions and Initial Condition

(1) Initial condition

For the solidification heat transfer process, the casting temperature is the same as the temperature of the molten steel in the tundish, and the meniscus in the mold is the initial time. For the reduction process, the thermally calculated temperature field is loaded into the initial conditions of the reduction model. The casting speed is 0.45 m/min, the roller speed is 0.025 rad/s, and the initial temperature of the roller is 300 °C.

(2) Boundary Conditions

The boundary conditions of heat transfer analysis refer to Reference [22] to set the mold zone, secondary cooling zone, and air cooling zone respectively. The Coulomb friction model is used to treat the interface friction in the three-dimensional bloom reduction model, and the friction coefficient is set to 0.33. The heat transfer coefficient between the reduction roller and the bloom during the continuous casting process is 8000 W/(m^2·°C). The plastic deformation energy of the reduction process is converted into heat energy, and the transformation coefficient of plastic energy is 0.9. The convective heat transfer coefficient between bloom and environment is 165 W/(m^2·°C).

2.2. Material Properties

GCR15-bearing steel was studied and its chemical composition is given in Table 1. The variations of thermal conductivity, density, specific heat, young's modulus, poisson's ratio, and thermal expansion coefficient with temperature were calculated using the thermodynamic database from JMatPro software (Material Digital R&D Center, Beijing, China), as shown in Figure 3. The physical parameters of bearing steel are related to temperature. Plastic strain parameters refer to Reference [33], which are related to deformation temperature and strain rate. The elastic modulus decreases with increasing temperature, and the value in the liquid region is infinitely close to 0, while the Poisson's ratio is 0.5 at the liquidus.

Table 1. Chemical composition of the steel bearing GCR15.

Composition	C	Si	Mn	P	S	Cr	Ni	V	Cu	Al	Fe
Mass fraction (%)	0.98	0.28	0.35	0.009	0.002	1.46	0.02	0.007	0.03	0.019	96.76

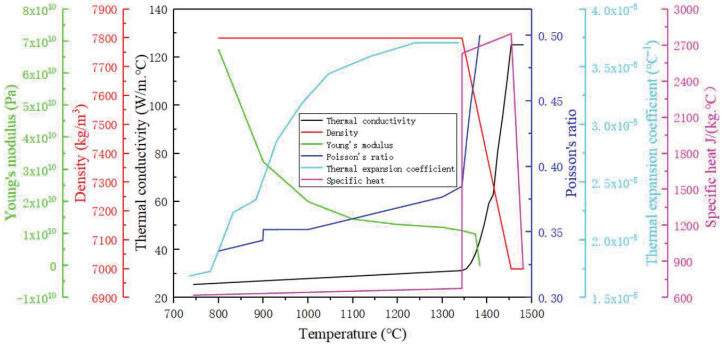

Figure 3. Physical parameters of the steel bearing GCR15.

3. Results and Discussion

3.1. Model Validation

The main casting parameters of GCR15-bearing steel are shown in Table 2. As shown in Figure 4, it is the distribution of center temperature and surface temperature of 380 mm × 450 mm bearing steel bloom. In the range of 14.1 m~17 m from the meniscus, the infrared thermometer is used to measure the temperature of the bloom surface in actual production. Table 3 shows the numerical simulation values and measured values of four temperature measuring points. According to the data in the table, the maximum error is 1.16%, which is less than 5%. It shows that the solidification heat transfer model in this study can accurately simulate the solidification process of the bloom.

Table 2. Main casting parameters of steel bearing GCR15.

Item	Value
Sectional dimension	380 mm × 450 mm
Casting speed	0.45 m/min
Pouring temperature	1481 °C
Water flux of mold cooling	222 m^3/h
Temperature difference between inlet and outlet of mold water	6 °C
Specific water of secondary cooling	0.11 L/kg
E-MES parameters	2.0 Hz/600 A
F-EMS parameters	6.0 Hz/650 A

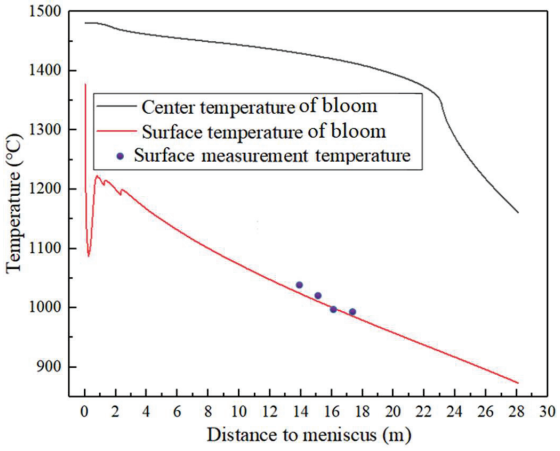

Figure 4. Variation tendency diagram of center and surface temperature of bloom with distance to the meniscus.

Table 3. The comparison of the simulated and measured surface temperatures.

Distance from the Meniscus (m)	Simulated Temperature (°C)	Measured Temperature (°C)	Error Value
14.1	1023	1035	1.16%
15	1011.8	1020	0.8%
16.2	998	995	0.3%
17	989	990	0.1%

3.2. Location of HR

The HR technology at the solidification end can inhibit the thermal expansion and volume shrinkage of the bloom, and reduce its suction effect on the concentrated solute in the center of the bloom. Choosing a reasonable reduction location is the key to improving the segregation of bloom under HR. Kojima S et al. [34] reduced the central solid fraction to between 0.8 and 1.0 of the bloom, the spot segregation on the cross-section of the bloom was greatly reduced, and there was no obvious V segregation on the longitudinal section. Nabeshima et al. [35] performed continuous reduction with a compression ratio of 0.92 on a 400 mm × 560 mm bloom at a central solid fraction of 0.87, and the V segregation effect was significantly improved. In fact, the reasonable reduction position to improve central segregation and V segregation is different. Some experts believe that the center solid fraction of the reasonable reduction range for improving the center segregation is 0.3–0.8 [34,35], but some scholars believe that the center solid fraction range of the reasonable reduction position is 0.6–0.8 [22,36]. The central solid fraction at the appropriate reduction position for improving V segregation should be higher than 0.8 [34,35]. Therefore, in this study, the reasonable range of central solid fraction is 0.6~1 to improve the macrosegregation of bloom by using the technology of HR at the end of solidification.

In the production process, the solidification end point of the bloom is mainly affected by the casting speed, cooling water, and superheat. Among them, the production line adopts intelligent water distribution, and the cooling intensity is a fixed value. Therefore, in this study, the influence of cooling water change on the solidification end point of bloom is ignored, and only the influence of casting speed and superheat change is considered. Figure 5 shows the effect of casting speed on the solidification end when the superheat is 26 °C. As can be seen from the figure, the black line, red line, and green line represent the changing trend of the center temperature of the billet with the position when the casting speed is 0.44 m/min, 0.45 m/min, and 0.46 m/min, respectively. It can be seen from the

figure that when the casting speed is 0.45 m/min, the solidification end point of 380 mm × 450 mm bearing steel bloom is 23.13 m away from the meniscus. When the casting speed decreases by 0.01 m/min, the solidification end point moves 0.51 m. Therefore, when the casting speed changes in the range of 0.44~0.46 m/min, the solidification end point of 380 mm × 450 mm bearing steel bloom changes in the range of 22.62~23.64 m from the meniscus.

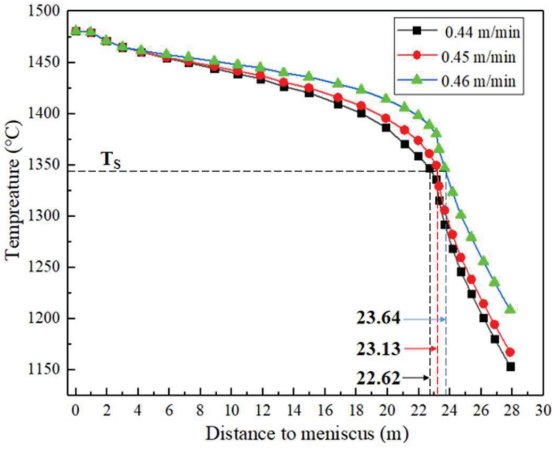

Figure 5. Effect of casting speed on the final solidifying end.

As shown in Figure 6, the effect of different superheats on the center temperature of 380 mm × 450 mm bearing steel bloom was studied when the casting speed was 0.45 m/min. As can be seen from the figure, the black line, red line, and blue line represent the superheat of 11 °C, 26 °C, and 41 °C, billet center temperatures change the trend with the position. It can be seen from the figure that the superheat mainly affects the liquidus disappearance position and the solidification end point during the solidification process of the bloom. When the superheat is 11 °C, 26 °C, and 41 °C respectively, the liquids disappearance position of 380 mm × 450 mm bearing steel bloom is 5.98 m, 6.48 m, and 6.98 m respectively from the meniscus, and the solidification end point is 22.81 m, 23.13 m, and 23.45 m respectively from the meniscus. In other words, for every 15 °C change in the superheat, the distance from the liquidus of the bearing steel bloom to the meniscus changes by 0.5 m, and the solidification end point changes by 0.32 m. When the superheat changes in the range of 11~41 °C, the disappearance position of the liquidus of the 380 mm × 450 mm bearing steel bloom moves within the range of 5.98~6.98 m from the meniscus, and the solidification end point fluctuates within the range of 22.81~23.45 m from the meniscus.

Comparing Figures 5 and 6, when the casting speed is 0.45 m/min and the superheat is 26 °C, the effect of casting speed on the solidification end point of 380 mm × 450 mm bearing steel bloom is much greater than that of superheat. It can be seen from Figure 1 that the arrangement range of the end casting roller 1 #~7 # of the bloom continuous caster is 18.67~27.17 m. As shown in Figure 7, the curve of center temperature and solid fraction of 380 mm × 450 mm bearing steel bloom with casting speed of 0.45 m/min and average superheat of 26 °C. It can be seen from the figure that the central solid fraction of the bloom at the 1 #~6 # roller is 0.45, 0.51, 0.6, 0.71, 0.9, and 1, respectively, and the central solid fraction of the bloom at the 7 #~9 # roller is 1. Combined with the roller arrangement and reasonable reduction range, the action position of HR is determined to be 3 #~6 # roller. Considering that the influence of casting speed and superheat on the solidification end point of the bloom can be up to 0.51 m, and that the local high-temperature phase or shrinkage cavity may aggravate the central segregation of the bloom, the actual reduction range is extended back to the 7 #. Therefore, the HR range at the solidification end of

380 mm × 450 mm bearing steel bloom with a casting speed of 0.45 m/min and an average superheat of 26 °C is 20.82 m~24.97 m from the meniscus, and the corresponding reduction roller is 3 #~7 #.

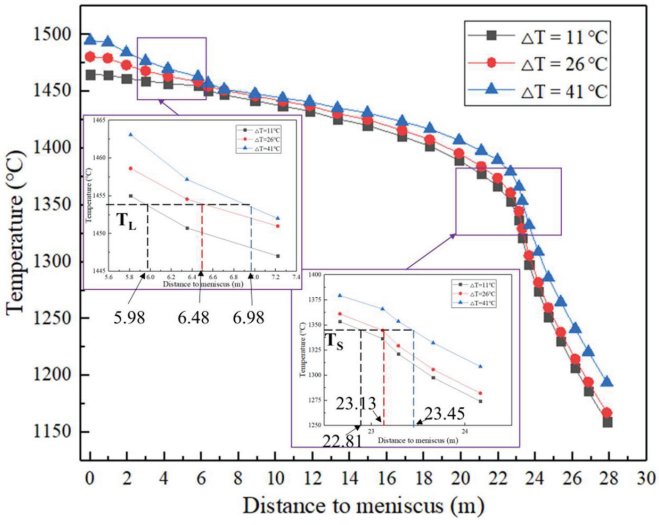

Figure 6. Effect of superheat on the center temperature of bloom.

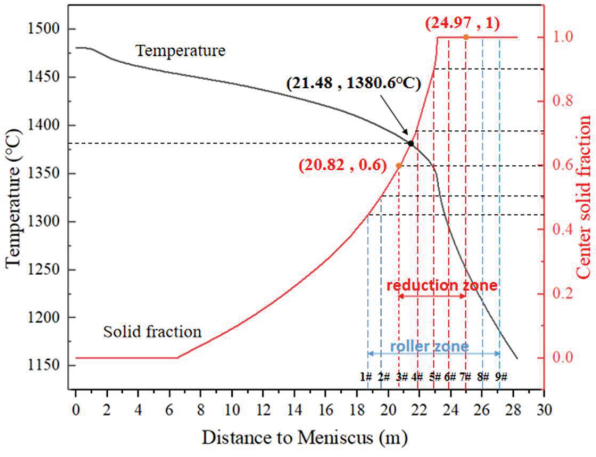

Figure 7. Variations of the temperature and solid fraction of bloom center of the case of casting speed of 0.45 m/min and average superheat of 26 °C.

3.3. Reduction Amounts of HR

During the reduction process, plastic strain may occur at the solidification front. When the stress and strain exceed the critical value, the bloom solidification front forms an internal crack, which deteriorates the quality of the bloom. Therefore, the amount of reduction depends on the high-temperature critical stress and strain value of the bloom at the reduction position. There are critical strain hypothesis, critical stress hypothesis, and critical time hypothesis to measure whether the solidification front of the bloom can produce cracks [37]. In this study, the critical strain of the solidification front was used as the criterion to determine the reduction amount. Generally, the solidification front is defined as the region between the solidus and liquidus. Some scholars [38–40] divided the

solidification front into three parts according to the temperature, as shown in Figure 8 [41], which are the liquid phase region (ZST ≤ T ≤ Tl), the filling region (LIT ≤ T ≤ ZST), and the crack high-incidence region (ZDT ≤ T ≤ LIT). Where Tl is the liquidus of liquid steel, and the liquidus of bearing steel in this study is 1454 °C; ZST, LIT, and ZDT are called zero strength temperature, viscosity temperature, and zero ductility temperature, respectively, and their corresponding solid fractions are 0.8, 0.9, and 1, respectively [42].

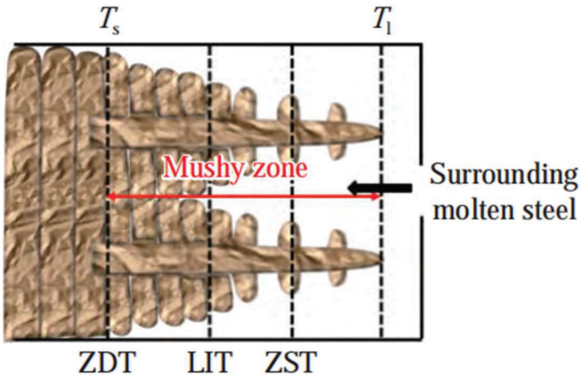

Figure 8. Temperature distribution at the solidification front in the bloom.

When the cumulative strain in the temperature brittleness interval exceeds the critical strain, the solidification front will produce internal cracks [41]. The molten steel in the liquid phase zone has good fluidity. The filling zone can be filled with molten steel in time [42]. Therefore, the range from ZDT to LIT in the solidification front is prone to cracks. In this paper, the temperature range of the high crack area of the bearing steel is from the solidus to 1355 °C. Cai [43] studied the critical strain solution criterion for internal cracks in the solidification front, as shown in Figure 9 [44], which is the relationship between carbon equivalent and critical strain.

$$C_{eq} = [C] + 0.02[Mn] + 0.04[Ni] - 0.1[Si] - 0.04[Cr] - 0.1[Mo] \quad (3)$$

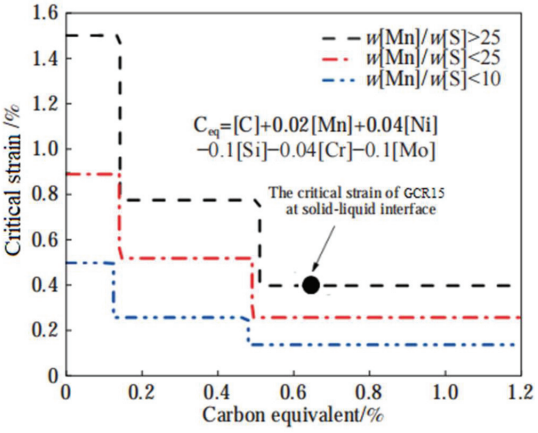

Figure 9. Relationship between the carbon equivalent and critical strain.

According to Formula (3), the carbon equivalent of GCR15 bearing steel is 0.65%, and w[Mn]/w[s] = 175, so the critical strain of GCR15 steel at the solidification front is 0.4%. As long as the reduction amount causes the single or cumulative strain of the bearing steel

bloom to be less than 0.4% in the solidus to 1355 temperature range, the solidification front will not crack.

According to the solidification heat transfer model, the temperature fields of the bloom cross-section corresponding to the central solid fraction of 0.6, 0.71, and 0.9 are obtained respectively, as shown in Figure 10. The area covered between the white semicircles (solidus to 1355 °C) in the diagram is the high crack area of the bloom at this reduction position. The high-incidence area of cracks is regarded as a concentric circle. When the central solid fraction of the bearing steel bloom is 0.60, 0.71 and 0.9, the corresponding ranges of the high-incidence area of cracks are 41 mm $\leq$ r $\leq$ 55 mm, 31.6 mm $\leq$ r $\leq$ 44.6 mm, and 0 $\leq$ r $\leq$ 19 mm, respectively. In short, when different reduction amounts are applied to the positions of 3 #~5 #, the plastic strain in the high crack area is lower than the critical strain value, which is a reasonable parameter.

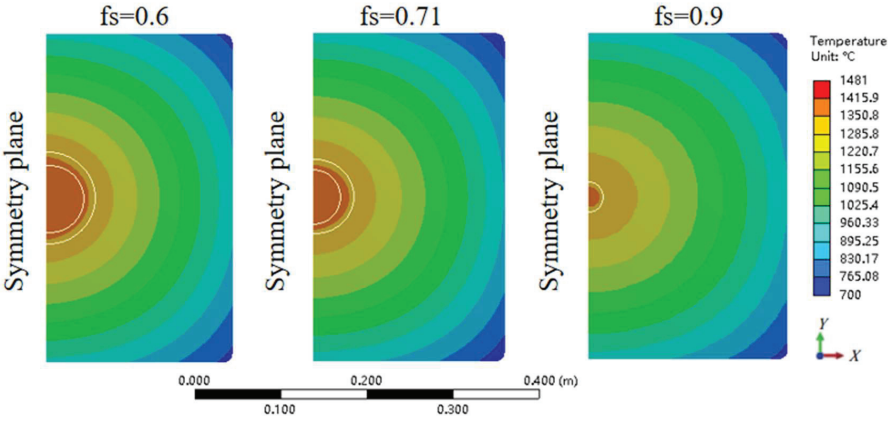

Figure 10. Temperature distribution at different central solidification fractions.

Zhong [45] studied the effect of different total reduction amounts on the center segregation of 350 mm × 470 mm bearing steel bloom. The results show that after applying the total reduction of 4.5 mm, 6 mm, 9 mm, and 13 mm respectively, the total reduction of 6 mm is the most obvious to improve the center segregation, while the total reduction of 9 mm is the second. Wu et al. [44] studied the effect of reduction on macrosegregation of high carbon steel bloom, and the results showed that for 400 mm thickness bloom, the reasonable total reduction was 20~30 mm. The thickness of the bearing steel bloom in this study is 380 mm. According to the research conclusions of Wu et al., the total reduction was set to 30 mm.

Isobe et al. [46] found that the reasonable reduction rate for improving macrosegregation is 1.8~6.6 mm/m or 0.72~4.7 mm/m, and the reduction efficiency is 7~34%. In this study, the roller spacing between 3 #~7 # reduction rollers in the reduction zone of bearing steel bloom is the distance from 3 # to 4 # roller is 900 mm, the distance from 4 # to 5 # roller is 1200 mm, the distance from 5 # to 6 # roller is 900 mm, and the distance from 6 # to 7 # roller is 1100 mm. When the casting speed is 0.45 m/min and the superheat is 26 °C, the solidification end point of the bloom is between 5 # and 6 # rollers. Therefore, according to the Isobe research conclusion, the reduction rate of improving the macrosegregation of the bloom was set to 4.7 mm/m, and the corresponding reasonable reduction amounts of 3 # to 5 # rollers are 4.23 mm, 5.64 mm, and 4.23 mm respectively.

In the original continuous multi-roller reduction process, the corresponding reduction amounts of 1 #~8 # rollers are 2 mm, 4 mm, 2 mm, 4 mm, 6 mm, 6 mm, 6 mm, and 6 mm respectively. The macrosegregation is serious under the original process conditions. In order to improve the macrosegregation, the reduction of 3 # and 4 rollers is increased to 4 mm and 5 mm respectively. According to the solid fraction distribution in the center of the

bloom, the 5 # roller is mainly to improve the V segregation. Compared with the original process, the reduction amounts of the 5 # roller should be greater than 6 mm. Considering that the maximum reduction amount of single rollers is 9 mm, the range of reduction of 5 # is 6 mm~9 mm. Based on the thermal-mechanical coupling model in Figure 2 and the temperature field in Figure 10, the numerical simulation of casting and rolling with different reductions on the inner arc side of the bloom with the central solid phase rate fs of 0.9 is carried out.

Figure 11 shows the equivalent plastic strain distribution on the cross-section of the bloom under different reduction amounts at the solid fraction of 0.9, and the left side of the cross-section is a symmetrical surface. It can be seen from Figure 11 that the plastic strain of the bloom is mainly concentrated on the inner arc side (top surface) and the outer arc side (down surface). The maximum equivalent plastic strain of the bloom is mainly distributed in the corner. Taking the intersection of the center line and the symmetry line in the thickness direction of the bloom as the center, it can be seen from the figure that when the reduction amount is 7 mm, the maximum equivalent plastic strain of the bloom in the range of $0 \leq r \leq 57$ mm is 0.2%. When the reduction amount is 8 mm, the maximum equivalent plastic strain is 0.33% in the range of 37 mm $\leq r \leq$ 84 mm; when the reduction amount is 9 mm, the maximum equivalent plastic strain is 0.36% in the range of 2 mm $\leq r \leq$ 87 mm. Compared to the temperature field with the central solid fraction of 0.9 in Figure 10, it can be seen that when the reduction amount of 7 mm, 8 mm, and 9 mm is applied to the inner arc side of the bloom respectively, the maximum equivalent plastic strain at the solidification front is less than 0.4%, so the solidification front will not produce internal cracks.

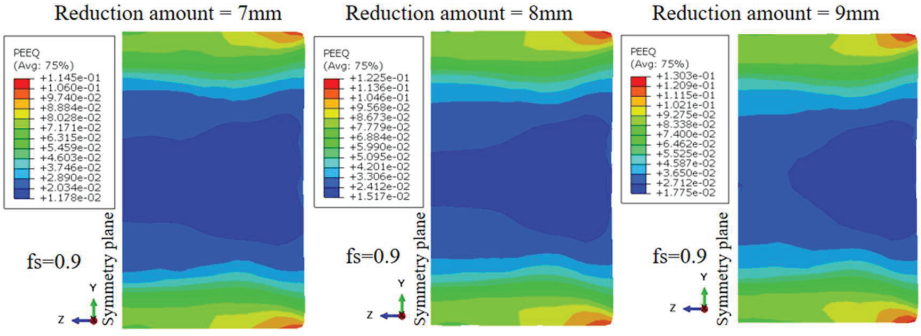

Figure 11. Equivalent plastic strain under different reductions.

Formula (4) is obtained by Zhong [45] modifying Barber's [47] solidification front strain formula. According to the range of the brittle zone at the solidification front of the 3 # and 4 # rollers, the shell thickness of the 3 # and 4 # rollers is 135 mm and 145.4 mm when the central solid fraction of the bloom is 0.6 and 0.71, respectively. Based on the above-mentioned roller spacing, the strain at the solidification front of the bloom is 0.09% and 0.005%, respectively, when the reduction amounts of 3 # and 4 # rollers are 4 mm and 5 mm respectively, which is less than the critical strain value of 0.4%. Therefore, when the reduction amount of 3 # roller and 4 # roller is 4 mm and 5 mm respectively, there will be no internal cracks in the solidification front of the bloom reduction by a single roller.

$$\varepsilon = \frac{300kaS\delta}{l^2 f_s} \tag{4}$$

In the formula, k is the correction coefficient, 1.05; a is the width shape coefficient, 1.01; s is shell thickness, mm; δ is the reduction amounts, mm; l is the roller spacing, mm; f_s is the central solid fraction.

As shown in Figure 12, the equivalent plastic strain distribution of the cross-section of the bloom under different reduction amounts conditions of 3 #~7 # rollers in turn. It can be seen from the figure that the equivalent plastic strain of the bloom gradually increases as the bloom passes through the 3 #~7 # rollers in turn. When the bloom passes through the 3 # roller, the reduction amount is 4 mm, the equivalent plastic strain in the center of the bloom is 0, and the equivalent plastic strain range of the solidification front in the high-incidence area of the crack is 0.066~0.13%. The theoretical calculation value of the plastic strain at the solidification front of the bloom is 0.009% when the reduction amount of the 3 # roller is 4 mm, which is almost equal to the average value of 0.098% using the thermal coupling of the reduction model, indicating that the calculation result of the reduction model is accurate. When the bloom passes through the 4 # roller, the reduction amount is 5 mm, the maximum equivalent plastic strain at the center of the bloom is 0.13%, and the cumulative equivalent plastic strain at the solidification front in the high crack area is 0.13~0.24%. When the bloom passes through the 5 # roller, the reduction amount is 9 mm, the maximum equivalent plastic strain in the center of the bloom is 0.35%, and the cumulative equivalent plastic strain range of the solidification front in the high-incidence area of cracks is 0.17~0.35%. The cumulative strain is less than 0.4%, after the high-temperature bloom in turn passes through 3 #~7 # roller, bloom solidification front will not produce internal cracks. In summary, the macrosegregation of 380 mm × 450 mm bearing steel bloom can be improved when the reduction amount of 3 #~7 # rollers is 4 mm, 5 mm, 9 mm, 7 mm, and 5 mm respectively in the range of 20.82 m~24.97 m from meniscus under the condition of casting speed of 0.45 m/min and average superheat of 26 °C, and the solidification front of the bloom will not occur internal Crack.

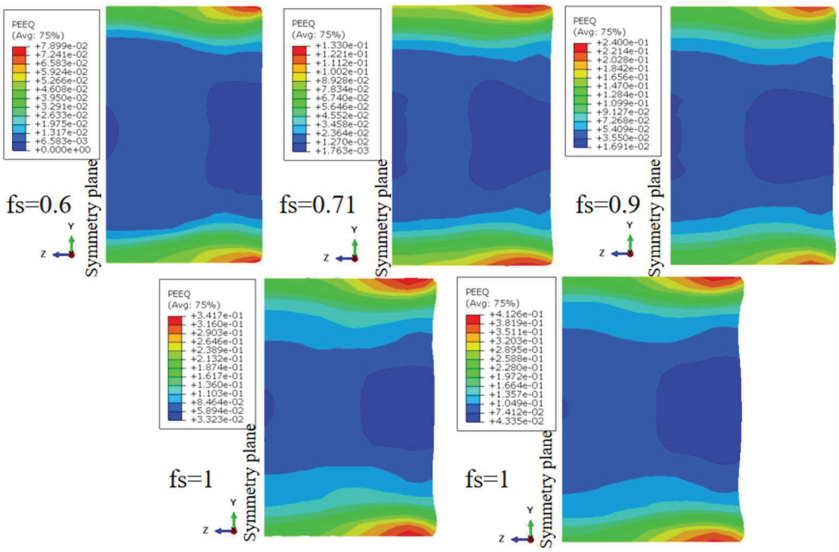

Figure 12. Equivalent plastic strain distribution on the transversal section of bloom under HR.

3.4. Plant Trails

Plant trials were conducted at the first strand of the continuous caster. The casting speed, pouring temperature, and secondary cooling intensity in the trials were 0.45 m/min, 1481 °C, and 0.11 L/kg, respectively, and the casting conditions were kept at a relatively steady state. Before the experiment, the reduction amounts of 3 #~7 # roller were set in the straightening machine system. After the bloom was out of the air cooling zone, the bloom under different processes was sampled by an offline flame cutter, and the high-temperature blooms were taken out and placed in the slow cooling zone until room temperature. In order to reveal the improvement of V segregation and central segregation of bloom, each sample

was sliced, polished, and etched, and the macrosegregation of bloom was quantitatively analyzed by drilling cuttings method and direct reading spectrometer.

Aiming at the analysis of the macrosegregation, the bloom slices were sampled in both transverse and longitudinal directions, as shown in Figure 13a. Thereafter, the samples were etched for 15 min using a hydrochloric acid solution with a concentration of 50% and a temperature of 75 °C and then photographed, as shown in Figure 13b. On the longitudinal sample, no optimized HR, there are continuous V segregation and centerline segregation in the bloom, and the segregation channel is particularly obvious, which is a concentric ellipse in the transverse sample. After optimization, there is no continuous V segregation on the longitudinal sample, the segregation channel is not obvious, the centerline segregation degree is also reduced, and the projection of V segregation on the cross-section is not obvious. Without HR, V segregation is found on the longitudinal sample. The V segregation exhibits lots of discontinuous black strips and distributes non-uniformly near the bloom center, which can be regarded as the flow channels of enriched liquid and has a close relationship with central segregation [48,49]. As for the transverse sample, severe central segregation is observed around the bloom center. By applying HR, the V segregation and the central segregation are alleviated, especially for the V segregation on the transverse sample. This phenomenon indicates that the liquidity of the enriched liquid is enhanced and the central segregation of the bloom is improved by HR. Moreover, no surface or internal cracks were observed in the above samples. It indicates that the optimized HR can effectively avoid the formation of cracks.

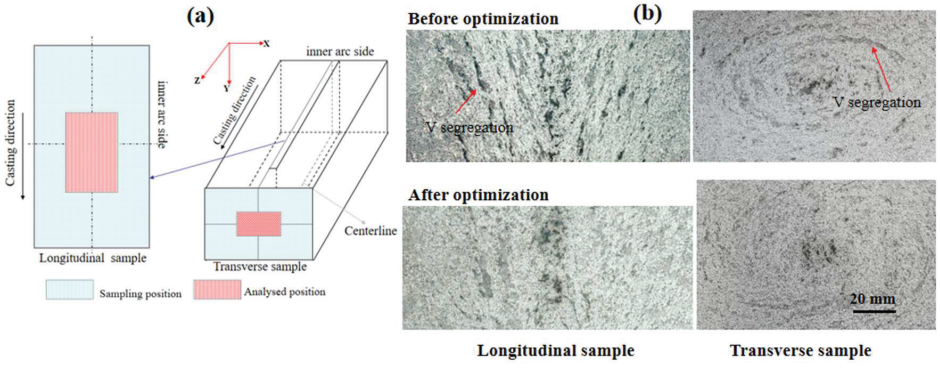

Figure 13. Schematic diagram of (**a**) sampling positions and (**b**) macrographs of etched samples.

In order to quantitatively explore the improvement of V segregation by HR, a part of the longitudinal sample is intercepted from Figure 13a, the back of the longitudinal sample is drawn and traced, and the interval between each line and each point is 10 mm, respectively. The carbon content of each point is measured using a direct-reading spectrometer, and the carbon content of one point in the V segregation channel and one point in the non-channel are randomly extracted on each line, as shown in Figure 14a. Among them, the point of the triangle is located in the V segregation channel, and the point of the circle is located in the non-channel. As shown in Figure 14b, the curves of carbon content in the V segregation channel and non-channel at different positions optimize before and after HR are shown. It can be seen from the diagram that optimizes before and after HR, the average carbon content in the V segregation channel is 1.2% and 1.16% respectively; the average carbon content in the non-segregation channel is 0.93% and 0.95% respectively, and the average range of carbon content is 0.27% and 0.21% respectively. With the optimized HR, the average carbon content in the V segregation channel of 380 mm × 450 mm bearing steel bloom is reduced by 0.04%, the average carbon content in the non-segregation channel is increased by 0.02%, and the average range of carbon content is reduced by 0.06%. This indicates that the optimized HR improves the V segregation of the bearing steel bloom.

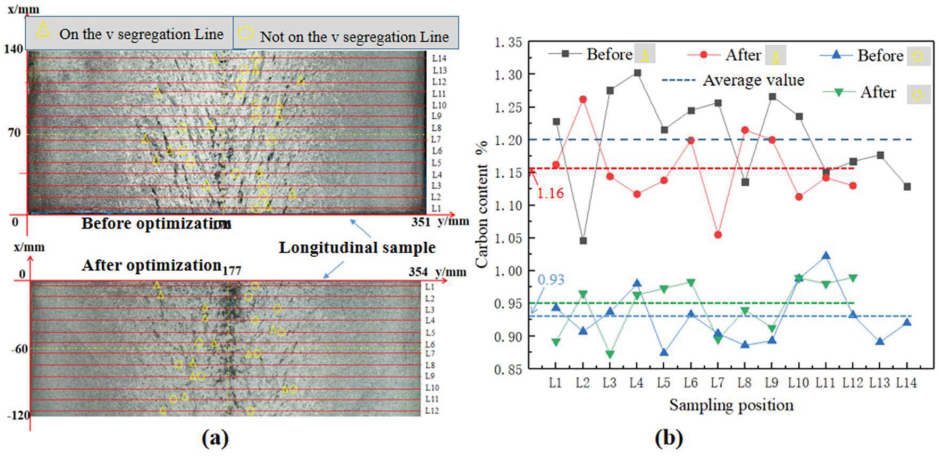

Figure 14. Schematic diagram of (**a**) sampling positions and (**b**) carbon content of different positions.

The central segregation degree is represented by a carbon segregation index of the bloom center. For the bloom sample, the 30 mm flame-cutting range was removed at both ends of the sample, as shown in Figure 15a. A thin slice with a thickness of 20 mm was taken at both ends of the bloom. The center and diagonal quarter of each sample were drilled to 10 mm depth by alloy drills with a diameter of 5 mm. All the drillings were analyzed by a carbon-sulfur analyzer. The carbon segregation index is defined as 4 C/(N1 + N2 + W1 + W2), where C is the carbon content in the central position, N1, N2 and W1, W2 are the carbon content in the quarter position near the inner and outer arc diagonal, respectively. Figure 15b is the distribution of the central carbon segregation degree of bearing steel bloom. It can be seen that the central segregation degree of each condition distributes non-uniformly. Without HR optimization, the carbon segregation degree of the 1 # center of the bloom cross section is 1.23, the carbon segregation degree of the 2 # center is 1.11, and the average carbon segregation degree is 1.17. After optimized HR, the average central carbon segregation degree of the bloom cross section decreases from 1.17 to 1.15. It shows that the optimized HR can improve the central segregation of the bloom.

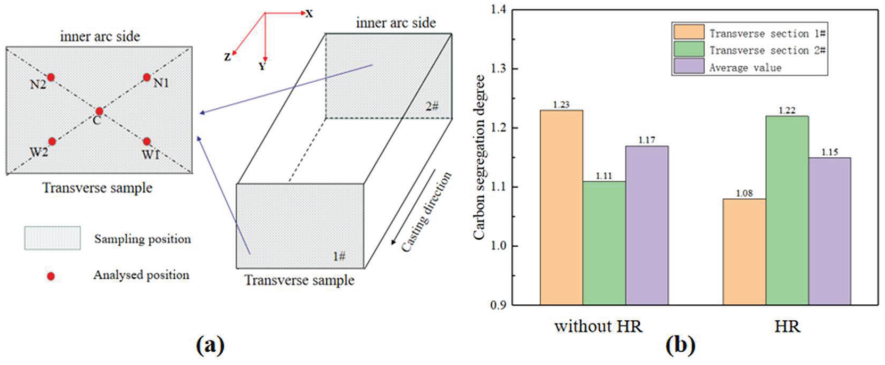

Figure 15. Schematic diagram of (**a**) sampling positions and (**b**) comparison of carbon segregation at different positions.

4. Conclusions

In this study, the solidification heat transfer model of 380 mm × 450 mm GCR15 bearing steel bloom was established and verified. On this basis, a thermal-mechanical coupling model was established. Based on the above two models, the reasonable reduction location

and reduction amounts were discussed and determined to optimize the macrosegregation of bloom. Thereafter, plant trials were conducted to verify the effect of the optimized HR on the inner quality of the bloom.

The following conclusions can be drawn.

(1) The solidification end point of 380 mm × 450 mm bearing steel bloom is 23.13 m from the meniscus. When the casting speed changes 0.01 m/min, the solidification end point changes 0.51 m. For every 15 °C change in superheat, the liquidus end-point of the bloom changes by 0.5 m, and the solidification end point changes by 0.32 m.

(2) The central solid fraction of the solidification end of the 380 mm × 450 mm bearing steel bloom at the position of the 1 #~9 # pressure roller is 0.45, 0.51, 0.6, 0.71, 0.9, 1, 1,1, and 1, respectively. After optimizing HR, the central solid fraction range of the bloom reduction position is 0.6~1, the required reduction roller range is 3 #~7 #, and the distance to the meniscus is 20.82 m~24.97 m.

(3) When the central solid fraction of 380 mm × 450 mm bearing steel bloom is 0.6, 0.71, and 0.9, the radius range of the high-incidence area of solidification front crack is 41 mm $\leq$ r $\leq$ 55 mm, 31.6 mm $\leq$ r $\leq$ 44.6 mm, and 0 $\leq$ r $\leq$ 19 mm, respectively.

(4) After optimization, the total reduction amounts of HR is 30 mm, and the reduction of 3 #~7 # rollers are 4 mm, 5 mm, 9 mm, 7 mm, and 5 mm respectively. The reduction will not make the bearing steel bloom solidification front crack.

(5) The results of plant experiments show that the optimized HR can effectively improve the macrosegregation of bearing steel GCR15 bloom. The average carbon content in the V segregation channel is reduced from 1.2% to 1.16%, and the average carbon content in the non-channel is increased from 0.93% to 0.95%. Meanwhile, the central carbon segregation degree decreased from 1.17 to 1.15.

Author Contributions: Conceptualization, M.W. and H.Z.; methodology, H.Z.; software, X.W.; validation, B.Y., M.W. and H.Z.; formal analysis, B.Y.; investigation, G.W.; resources, H.Z.; data curation, S.L.; writing—original draft preparation, B.Y.; writing—review and editing, M.W. and B.Y. All authors have read and agreed to the published version of the manuscript.

Funding: This research received no external funding.

Informed Consent Statement: Informed consent was obtained from all subjects involved in the study.

Conflicts of Interest: The authors declare no conflict of interest.

References

1. Cen, Y.D.; Chen, L.; Dong, R. Effect of self-tempering on fatigue crack growth of heavy rail steel. *Mater. Rep.* **2021**, *35*, 12–36. [CrossRef]
2. Li, H.G.; Ji, C.; Jiang, D.B.; Chen, T.M.; Guan, R.; Chen, L. Formation mechanism and control of semi-micro-segregation in rail steel bloom. *Iron Steel* **2021**, *56*, 59. [CrossRef]
3. Wang, Y.D.; Zhang, L.F.; Zhang, H.J. Simulation of the macrosegregation in the gear steel billet continuous casting process. *Chin. J. Eng.* **2021**, *43*, 561. [CrossRef]
4. Zhai, Y.Y.; Li, Y.; Yan, C.; Zhang, Y. Computational Prediction Model of Macrosegregation in Continuously Casting Steel Blooms. In Proceedings of the Second International Conference on Digital Manufacturing & Automation, Zhangjiajie, China, 5–7 August 2011; pp. 316–319.
5. Sun, H.; Li, L. Application of swirling flow nozzle and investigation of superheat dissipation casting for bloom continuous casing. *Ironmak. Steelmak.* **2016**, *43*, 228. [CrossRef]
6. Ren, B.; Chen, D.-F.; Wang, H.-D.; Long, M.-J.; Han, Z.-W. Numerical simulation of fluid flow and solidification in bloom continuous casting mould with electromagnetic stirring. *Ironmak. Steelmak.* **2015**, *42*, 401. [CrossRef]
7. Wang, S.; De Toledo, G.A.; Välimaa, K.; Louhenkilpi, S. Magnetohydrodynamic phenomena, fluid control and computational modeling in the continuous casting of billet and bloom. *ISIJ Int.* **2014**, *54*, 2273. [CrossRef]
8. Domitner, J.; Wu, M.; Kharicha, A.; Ludwig, A.; Kaufmann, B.; Reiter, J.; Schaden, T. Modeling the effects of strand surface bulging and mechanical softreduction on the macrosegregation formation in steel continuous casting. *Metall. Mater. Trans. A* **2014**, *45*, 1415. [CrossRef]
9. Han, Y.; Yan, W.; Zhang, J.; Chen, W.; Chen, J.; Liu, Q. Optimization of Thermal Soft Reduction on Continuous-Casting Billet. *ISIJ Int.* **2022**, *60*, 106–113. [CrossRef]

10. Lan, P.; Tie, Z.P.; Zhang, W. Research Progress on Spot Segregation Defects in Continuously Cast semi-products. *Iron Steel* **2020**, *55*, 11–20.
11. Oh, K.S.; Chang, Y.W. Macrosegregation Behavior in Continuously Cast High Carbon Steel Blooms and Billets at the Final Stage of Solidification in Combination Stirring. *ISIJ Int.* **1995**, *35*, 866. [CrossRef]
12. Han, Z.; Chen, D.; Feng, K.; Long, M. Development and Application of Dynamic Soft-reduction Control Model to Slab Continuous Casting Process. *ISIJ Int.* **2010**, *50*, 1637. [CrossRef]
13. Moon, C.H.; Oh, K.S.; Lee, J.D.; Lee, S.J.; Lee, Y. Effect of the Roll Surface Profile on Centerline Segregation in Soft Reduction Process. *ISIJ Int.* **2012**, *52*, 1266. [CrossRef]
14. Zhao, X.; Zhang, J.; Lei, S.; Wang, Y. The Position Study of Heavy Reduction Process for Improving Centerline Segregation or Porosity with Extra-Thickness Slabs. *Steel Res. Int.* **2014**, *85*, 645. [CrossRef]
15. Rogberg, B.; Ek, L. Influence of Soft Reduction on the Fluid Flow, Porosity and Center Segregation in CC High Carbon- and Stainless Steel Blooms. *ISIJ Int.* **2018**, *58*, 478. [CrossRef]
16. Sivesson, P.; Raihle, C.-M.; Konttinen, J. Thermal soft reduction in continuously cast slabs. *Mater. Sci. Eng. A* **1993**, *173*, 299. [CrossRef]
17. Raihle, C.M.; Sivesson, P.; Tukiainen, M.; Fredriksson, H. Improving inner quality in continuously cast billets: Comparison between mould electromagnetic stirring and thermal soft reduction. *Ironmak. Steelmak.* **1994**, *21*, 487.
18. Sivesson, P.; Örtlund, T.; Widell, B. Improvement of inner quality in continuously cast billets through thermal soft reduction and use of multivariate analysis of saved process variables. *Ironmak. Steelmak.* **1996**, *23*, 504.
19. Sivesson, P.; Häilen, G.; Widell, B. Improvement of inner quality of continuously cast billets using electromagnetic stirring and thermal soft reduction. *Ironmak. Steelmak.* **1998**, *25*, 239.
20. Ray, A.; Bhor, P.; Basu, D.; Sahay, S.; Paul, A.; Pradhan, N.; Tiwary, C.; Das, S.; Bandyopadhyay, A.; Bohidar, N. Improvement in internal quality of boiler plates at Bhilai Steel Plant. *Ironmak. Steelmak.* **2000**, *27*, 189. [CrossRef]
21. Jung, Y.J.; Kim, J.J.; Kim, S.K.; Kang, C.G.; Korean, J. Investigated TSR on the centerline macro-segregation of stainless steel slab by numerical simulation and industrial test. *Inst. Met. Mater.* **2003**, *41*, 797.
22. Yim, C.H.; Kil Park, J.; You, B.D.; Yang, S.M. The effect of soft reduction on center segregation in C.C. slab. *ISIJ Int.* **1996**, *36*, 231. [CrossRef]
23. Chiang, L.K. Application of soft reduction technique for improving centerline segregation in continuously cast slab. In *Steelmaking Conference Proceeding*; Iron and Steel Society: Chicago, IL, USA, 1989; Volume 81.
24. Engstrom, G.; Fredriksson, H.; Rogberg, B. On the mechanism of macrosegregation formation in continuously cast steels. *Scand. J. Metall.* **1983**, *12*, 3.
25. Raihle, C.M.; Fredriksson, H. On the formation of pipes and centerline segregates in continuously cast billets. *Metall. Mater. Trans. B* **1994**, *25*, 123. [CrossRef]
26. Han, Z.Q.; Lewis, R.W.; Liu, B.C. Modelling of the thermosolutal convection and macrosegregation in the solidification of an Fe-C binary alloy. *Int. J. Numer. Methods Heat Fluid Flow* **2007**, *17*, 313–321. [CrossRef]
27. Jiang, D.; Wang, W.; Luo, S.; Ji, C. Mechanism of Macrosegregation Formation in Continuous Casting Slab: A Numerical Simulation Study. *Metall. Mater. Trans. B* **2017**, *48*, 3120–3131. [CrossRef]
28. Tomono, H.; Hitomi, Y.; Ura, S.; Teraguchi, A.; Iwata, K.; Yasumoto, K. Mechanism of formation of the V-shaped segregation in the large section continuous cast bloom. *ISIJ Int.* **1984**, *24*, 917–922. [CrossRef]
29. Abbott, T.B.; Hoyle, I.B.; Woodyatt, A.S. The 3-dimensional structure of macrosegregation in continuously cast high-carbon steel. *Steel Res.* **1994**, *65*, 28–131. [CrossRef]
30. Ma, X.P.; Li, D.Z. Characterization, Mechanism and Control Measures of V Segregation in Continuous Casting Billet of C-Mn Steel. *Metall. Mater. Trans. B* **2019**, *50*, 1161–1170. [CrossRef]
31. Zeng, Z.; Ji, C.X.; Zhang, H.Y.; Li, X.K.; Li, F.; Yang, X.S. Optimization experiment of soft reduction of continuous casting slab. *Contin. Cast.* **2018**, *43*, 23.
32. Wang, W.; Hu, X.; Ning, L. Improvement of Center Segregation in High Carbon Steel Billets using Soft Reduction. *J. Beijing Univ. Sci. Technol. Miner. Metall. Mater.* **2006**, *13*, 490. [CrossRef]
33. Wang, Z.M.; Wang, Y.H.; Cao, W.Q. Hot deformation behavior and processing maps of GCr15 bearing steel. *Trans. Mater. Heat Treat.* **2017**, *38*, 193.
34. Kojima, S.; Mizota, H.; Kushida, K. Concept of continuous forging process and experimental analysis of forged blooms. *Kawasaki Steel Tech. Rep.* **1994**, *26*, 1.
35. Nabeshima, S.; Nakato, H.; Fujii, T.; Fujimura, T.; Kushida, K.; Mizota, H. Control of centerline segregation of continuously cast billet by continuous forging process. *Testu Hagane* **1993**, *79*, 479. [CrossRef]
36. Preßlinger, H.; Ilie, S.; Reisinger, P.; Schiefermüller, A.; Pissenberger, A.; Parteder, E.; Bernhard, C. Methods for assessment of slab center segregation as a tool to control slab continuous casting with soft reduction. *ISIJ Int.* **2006**, *46*, 1845. [CrossRef]
37. Gan, Y.; Ni, M.S.; Yu, Z.X. *Handbook of Modern Continuous Casting*; Metallurgical Industry Press: Beijing, China, 2010.
38. Clyne, T.W.; Wolf, M.; Kurz, W. The effect of melt composition on solidification cracking of steel, with particular reference to continuous casting. *Metall. Mater. Trans. B* **1982**, *13*, 259. [CrossRef]
39. Li, C.S.; Thomas, B.G. Thermomechanical finite-element model of shell behavior in continuous casting of steel. *Metall. Mater. Trans. B* **2004**, *35*, 1151. [CrossRef]

40. Kim, K.; Han, H.N.; Yeo, T. Analysis of surface and internal cracks in continuously cast beam blank. *Ironmak. Steelmak.* **1997**, *24*, 249.
41. Won, Y.M.; Yeo, T.J.; Seol, D.J.; Oh, K.H. A new criterion for internal crack formation in continuously cast steels. *Metall. Mater. Trans. B* **2000**, *31*, 779. [CrossRef]
42. Cai, Z.Z.; Ji, C.; Wang, W.L. Study on crack sensitivity of solidified billet shell in thick and wide slab continuous casting mould. In Proceedings of the 2012 Symposium on Crack Control Technology forContinuous Casting of Micro Alloyed Steel, Jiujiang, China, 1 May 2012; Volume 22.
43. Cai, K.K. *The Quality Control of the Continuous Casting Billet*; Metallurgical Industry Press: Beijing, China, 2010.
44. Wu, M.H.; Josef, D.; Andreas, L. Using a Two-Phase Columnar Solidification Model to Study the Principle of Mechanical Soft Reduction in Slab Casting. *Metall. Mater. Trans. A* **2012**, *43*, 945–964. [CrossRef]
45. Zhong, X.D. *Research on the Theory and Process of Soft Reduction in 350 mm × 470 mm Billet Continuous Casting*; Northeast University: Shenyang, China, 2018.
46. Kohichi, I. The realities of v segregation and the formation mechanism of segregation of continuously cast billets. *Camp-ISIJ* **2008**, *21*, 102–105.
47. Barber, B.; Perkins, A. Strand deformation in continuous casting. *Ironmak. Steelmak.* **1989**, *16*, 406–411.
48. Moore, J.J.; Shah, N.A. Mechanisms of formation of A- and V-segregation in cast steel. *Int. Mater. Rev.* **2013**, *28*, 336–356. [CrossRef]
49. Santos, R.G.; Melo, M.L.N.M. Permeability of interdendritic channels. *Mater. Sci. Eng. A* **2005**, *391*, 151–158. [CrossRef]

metals

MDPI

Article

Effects of Alloying Elements on Solidification Structures and Macrosegregation in Slabs

Pan Zhang [1], Minglin Wang [1,*], Pengzhao Shi [1] and Lijun Xu [1,2,*]

[1] National Engineering Research Center of Continuous Casting Technology, Central Iron and Steel Research Institute, Beijing 100081, China
[2] Material Digital R&D Center, Central Iron & Steel Research Institute Group, Beijing 100081, China
* Correspondence: wangminglin2005@sina.com (M.W.); ljxuah@sina.com (L.X.)

Abstract: A Cellular Automaton-Finite Element (CAFE) model and a secondary dendrite arm spacing (SDAS) model are established to study the evolutionary behavior of the macrostructure and the secondary dendrites on a 295 × 2270 mm^2 slab cross-section of experimental steel, respectively. The relationship between the element content, SDAS, equiaxed crystal ratio (ECR) and macrosegregation in continuously cast experimental slabs was studied comprehensively. It is found that with the increase in carbon content, the ECR increases at first and then decreases, and the ECR reaches the maximum value when the carbon content is 0.3%. With the increase in carbon content, the SDAS and average grain size of the equiaxed crystal zone increase, whereas the Si and Al content evidently affects the SDAS and average grain size of the equiaxed crystal zone to a greater extent than the Mn content. In addition, the SDAS can be reduced by reducing the content of C and Si within the acceptable range of alloy composition.

Keywords: CAFE; secondary dendrite arm spacing; equiaxed crystal ratio; element content; macrosegregation

Citation: Zhang, P.; Wang, M.; Shi, P.; Xu, L. Effects of Alloying Elements on Solidification Structures and Macrosegregation in Slabs. *Metals* **2022**, *12*, 1826. https://doi.org/10.3390/met12111826

Academic Editors: Mohsen Eshraghi and Joan-Josep Suñol

Received: 9 September 2022
Accepted: 24 October 2022
Published: 27 October 2022

1. Introduction

The cast structure and segregation in continuously cast carbon steel billets can affect the quality of finished products [1]. The solidification microstructure is closely related to the quality and properties of the casting products [2], and macrosegregation is closely related to the macro- and micro-solidification structures [3,4]. Both primary dendritic arms spacing (PDAS) and SDAS are significant parameters that characterize the solidification structure [5]. Centre segregation is chiefly caused by the interdendritic liquid rich in impurity elements flowing along V-channels and towards the centerline [6]; the fluid flow in the interdendritic channels depends on the PDAS and SDAS, and the smaller the PDAS and SDAS, the denser the solidification microstructure of the bloom, which can contribute to reducing the occurrence frequency of center segregation [7].

The main factors affecting dendrite spacing include the dendrite growth rate, cooling rate, temperature gradient, local solidification time, and steel composition [8,9]. Many studies on the effect of the CC process parameters on the SDAS and ECR have been carried out using experimental and numerical simulation methods [10–12]. In the bloom continuous casting process, the major factor influencing the values of SDAS in different locations of a bloom is the local cooling rate under the condition of defined alloy elements composition [13]. Therefore, in the continuous casting process, under the same specific water flow, the main factor affecting the PDAS and SDAS of the billet is the steel composition. However, there are few studies on the influence of element content on the ECR and SDAS in the billet [8,10,14], especially the impact of C content on the ECR [15,16]. In addition, there are fewer studies on slabs, especially on the effect of element content on the ECR. To study the effect of element content on the ECR and SDAS, it is necessary to ensure that the slab has the same continuous casting process parameters. The continuous casting process for five kinds of steel is studied with an industrial experiment, and the

macrostructure and microstructure of different kinds of steel are analyzed. Compared with previous research, the influence of element content on the slab microstructure is further studied by numerical simulation.

In the present study, the CAFE model of ProCAST was used to predict the solidification process of different slabs with an area of 2270 × 295 mm^2, based on the continuous casting production process conditions. The solidification structure of the continuous casting slab was numerically simulated, and the microstructure of the slab during the solidification process was analyzed and verified by nail shooting, surface temperature measurement, and acid etching experiments. The effect of C content on the ECR is studied. Based on the simulation of the slab temperature field, a SDAS model was established. Combined with the PDAS model, the effect of element content on the SDAS and grain size of the equiaxed zone is investigated. Then, the macrostructure, microstructure, and carbon segregation in different slabs are analyzed. The influences of element content on the ECR, SDAS, and carbon segregation are further studied. Finally, ways to reduce carbon segregation are suggested.

2. Model Descriptions

2.1. Solidification Heat Transfer Model

When establishing the slab solidification model, in order to ensure the accuracy of the calculation process, it is necessary to remove some secondary factors that have little effect on the model. According to the heat transfer characteristics of continuous casting slabs and the actual production situation, the following assumptions are made in the mathematical model [17]:

(1) Heat transfer along the casting direction is ignored.
(2) The effect of the fluid flow of molten steel on the internal heat transfer and structure is ignored during the calculations.
(3) The heat transfer of each part of the secondary cooling zone is uniform, and the heat transfer coefficient can be used to describe the heat exchange of the slab in the secondary cooling zone.
(4) The heat transfer in the mold is calculated by the average heat flux.
(5) The influence of mold vibration and protective slag film on heat transfer was ignored.

Equations (1) and (2) are the two-dimensional heat transfer governing equations for slab continuous casting.

$$\frac{\partial}{\partial x}\left(\lambda\frac{\partial T}{\partial x}\right)+\frac{\partial}{\partial y}\left(\lambda\frac{\partial T}{\partial y}\right)=\rho\frac{\partial H}{\partial T} \tag{1}$$

$$H=\int_0^T C_P dT+L\,(\,1\,-\,f_s\,) \tag{2}$$

where T is the temperature, t is the time, ρ is the liquid density, C_P is the heat capacity, λ is the effective thermal conductivity, L is the latent heat of fusion, and f_s is the solid fraction.

2.2. Nucleation Model

In 1989, Rappaz [18] proposed a continuous nucleation model based on the Gaussian distribution, as shown in Equations (3) and (4):

$$n(\Delta T)=\int_0^{\Delta T}\frac{dn}{d(\Delta T)}d(\Delta T) \tag{3}$$

$$\frac{dn}{d(\Delta T)}=\frac{n_{max}}{\sqrt{2\pi}\Delta T_\sigma}exp\Big[-\frac{(\Delta T-\Delta T_n)^2}{\Delta T_\sigma{}^2}\Big] \tag{4}$$

where ΔT is the undercooling, K; n_{max} represents the maximum nucleation density, the unit of volume nucleation density is m^{-3} and the unit of surface nucleation density is m^{-2}; ΔT_σ is the standard deviation undercooling, K; ΔT_n represents the mean undercooling, K. The compositions of the experimental steels are shown in Table 1. The surface and volume

nucleation (ΔT_S, ΔT_V), standard deviation undercooling ($\Delta T_{S,\sigma}$, $\Delta T_{V,\sigma}$), surface and volume nucleation density (n_S, n_V), and the liquidus and solidus temperature of the experimental steels are shown in the Table 2.

Table 1. Chemical compositions (mass%) of the slab under investigation.

Steel	C	Si	Mn	P	S	Cr	Al
S-1	0.1319	0.3639	1.4767	0.0182	0.0021	\	\
S-2	0.1557	0.1326	0.5548	0.0168	0.0039	\	\
S-3	0.1657	0.2802	1.4503	0.0184	0.0026	\	\
S-4	0.3994	0.3071	1.4604	0.0198	0.0027	1.9	0.0153
S-5	0.4878	0.2056	0.5308	0.0145	0.0026	0.0215	0.0189

Table 2. Nucleation parameters of CAFE model.

Parameters	ΔT_S (K)	$\Delta T_{S,\sigma}$ (K)	n_S	ΔT_V (K)	$\Delta T_{V,\sigma}$ (K)	n_V	α_2	α_3	Liquidus (°C)	Solidus (°C)
S-1	1	0.1	1×10^8	2.5	1	3.0×10^9	2.022×10^{-6}	9.413×10^{-6}	1513	1477
S-2	1	0.1	1×10^8	1.9	1	3.0×10^9	5.227×10^{-6}	1.630×10^{-5}	1519	1483
S-3	1	0.1	1×10^8	2.6	1	3.0×10^9	2.645×10^{-6}	8.105×10^{-6}	1511	1473
S-4	1	0.1	1×10^8	4.0	1	3.0×10^9	1.551×10^{-6}	1.412×10^{-6}	1488	1431
S-5	1	0.1	1×10^8	5.0	1	3.0×10^9	1.639×10^{-6}	1.189×10^{-6}	1489	1424

2.3. Dendrite Tip Growth Kinetics Model

In continuous casting, dendrite tip growth kinetics, namely the KGT model [19,20], are used to calculate the growth kinetics of columnar crystals and equiaxed crystals. Based on the marginal stability criterion, Equation (5) is obtained:

$$V^2 \frac{\pi^2 \Gamma}{P^2 D^2} + V \frac{mC_0(1-k_0)}{D[1-(1-k_0)Iv(P)]} + G = 0 \quad (5)$$

where V is the dendritic tip growth rate, m·s^{-1}; Γ represents the Gibbs–Thomson coefficient; P is the solutal Peclet number; D is the solute diffusion coefficient; m is the liquidus slope; C_0 is the nominal concentration; k_0 is the partition coefficient; G is the temperature gradient; $Iv(P)$ is the Ivantsov function, $Iv(P) = Pexp(P)E_1(P)$, and E_1 is the exponential integral.

In the actual calculation process, to accelerate the calculation process, the KGT model is fitted to obtain the following equation (Equations (6)–(8)) [21]:

$$V(\Delta T) = \alpha_2 \Delta T^2 + \alpha_3 \Delta T^2 \quad (6)$$

$$\alpha_2 = \left[\frac{-\rho}{2mC_0(1-k)^2 \Gamma k} + \frac{1}{mC_0(1-k)D}\right] \frac{D^2}{\pi^2 \Gamma} \quad (7)$$

$$\alpha_3 = \frac{D}{\pi \Gamma} \cdot \frac{1}{(mC_0)^2(1-k)} \quad (8)$$

where α_2 and α_3 are the fitting polynomial coefficients of dendrite tip growth kinetic parameters, and the units are m·s^{-1}·K^{-2} and m·s^{-1}·K^{-3}, respectively; and ρ is the density of steel.

Five processed steels are selected in the current experimental study. Their chemical compositions (in mass%) are listed in Table 2. The distribution coefficient k, liquidus slope m, solute diffusion coefficient D [22] and *Gibbs–Thompson coefficient* Γ [23] of Fe-X alloys are shown in Table 3.

Table 3. Liquidus slope, solute partition coefficient, diffusion coefficient, and Gibbs–Thompson coefficient of binary Fe-X steels.

Steel	Element / Parameters	C	Si	Mn	P	S	Cr	Al
S-1	k	0.16	0.58	0.72	0.33	0.045	/	/
	m/K·(wt.%)$^{-1}$	−84.78	−17.37	−5.1	−29.09	−44.16	/	/
S-2	k	−79.8	0.16	−5.2	−27.2	−38.0	/	4.0
	m/K·(wt.%)$^{-1}$	0.17	0.60	0.72	0.29	0.03	/	1.13
S-3	k	−80.7	−16.7	−5.2	−28.4	−38.4	/	/
	m/K·(wt.%)$^{-1}$	0.16	0.56	0.71	0.26	0.03	/	/
S-4	k	−87.2	−16.7	−5.3	−32.3	−44.9	−1.7	5.0
	m/K·(wt.%)$^{-1}$	0.16	0.61	0.71	0.25	0.06	0.89	1.22
S-5	k	−88.1	−17.2	−5.2	−30.8	−48.4	/	3.9
	m/K·(wt.%)$^{-1}$	0.17	0.60	0.70	0.30	0.05	/	1.19
All	$D \times 10^{-9}$/ m^2·s^{-1}	11	3.5	2.4	1.9	3.9	3.0	3.0
	Γ/m·K				3×10^{-7}			

2.4. SDAS Model

Pequet et al. [24] established a SDAS model at the mushy zone, as follows (Equation (9)):

$$\lambda_2 = [M(t)t_f]^{1/3} \tag{9}$$

where λ_2 represents the SDAS, $M(t)$ is the SDAS factor which mainly depends upon the properties of the alloy elements, and t_f is the local solidification time (LST).

3. Solution Conditions and Model Validation

3.1. Geometric Model

The solidification process of the slab is simulated by the thin-slicing method. In order to save computing time and simplify the calculation process, half of the slab section is used for calculation, and the slice size is 1135 mm × 295 mm × 10 mm. Then, ProCAST software is used for grid division. The geometric model and mesh are shown in Figure 1.

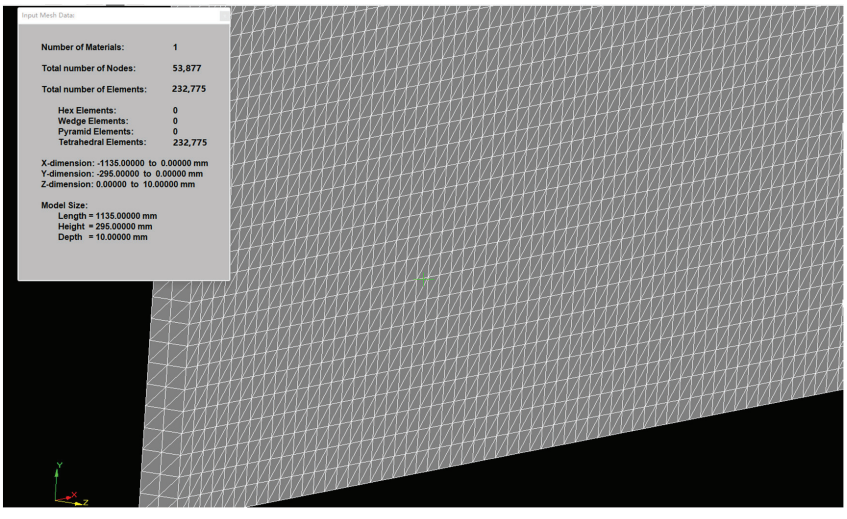

Figure 1. Information about geometric model.

3.2. Selection of the Calculation Parameters

3.2.1. Thermal properties of the Material

The thermal conductivity, density, enthalpy, and solid fraction can be obtained from the ProCAST software database according to the steel compositions. The thermal properties of different steels are shown in the Figure 2.

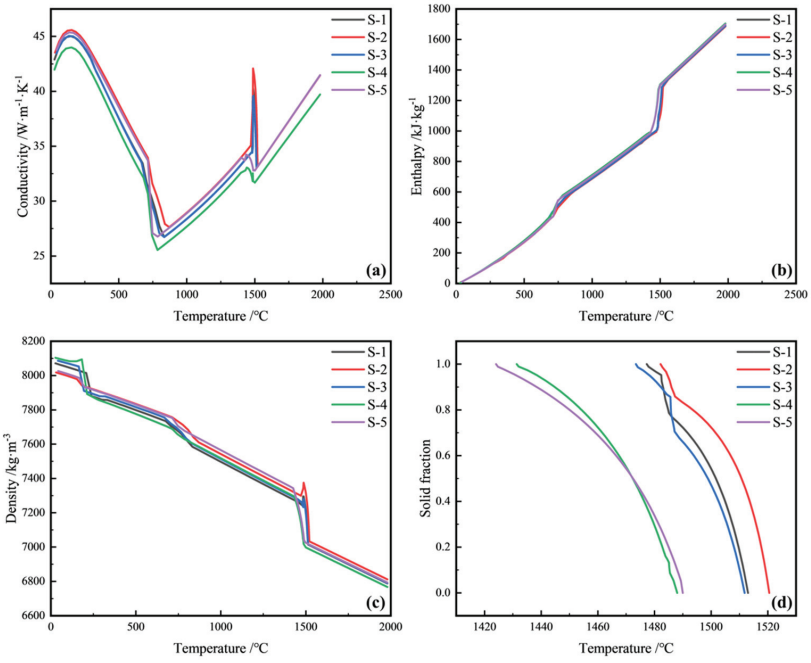

Figure 2. Variations in the thermo−physical parameters of steels with temperature: (**a**) thermal conductivity; (**b**) enthalpy; (**c**) density; (**d**) solid fraction.

3.2.2. Initial Condition and Calculation method for Boundary Conditions

The initial condition is given by Equation (10):

$$T_0 = T_C \tag{10}$$

where T_0 is the initial temperature, K; and T_C is the casting temperature, K.

In the mold, the heat flux was calculated using Equations (11) and (12) [25]:

$$q_m = (2.688 - \beta\sqrt{t}) \times 10^6 \tag{11}$$

$$\beta = \frac{1.5 \times (2.688 \times 10^6 - q_c)}{\sqrt{l_m / v}} \tag{12}$$

where q_m is the heat flux of the crystallizer, $W{\cdot}m^{-2}$; β is a coefficient depending on the mold cooling conditions, $W{\cdot}m^{-2}{\cdot}s^{-1/2}$; q_c is the average heat flux in the mold, $W{\cdot}m^{-2}$; l_m is the effective length of the mold, m; t is the time in the mold, s; and v is the casting speed, $m{\cdot}s^{-1}$. The lengths, the boundary conditions, and the relevant formulas of the foot roller section, secondary cooling zone, and air-cooling zone are shown in Table 4. In addition, when the superheat is 20 °C and the specific water ratio is 0.32 L/kg, the water amounts at different sections are shown in Table 3. h_f and h_k are the heat transfer coefficients of the foot roller section and the secondary cooling zone, $W/(m^2{\cdot}K)$; W is the water flow rate, $L/(m^2{\cdot}s)$; T_w is the temperature of the environment, K; α and β are

the correction factors; ε is the radiation coefficient; and σ is Stefan–Boltzmann constant, 5.67×10^{-8} W/(m^2·K^4).

Table 4. Parameters and relevant computational formulas at different sections of the secondary cooling zone.

Secondary Cooling Zone	Length, m	Water Flow Rate, L·min^{-1}	Computational Formula
Foot roller section (W)	0.29	72.6	$h_f = \alpha \cdot [581W^{0.541}(1 - 0.0075T_W)$
Foot roller section (N)	0.89	182.7	
L2	3.45	174.2	$h_k = \gamma \cdot (130 + 350W)$
L3	1.87	123.5	
L4	2.14	66	
L5	2.13	31	
L6	9.2	66.2	
L7	2.36	28.5	
L8	22.68	68.75	
Air cooling zone	/	$q_a = \varepsilon\sigma(T^4 - T_a{}^4)$	$\varepsilon = 0.85/(1 + \exp(42.68 - 0.02682T_s)^{0.0115})$ [26]

3.3. Model Validation

3.3.1. Validation of Heat Transfer

In this paper, the accuracy of the solidification heat transfer model is verified by the nail shooting experiment. The installation position of the nail shooting device is at the end of segments 8, 9, and 10 of the caster (the distances from the meniscus are 24.63 m, 27.22 m, and 29.77 m, respectively), which are located above one quarter of the broad surface of the slab, and the length of the nail is 200 mm. The nail shooting position is shown in the Figure 3.

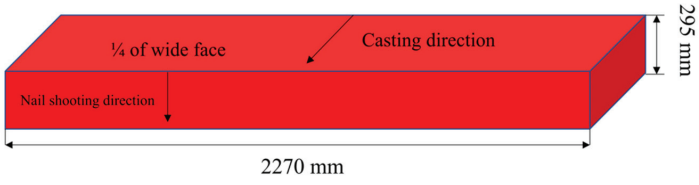

Figure 3. Nail shooting position.

During the experiment, nails with sulfur (S) are hit into the solidifying slab, the nail tip is melted in the molten steel, and then the S is rapidly distributed into the molten steel. The thickness of the solidified shell can be judged by the diffusion of sulfur in the slab. As can be seen from the acid pickling results in Figure 4a, the liquid zone thickness at the end of segment eight is 30 mm, the actual shell thickness is 132.8 mm, and the simulated shell thickness is 132.5 mm, with an error of 0.23%. The measured value agrees well with the calculated value. The nails at the end of the ninth and tenth segments do not melt in the slab, and sulfur diffusion does not occur, so it is concluded that the slab has completely solidified when it enters the ninth segment. To further confirm the accuracy of the simulation results, the surface temperature measured at one quarter of the broad surface of the slab is compared with the simulation results, as shown in Figure 5. It can be seen that the error between simulated temperature and the measured temperature is within 4%. The absolute error is not more than 40 K, which indicates that the processing of the model boundary conditions is close to the actual continuous casting process. The simulation accurately reflects the solidification characteristics of the slab continuous casting process.

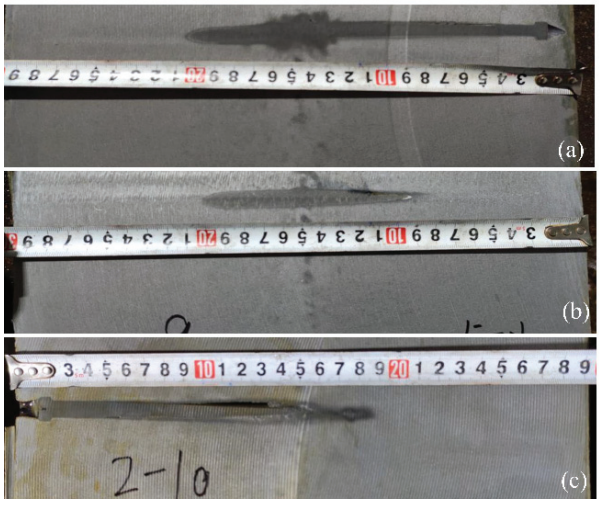

Figure 4. Photographs of sulfur printing samples for nail shooting experiments on S-4 steel: (**a**) The end of segment 8; (**b**) the end of segment 9; (**c**) the end of segment 10.

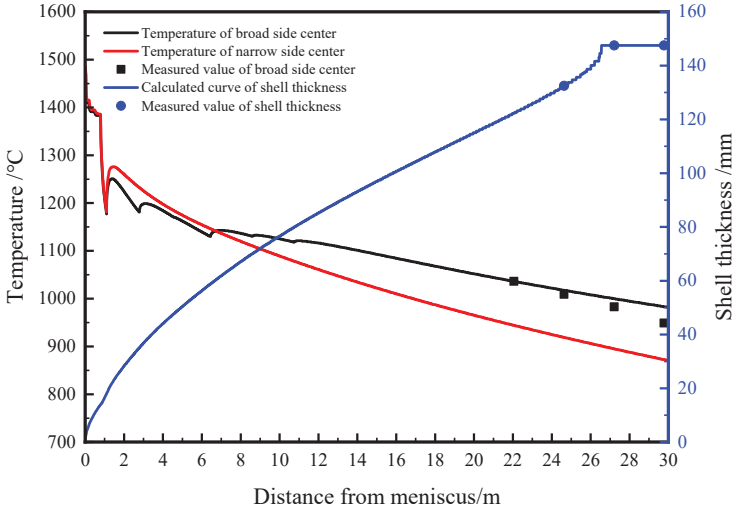

Figure 5. Comparison of the calculated temperature of the slab narrow side center and of the shell thickness with measured values.

3.3.2. Validation of Solidification Structure

Figure 6 shows the comparison of the numerical and experimental solidification structures of S-1 steel. Different colors in Figure 6 represent grain orientation. The ECR of the slab is about 24.41%, while the calculated ECR is also 25.42%. The experimental and simulated equiaxed crystal ratios are almost identical, which indicates the model used in this study can better simulate the evolution of the solidification structure of the slab, and that the model used is reasonable.

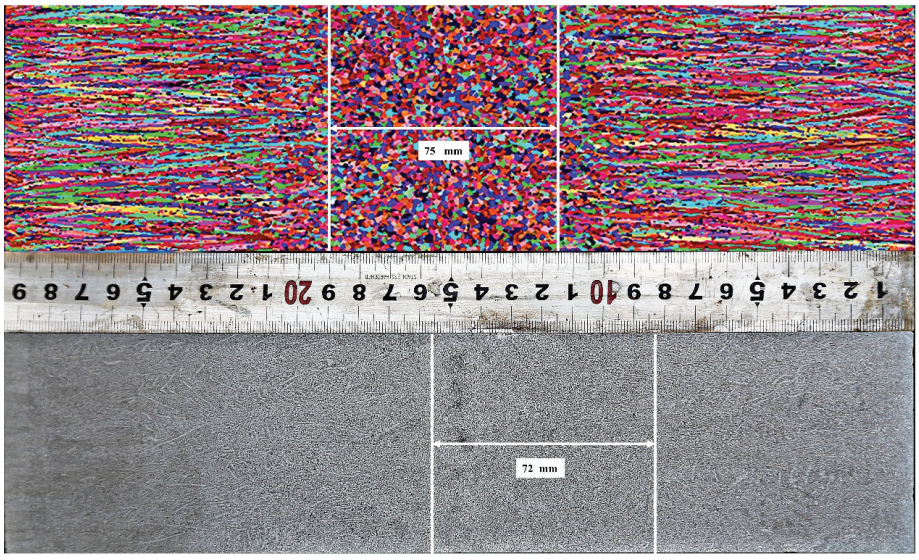

Figure 6. Comparison of numerical and experimental structures of S-1 steel.

To further prove the accuracy of the model, the solidification structure of S-5 steel is simulated under the same continuous casting industrial parameters as S-1 steel. The solidified structures after pickling and simulation are shown in Figure 7. It can be seen from the figure that there are basically no equiaxed crystals in Figure 7a,b, indicating that the model and the actual situation have reached a good correspondence.

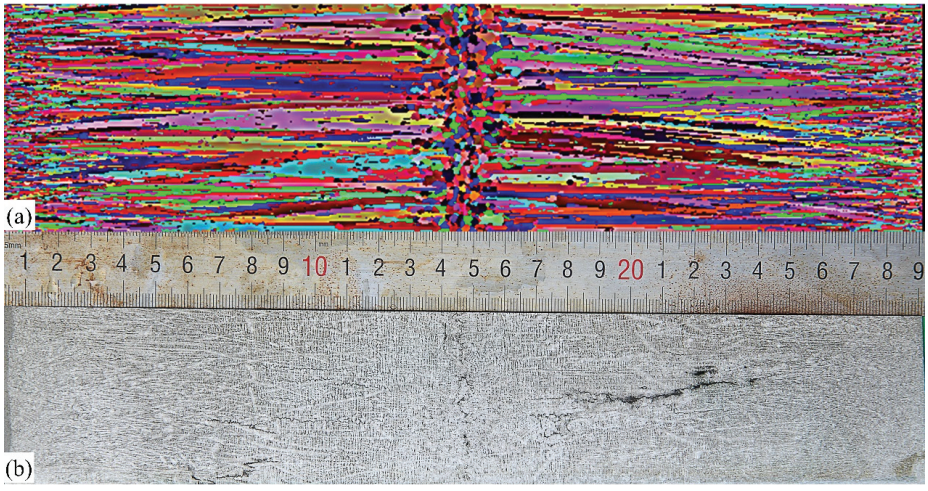

Figure 7. Comparison of the numerical and experimental structures of S-5 steel: (**a**) simulated solidification structure (**b**) experimental solidification structure

3.3.3. Validation of SDAS Model

Nine samples are taken from the surface to the center of the slab, as shown in Figure 8. The etching solution, $V(HNO_3):V(C_2H_6O)$ = 5:95, is used to etch the dendrite and observed under a metallographic microscope. The average SDAS of each sample is measured at 50 times magnification. Micrographs of the samples are shown in Figure 9.

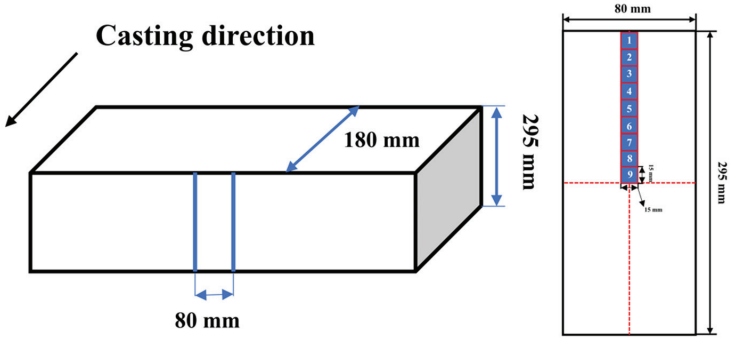

Figure 8. Schematic diagram: Samples for SDAS.

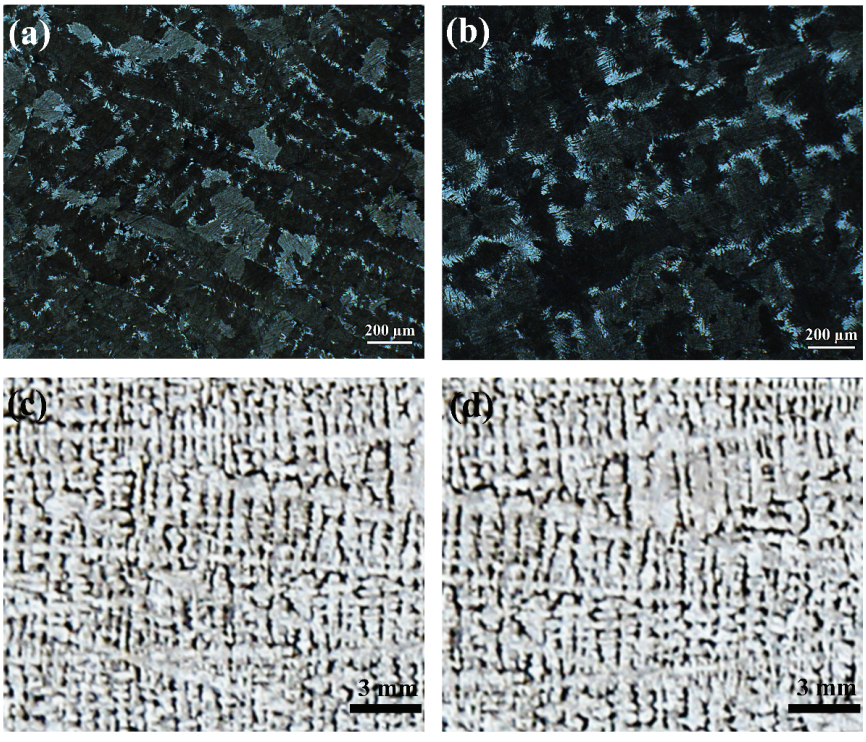

Figure 9. Dendritic microstructure from surface to center in bloom cross-section for S-4 and S-5, (**a**) S-4, 10 mm, (**b**) S-4, 40 mm, (**c**) S-5, 100 mm, (**d**) S-5, 120 mm.

Marrero and Galindo [8] studied four kinds of steel with different compositions and fitted an empirical formula suitable for low alloy steel and high alloy steel through the ordinary least squares, which can be expressed as Equation (13):

$$\lambda_2 = t_{1/3}^{f}[70(\%C) + 50(\%Si) - 0.178(\%Mn) - 430(\%Al) + 0.755(\%Ni) - 3.42(\%Cr)] \quad (13)$$

According to Equations (9) and (13), the $M(t)$ of different steel grades in this study were calculated by a simple model, such as Equation (14):

$$M(t)^{1/3} = [70(\%C) + 50(\%Si) - 0.178(\%Mn) - 430(\%Al) + 0.755(\%Ni) - 3.42(\%Cr)] \quad (14)$$

The comparison between the SDAS values calculated by the model and the measured ones is shown in Figure 10. It can be seen that there is little difference between the calculated results and the measured results. In the continuous casting process, with the increase in the cooling rate, the SDAS decreases. On the surface area of the slab, the SDAS is small because the cooling intensity in the mold and the foot roll zone is large, and the cooling rate is high. In the interior, the SDAS is larger due to the slower cooling rate. When the distance from the surface of the slab increases to 115–147.5 mm, the SDAS becomes stable and reaches the maximum value near 125 mm, then decreases slowly.

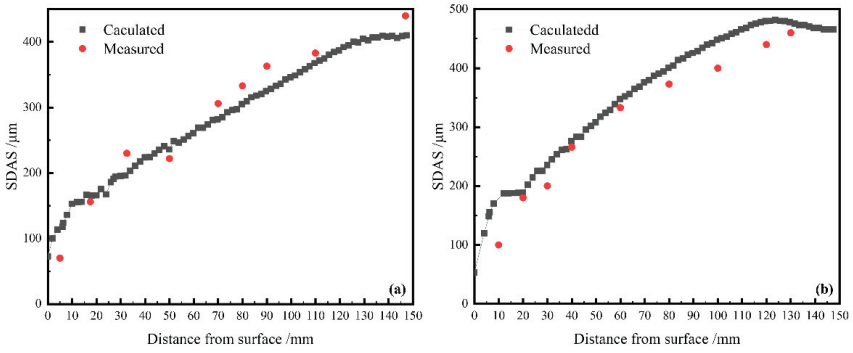

Figure 10. Comparison between calculated and measured SDAS: (**a**) S-4; (**b**) S-5.

4. Results and Discussion

4.1. Effect of Alloying Elements on the Solidification Structure of the Slab

The influence of carbon content on the ECR of the billets is shown in Figure 11 [27]. When the carbon content in steel is 0.09%, the peritectic reaction occurs. At this time, the mushy zone is short and the temperature gradient increases sharply, which is conducive to the growth of columnar crystals. When the carbon content in the steel is between 0.1% and 0.53%, δ-Fe is formed by solidification, and the rest of the molten steel is transformed into γ-Fe by the peritectic reaction. Consequently, the Fe-C equilibrium phase diagram can be used to derive ferrite/austenite fractions during solidification by simply applying the lever rule. The ECR reaches the maximum value when the carbon is 0.3%.

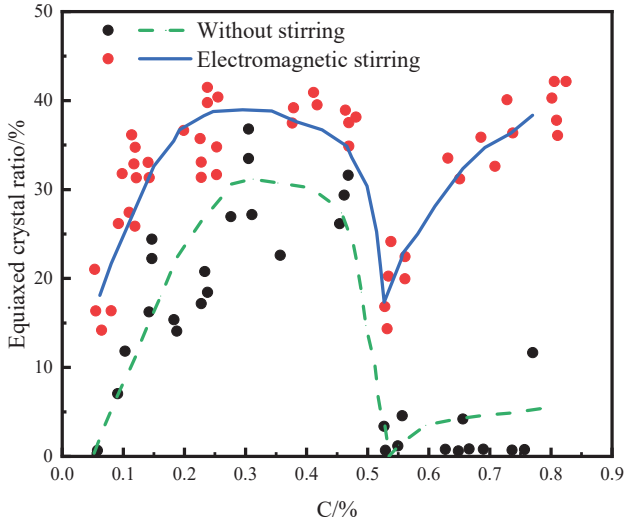

Figure 11. Effect of carbon content on the equiaxed grain ratio of billets [27].

The solidification microstructures of general steel are significantly influenced by the carbon content. To further verify the effect of C content on the ECR, the steels with C contents of 0.20 wt%, 0.25 wt%, 0.30 wt%, and 0.35 wt% were numerically simulated. The composition of the simulated steels is shown in Table 5. The nucleation parameters and growth parameters are shown in Table 6. The simulated solidification structures of different steels are shown in Figure 12. The comparison of the simulation results and calculation curves showing the effect of C content on the ECR of the slab are shown in Figure 13. It can be seen that when the carbon content is 0.1657 wt%, 0.2 wt%, 0.25 wt%, 0.3 wt%, 0.35 wt%, and 0.3994 wt%, the ECR is 28.14%, 32.20%, 35.60%, 37.63%, 36.27%, and 26.44%, respectively. This indicates that with the increase in carbon content, the ECR increases at first, then decreases. For alloys with a carbon content of 0.09 wt% to 0.17 wt%, due to the large amount of ferrite, a part of the ferrite remains after the peritectic reaction. At the same time, the amount of austenite is relatively small, so the ECR rapidly increases. With the further increase in carbon content, the ferrite content decreases continuously, and the growth rate of the equiaxed crystal ratio decreases. When the carbon content is about 0.3 wt%, the ECR reaches the maximum value. The austenite content formed by the peritectic reaction increases continuously as the carbon content increases from 0.3 wt% to 0.53 wt%, and the heat flow increases continuously, which promotes the growth of columnar crystals. When the carbon content is about 0.53 wt%, the ECR reaches the lowest value.

Table 5. Chemical compositions (mass%) of simulated steel.

Steel	C	Si	Mn	P	S
C-0.20	0.2	0.2802	1.4503	0.0184	0.0026
C-0.25	0.25	0.2802	1.4503	0.0184	0.0026
C-0.30	0.3	0.2802	1.4503	0.0184	0.0026
C-0.35	0.35	0.2802	1.4503	0.0184	0.0026

Table 6. Nucleation parameters of CAFE model.

Parameters	ΔT_S (K)	$\Delta T_{S,\sigma}$ (K)	n_S	ΔT_V (K)	$\Delta T_{V,\sigma}$ (K)	n_V	α_2	α_3
C-0.2	1	0.1	1×10^8	2.8	1	3.0×10^9	2.652×10^{-6}	6.300×10^{-6}
C-0.25	1	0.1	1×10^8	3.0	1	3.0×10^9	2.572×10^{-6}	4.535×10^{-5}
C-0.30	1	0.1	1×10^8	3.2	1	3.0×10^9	2.412×10^{-6}	3.402×10^{-6}
C-0.35	1	0.1	1×10^8	3.4	1	3.0×10^9	2.230×10^{-6}	2.634×10^{-6}

Marrero and Galindo [8] used the operation data of the billet caster, such as casting speed, steel temperature, and cooling conditions of the spray zone, to predict the dendrite structure of the solidified steel. For this purpose, semi-empirical equations to calculate primary and secondary arm spacing were derived from uni-directional solidification experiments of steel samples with various compositions, as shown in Equation (15):

$$\lambda_1 = R^{-1/4} G^{-1/2} [1990(\%C) + 380(\%Si) - 0.221(\%Mn) - 9840(\%Al) + 20(\%Ni) - 40(\%Cr) \quad (15)$$

where λ_1 is the PDAS, μm; R is the solidification rate, cm·s^{-1}; and G is the thermal gradient, K·cm^{-1}.

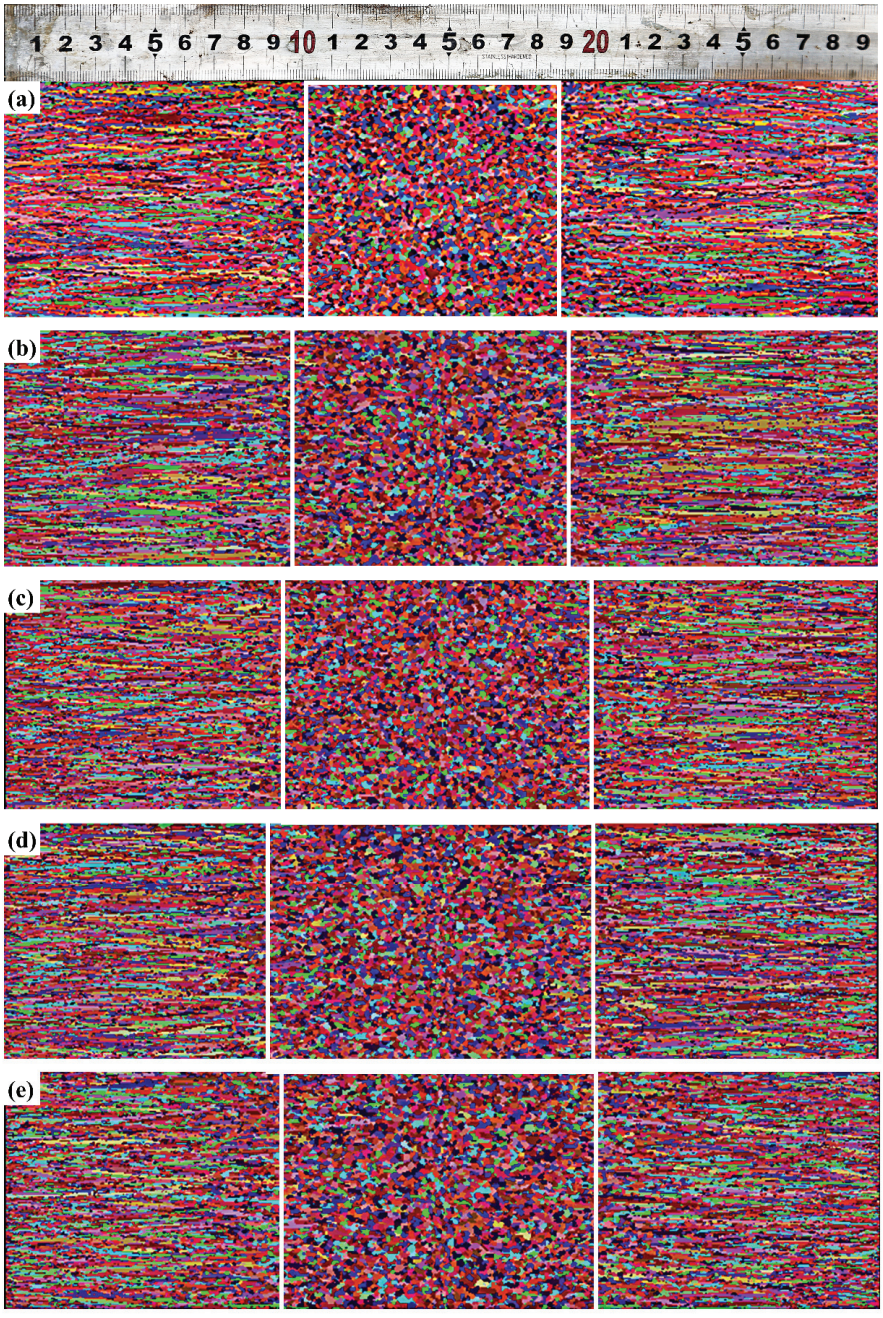

Figure 12. The simulated solidification structures of different slabs: (**a**) S-3; (**b**) C-0.20; (**c**) C-0.25; (**d**) C-0.30; (**e**) C-0.35.

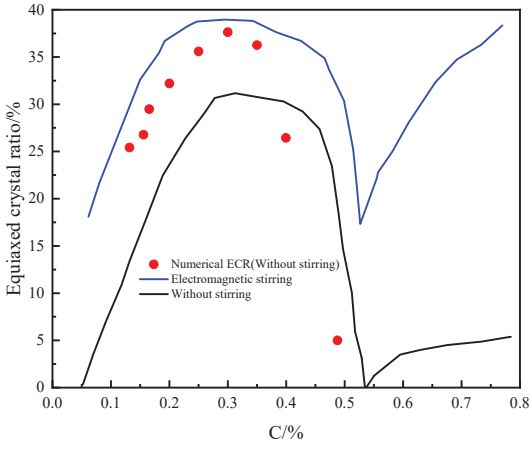

Figure 13. Comparison of simulation results and calculation curves showing the effect of C content on the slab ECR.

For equiaxed crystals, the PDAS is usually the grain diameter [28]. Therefore, the PDAS is used to describe the grain size of the equiaxed crystal zone of the slab. The corresponding values of the average grain size of the equiaxed crystal zone for each slab are displayed in Figure 14. According to the Equation (15), it is obvious that the addition of C, Si, and Ni increases the PDAS, while the addition of Mn, Al, and Cr decreases the PDAS. C promotes the largest increases in PDAS, whereas Al produces the strongest diminution. As for the role of Si and Mn, it is obvious that the coefficient affecting Si is one order of magnitude larger than that of Mn, indicating that Si has a greater influence on the PDAS than Mn. The average grain size of the S-2 steel is smaller than that of S-1 steel. This is mainly due to the Si content of S-2 steel being less than that of S-1 steel; specifically, it is one-third of that of S-1 steel. The simulation and experimental results show that with the decrease in Si content, the ECR in the slab increases, the number of grains increases, and the average grain radius decreases. Increasing Cr content can increase the ECR, reduce the average grain size, and increase the number of grains. The increase in Mn content serves to increase the ECR. Another important fact worth mentioning is that Mn element has little influence on the average radius of the grains, which is in agreement with some results published by other researchers [15,16].

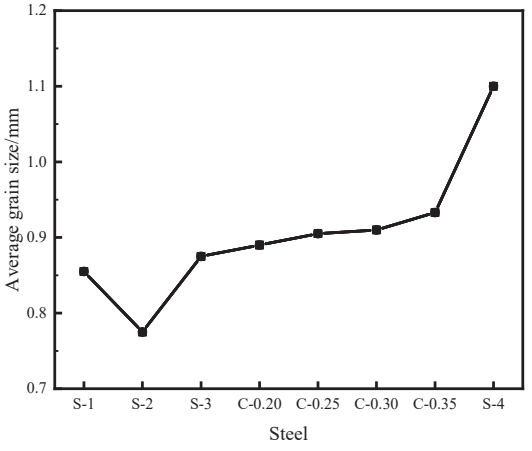

Figure 14. Average grain size of the equiaxed zone of different steels.

4.2. Effect of Alloying Elements on Macrosegregation

The comparison of the transverse and longitudinal morphologies of typical defects of experimental steels is shown in Figure 15. The existence of V-segregation can be seen from the cross section of the slabs after pickling. The V-segregation line will occur if (1) equiaxed dendrite crystals grow large even while the molten steel pool remains large, (2) columnar crystals grow to the vicinity of the central axis, and (3) the bridges are not ruptured, thereby functioning as an effective filter against equiaxed dendrite crystals [1]. In this actual production, under the cooling conditions described in this paper, the secondary cooling intensity is large. The casting speed is very stable and the roll spacing is small, which makes the bulging amount small and have little effect on the central segregation. Therefore, the effect of bulging on central segregation is excluded. In a low-carbon steel slab, small V-lines occur in large numbers, probably because the size of the equiaxed dendrite is small, as shown in Figure 16. This is mainly because the solidification temperature range of low-carbon steel is narrower than that of the medium-carbon steel, as shown in Figure 2d. The equiaxed crystals have a short growth period, so that they cannot fully grow.

According to the solidification structure of the slabs, the slab can be divided into three types. In Figure 15 (S-1) (S-3) (S-4), the columnar crystal is tiny and the equiaxed crystal area is wide (about 25%). The columnar crystals occupy about 75% of the area, and there are tiny pipes around the central axis. In Figure 15 (S-2), the average grain size is the smallest, and the equiaxed crystal area is the widest (about 28%); no obvious V-segregation line was observed, and the center porosity is characterized by the absence of pipes around the central axis where a wide porous area is observed. In Figure 15 (S-5), the columnar crystals are seen elongated and merging into branched columnar crystals which extend to the vicinity of the central axis. In addition, cracks along columnar crystals are found on the inner and outer arc sides.

The solid–liquid zone at the solidification front of the slab is called the mushy zone of the slab. The mushy zone is composed of dendrites, which block the liquid flow in the mushy zone. The solutes discharged from the solid phase at the solidification front are macroscopically distributed in the mushy zone, forming the central segregation of the slab. Dendrite arm spacing is the main micro-parameter affecting permeability [29]. The calculation formula for permeability is usually the Kozeny Carman formula [30]:

$$K_P = \frac{\lambda_2^2 \times (1 - f_s)^3}{180 \times f_s^2} \tag{16}$$

where K_P represents the permeability of the solid–liquid zone, μm^2. For the slab, the solidification front is based on the position of zero strength temperature, which is generally between 20–30 K above the solidus, and the corresponding solid fraction is 0.8 [31]. When the solid fraction is 0.8, the permeability is proportional to the square of the SDAS, as shown in Equation (16). With the increase in the SDAS, the permeability of the mushy zone increases sharply. When the permeability is high, the solute is continuously enriched, which increases macrosegregation.

In general, the dendrite spacing is the vertical distance between dendrites. The dendrite growth morphology and SDAS determine the density and the morphology (columnar crystal and equiaxed crystal) of the solidification structure. The size of the dendrite spacing is closely related to macrosegregation, microcracks, and porosity in the solidification structure. The SDAS curves of different slabs from the slab surface to the center are shown in Figure 16. According to Equation (11), C and Si promote a larger increase in the SDAS, and conversely Al produces the strongest decrease. As for the role of Mn, Ni, and Cr, it is apparent that they have little effect on the SDAS. Although the C content of S-3 steel is higher than that of S-1 steel, the SDASs of S-1 and S-3 steel are basically equal due to the relatively high Si content of S-1 steel. Since the ECR of S-1, S-2, S-3, and S-4 steel are not much different, the main factor affecting the macrosegregation of the slab is the SDAS. The internal quality of the S-2 slab is significantly higher than that of the S-3 slab, which is

mainly because smaller SDAS can reduce the frequency of central segregation. When the SDAS is 100-220 μm, the dendrite belongs to a fine dendrite structure with a small dendrite gap and a small volume fraction of enriched solute, which reduce the macrosegregation [32]. The internal quality of the S-1 slab is not much different from that of the S-3 slab, mainly because the SDAS is not much different. Although the ECR of S-3 steel is higher than that of S-1, the grain size of S-1 steel is smaller than that of S-3. For S-4 and S-5 steel, due to the large SDAS, the slab has more serious central segregation, and for S-5 steel, due to its ECR close to 0% and large grain size, the central segregation is most serious.

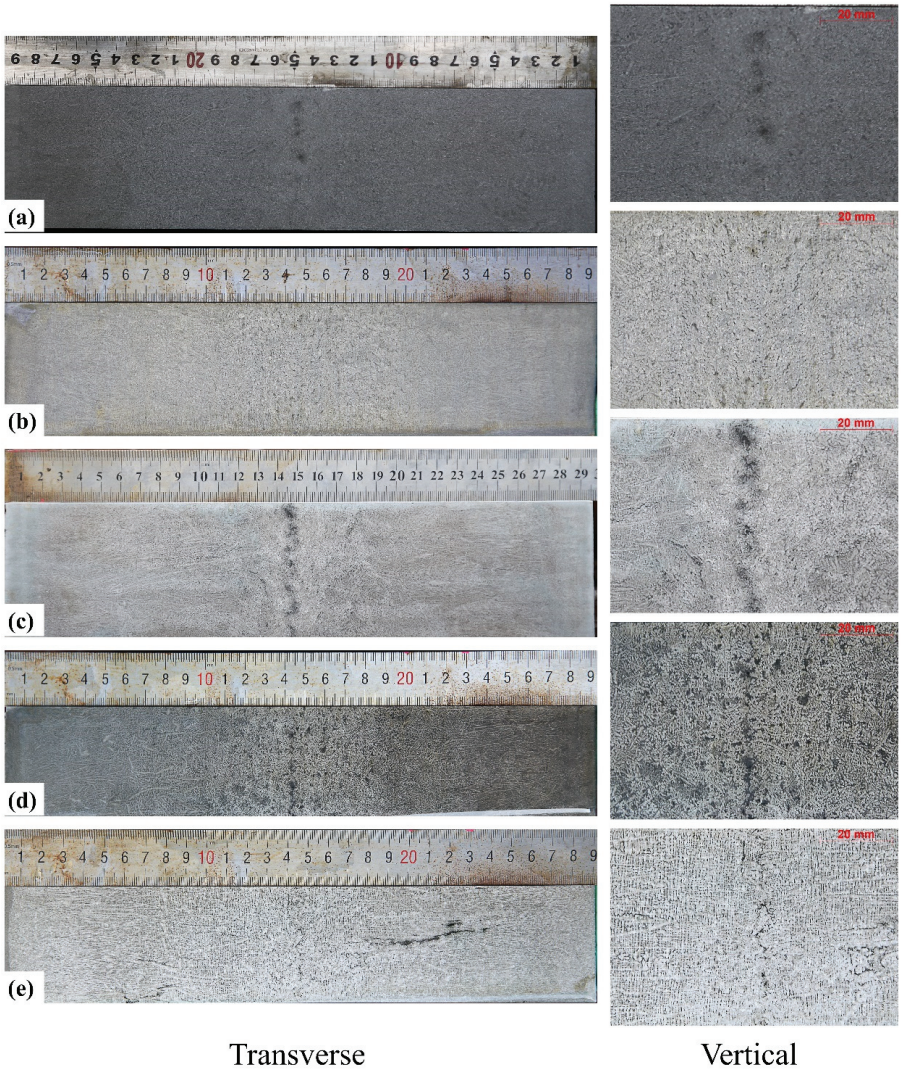

Figure 15. Central segregation rating of 295 × 2270 mm steel slabs: (**a**) S-1; (**b**) S-2; (**c**) S-3; (**d**) S-4; (**e**) S-5.

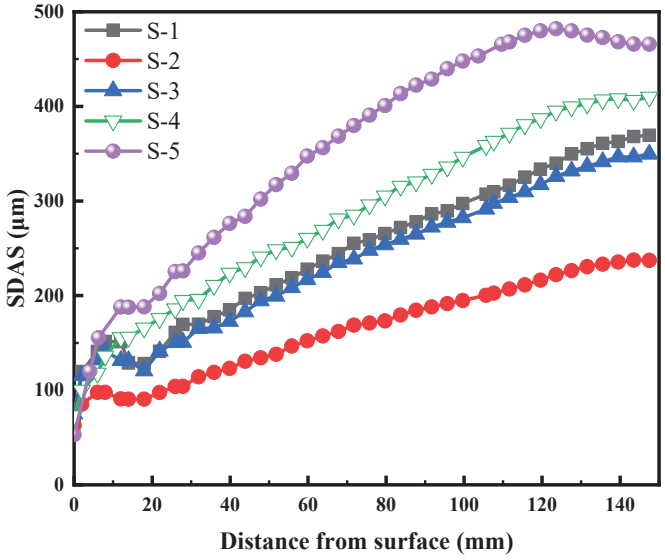

Figure 16. SDAS at different positions from the slab surface of different slabs.

To quantitatively describe the macrosegregation, the carbon segregation index of the slabs was quantitatively measured by chemical analysis of the drillings, as shown in Figure 17. A carbon–sulfur analyzer was used to obtain the carbon content at different locations in the slabs. The calculation formula for the C segregation index is as follows:

$$C_i = \frac{C}{C_0} \tag{17}$$

where C represents the carbon content of the drillings, and C_0 is the carbon content of the liquid steel in the tundish.

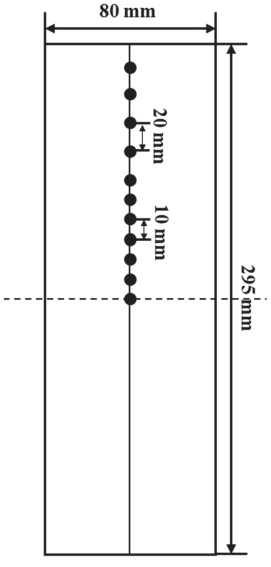

Figure 17. Carbon segregation sampling schematic.

The comparison of the carbon segregation index between S-1, S-2, and S-3 billets is shown in Figure 18. As shown in Figure 18, the carbon segregation degree ranges from 0.971 to 1.085 and the standard mean deviation is 0.035 for the S-2 slab, and the carbon segregation degree decreases to 0.890–1.077 and the standard mean deviation is 0.042 for the S-3 slab. It can be seen that the carbon segregation at the center of the S-2 slab is 0.972, and the carbon segregation of the S-3 slab is 1.077. In addition, the standard average deviation of the carbon segregation of the S-2 slab is 0.038. This is basically consistent with the results of our previous analysis. The quality rate of the S-1 slab is better than that of the S-3 slab, mainly because the grain size of the S-3 slab is larger. The final results show that decreasing the SDAS and average grain size can improve the central segregation of the slab.

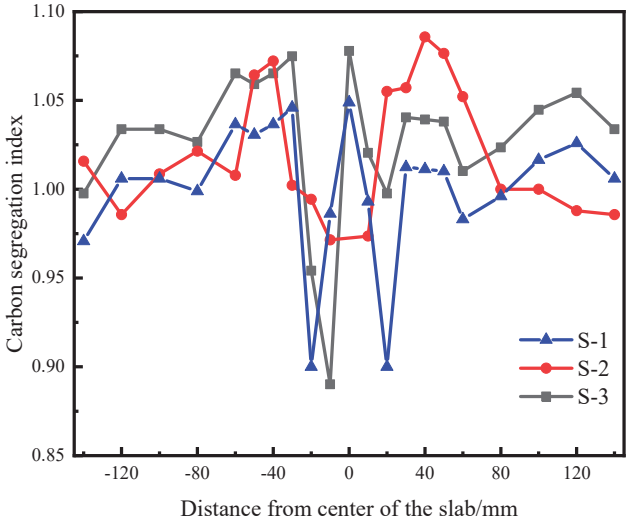

Figure 18. Comparison of carbon segregation index between the S−1, S−2, and S−3 slab.

5. Conclusions

The effect of element content on solidification structure, SDAS, average grain size and macrosegregation in continuously cast 295 mm × 2270 mm experimental steels was investigated by physical experiments, numerical simulations, and industrial trials. Based on numerical simulations and experiments, the effect of element content on the solidification process, macrostructure, and SDAS were investigated, and the following conclusions can be obtained.

(1) The heat transfer model is established and verified by surface temperature measurements and the nail shooting test. Based on the temperature field, the solidification structure of different slabs is simulated, which is in good agreement with the results of macro-etch experiments. The SDAS model for experimental slabs was obtained, and the calculated value of the model is in good agreement with the value obtained through metallographic observation.

(2) With the increase in carbon content, the ECR increases at first, and then decreases. The ECR reaches the maximum value when the carbon content is 0.3%. When the carbon content is about 0.53 wt%, the equiaxed crystal rate reaches the lowest value. Therefore, in the actual production, within the acceptable range of carbon content, the content of C can be controlled by this rule to improve the ECR.

(3) The SDAS increases with the increase in C and Si content. Compared with S-2 steel, the degree of central segregation in S-1 steel is lower. The effect of Si content on SDAS is second only to that of C content. Properly reducing Si content can reduce SDAS and effectively reduce central segregation.

(4) The average grain size of the equiaxed crystal zone can be expressed by the primary dendrite spacing, which is closely related to the element content. Additions of C, Si, and Ni increase the arm spacing, while additions of Mn, Al, and Cr diminish them. C promotes the largest increases in PDAS, and conversely Al produces the strongest diminution. The grain size of the equiaxed zone can be controlled by controlling the alloying content to reduce the macrosegregation.
(5) The macrosegregation is closely related to the SDAS, ECR and average grain size. Smaller SDAS can make the solidification structure more compact, and a high ECR and small grain size can reduce macrosegregation.

Author Contributions: Original draft preparation, validation, P.Z.; writing—review and editing, M.W. and L.X.; Conceptualization, M.W.; formal analysis, P.S.; methodology, L.X. All authors have read and agreed to the published version of the manuscript.

Funding: This research received no external funding.

Data Availability Statement: Not applicable.

Conflicts of Interest: The authors declare no conflict of interest.

References

1. Hisashi, M.; Nobuyoshi, T.; Norio, S.; Masazumi, H. Macrostructure of and Segregation in Continuously Cast Carbon Steel Billets. *Trans. Iron Steel Inst. Jpn.* **1972**, *12*, 102–111.
2. Cicutti, C.; Boeri, R. On the relationship between primary and secondary dendrite arm spacing in continuous casting products. *Scr. Mater.* **2001**, *45*, 1455–1460. [CrossRef]
3. Ludlow, V.; Normanton, A.; Anderson, A. Strategy to minimize central segregation in high carbon steel grades during billet casting. *Ironmak. Steelmak.* **2005**, *32*, 68–74. [CrossRef]
4. Ayata, K.; Mori, T.; Fujimoto, T.; Ohnishi, T.; Wakasugi, I. Improvement of macrosegregation in continuously cast bloom and billet by electromagnetic stirring. *Trans. Iron Steel Inst. Jpn.* **1984**, *24*, 931–939. [CrossRef]
5. Imagumbai, M. Relationship between Primary- and Secondary-dendrite Arm Spacing of C-Mn Steel Uni-directionally Solidified in Steady State. *ISIJ Int.* **1994**, *34*, 986. [CrossRef]
6. Ayata, K.; Mor, T.; Taniguchi, K.; Matsuda, H. Low superheat teeming with electromagnetic stirring. *ISIJ Int.* **1995**, *35*, 680–685. [CrossRef]
7. An, H.; Bao, Y.; Wang, M.; Yang, Q.; Dang, Y. Numerical and experimental investigation of solidification structure evolution and reduction of centre segregation in continuously cast GCr15 bloom. *Ironmak. Steelmak.* **2020**, *47*, 1063–1077. [CrossRef]
8. Cabrera-Marrewo, J.M.; Carreno-Galindo, V.; Morales, R.D.; Chávez-Alcalá, F. Macro-micro modeling of the dendritic microstructure of steel billets processed by continuous casting. *ISIJ Int.* **1998**, *38*, 812–821. [CrossRef]
9. Weisgerber, B.; Hecht, M.; Harste, K. Investigations of the solidification structure of continuously cast slabs. *Steel Res.* **1999**, *70*, 403–411. [CrossRef]
10. Gao, X.; Yang, S.; Li, J. Effects of micro-alloying elements and continuous casting parameters on reducing segregation in continuously cast slab. *Mater. Des.* **2016**, *110*, 284–295. [CrossRef]
11. Wang, W.; Ji, C.; Luo, S.; Zhu, M. Modeling of dendritic evolution of continuously cast steel billet with cellular automaton. *Metall. Mater. Trans. B* **2017**, *49*, 200–212. [CrossRef]
12. Jing, C.L.; Wang, X.H.; Jiang, M. Study on solidification structure of wheel steel round billet using FE-CA coupling model. *Steel Res. Int.* **2011**, *82*, 1173–1178. [CrossRef]
13. Wang, Q.; Yan, H.; Wang, F.; Li, B. Impact of electromagnetic stirring on grain structure of electroslag remelting ingot. *JOM* **2015**, *67*, 1821–1829. [CrossRef]
14. Pierer, R.; Bernhard, C. On the influence of carbon on secondary dendrite arm spacing in steel. *J. Mater. Sci.* **2008**, *43*, 6938–6943. [CrossRef]
15. Bai, L.; Liu, H.; Zhang, Y.; Miao, X.; Ruan, X. Numerical simulation of the microstructure of 22CrMoH billets and the effects of alloying elements. *Chinese J. Eng.* **2011**, *33*, 1091–1098. [CrossRef]
16. Han, L.; Feng, Y.; Wu, H.; Chen, Z. Numerical simulation of effects of alloying elements on solidification structure of 20CrMnTi billets. *Iron Steel* **2016**, *51*, 36–42.
17. Lally, B.; Biegler, L.; Henein, H. Finite difference heat transfer modeling for continuous casting. *Metall. Mater. Trans. B* **1990**, *21*, 761–770. [CrossRef]
18. Rappaz, M.; Gandin, C.A. Probabilistic modelling of microstructure formation in solidification processes. *Acta Metall. Mater.* **1993**, *41*, 345–360. [CrossRef]
19. Kurz, W.; Giovanola, B.; Trivedi, R. Theory of microstructural development during rapid solidification. *Acta Metallurgica.* **1986**, *34*, 823–830. [CrossRef]
20. Kurz, W.; Fisher, D.J. *Fundaments of Solidification*, 4th revised ed.; Trans Tech Publishers: Aedermannsdorf, Switzerland, 1998; p. 77.

21. Bai, L.; Wang, B.; Zhong, H.; Ni, J.; Zhai, Q.; Zhang, J. Experimental and numerical simulations of the solidification process in continuous casting of slab. *Metals* **2016**, *6*, 53. [CrossRef]
22. Li, W.C. *Metallurgy and Physical Chemistry of Materials*; Metallurgical Industry Press: Beijing, China, 2001; pp. 531–533. (In Chinese)
23. Fang, Q.; Ni, H.W.; Zhang, H.; Wang, B.; Lv, Z.A. The effects of a submerged entry nozzle on flow and initial solidification in a continuous casting bloom mold with electromagnetic stirring. *Metals* **2017**, *7*, 146. [CrossRef]
24. Pequet, C.; Rappaz, M.; Gremaud, M. Modeling of microporosity, macroporosity, and pipe-shrinkage formation during the solidification of alloys using a mushy-zone refinement method: Applications to aluminum alloys. *Metall. Mater. Trans. A* **2002**, *33*, 2095–2106. [CrossRef]
25. Savage, J.; Pritchard, W.H. The problem of rupture of the billet in the continuous casting of steel. *J. Iron Steel Inst.* **1954**, *178*, 269–277.
26. Hardin, R.A.; Liu, K.; Beckermann, C.; Kapoor, A. A transient simulation and dynamic spray cooling control model for continuous steel casting. *Metall. Mater. Trans. B* **2003**, *34*, 297–306. [CrossRef]
27. Cai, K. *Quality Control of Continuous Casting Billet*; Metallurgical Industry Press: Beijing, China, 2010; pp. 279–282. (In Chinese)
28. Hu, H.Q. *Metal Solidification Principle*; Machine Press: Beijing, China, 2000; pp. 131–133. (In Chinese)
29. Yoo, H.; Viskanta, R. Effect of anisotropic permeability on the transport process during solidification of binary a mixture. *Int. J. Heat Mass Transf.* **1992**, *35*, 2335. [CrossRef]
30. Piorier, D.R. Permeability for flow of dendritic liquid in columnar dendrite alloys. *Metall. Trans. B* **1987**, *18*, 245. [CrossRef]
31. Cornelissen, M.C.M. Mathematical model for solidification of multicomponent alloys. *Ironmak. Steelmak.* **1986**, *13*, 204–212.
32. Shen, H.F.; Beckermann, C. Experimental study on the mush deformation and solute redistribution. *Acta Metall. Sin.* **2002**, *38*, 352–358.

metals

MDPI

Article

Prediction of Thermal Distortion during Steel Solidification

Ghavam Azizi, Brian. G. Thomas * and Mohsen Asle Zaeem

Department of Mechanical Engineering, Colorado School of Mines, 1610 Illinois Street, Golden, CO 80401, USA
* Correspondence: bgthomas@mines.edu

Abstract: Thermal distortion during the initial stages of solidification is an important cause of surface quality problems in cast products. In this work, a finite element model including non-linear temperature-, phase-, and carbon-content-dependent elastic–viscoplastic constitutive equations is applied to study the effect of steel grade and interfacial heat flux on thermal distortion of a solidifying steel droplet. Due to thermal contraction, the bottom surface of the droplet bends away from the chill plate and a gap forms. It is shown that, regardless of the nature of the heat flux, the gap forms and grows the most very early during solidification (~0.1 s) and remains almost unchanged afterward. Increasing the heat flux decreases the time for evolution of the gap and increases its depth. When the carbon content is less than 0.10%C, the gap depth is very sensitive to the heat flux, but for higher carbon contents, this sensitivity is much weaker. The highest gap depths are predicted in ultra-low carbon (0.003%C) and peritectic steels (0.12%C), and agree both qualitatively and quantitatively with the experimental measurements. Thus, the current thermal-mechanical model, including its phase-dependent properties, captures the mechanism responsible for nonuniform solidification, depression sensitivity and surface defects affecting these steels.

Keywords: solidification; peritectic steel; thermal distortion; thermo-elasto-viscoplastic model

Citation: Azizi, G.; Thomas, B.G.; Asle Zaeem, M. Prediction of Thermal Distortion during Steel Solidification. *Metals* **2022**, *12*, 1807. https://doi.org/10.3390/met12111807

Academic Editor: Gunter Gerbeth

Received: 22 September 2022
Accepted: 17 October 2022
Published: 25 October 2022

Publisher's Note: MDPI stays neutral with regard to jurisdictional claims in published maps and institutional affiliations.

1. Introduction

Continuous casting technology is the primary method of producing semi-finished steel products, and over 96% of the world's steel is made using this process [1]. One of the most important features of continuously cast strands is their surface quality, which is mainly controlled by initial solidification at the meniscus [2–4]. In this region, the solidifying shell is subjected to complicated thermal and mechanical loading conditions [5] which may lead to formation of surface defects such as depressions [6], oscillation marks [7,8], and cracks [9,10].

Understanding the root causes of surface defect formation is the main key to control the strand surface quality [11,12]. It is well known that steel grade is the most critical parameter that affects depression severity [4,11,13,14]. Ultra-low carbon steels (<0.005%C) suffer from poor surface quality [5], and steels which undergo the peritectic transformation (~0.09 < %C <~0.17) and experience "peritectic behavior" [15] exhibit the deepest surface depressions, with a peak in severity typically observed around 0.10%C [16,17], depending on the other alloying elements [15]. Surface depressions during steel solidification are responsible for many other surface defects [18–21] and often have been attributed to the shrinkage associated with the δ-ferrite to austenite solid-state phase transformation [22].

During continuous casting, initial solidification at the meniscus is influenced by many complicated transient phenomena such as mold oscillation [21], slag infiltration [23], movement of the slag rim [24], turbulent fluid flow [25], liquid surface level drops [26], liquid overflow of the shell tip [27], and surface tension effects [28], in addition to the high local heat flux and thermal distortion [11]. These all cause transient changes to the meniscus shape and affect the final shape of the surface of the solidified shell including surface depressions [5]. Thus, it is almost impossible to isolate the effect of thermal deformation due to phase transformation on the final surface shape. To this end, laboratory experimental methods have been developed to characterize the surface shape variations

with steel grade during initial solidification, such as the "dip test" [29] in which a copper chill block is immersed into a liquid steel bath for a short time. Visualizing and measuring the roughness of the thin steel shell that solidifies onto the plate provides an indication of the susceptibility of the steel grade to surface depressions during casting. Another simple experiment, the "droplet test", was proposed by Dong and coworkers [30–32] in which a small liquid steel droplet is placed on a chill plate and the free deformation of the bottom of this droplet is measured. In spite of its differences with the actual production method, the effect of steel grade on the surface shape was found to match with experience in commercial continuous casters. Thus, the effect of thermal distortion on solidifying shell shape under a sharp temperature gradient can be isolated and studied using the droplet test.

Previously, the droplet test was used to investigate the effect of carbon content on free deformation during steel droplet solidification [31]. Small liquid steel droplets of 4–8 g were levitated and dropped 35 mm onto a water-cooled chill plate made of either graphite for slow cooling, or copper for fast cooling. After solidification and cooling to room temperature, the bottom surface of the droplets took a parabolically-curved shape, indicating that a gap formed between the bottom surface and the chill plate. The bottom surface of each solidified droplet was fitted to a parabola and the curvature was characterized with a single fitting parameter, N_d:

$$\text{gap} = N_d R^2 \quad (1)$$

where R is the horizontal distance from the center of the droplet bottom surface. The curvature of the bottom surface was measured for different grades and droplet sizes [31,32]. It was found that the bottom surface curvature is controlled by the composition, with two peaks: at near pure iron (carbon content is almost zero) and at around 0.12%C. Positive curvature (gap increasing with R) was observed in all small droplets with < 0.6%C. In addition to steel grade, the heat transfer rate between the solidifying droplet and chill plate has a great effect on thermal distortion. The measured curvatures of the droplet bottom surface solidified onto a copper chill plate are much larger than those on a graphite chill plate, especially with peritectic steels [31,32]. This is because the average heat transfer coefficient at the steel shell/graphite chill plate interface is about one third of that at the steel/copper interface [31].

Several computational models of thermal-mechanical behavior of steel during initial solidification have been developed in previous works [26,33–44]. Analytical solutions of thermal stress during solidification have predicted air gap formation during the casting process, including the effects of mold taper and superheat, but these simple models neglect the effects of alloy solidification range, solid-state phase transformations, plasticity and creep [35,36,39]. Advanced computational models based on numerical methods such as the finite element method, are able to include these effects with realistic temperature-dependent thermal and mechanical properties. Several such models have investigated gap formation during steel continuous casting in the mold [26,41–43,45–52], and many of them have shown that shell shrinkage is greatest towards the mold corners, which generates large gaps between the shell and mold there [42,43,45–47]. These gaps become filled with mold flux, [40,47] leading to lower heat transfer [40], hot spots [41] and longitudinal depressions [45,47] on the shell surface in the off-corner regions of the strand. Shell shrinkage in the mold was found to decrease with increasing casting speed, owing to the decreased time in the mold, leading to a hotter, thinner shell, [42] so less taper is required to compensate for the shrinkage [53].

Other such thermal-mechanical finite-element models have been applied to investigate sudden liquid level drops during the continuous casting process on thermal distortion of the shell during initial solidification and surface depression formation [26,33]. These models showed that shell tip distortion increases with increasing level drop and is largest for ultra-low carbon and peritectic steels [26,33].

Parkman et al. [34] simulated thermal distortion of solidifying steel droplets with an elastic-viscoplastic finite element model including the effect of phase transformation strains. Simulations showed that the gap forms and reaches its maximum depth at very early stages

of solidification (within 0.1 s). Based on temperature measurements during the droplet test [31], the heat transfer coefficient dropped suddenly from 17.8 to 5.0 kW/m^{2}K. The transition was postulated to occur when the solid layer gained sufficient strength to support the ferrostatic pressure and bend away from the chill plate [30,31]. Suddenly dropping the heat transfer coefficient in the simulation from 20 to 5 kW/m^{2}K after 0.05 s was found to increase the droplet surface curvature (gap depth) [31]. Increasing the heat transfer coefficient or decreasing the transition time both increased the gap depth [31]. Similar to the experimental work in [31], their model investigation of the effect of carbon content on gap depth revealed two peaks at nearly pure iron (0.003%C) and 0.12%C (peritectic steel) [34]. However, despite predicting the gap depth trend with carbon content very accurately, the magnitude of the simulated gap depths (surface curvatures) [34] was much higher than measured [31].

The solid state $\delta \rightarrow \gamma$ phase transformation has been established to be the main cause of surface depressions and the associated surface quality problems in continuously cast steel products. However, no previous fundamental model appears to be able to quantitatively predict the steel surface shape under the heat transfer conditions of continuous casting. Accurate prediction of the severity of surface depressions for a specific steel grade under real conditions would enable appropriate action(s) to be taken at the caster to improve surface quality. The aim of this work is to study the effects of steel grade (carbon content) and heat flux conditions on shrinkage and thermal distortion of a solidifying steel droplet. The same conditions as in the experimental droplet test [31] are used for the simulations, and predictions of the curvature of the bottom surface of the droplet are validated with the measurements. Furthermore, the effect on this behavior is investigated to reveal new insights into thermal distortion during initial solidification.

2. Model Description

The computational model used in this work to model initial thermal-mechanical behavior of steel during initial solidification, including the simulation domain, heat transfer model, stress model, and solution details are described in this section.

2.1. Model Domain and Boundary Conditions

Thermal distortion of a steel droplet is simulated with a cylindrical domain for the conditions of the experimental droplet test [31]. In the experimental study, 4 g steel samples of 10 mm-diameter steel rod with different carbon contents were re-melted in a levitation coil and dropped on the surface of a chill plate which was 35 mm below the coil. To investigate the effect of heat flux on surface distortion, two different chill plates, (copper chill (cc) and a graphite chill (gc)) were used [31]. In the current study, a two-dimensional axisymmetric finite-element model is used to simulate the thermal-mechanical behavior of the solidifying droplet. A micrograph of a typical solidified droplet is shown in Figure 1, together with the simulation domain and its finite-element mesh in red, deformed (at 1:1 scale) to show the final distorted shape. The cylindrical domain has 5 mm radius and 6 mm height which weighs 4 g, considering the steel density of 7.8 kg/m^3. The effect of droplet size and shape is explored in the last section. Heat flux is applied uniformly on the bottom surface and the other surfaces are insulated. There is no mechanical constraint on the domain surfaces, so they can deform freely.

Thus, the surfaces are stress free, except for a surface traction equivalent to the gravitational body force, ρgh, applied on the bottom surface. This effectively pushes the thin solidifying steel shell towards the chill plate, according to the liquid pressure above it. Applying this pressure at the bottom avoids convergence problems associated with loading the weak liquid, while having negligible effect on the results.

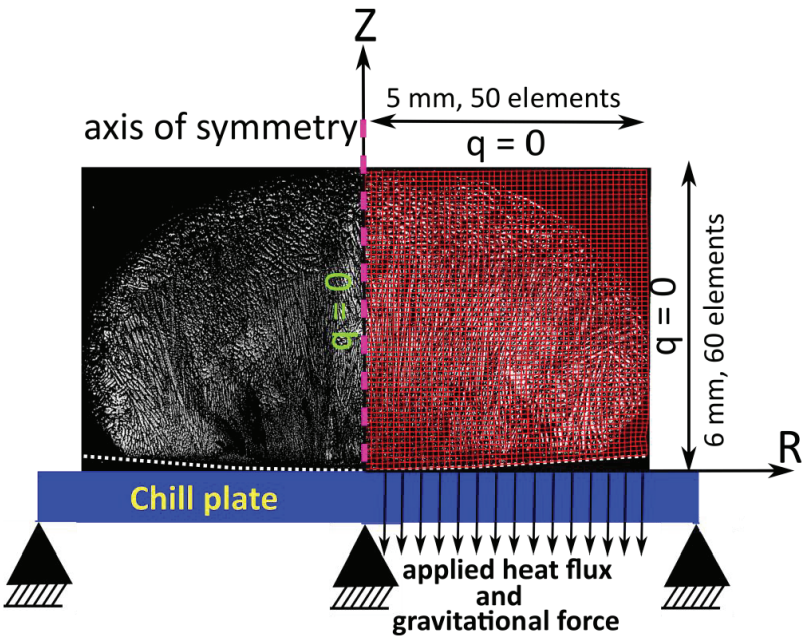

Figure 1. Cross section of the droplet showing the deformed simulation domain after solidification (red mesh) superimposed on the real solidified droplet.

2.2. Heat Transfer Model and Applied Heat Flux

The two-dimensional transient heat conduction equation is solved for the temperature field of the solidifying droplet in cylindrical coordinates:

$$\rho\left(\frac{\partial H}{\partial t}\right) = \nabla\cdot(k\nabla T) \tag{2}$$

In this equation, ρ is temperature-dependent mass density, (kg/m^3) H is temperature-dependent specific enthalpy (J/kgK) which includes the latent heats of phase transformations, t is time (s), k is isotropic temperature-dependent thermal conductivity, (W/mK) and T is temperature (°C).

Heat flux is applied on the bottom surface in Figure 1, and the other three surfaces are insulated. The initial temperature of the domain for each steel grade is set to be 10 °C above the liquidus temperature (i.e., constant superheat) to facilitate fair comparison of steels with different carbon contents.

As a curve fit of measurements on typical slab casters, [44] instantaneous heat flux during continuous casting can be represented as a function of time by $\dot{q}_{standard} = \frac{6.36}{\sqrt{t}+1.032}$ (MW/m^2). This standard heat flux (SHF = $\dot{q}_{standard}$) and high heat flux (HHF = $2\dot{q}_{standard}$) conditions were used in this work to investigate the effect of heat flux during continuous casting on thermal distortion. More realistically, the droplet usually experiences a transition in heat flux (THF), where the heat transfer coefficient (h) in the heat convection equation ($\dot{q} = h\Delta T$) drops (e.g., from 17.8 to 5.0 kW/m^{2}K at 0.06 s) at the solid shell/chill plate interface, once the solid shell starts to deform [32]. This sudden decrease of heat transfer coefficient is due to the formation of an air gap at the shell/plate interface between the solidifying steel shell and the chill plate. In order to compare the simulation results of this work with the measurements in [31], the instantaneous heat flux for the validation cases was set to suddenly drop from $3.2\dot{q}_{standard}$ to $\dot{q}_{standard}$ at t = 0.06 s, which approximates the time when the solid shell starts to bend away from the chill plate. This THF case was

chosen to match exactly with the conditions of 17.8 to 5.0 kW/m^{2}K at t = 0.06 s reported in the experimental paper [31].

2.3. Stress Model

During solidification, strains are in the order of only a few percent, so it is reasonable to adopt the small strain assumption. The mechanical behavior of the solidifying steel droplet is governed by the quasi-static momentum balance equation:

$$\nabla \cdot \underline{\underline{\sigma}} + b = 0 \tag{3}$$

where $\underline{\underline{\sigma}}$ is the second-order Cauchy stress tensor, and b is an applied body force which is equal to zero in this work [43,44].

The total strain rate is divided into elastic ($\dot{\varepsilon}_{el}$), inelastic ($\dot{\varepsilon}_{ie}$), thermal ($\dot{\varepsilon}_{th}$), and fluid strain ($\dot{\varepsilon}_{fl}$) components.

$$\dot{\varepsilon} = \dot{\varepsilon}_{el} + \dot{\varepsilon}_{ie} + \dot{\varepsilon}_{th} + \dot{\varepsilon}_{fl} \tag{4}$$

where inelastic strain includes the effects of time-independent plasticity and creep. The fluid strain is the inelastic strain generated while the steel is liquid. Fluid strain represents a measure of liquid feeding to accommodate thermal shrinkage of the solidifying shell. Stress and strain are related by phase-dependent unified constitutive equations. The liquid phase is considered as a perfectly-plastic material with elastic modulus of 1 GPa, Poisson's ratio ν = 0.3 and σ_{yield} = 10 kPa. The δ-ferrite phase is modeled with the Zhu modified power law [44], and the austenite phase uses model III from Kozlowski [54]. Further details on the formulation of this thermal-mechanical finite-element model are given elsewhere [43,44].

2.4. Phase Fractions and Thermal Properties

In this work, six steel grades with different carbon weight percent of 0.003%, 0.05%, 0.10%, 0.12%, 0.16% and 0.23%, were examined. The mass fractions of liquid, δ-ferrite, and austenite (γ) for each steel are calculated as a function of temperature and steel composition, using the lever rule, as plotted in Figure 2. The phase diagram used in this work is a pseudo-binary phase diagram which is constructed based on 15 points in temperature-composition space that changes with alloying elements [43]. A rule for multicomponent ternary systems is applied in the non-equilibrium three-phase region [44]. In this model, complete mixing of solute elements in the liquid phase and local equilibrium at liquid-δ, liquid-γ and δ-γ interfaces is assumed to calculate phase fractions. Thus, non-equilibrium thermal undercooling effects are neglected.

Temperature dependent properties include thermal conductivity, enthalpy, mass density and thermal linear expansion, as shown in Figure 3, and are calculated using the method presented by Li and Thomas [43]. In mixed phase regions, specific heat, thermal linear expansion, and enthalpy are calculated using a weighted average (mixture rule) based on the mass fraction of the phases present at that temperature [43]. The thermal linear expansion (TLE) function for each phase is obtained from measurements of the solid-phase mass density [44,55] and liquid density [56]. Further details on the TLE calculation can be found elsewhere [44].

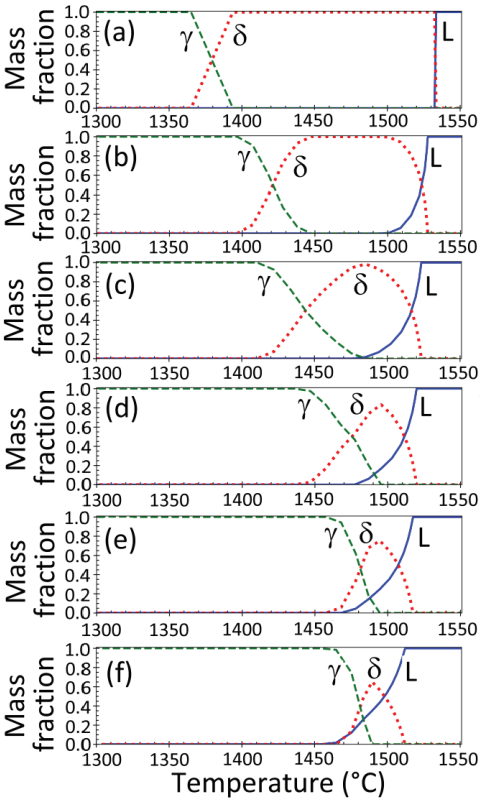

Figure 2. Phase fractions for six different examined steel grades: (**a**) Fe-0.003%C; (**b**) Fe-0.05%C; (**c**) Fe-0.10%C; (**d**) Fe-0.12%C; (**e**) Fe-0.16%C, and (**f**) Fe-0.23%C.

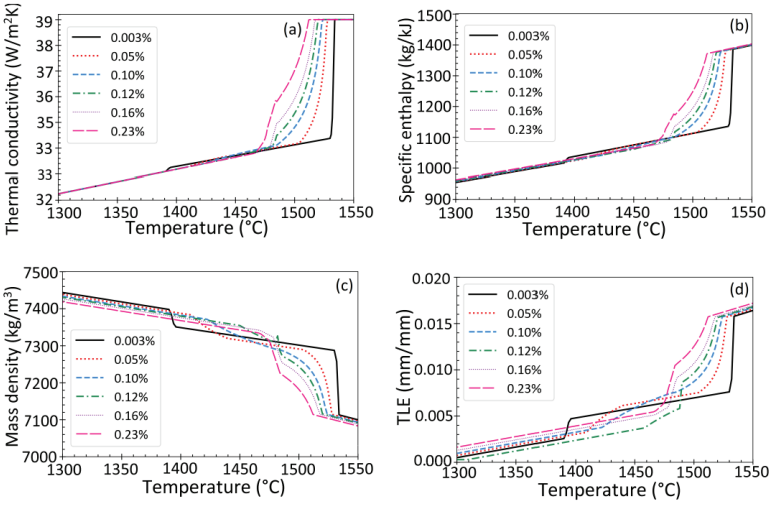

Figure 3. Temperature-dependent properties of six steel grades investigated: (**a**) thermal conductivity; (**b**) specific enthalpy; (**c**) mass density, and (**d**) thermal linear expansion.

2.5. Numerical Details

ABAQUS/Standard (implicit) [57] was used to solve the governing equations in two steps: the heat transfer analysis followed by the mechanical analysis. The ABAQUS user subroutine DFLUX [58] was used to apply the heat flux boundary condition. The calculated temperature field at each time step is an input to the mechanical analysis to calculate the thermal strain. Four-node axisymmetric convection/diffusion quadrilateral elements (DCCAX4) and 4-node hybrid, bilinear axisymmetric quadrilateral, constant pressure elements (CAX4H) were used for the thermal and stress analyses, respectively. The time step size varied from 0.0001 to 1 s, and was controlled to keep the maximum temperature change per time step within 50 K.

2.6. Mesh Resolution study and Model Verification

The finite element mesh, shown in Figure 1, consists of 50 × 60 elements, with a constant element size of 0.1 mm. This mesh refinement was chosen based on a convergence study conducted for temperature, stress and distortion results for low-carbon steel. In this study, LC steel (0.05%C) with standard heat flux was simulated with different element sizes, (1, 0.5, 0.2, 0.1, and 0.05 mm), keeping the element aspect ratio (in radial r and height z directions) fixed at 1 (square elements). Figure 4 shows results at the centerline symmetry axis for the five different mesh refinement cases after 5 s of solidification with the SHF cooling condition. Although larger elements (1, 0.5, and 0.2 mm) can accurately reproduce the temperature history, shown in Figure 4a, a much more refined mesh is needed to resolve the stress and strain behavior, shown in Figure 4b–d. The inelastic strain results, shown in Figure 4c, are the least accurate, especially near the chill surface. Only meshes with 0.2-mm elements or smaller (60 and 120 elements through droplet height) predict the strain profile accurately. Results for these meshes with 0.1 mm and 0.2 mm elements all match everywhere within 1%. Thus, the 50 × 60 element mesh, with 0.1 mm elements, was chosen for the rest of this work. The model was also verified with the well-known analytical solution for thermal stress during unconstrained plate solidification by Boley and Weiner [59], as documented elsewhere [44].

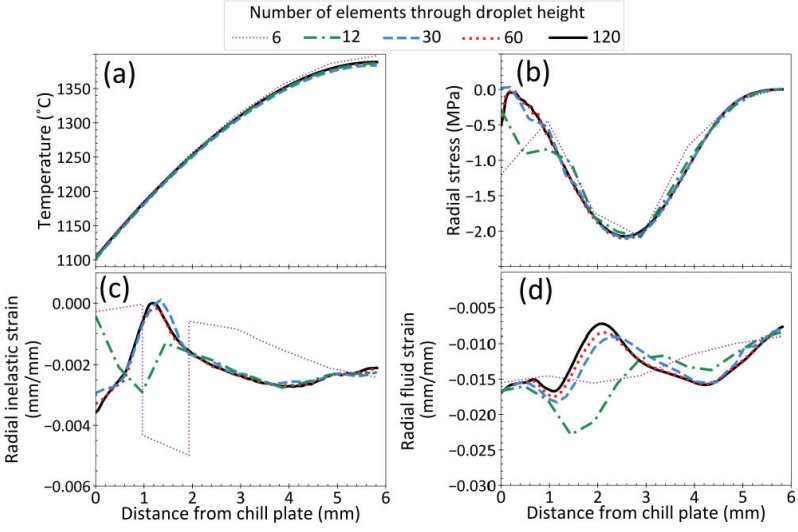

Figure 4. Mesh convergence study results through droplet height at centerline symmetry axis for low-carbon steel (0.05%C) at 5 s with SHF: (**a**) Temperature; (**b**) Radial-stress; (**c**) Radial inelastic strain; (**d**) Radial fluid strain.

3. Results

Carbon content and cooling conditions are investigated here as the main factors that influence thermal distortion during steel solidification. The effects of these parameters on temperature distribution, stress distribution and gap formation during solidification of the steel droplet are discussed in the next sections.

3.1. Temperature Distribution

Figure 5a shows temperature profiles through the droplet height after 1 s of solidification for different carbon contents and heat fluxes. For a given heat flux profile, it can be seen that the temperature profile through the droplet for all the examined cases is almost the same with temperatures within ~15 °C. This demonstrates how steel grade has little direct effect on properties and heat transfer, for the same gap profile. Also, it is evident that the temperature gradient with HHF is much steeper than SHF and THF after the transition to lower heat flux. At very early times (≤0.06 s), the temperature gradient with THF is steeper.

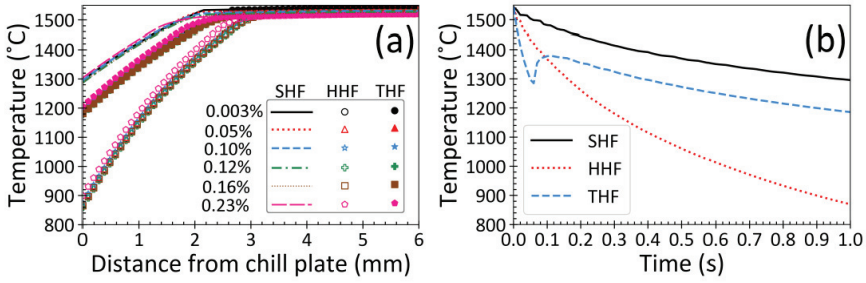

Figure 5. (**a**) Temperature profile through the droplet height calculated at centerline symmetry axis after 1 s of solidification for six steel grades and different heat fluxes, and (**b**) Evolution of bottom surface temperature with time for steel with 0.003%C and different heat fluxes.

Figure 5b shows temperature evolution of the bottom surface for different heat flux profiles, choosing 0.003%C steel as representative. With SHF and HHF, the surface temperature decreases continuously with time, while with THF, the bottom surface temperature increases by 94 °C after the drop in the heat flux. This reheating of the bottom surface takes place because the heat from inside the droplet is conducted to the surface faster than it can be removed. This demonstrates that such recoalescence behavior can be explained solely by the droplet surface lifting up from the chill plate, and does not require nonequilibrium undercooling during solidification (which is neglected in the current model).

Table 1 presents phase transformation temperatures for the 6 investigated alloys, in addition to the time when the bottom surface reaches the solidus and $\delta \rightarrow \gamma$ transformation temperatures, the droplet solidification time when the top surface reaches the solidus temperature, and the incubation time (introduced in Section 3.5). It takes 18 s, 8 s and 17 s for the bottom surface to reach 300 °C (final state at end of simulation) for the SHF, HHF and THF cases. With THF, the sudden drop in heat flux which accompanies gap formation results in surface reheating, thermal expansion of the surface layer, and a very large increase in the gap depth for all steel grades.

The average heat transfer coefficient can be extracted from these results, based on the bottom surface temperature in Figure 5b and choosing a chill plate temperature, such as 200 °C. From the instantaneous heat flux, $\dot{q} = h\Delta T$, the average heat transfer coefficient, h, in the first 1 s is calculated to be 4.4 kW/m^2 °C for SHF and 11.4 kW/m^2 °C for HHF. With THF, h drops from 16.8 to 4.7 kW/m^2 °C after the first 0.06 s, which is very similar to the experimental measurements for pure iron [31].

Table 1. Phase transition temperatures and times when droplet surfaces reach these temperatures for six investigated steels at different cooling conditions.

Carbon Content (wt%)	Liquidus Temp. (°C)	Solidus Temp. (°C)	δ→γ Transformation Start Temp. (°C)	Heat Flux Case	Time Bottom Surface Reaches Solidus Temp. (s)	Time Bottom Surface Reaches δ→γ Temp.(s)	Incubation Time (s)	Time Top Surface Reaches Solidus Temp. (s)
0.003%C	1532	1532	1393	SHF	0.01	0.38	0.40	4.3
				HHF	<0.01	0.08	0.05	2.4
				THF	<0.01	0.02	0.01	3.2
0.05%C	1528	1500	1445	SHF	0.05	0.19	0.52	4.7
				HHF	0.01	0.04	0.15	2.7
				THF	<0.01	0.02	0.06	3.3
0.10%C	1525	1480	1481	SHF	0.09	0.09	0.30	4.8
				HHF	0.02	0.02	0.10	2.7
				THF	0.01	0.01	0.04	3.6
0.12%C	1521	1479	1494	SHF	0.08	0.05	0.26	4.8
				HHF	0.02	0.01	0.07	2.7
				THF	0.01	<0.01	0.03	3.7
0.16%C	1519	1470	1494	SHF	0.09	0.04	0.28	4.8
				HHF	0.03	0.01	0.08	2.8
				THF	0.01	<0.01	0.04	3.8
0.23%C	1514	1463	1491	SHF	0.12	0.03	0.57	5.8
				HHF	0.03	0.01	0.21	2.9
				THF	0.01	<0.01	0.06	3.8

3.2. Stress Distribution

Radial stress profiles through the droplet height at different times are presented in Figure 6a for the 0.10%C steel and HHF cooling conditions. After 1 s of solidification, slight tension is generated along the droplet surface due the cooling shrinkage, and the interior is under slight compression. This may increase the risk of surface crack formation and this issue is more severe in peritectic steels.

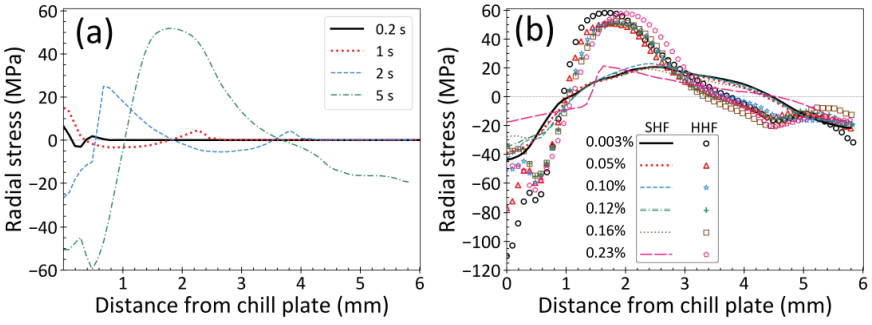

Figure 6. Radial stress profiles through the droplet height calculated at centerline symmetry axis. (**a**) Evolution with time for 0.10%C steel with HHF, and (**b**) Final profiles for six examined steels and different heat fluxes.

With further cooling to 2 s, the stress profile reverses to compression along the bottom surface and tension in the interior. This reversal to the classic solidification stress profile is due to the most recently solidified steel towards the interior cooling and shrinking faster than the surface, as explained in previous work [44]. This stress profile naturally produces thermal distortion and gap formation that exhibits positive curvature of the droplet bottom surface.

At the end of solidification, at ~5 s for HHF, both the top and bottom surface layers are under compression with a balancing tension in the central part of the droplet. The average stress through the cross section must always equal zero, as the droplet exterior is unconstrained. Further cooling increases the stresses, but causes little further thermal distortion and gap depth increase, owing to the tension at the top surface being similar to that at the bottom.

Figure 6b compares the final stress state after the bottom surface temperature reaches 300 °C for the different steel grades for both SHF and HHF conditions (i.e., 18 s for SHF and 8 s for HHF). The HHF case generates the maximum compression at the bottom surface, that is 50% more than that of the SHF case. Furthermore, the maximum tension in the interior with HHF is almost 150% greater than with SHF. These results show that increasing heat flux increases stress gradients in the droplet.

3.3. Strain Distribution

Figure 7 shows the final radial strain distribution through the droplet height at centerline symmetry axis when the bottom surface is 300 °C with SHF cooling condition. With no external load except gravity, the strains are all very small and thermal strain dominates the mechanical behavior. This strain is entirely shrinkage (negative), and increases towards the droplet bottom surface to a maximum of 2.4%. The strain needed to accommodate fluid flow is also very important and reaches almost 1% as liquid is pushed out of and into the domain. Initially, the radial fluid flow is positive, as radial shrinkage from solidification decreases the cross-sectional area of the droplet and squeezes liquid upward. Later, the radial fluid flow becomes negative, as cooling and general shrinkage of the droplet draws liquid back down into the middle of the domain. This fluid flow is responsible for macrosegregation, which is obviously tiny in a droplet with such small strains. The mismatch between thermal strains causes inelastic strains, which although they are tensile, are also small, <0.2%, so cracks, even hot tears, will not happen. The mismatch also causes elastic strains, which are very small, but critical, because they are directly responsible for the stresses. Creep lessens the elastic strains with time, but time is short, which partly explains why inelastic strains are small. Elastic and inelastic strains are also small because the shell can bend to accommodate them, rather than building up strain and stress which occurs in larger castings which have more constraints.

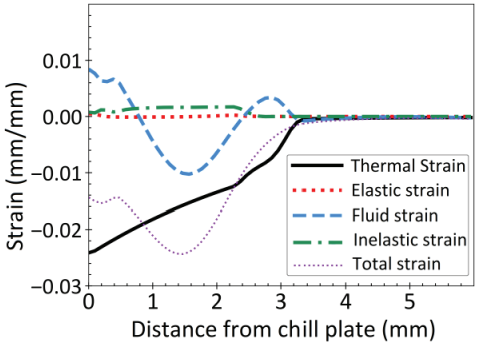

Figure 7. Final radial strain profile through droplet height calculated at centerline symmetry axis with SHF for 0.10%C steel.

3.4. Thermal Distortion and Model Validation

Figure 8 shows the gap depth profiles of the solidified droplet for the six steels investigated for the three different heat flux conditions. The shape of the bottom surface in all cases is a parabola with different positive curvatures. The gap depth is largest in the peritectic steels, especially those containing 0.10%C and 0.12%C, with 0.16%C almost as deep. The ultra-low carbon steel (0.003%C) also experiences a very deep gap, especially with HHF.

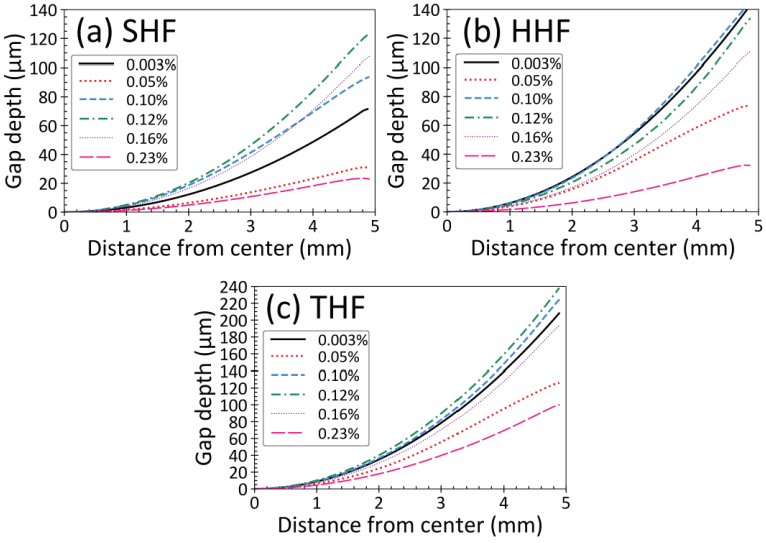

Figure 8. Gap depth profiles for six steel grades investigated and different heat fluxes at time when bottom surface temperature is 300 °C: (**a**) SHF; (**b**) HHF; and (**c**) THF.

The low-carbon steels (0.05%C) and high-carbon steels, 0.23%C, consistently have shallow gaps. This trend of gap depth change with carbon content agrees with the experimental measurements [11,18].

Figure 9 compares the simulated curvatures of the bottom surface, (N_d in Equation (1) fitted from the results in Figure 8 in this work), with the droplet test measurements on the copper and graphite chill plates [31]. The simulated results with THF, which correspond closely with the experimental heat flux conditions on the copper chill plate (Exp-cc), match very well with the measurements, both qualitatively and quantitatively. In addition, the model predictions at lower cooling rate, SHF, match reasonably well with the experimental measurements on the graphite chill plate (Exp-gc). Of greatest significance, the model accurately captures the complicated trend with steel grade, where thermal distortion of the droplet bottom surface is greatest for peritectic and ultra-low carbon steels.

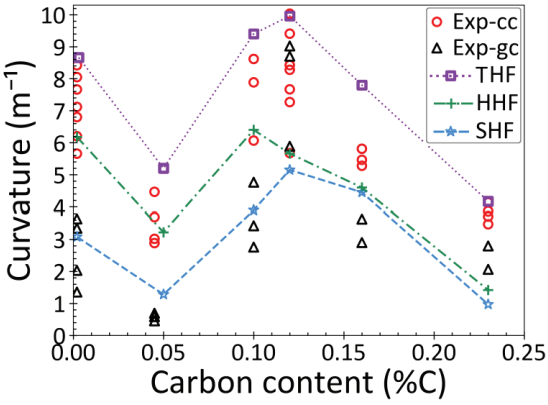

Figure 9. Comparison of predicted (lines) and measured (symbols: Exp-cc and Exp-gc) curvature of the bottom surface of the solidified droplets for six steel grades investigated with different heat flux profiles.

It should be noted that the experiments were repeated several times for each steel grade, and the measured curvatures exhibit significant variations, most likely due to variability in the heat flux conditions. Nevertheless, the agreement demonstrates that the current computational model captures the phenomena that govern thermal distortion during initial solidification, and that determine the shape of the final surface during steel casting.

3.5. Effect of Heat Flux Condition

Figure 9 contains many results showing the effect of heat flux profile on the thermal distortion results. The gap depths are all significantly higher with THF, where the heat flux drops from $3.2\dot{q}_{standard}$ to $\dot{q}_{standard}$ at $t = 0.06$ s. This shows that the high initial heat flux has a great effect in generating thermal distortion, even though it lasts for only a very short time. The SHF and HHF cases with constant heat flux generate much lower gap depths, even though the HHF heat fluxes and cooling rates greatly exceed those of THF for all times after 0.06 s. This shows that regardless of steel grade and heat flux, the air gap forms and grows mainly during the very early stage of solidification. Thus, the final gap depth is very sensitive to the initial heat flux, while the later heat flux has little effect.

Figure 10 shows the evolution of the gap depth for the two most depression-sensitive steels, 0.003%C and 0.12%C, with different heat flux conditions. For all cases, the gap develops in three distinct stages. At the start of solidification, the gap depth remains at zero for a time period called "incubation time" in this paper. During this first stage, the steel shell is too weak to support even the small ferrostatic pressure from the liquid above it, so stays flat against the chill plate. The incubation time depends greatly on both steel grade and heat transfer coefficient, as shown in Table 1, and greatly affects the final gap depth. After this incubation time, the shell has strengthened enough to overcome gravity and lift off of the plate. The gap grows very rapidly for a short time during this second stage: "growth". Finally, there is a long third "steady-state" stage, when the gap remains relatively constant.

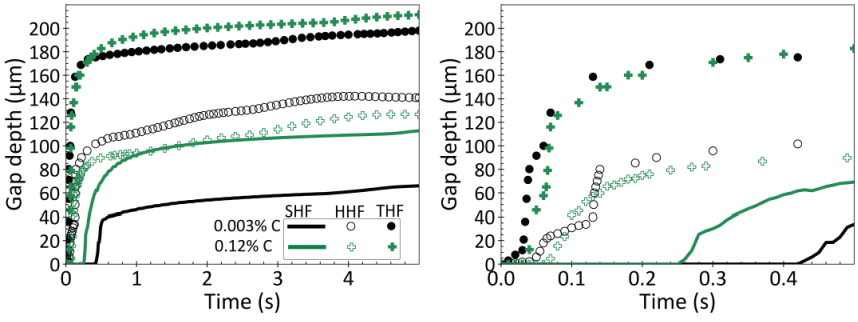

Figure 10. Gap depth evolution with time, comparing steels with 0.003%C and 0.12%C at different heat fluxes.

By increasing the heat flux from SHF to HHF, Figure 9 shows that the gap depths (and corresponding curvatures) of steels with the lowest carbon contents, 0.003%C, 0.05%C and 0.10%C, increase significantly: by 100%, 140% and 100%, respectively. In contrast, the gap depths increase only slightly (12%, 5%, and 18%) for the other three grades, which have higher carbon content. Thus, there appears to be a general decrease in sensitivity to the higher heat flux with increasing C content, causing the jump in gap depth to decrease with increasing C content.

The higher sensitivity to heat flux in steels with carbon content less than 0.1%C stems from the different phase transformation sequence in these steels, compared with higher carbon steels. As can be seen in Figure 2a–c steels with $\leq$ 0.1%C solidify completely as δ-ferrite before transforming to austenite. In these steels, by increasing heat flux from SHF to HHF, the δ-ferrite becomes thick enough to overcome ferrostatic pressure sooner, which

in turn decreases the incubation time and increases the gap depth considerably. On the other hand, in steels with higher carbon content, the liquid partly transforms to δ-ferrite and then the remaining liquid solidifies as δ-ferrite and austenite via the peritectic reaction. The incubation time always occurs after the start of the δ→γ phase transformation, as shown in Table 1, except for 0.003%C steel, where this transformation is delayed. Increasing heat flux from SHF to HHF causes this transformation to occur sooner, as observed in Figure 10 for 0.12%C steel. With THF, the incubation time occurs even sooner after the δ-γ transformation starts, especially for peritectic or partly-peritectic steels.

Further increasing the initial heat flux from HHF to THF causes the final gap depth to increase by about 100% for all grades. This is due to the large decrease in incubation time in all cases, caused by the high initial heat flux of THF.

3.6. Effect of Steel Composition

Depression sensitivity varies greatly with steel grade, as indicated by the final surface shape (curvature), shown in Figure 9. Figure 10 shows that, for the ultra-low carbon steel (0.003%C) with SHF, the incubation time is relatively long, 0.4 s, at which time the gap depth increases to 38 μm over 0.1 s. This long incubation time is due to the weakness of the pure delta-ferrite initial shell, which is also very hot and thin due to the low heat flux, so it cannot overcome gravity during this long initial stage of solidification. The gap only starts to grow when austenite starts to form, after the surface has cooled to just below 1390 °C. With HHF, the solidified δ layer thickness increases faster, enabling the shell surface to cool and gain strength sooner, so the incubation time is only 0.05 s. This leads to an initial gap depth of 90 μm, which is more than twice as deep as with SHF. Further increasing the initial heat flux from HHF to THF further decreases the incubation time to only 0.01 s, which doubles the initial gap depth again. This steel has a very short solidification temperature range compared with all other steels. Thus, this steel can solidify more solid, for the same heat transfer and time, which enables the solid shell to become thicker and stronger, even though it is composed of soft delta-ferrite. Thus, this steel has the second highest gap depths and sensitivity to surface depressions of all steel grades investigated.

For 0.12%C steel with SHF, the incubation time is only 0.26 s and the gap quickly grows to an initial depth of 81μm. This incubation time is shorter than that for ultra-low carbon and is due to the formation of the strong austenite phase very quickly after the start of solidification. For this steel, δ-ferrite is only stable for a 20 °C range, and quickly transforms to austenite via the peritectic reaction and subsequent peritectic transformation. Austenite is almost one order of magnitude stronger than δ-ferrite at the same temperature [60]. Thus, the solidified layer of 0.12%C steel quickly transforms to austenite, is strong enough to overcome ferrostatic pressure, and forms a gap very soon after the start of solidification. With HHF conditions, the incubation time is only 0.07 s for steel with 0.12%C steel. After this incubation time, the gap depth suddenly increases to 91μm. Increasing heat flux from SHF to HHF has little effect on gap depth because the incubation time to strong austenite formation is short in both cases. Further increasing initial heat flux to THF conditions, the incubation time decreases to only 0.03 s and the gap depth increases to the largest final depth of 190 μm. As mentioned earlier, surface depressions during steel solidification are attributed to the shrinkage associated with the solid-state δ→γ phase transformation. In 0.12%C steel this transformation coincides with a sudden drop in TLE (from 0.008 to 0.006) at 1490 °C (see Figure 3). Because the new phase is the strong γ-phase (almost 10 times stronger than δ-ferrite), the transformed austenite layer can overcome ferrostatic pressure even when it is very thin, (after only 0.03 s), which aggravates the sudden TLE drop and deepens the gap. As a result, this peritectic steel experiences the most severe gaps and sensitivity to surface depressions.

Figure 11 shows the evolution of the gap depth for all six investigated steels with THF, which has the highest initial heat flux. The peritectic steel, (0.12%C) transforms to austenite the fastest, so has the largest drop in TLE immediately below the solidus temperature, very short incubation time (0.03 s), and consequently exhibits the deepest gap. For low-

carbon (0.05%C), and high-carbon (0.23%C) steels, there is a greater temperature from the solidus to the start of transformation to austenite (see Figure 3d and Table 1). This delay in the shrinkage (TLE drop), causes the shells of these steels to remain weak for a longer incubation time (0.06 s). The longer incubation time causes smaller temperature gradients across the thin initial shell, leading to the smallest final gaps, and the least propensity towards surface depressions. The partly-peritectic steels (0.10%C and 0.16 %C) quickly transform to austenite, so have incubation times of only ~0.04 s, and thus these steels develop gaps almost as deep as the fully-peritectic steel of 0.12%C steel.

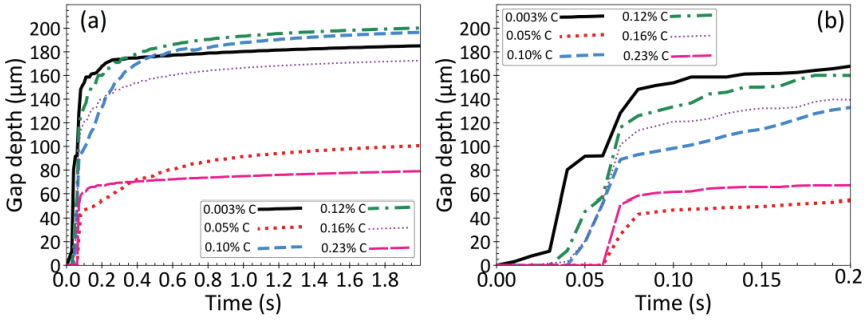

Figure 11. Gap depth evolution with time, with THF, for the six investigated steel grades, (**a**) for short times 0–2 s; (**b**) for very short times 0–0.2 s.

These results show that the gap increases when the δ→γ transformation occurs sooner, (closer to the solidus temperature) and experiences the associated large drop in TLE when the shell is thinner. Ultra-low carbon steel has the shortest incubation time of 0.01 s and its gap depth is close to that of 0.12%C steel.

It should be noted that with THF, for all grades, heat flux drops at 0.06 s and the gap depth forms at either this time or earlier, (see incubation times in Table 1). With HHF conditions, heat flux is constant throughout solidification and cooling, but the gap still forms at roughly this time. With HHF, the droplet solidifies much sooner than with THF, but the gap depth is deeper with THF. These results confirm that the gap depth is controlled by heat flux during the very early stage of solidification, and usually starts soon after the start of the δ→γ phase transformation. Shorter incubation times produce deeper gaps. After that, changes in gap depth are very small, regardless of the heat flux.

3.7. Effect of Droplet Size/Shape and Discussion

Finally, the effect of droplet size and shape was investigated for three different simulation domains. Figure 1 shows the 2D cylindrical simulation domain of 5 mm width and 6 mm height, used in this study to approximate the droplet shape. To investigate the importance of this approximation on the shape evolution, two more domains were simulated. Domain 2 has height decreased by half to 3 mm (same 5 mm width) and Domain 3 has width decreased by half to 2.5 mm width (same 6 mm height).

The final shape of the bottom surface and the incubation times are shown in Figure 12 for these three domains with Fe-0.10% C steel with different cooling conditions. The bottom surface profiles differ by less than 10% for a given cooling condition. Domain 2 has the largest bottom curvature, due to the smaller head of liquid metal causing less ferrostatic pressure from gravity to restrain the shrinkage. Domain 3 has the smallest curvature. Figure 12b shows that the incubation times are the same for all domains with HHF and THF conditions and differ by only ~10% with SHF.

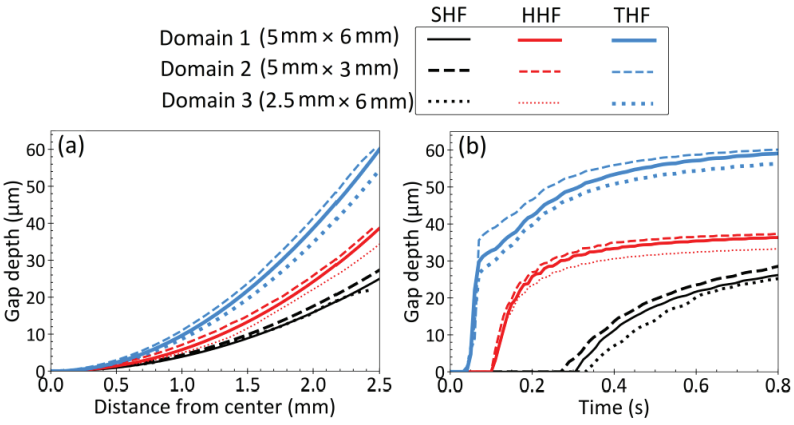

Figure 12. Effect of droplet domain shape and heat flux on gap depth for 0.10%C steel; (**a**) Final gap depth profiles; (**b**) Gap depth evolution at early times.

These results show that the size and shape of the droplet and its simulation domain have only a minor effect on the findings presented in this work. This confirms that the cylindrical approximation of the droplet shape is reasonable. The good agreement of the current model (see Figure 9) also shows that other phenomena/parameters neglected in the model, such as the contact angle between the liquid droplet and the chill surface, surface tension, and fluid flow inside the droplet, are all negligible. The only influence of these phenomena on the droplet thermal distortion mechanism is their tiny effect on the ferrostatic pressure acting on the initial solidifying shell, which can be neglected.

Furthermore, the success of the current model, with its simple treatment of the mold wall and heat transfer coefficients adopted from other research, suggests that initial solidification behavior may be generalized to other processes. Thus, these results suggest that the behaviors presented and explained in this work regarding the depths, trends and mechanisms of the formation of surface depressions during initial solidification should be similar in real commercial steel-casting processes, such as the continuous casting of steel.

4. Conclusions

The effects of steel carbon content and heat flux on the distortion of a steel droplet during solidification were investigated using a thermo-elasto-viscoplastic finite element model. Following the droplet test [31] as a benchmark experiment, the same chemical composition, geometry, and heat flux conditions were simulated to validate the model predictions of curvature of the bottom surface of the droplet with the measurements. The main findings are:

- The thermo-mechanical model captures the phenomena which govern gap formation during the initial stages of steel droplet solidification both qualitatively and quantitatively.
- Carbon content is the main factor that controls thermal distortion and bottom surface shape during steel solidification. The highest distortion, as indicated by the curvature of bottom surface of the droplet, is found in ultra-low carbon and peritectic steel grades.
- Heat flux also plays an important role in controlling thermal distortion during solidification. Increasing heat flux during the initial stages of solidification causes the gap depth (curvature of solidified droplet surface) to increase. This effect is most evident in ultralow carbon steels, and decreases with increasing carbon content, if the heat flux does not suddenly change.
- A sudden drop in heat flux typically accompanies gap formation, and is called the incubation time. This causes surface reheating, thermal expansion of the surface layer, and a very large increase in the gap depth, for all steel grades.

- Shorter incubation times lead to deeper gaps, owing to the higher temperature gradient across the thinner shell when the thermal distortion occurs.
- For every steel grade and heat flux condition investigated, the gap forms very early during solidification, within 0.06 s for fast cooling and within 0.4 s for slow cooling, and remains relatively constant after that. The heat flux rate at later times, after the first 1 s, has little effect on the final thermally-distorted shape.
- The incubation time for gap formation is usually near or after the start of the $\delta \rightarrow \gamma$ phase transformation, which is controlled by the steel grade and initial heat flux. Thus, the gap forms sooner with faster initial cooling rates, and in peritectic steels.
- The gap depth is greatly affected by the $\delta \rightarrow \gamma$ phase transformation. In peritectic steel grades, this transformation occurs very soon after a thin solid shell has formed, which leads to deep gaps, implying deep surface depressions in cast products.
- Increasing the cooling rate and temperature gradient during initial solidification increases the severity of $\delta \rightarrow \gamma$ phase transformation, and results in a deeper gap.
- The findings of this fundamental model and gap formation mechanism have important implications for the formation of surface depressions and related defects in commercial steel continuous casting processes.
- Large changes in droplet/domain shape/size have only a minor effect on the thermal-mechanical behavior and final curvature of bottom surface. Thus, the above findings are expected to be similar in commercial steel casting processes.

Author Contributions: G.A.: Conceptualization, methodology, software, formal analysis, writing—original draft. B.G.T.: supervision, conceptualization, methodology, formal analysis, Writing—review & editing, funding acquisition. M.A.Z.: Supervision, conceptualization, methodology, formal analysis, writing—review & editing, funding acquisition. All authors have read and agreed to the published version of the manuscript.

Funding: This research received no external funding.

Data Availability Statement: Raw data will be provided upon request from the corresponding author.

Acknowledgments: The authors wish to thank the contributing companies of the Continuous Casting Center at the Colorado School of Mines for funding that enabled this research.

Conflicts of Interest: The authors declare no conflict of interest.

References

1. Thomas, B.G. Review on modeling and simulation of continuous casting. *Steel Res. Int.* **2018**, *89*, 1700312. [CrossRef]
2. Brimacombe, J.K.; Sorimachi, K. Crack formation in the continuous casting of steel. *Metall. Mater. Trans. B* **1977**, *8*, 489–505. [CrossRef]
3. Lyu, P.; Wang, W.; Zhang, H. Mold Simulator Study on the Initial Solidification of Molten Steel Near the Corner of Continuous Casting Mold. *Metall. Mater. Trans. B* **2017**, *48*, 247–259. [CrossRef]
4. Wolf, M.; Kurz, W. The effect of carbon content on solidification of steel in the continuous casting mold. *Metall. Mater. Trans. B* **1981**, *12*, 85–93. [CrossRef]
5. Sengupta, J.; Thomas, B.G.; Shin, H.J.; Lee, G.G.; Kim, S.H. A new mechanism of hook formation during continuous casting of ultra-low-carbon steel slabs. *Metall. Mater. Trans. A* **2006**, *37*, 1597–1611. [CrossRef]
6. Grill, A.; Sorimachi, K.; Brimacombe, J.K. Heat flow, gap formation and break-outs in the continuous casting of steel slabs. *Metall. Trans. B* **1976**, *7*, 177–189. [CrossRef]
7. Badri, A.; Natarajan, T.T.; Snyder, C.C.; Powers, K.D.; Mannion, F.J.; Byrne, M.; Cramb, A.W. A mold simulator for continuous casting of steel: Part II. The formation of oscillation marks during the continuous casting of low carbon steel. *Metall. Mater. Trans. B* **2005**, *36*, 373–383. [CrossRef]
8. Schwerdtfeger, K.; Sha, H. Depth of oscillation marks forming in continuous casting of steel. *Metall. Trans. B* **2000**, *31*, 813–826. [CrossRef]
9. Kim, K.; Han, H.N.; Yeo, T.; Lee, Y.; Oh, K.H.; Lee, D.N. Analysis of surface and internal cracks in continuously cast beam blank. *Ironmak. Steelmak.* **1997**, *24*, 249–256.
10. Maehara, Y.; Yasumoto, K.; Tomono, H.; Nagamichi, T.; Ohmori, Y. Surface cracking mechanism of continuously cast low carbon low alloy steel slabs. *Mater. Sci. Technol.* **1990**, *6*, 793–806. [CrossRef]
11. Singh, S.N.; Blazek, K.E. Heat transfer and skin formation in a continuous-casting mold as a function of steel carbon content. *JOM* **1974**, *26*, 17–27. [CrossRef]
12. Konishi, J.; Militzer, M.; Samarasekera, I.V.; Brimacombe, J.K. Modeling the formation of longitudinal facial cracks during continuous casting of hypoperitectic steel. *Metall. Mater. Trans. B* **2002**, *33*, 413–423. [CrossRef]

13. Clyne, T.W.; Wolf, M.; Kurz, W. The effect of melt composition on solidification cracking of steel, with particular reference to continuous casting. *Metall. Trans. B* **1982**, *13*, 259–266. [CrossRef]
14. Kim, K.H.; Han, S.; Yeo, T.J.; Oh, K.H.; Lee, D.N. Effect of carbon and sulfur in continuously cast strand on longitudinal surface cracks. *ISIJ Int.* **1996**, *36*, 284–289. [CrossRef]
15. Azizi, G.; Thomas, B.G.; Asle Zaeem, M. Review of Peritectic Solidification Mechanisms and Effects in Steel Casting. *Metall. Mater. Trans. B* **2020**, *51*, 1875–1903. [CrossRef]
16. Won, Y.M.; Yeo, T.J.; Seol, D.J.; Oh, K.H. A new criterion for internal crack formation in continuously cast steels. *Metall. Mater. Trans. B* **2000**, *31*, 779–794. [CrossRef]
17. Xia, G.; Bernhard, C.; Ilie, S.; Fuerst, C. A study about the influence of carbon content in the steel on the casting behavior. *Steel Res. Int.* **2011**, *82*, 230–236. [CrossRef]
18. Suzuki, M.; Yu, C.H.; Sato, H.; Tsui, Y.; Shibata, H.; Emi, T. Origin of heat transfer anomaly and solidifying shell deformation of peritectic steels in continuous casting. *ISIJ Int.* **1996**, *36*, S171–S174. [CrossRef]
19. Bernhard, C.; Xia, G. Influence of alloying elements on the thermal contraction of peritectic steels during initial solidification. *Ironmak. Steelmak.* **2006**, *33*, 52–56. [CrossRef]
20. Bernhard, C.; Reiter, J.; Presslinger, H. A model for predicting the austenite grain size at the surface of continuously-cast slabs. *Metall. Mater. Trans. B* **2008**, *39*, 885–895. [CrossRef]
21. Badri, A.; Natarajan, T.T.; Snyder, C.C.; Powers, K.D.; Mannion, F.J.; Cramb, A.W. A mold simulator for the continuous casting of steel: Part I. The development of a simulator. *Metall. Mater. Trans. B* **2005**, *36*, 355–371. [CrossRef]
22. Zhu, L.G.; Kumar, R.V. Shrinkage of carbon steel by thermal contraction and phase transformation during solidification. *Ironmak. Steelmak.* **2007**, *34*, 71–75. [CrossRef]
23. Ramirez-Lopez, P.E.; Lee, P.D.; Mills, K.C. Explicit modelling of slag infiltration and shell formation during mould oscillation in continuous casting. *ISIJ Int.* **2010**, *50*, 425–434. [CrossRef]
24. Perrot, C.; Pontoire, N.J.; Marchionni, C.; Ridolfi, M.R.; Sancho, L.F. Several slag rims and lubrication behaviours in slab casting. *Metall. Res. Technol.* **2005**, *102*, 887–896. [CrossRef]
25. Thomas, B.G.; Najjar, F.M. Finite element modelling of turbulent fluid flow and heat transfer in continuous casting. *Appl. Math. Model.* **1991**, *15*, 226–243. [CrossRef]
26. Sengupta, J.; Ojeda, C.; Thomas, B.G. Thermal-mechanical behaviour during initial solidification in continuous casting: Steel grade effects. *Int. J. Cast Met. Res.* **2009**, *22*, 8–14. [CrossRef]
27. Harada, S.; Tanaka, S.; Misumi, H.; Mizoguchi, S.; Horiguchi, H. A formation mechanism of transverse cracks on CC slab surface. *ISIJ Int.* **1990**, *30*, 310–316. [CrossRef]
28. Mukai, K.; Zeze, M. Motion of fine particles under interfacial tension gradient in relation to continuous casting process. *Steel Res. Int.* **2003**, *74*, 131–138. [CrossRef]
29. Balogun, D.; Roman, M.; Gerald, R.E.; Huang, J.; Bartlett, L.; O'Malley, R. Shell Measurements and Mold Thermal Mapping Approach to Characterize Steel Shell Formation in Peritectic Grade Steels. *Steel Res. Int.* **2022**, *93*, 2100455. [CrossRef]
30. Dong, S.; Niyama, E.; Anzai, K.; Matsumoto, N. Free deformation of the initial solid layer of some non-ferrous alloys. *Tets Hagané* **1993**, *79*, 1060–1066.
31. Dong, S.; Niyama, E.; Anzai, K. Free deformation of initial solid shell of Fe-C alloys. *ISIJ Int.* **1995**, *35*, 730–736. [CrossRef]
32. Dong, S. Free Deformation of the Initial Solid Layer of Alloys. Ph.D. Thesis, Tohoku University, Sendai, Japan, 1995.
33. Thomas, B.G.; Zhu, H. Thermal Distortion of solidifying shell near meniscus in continuous casting of steel. In Proceedings of the JIM/TMS Solidification Science and Processing Conference, Honolulu, HI, USA, 13–15 December 1995; pp. 197–208.
34. Thomas, B.G.; Parkman, J.T. Simulation of thermal distortion of a steel droplet solidifying on a copper chill. In Proceedings of the TMS Annual Meeting, San Antonio, TX, USA, 15–19 February 1998.
35. Vynnycky, M. On the onset of air-gap formation in vertical continuous casting with superheat. *Int. J. Mech. Sci.* **2013**, *73*, 69–76. [CrossRef]
36. Florio, B.J.; Vynnycky, M.; Mitchell, S.L.; O'Brien, S. Mould-taper asymptotics and air gap formation in continuous casting. *Appl. Math. Comput.* **2015**, *268*, 1122–1139. [CrossRef]
37. Niu, Z.; Cai, Z.; Zhu, M. Dynamic distributions of mold flux and air gap in slab continuous casting mold. *ISIJ Int.* **2019**, *59*, 283–292. [CrossRef]
38. Wang, T.M.; Cai, S.W.; Xu, J.; Du, Y.Y.; Zhu, J.; Xu, J.J.; Li, T.J. Continuous casting mould for square steel billet optimised by solidification shrinkage simulation. *Ironmak. Steelmak.* **2010**, *37*, 341–346. [CrossRef]
39. Florio, B.J.; Vynnycky, M.; Mitchell, S.L.; O'Brien, S. On the interactive effects of mould taper and superheat on air gaps in continuous casting. *Acta Mech.* **2017**, *228*, 233–254. [CrossRef]
40. Cai, Z.Z.; Zhu, M.Y. Simulation of air gap formation in slab continuous casting mould. *Ironmak. Steelmak.* **2014**, *41*, 435–446. [CrossRef]
41. Cai, Z.; Zhu, M. *Simulation of Heat Transfer in SLAB Continuous Casting Mold and New Formation Mechanism of Shell Hot Spots*; Springer: Cham, Switzerland, 2016.
42. Hostos, J.C.A.; Cabrera, E.S.P.; Bencomo, A.D. Stress Analysis of a Continuous Casting Process, on the Basis of the Element-Free Galerkin Formulation. *Steel Res. Int.* **2017**, *88*, 1600019. [CrossRef]
43. Li, C.; Thomas, B.G. Thermomechanical finite-element model of shell behavior in continuous casting of steel. *Metall. Mater. Trans. B* **2004**, *35*, 1151–1172. [CrossRef]

44. Zappulla, M.L.; Hibbeler, L.C.; Thomas, B.G. Effect of Grade on Thermal–Mechanical Behavior of Steel During Initial Solidification. *Metall. Mater. Trans. A* **2017**, *48*, 3777–3793. [CrossRef]
45. Park, J.K.; Thomas, B.G.; Samarasekera, I.V. Analysis of thermomechanical behaviour in billet casting with different mould corner radii. *Ironmak. Steelmak.* **2002**, *29*, 359–375. [CrossRef]
46. Thomas, B.G.; Moitra, A.; McDavid, R. Simulation of longitudinal off-corner depressions in continuously cast steel slabs. *Iron Steelmak.* **1996**, *23*, 57–70.
47. Niu, Z.; Cai, Z.; Zhu, M. Formation Mechanism of a Wide-Face Longitudinal Off-Corner Depression during Thick Slab Continuous Casting. *Metall. Mater. Trans. B* **2021**, *52*, 2737–2752. [CrossRef]
48. Risso, J.M.; Huespe, A.E.; Cardona, A. Thermal stress evaluation in the steel continuous casting process. *Int. J. Numer. Methods Eng.* **2006**, *65*, 1355–1377. [CrossRef]
49. Kristiansson, J.O. Thermal stresses in the early stage of solidification of steel. *J. Therm. Stress.* **1982**, *5*, 315–330. [CrossRef]
50. Zuo, X.J.; Lin, R.G.; Wang, N.; Yang, J.; Meng, X.N.; Zhu, M.Y. Formation of Initial Defects at Meniscus in Oscillating Mold. *Steel Res. Int.* **2016**, *87*, 413–423. [CrossRef]
51. Hebi, Y.; Man, Y.; Huiying, Z.; Dacheng, F. 3D stress model with friction in and of mould for round billet continuous casting. *ISIJ Int.* **2006**, *46*, 546–552. [CrossRef]
52. Cai, Z.Z.; Zhu, M.Y. Thermo-mechanical behavior of peritectic steel solidifying in slab continuous casting mold and a new mold taper design. *ISIJ Int.* **2013**, *53*, 1818–1827. [CrossRef]
53. Thomas, B.G.; Ojeda, C. Ideal taper prediction for slab casting. In Proceedings of the ISSTech Steelmaking Conference, Indianapolis, IN, USA, 27–30 April 2003.
54. Kozlowski, P.F.; Thomas, B.G.; Azzi, J.A.; Wang, H. Simple constitutive equations for steel at high temperature. *Metall. Mater. Trans. A* **1992**, *23*, 903. [CrossRef]
55. Jablonka, A.; Harste, K.; Schwerdtfeger, K. Thermomechanical properties of iron and iron-carbon alloys: Density and thermal contraction. *Steel Res.* **1991**, *62*, 24–33. [CrossRef]
56. Jimbo, I.; Cramb, A.W. The density of liquid iron-carbon alloys. *Metall. Trans. B* **1993**, *24*, 5–10. [CrossRef]
57. DS SIMULIA Corp. *ABAQUS: ABAQUS 6.13 Theory Manual*; DS SIMULIA Corp.: Providence, RI, USA, 2013.
58. DS SIMULIA Corp. *ABAQUS: ABAQUS 6.13 Subroutine Manual*; DS SIMULIA Corp.: Providence, RI, USA, 2013.
59. Weiner, J.H.; Boley, B.A. Elasto-plastic thermal stresses in a solidifying body. *J. Mech. Phys. Solids* **1963**, *11*, 145–154. [CrossRef]
60. Wray, P.J. Tensile failure behavior of plain carbon steels at elevated temperatures. *Metall. Trans. A* **1984**, *15*, 2059–2073. [CrossRef]

metals

MDPI

Article

Analysis of Micro-Segregation of Solute Elements on the Central Cracking of Continuously Cast Bloom

Qiang Zeng [1], Chao Xiao [1,2,*] and Jianli Li [1,3,*]

[1] The State Key Laboratory of Refractories and Metallurgy, Wuhan University of Science and Technology, Wuhan 430081, China; zengqiang@wust.edu.cn
[2] Qingdao Special Iron and Steel Co., Ltd., CITIC Pacific Special Steel Institute Qingdao Branch, Qingdao 266409, China
[3] Hubei Provincial Key Laboratory for New Processes of Ironmaking and Steelmaking, Wuhan University of Science and Technology, Wuhan 430081, China
* Correspondence: yuyue@wust.edu.cn (C.X.); jli@wust.edu.cn (J.L.)

Abstract: On the basis of the Brody–Flemings model and modified Voller–Beckermann model, an analytical model of micro-segregation is established by considering the actual solidification cooling conditions of bloom. According to the developed model, the interdendritic solute distribution at the origin of the cracking gap is obtained. It is found that both phosphorus and sulfur have quite severe segregation, but both carbon and manganese have slight segregation; these results agree well with the semiquantitative analysis results of the scanning electron microscope (SEM). At the same time, the interdendritic segregation leads to an enhanced increase in the temperature range of crack formation; correspondingly, the possibility of cracking significantly increases and, thus, element segregation is the internal cause of crack formation. On the other hand, taking into account heat transfer, phase transformation, and metallurgical pressure, the strain of the solid shell is revealed through finite element software. When the solid shell thickness is equal to the distance of 90 mm between the opening point of the crack and the inner arc side, the tensile strain of the solid front is much bigger than the critical strain, which meets the external cause of crack formation; therefore, reasons for the cracking of blooms are successfully found.

Keywords: solute element; micro-segregation; central crack; analytical model; the strain of the solid shell

Citation: Zeng, Q.; Xiao, C.; Li, J. Analysis of Micro-Segregation of Solute Elements on the Central Cracking of Continuously Cast Bloom. *Metals* **2021**, *11*, 382. https://doi.org/10.3390/met11030382

Academic Editor: Paolo Ferro

Received: 22 January 2021
Accepted: 21 February 2021
Published: 25 February 2021

1. Introduction

Mathematical models can be used to analyze the quality of metallic materials [1]. For continuous casting bloom, central cracks are one of the major defects which appear during the casting process [2]. It is very important to predict and control the central crack in the production of high-quality and defect-free products in the steel industry. According to a previous investigation [3,4], the conclusion obtained was that the interdendritic solute redistribution has a significant impact on the formation of central crack. Carton steel has two typical characteristic temperatures under the high-temperature condition: the liquid impenetrable temperature (LIT) and the zero ductility temperature (ZDT). Many studies [5–9] support the point that internal cracks usually form in the temperature range from the LIT to the ZDT [9], and the solid fractions of 0.9 and 1.0 are believed to correspond to the LIT and ZDT, respectively. In view of the above, analyzing the solute micro-segregation and its effect on the LIT and the ZDT has practical significance for the control of internal cracks. Under the cooling rate of 0.5 °C/s, Kobayashi [10] gave the redistribution of solute elements C, Si, Mn, P, S, and Fe–C phase diagrams under nonequilibrium solidification using a mathematical model with the δ/γ phase transformation taken into account. Ueshima [11] assumed that the transverse cross-section of dendrite was approximated by a regular hexagon, and the interdendritic solute distribution with δ/γ phase transformation

was analyzed during the solidification. Depending on the model of Ueshima, under the cooling rate of 0.17 °C/s and the dendrite spacing of 1000 μm, Kim [3] discussed in detail the effect of solute micro-segregation in a continuously cast strand on surface longitudinal cracks.

At present, there are few papers focusing on the investigation of solute micro-segregation at the end of the columnar crystal zone of blooms. In view of the severe central cracks of blooms in domestic corporations, it is very necessary to find the formation mechanism of the cracks. In this paper, using the developed analytical model, the segregation of solute elements at the origin of the cracking gap located at the end of columnar crystal zone is obtained by taking into consideration the actual solidification cooling conditions, and the effect of solute segregation on the temperature range of crack formation from the LIT to the ZDT is discussed in detail. In addition, the strain of the solid shell during solidification is given through the finite element software (MSC Marc, MSC Software Corporation, Newport Beach, CA, USA), so as to find the reasons for the formation of central cracks.

2. Analytical Model

In this model, taking into account the Brody–Flemings model and the modified model suggested by Voller and Beckermann, the governing equations of the model were obtained as follows [12,13]:

$$C_{L,i} = C_{0,i}[1 - (1 - 2\alpha_i' k_i) \cdot f_S]^{(k_i - 1)/(1 - 2\alpha_i' k_i)}, \quad (1)$$

$$\alpha_i' = \alpha_i^+ \cdot [1 - \exp(-\frac{1}{\alpha_i^+})] - \frac{1}{2}\exp(-\frac{1}{2\alpha_i^+}), \quad (2)$$

$$\alpha_i^+ = \alpha_i + \alpha^c, \quad (3)$$

$$\alpha^c = 0.1, \quad (4)$$

$$\alpha_i = \frac{D_{S,i} t_f}{L^2}, \quad (5)$$

$$t_f = (T_L - T_S)/C_R, \quad (6)$$

where $C_{L,i}$ is the concentration of solute element i in liquid phase (wt. %), $C_{0,i}$ is the initial concentration of solute element i in liquid phase (wt. %), k_i is the equilibrium partition coefficient of solute element i, f_S is the solid fraction, α_i is the back-diffusion parameter, α_i' is the modified value of α_i, $D_{S,i}$ is the diffusion coefficient of solute element i in solid phase (cm^2/s), t_f is the local solidification time (s), T_L is the liquidus temperature (°C), T_S is the solidus temperature (°C), C_R is the cooling rate (°C/s), and L is the length scale of the micro-segregation domain (μm).

In the present study, the length scale was the final primary dendrite arm spacing λ, which was calculated as a function of cooling rate C_R and nominal steel carbon content (wt. %) from the following equation [14]:

$$\begin{cases} \lambda = 278.748(C_R)^{-0.206}([\%C])^{-0.316+2.033[\%C]} 0 < [\%C] \le 0.15 \\ \lambda = 278.748(C_R)^{-0.206}([\%C])^{-0.0189-0.492[\%C]} 0.15 < [\%C] \le 1.0 \end{cases} \quad (7)$$

The liquidus and solidus temperatures depend on steel composition as follows [15]:

$$T_L = T_{pure} - \sum_i m_i \cdot C_{0,i}, \quad (8)$$

$$T_S = T_{pure} - \sum_i n_i \cdot C_{0,i}, \quad (9)$$

where T_{pure} is the fusion temperature of pure iron (1536 °C), and m_i and n_i denote the slopes of the liquidus and solidus line of each solute element in the pseudo-binary Fe-phase diagram, respectively.

The solid/liquid interface temperature T_{int} is obtained by summing the contributions of all alloying elements.

$$T_{\text{int}} = T_{pure} - \sum_i m_i \cdot C_{L,i}, \tag{10}$$

where $C_{L,i}$ is the interface element concentration in the liquid, corresponding to a given solid/liquid interface. When fs = 1.0, T_{int} is just the solidus temperature.

Two solid phases, the δ-ferrite phase and the γ-austenite phase, occur naturally during the solidification of steel [16]. For carbon contents lower than 0.53%, when the liquid steel cools down slightly below the liquidus temperature, the solid nucleates and grows as the δ phase until solidification is complete at the low carbon content; however, for the intermediate carbon steel, once the carbon content exceeds 0.53% in the residual liquid, the solid γ phase starts to form around the periphery of the δ-phase dendrites until the completed solidification. For carbon contents over 0.53%, the solid nucleates from the melt as the γ phase, which grows until the end of solidification. The enrichment of solute elements in the interdendritic region during solidification causes a switch from δ-phase to γ-phase solidification once the carbon concentration exceeds 0.53%. This change suddenly lowers the diffusion rates, which increases micro-segregation and further lowers the solidus temperature. This behavior has an important effect on the metal properties that control micro-segregation, because of the very different solidification parameters in the two crystal phases (as shown in Table 1 [15]).

Table 1. Equilibrium partition coefficients, diffusion coefficients, and liquidus line slopes of the solute elements.

Element	$k^{\delta/L}$	$k^{\gamma/L}$	D^{δ} (cm^2/s)	D^{γ} (cm^2/s)	m (°C/%)	n (°C/%)
C	0.19	0.34	$0.0127 \times 10^{-52870.5/\text{RT}}$	$0.076 \times 10^{-87419.9/\text{RT}}$	78.0	415.3
Si	0.77	0.52	$8.0 \times 10^{-161737.6/\text{RT}}$	$0.3 \times 10^{-163368.6/\text{RT}}$	7.6	12.3
Mn	0.76	0.78	$0.76 \times 10^{-145808.5/\text{RT}}$	$0.055 \times 10^{-162009.4/\text{RT}}$	4.9	6.8
P	0.23	0.13	$2.9 \times 10^{149505.4/\text{RT}}$	$0.01 \times 10^{-118788.8/\text{RT}}$	34.4	124.5
S	0.05	0.035	$4.56 \times 10^{139447.7/\text{RT}}$	$2.4 \times 10^{145156.2/\text{RT}}$	38.0	183.9

Notes: R is the gas constant of 1.987 cal/mol K, and T is the temperature in Kelvin.

In order to incorporate the δ/γ transformation into the present model, it is assumed that only the carbon concentration controls this transition and other components do not influence the transition. The solid fraction at which the transition occurs can be calculated by using Equation (1) [17].

$$f_{S,\delta\to\gamma} = \frac{1}{2\alpha_i' k_i}\left[1 - \left(\frac{0.53}{C_0}\right)\right]^{(1-2\alpha_i' k_i)/(k_i-1)}, \tag{11}$$

where the ferritic data should be employed for α_i and k_i. For getting the segregation distribution corresponding to any solid fraction higher than $f_{S,\delta\to\gamma}$, a virtual zero concentration must be obtained. This could lead to the same concentration in residual liquid at the transition point by using Equation (1) and the solidification parameters of the austenitic phase. The corresponding calculation equation is expressed as follows:

$$C_{0,i}' = C_{L,\delta\to\gamma}\left[1 - (1 - 2\alpha_i' k_i)\cdot f_{S,\delta\to\gamma}\right]^{(1-k_i)/(1-2\alpha_i' k_i)}, \tag{12}$$

where the austenitic data should be employed for α_i and k_i.

In order to obtain the accurate liquidus and solidus temperatures, firstly, an estimate of the local solidification time is done by evaluating the equilibrium liquidus temperature and solidus temperature from Equations (8) and (10), respectively. From this initial guess, the value of T_s is improved with a few iterative steps through Equations (1)–(3) and (10) with $f_S = 1$, until consistent values are obtained for t_f, $C_{L,i}$, and $T_{\text{int}} = T_s$.

If carbon content is less than 0.53% and $f_S = 1$, then δ-phase properties are used in the previous procedure. If carbon content is greater than 0.53% and $f_S = 0$, then γ-phase prop-

erties are used throughout. If none of these conditions are met, then both phases may exist; thus, the procedure is repeated firstly for the δ phase. Once the carbon concentration of the residual liquid exceeds 0.53%, the virtual zero concentration is obtained, and the following γ-phase properties are adopted until completed solidification of the residual liquid.

After finding T_s, the previous procedure should be repeated to find T_{int} corresponding to any other desired f_S value without the need for further iteration. In practice, it is often desirable to find the relationship between the entire solid fraction and the temperature. Thus, it can be convenient to solve the above equations by incrementing the solid fraction in steps of 0.01.

3. Validation of Analytical Model

In order to assess the validity of the analytical model, under the steel compositions and cooling conditions (shown in Table 2) used in the unidirectional solidification experiment, the model predictions are compared with the experiment results suggested by Matsumiya [18].

Table 2. Steel compositions and cooling condition for the calculated model.

C	Si	Mn	P	S	C_R (°C/s)
0.13	0.35	1.52	0.016	0.002	0.045

As shown in Figure 1, it can be seen that the model calculations are in reasonable agreement with these measurements, which indicates that this model can accurately calculate the concentration of each element during solidification; thus, the segregation distribution of solute elements is predicted.

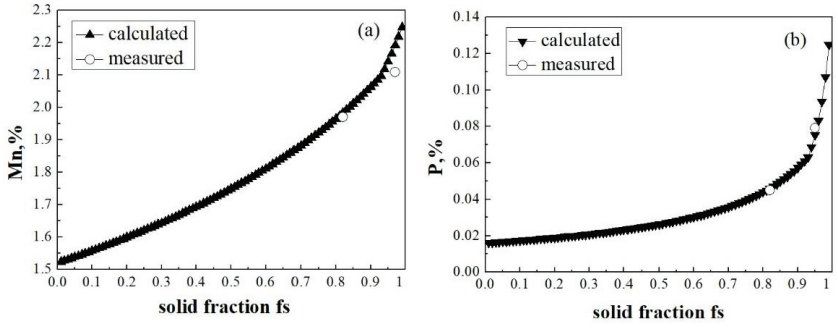

Figure 1. Comparison of (**a**) manganese and (**b**) phosphorus concentration in the liquid phase calculated and experimental measurements.

4. Analysis of Solute Segregation on the Central Cracking

The etching print of the bloom transverse section with typical central cracks is shown in Figure 2a. According to the statistical data from the etched prints of massive blooms, it is found that the central cracks all appear at the inner arc side, the distance between the opening point of the crack and the inner radius of the surface mainly concentrates in the scope of 90–105 mm, and the width of the cracks mainly occurs in the range of 0.5–2 mm.

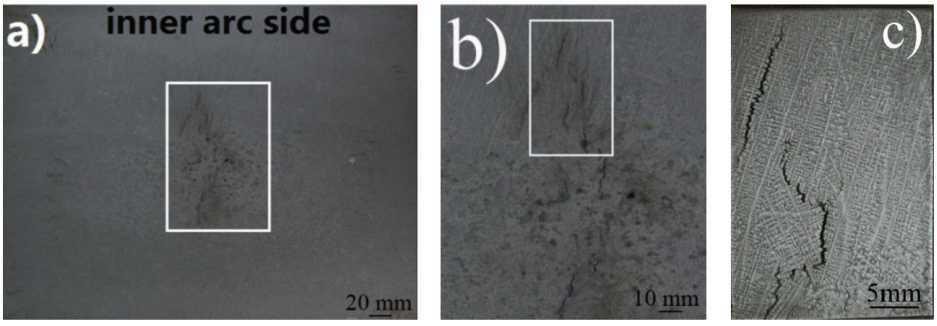

Figure 2. Macrograph of central crack on transverse section at etching print by hydrochloric acid ((**a**) typical central cracks; (**b**) enlarged crack morphology; (**c**) crystal structure under optical microscope).

After the typical central crack samples are mechanically ground, polished, and etched using picric acid, they are visualized using a video camera to observe the relationship between the crack and the columnar or equiaxed crystal. As shown in Figure 2b,c, the columnar crystal of crack samples is developed such that the length of the primary dendrite arm spacing reaches approximately 1000 μm. In addition, the central cracks all occur in the gap between two adjacent primary dendrites at the end of the columnar crystal zone, thus exhibiting typical cracking along the gap between the columnar crystals. Chemical compositions of the crack sample (Table 3) were detected using XRF (sequential X-ray fluorescence spectrometer, ZSXPrimus IV).

Table 3. Chemical compositions of crack sample (wt. %).

Steel Grade	C	Si	Mn	P	S	C_r	Mo	Ni
49MnVS3	0.475	0.373	0.734	0.009	0.0483	0.161	0.007	0.18

As described in Figure 3, with the increasing solid fraction, the segregation of both carbon and manganese is quite slight, whereby they only have a little enhancement at the final stages of solidification. However, for phosphorus and sulfur, their segregation is very severe, especially at the final stages of solidification, whereby the maximum index values reach 16.6 and 33.3, respectively. The segregation distributions of elements near the crack are shown in Figure 4 using the line scanning of SEM (field-emission scanning electron microscopy, Apreo S HiVac). Here, it is clear that the fluctuation peaks of carbon, phosphorus, sulfur, and manganese all appear at the cracking gap, which means that all of these four elements have a certain amount of enrichment at the cracking gap, basically coinciding with the results calculated using the segregation model.

According to the investigation of previous researchers [19,20], central cracks generally form in the temperature range from the LIT to the ZDT under high temperature, and the solute segregation has a significant influence on this temperature range. However, the difference between the LIT and the ZDT is 69.1 °C when segregation of the elements is considered, but it is only 7.9 °C without segregation. Therefore, solute segregation facilitates an enhanced increase in cracking. From the previous line scanning analysis, it can be seen that carbon, phosphorus, sulfur, and manganese all have a certain amount of enrichment at the cracking gap, while the segregations of phosphorus and sulfur are especially serious at the final stages of solidification. Hence, the element segregation leads to an obvious increase in the temperature range of crack formation; thus, the conclusion can be obtained that the solute segregation is the internal reason for crack formation.

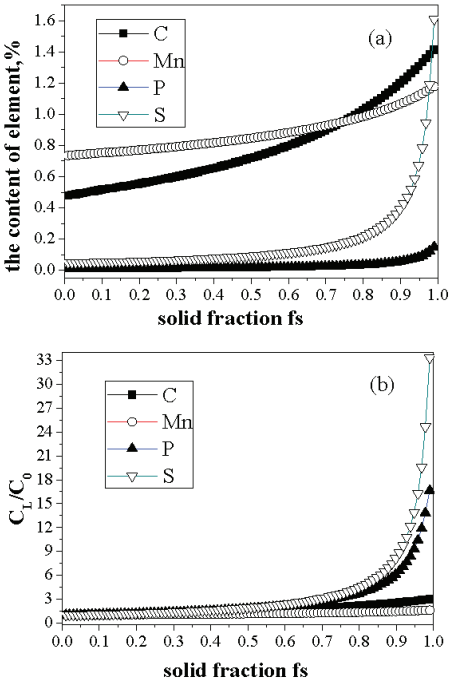

Figure 3. (**a**) Concentration and (**b**) segregation indices of elements C, P, and S in liquid phase at the mushy zone.

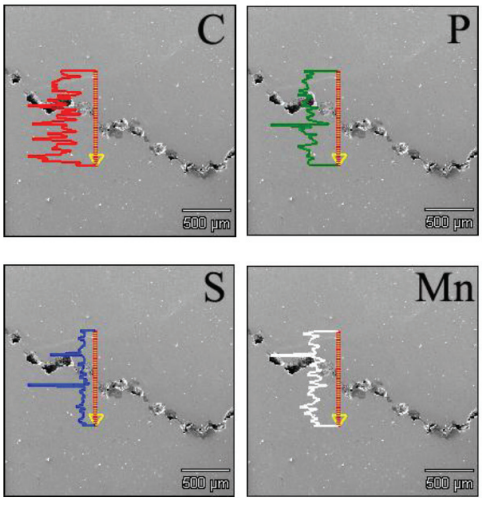

Figure 4. Line scanning of SEM in the crack band.

Subsequently, the crack samples were ground, polished, and etched using a nitric acid alcohol solution in which the alcohol occupied 4 wt.%. Then, they were placed in an optical microscope to observe the structure. It can be seen from Figure 5 that the cracking and extending directions of the crack were always along the grain boundaries, thus exhibiting a typical fracture mode along the grain boundaries.

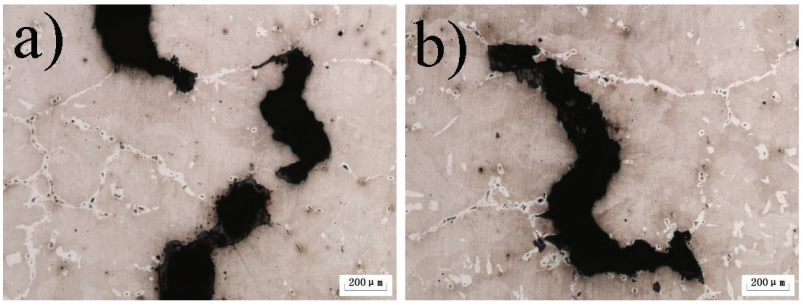

Figure 5. Morphology of central crack at etching print ((**a**) typical fracture crack a; (**b**) typical fracture crack b).

The fracture morphologies of the cracks are of great help to find the formation temperature of cracks. As shown in Figure 6, it is clear that the fracture surfaces of the cracks are so smooth that there are no dimples to be found, which is very similar to the fracture surface which forms in the mushy zone. This indicates that the temperature range of crack formation should be at the mushy zone, denoting steel cracking with a low melting point.

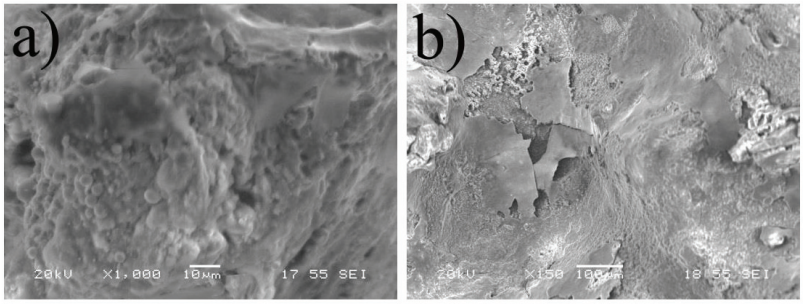

Figure 6. Photograph of surface on central crack by SEM ((**a**) enlarged fracture surfaces of the cracks; (**b**) fracture surface morphology of cracks).

In order to analyze the mechanism of crack formation, the following assumption is considered: the position with the shortest distance from the inner radius is just the opening point. Depending on the statistical data from the etched prints of massive blooms, when the bloom begins to crack, the solid shell thickness is within the scope of 90–105 mm. At this time, the thickness of 95 mm is selected when the distance from the meniscus is about 13.5 m. Then, the strain of the solid shell is simulated by using finite element software (MSC Marc), where the factors included heat transfer, phase transformation, and metallurgical pressure. The thermo-elastic–plastic constitutive equation is as follows:

$$\varepsilon_{ij} = \varepsilon_{ij}^{e} + \varepsilon_{ij}^{ie} + \varepsilon_{ij}^{T}, \tag{13}$$

where ε_{ij}^{e} is the elastic strain, ε_{ij}^{ie} is the inelastic strain, and ε_{ij}^{T} is the thermal strain. In the analysis, the von Mises yield criterion is used to describe the thermo-elastic–plastic property. As can be seen in Figure 7, a positive value denotes tensile strain, and a negative value indicates compressive strain. Clearly, tensile strain near the solid front reaches the maximum value of 2.77–3.22%. Otherwise, Hiebler [21] gave the relationship between the critical strain and the carbon equivalent by summing up the results of previous studies, and the experimental data used in Figure 8 were obtained under the typical strain rate of a continuous casting process. According to Equation (14) and the chemical composition of steel 49MnVS3, the carbon equivalent content of 0.452% and the Mn/S index of 15.2 are obtained; therefore, the critical strain of this steel grade is approximately 0.50%, which is

much smaller than the tensile strain of the solid front. Therefore, it is very easy for tearing to occur, thus forming a central crack. The carbon equivalent can be calculated as follows:

$$Cp = \mathrm{C} + 0.02\mathrm{Mn} + 0.04\mathrm{Ni} - 0.1\mathrm{Si} - 0.04\mathrm{Cr} - 0.1\mathrm{Mo}. \quad (14)$$

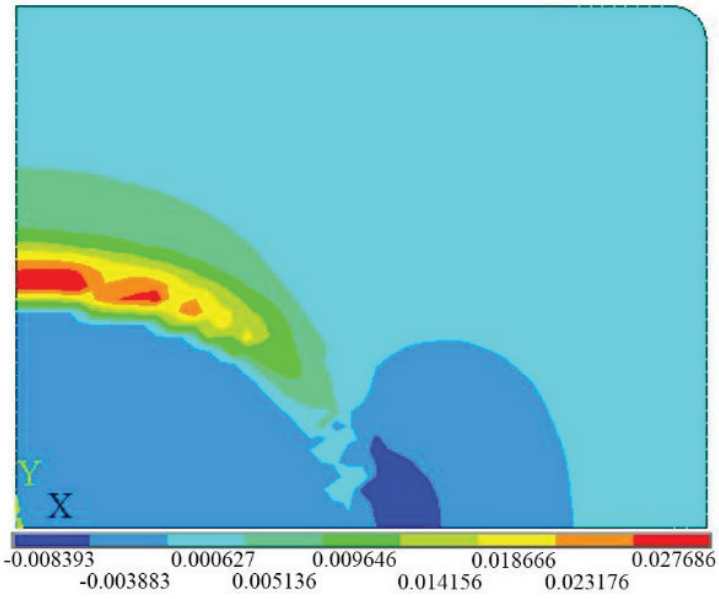

Figure 7. Simulation analysis of the strain of the solid shell for the opening point of the crack.

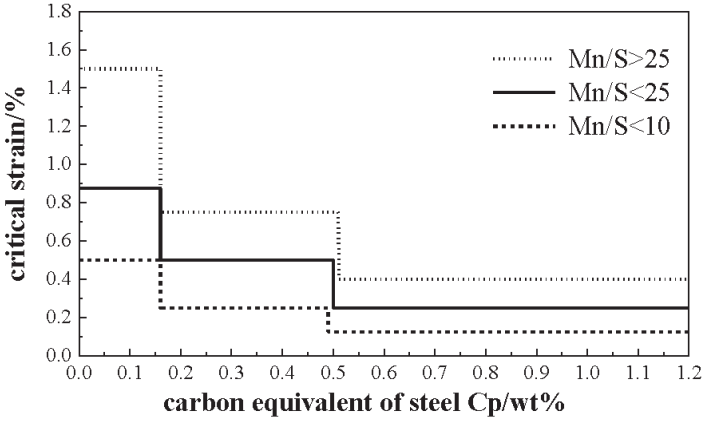

Figure 8. Relationship between the critical strain and carbon equivalent of steel.

During the solidification process of bloom, columnar crystals are developed such that the interdendritic segregation is quite severe. On the one hand, enriched solute elements exist in the grain boundaries and form inclusions and others, thereby greatly reducing the high-temperature strength and the high-temperature plasticity of the dendrite grain boundaries [22]. Correspondingly, the critical strain value of steel significantly decreases, thus causing increased brittleness of grain boundaries and extending the path of the crack. On the other hand, interdendritic segregation reduces the melting point of the dendritic liquid film, which leads to the freezing temperature of steel significantly decreasing and

the difference between the LIT and the ZDT obviously increasing; thus, the possibility of racking is increased. During the solidification process of bloom, when the solid shell thickness grows to approximately 95 mm, the tensile strain of the solid front becomes much larger than the critical strain of blooms. This easily results in cracking of the solid front, which extends along the grain boundaries. In addition, once cracking of the solid front happens, the solute-rich liquid ahead of the solidification interface is immediately sucked into the cracking gap, accompanied by the solidification of liquid steel. Moreover, due to the effect of negative pressure, the liquid steel containing the enriched impurities is continuously sucked into the cracks, which leads to the cracking gap extending to the center of the bloom, thus forming a severe central crack.

5. Conclusions

(1) Taking into account the Brody–Flemings model and the modified Voller–Beckermann model, an analytical model of micro-segregation was established by considering the actual solidification cooling conditions of bloom, and the accuracy of the model was verified using the results of directional solidification experiments.

(2) Through the developed analytical model, the solute segregation at the opening point of the crack was analyzed. The segregation of both phosphorus and sulfur was quite severe, while that of carbon and manganese was relatively light, which agrees well with the semi-quantitative analysis results from the SEM. Moreover, interdendritic segregation led to an increase in the temperature range of crack formation; therefore, it was concluded that element segregation is the internal cause of crack formation.

(3) Taking into consideration heat transfer, phase transformation, and metallurgical pressure, the strain of the solid shell was obtained through finite element software (MSC Marc). It was found that, when the solid shell thickness grows to approximately 95 mm, the tensile strain of the solid shell is much bigger than the critical strain, representing the external cause of crack formation.

Author Contributions: Conceptualization, C.X. and J.L.; methodology, C.X.; software, Q.Z.; formal analysis, C.X. and Q.Z.; investigation, J.L.; data curation, C.X.; writing—original draft preparation, C.X.; writing—review and editing, Q.Z.; project administration, J.L.; funding acquisition, J.L. All authors have read and agreed to the published version of the manuscript.

Funding: This work was financially supported by the National Natural Science Foundation of China (No. 51974210), the Hubei Provincial Natural Science Foundation (No. 2019CFB697), and the State Key Laboratory of Refractories and Metallurgy, Wuhan University of Science and Technology.

Institutional Review Board Statement: Not applicable

Informed Consent Statement: Not applicable.

Data Availability Statement: Data available on request due to privacy.

Acknowledgments: The authors would like to thank the above funding bodies for this investigation.

Conflicts of Interest: The authors declare no conflict of interest.

References

1. Zinigrad, M.; Mazurovsky, V.; Borodianskiy, K. Physico-chemical and mathematical modeling of phase interaction taking place during fusion welding processes. *Mater. Sci. Eng. Technol.* **2005**, *36*, 489–496. [CrossRef]
2. Li, S.; Han, Z.; Zhang, J. Numerical Modeling of the Macrosegregation Improvement in Continuous Casting Blooms by Using F-EMS. *JOM* **2020**, *72*, 4117–4126. [CrossRef]
3. Kim, K.; Han, H.; Yeo, T.; Lee, Y.; Oh, K.; Lee, D. Analysis of surface and internal cracks in continuously cast beam blank. *Ironmak. Steelmak.* **1997**, *24*, 249–256.
4. Thomas, B.; Brimacombe, J.; Samarasekera, I. The formation of panel cracks in steel ingots: A state-of-the-art review, Part I Hot Ductility of Steel. *Trans. Iron Steel Soc.* **1987**, *7*, 7–20.
5. Clyne, T.W.; Wolf, M.; Kurz, W. The effect of melt composition on solidification cracking of steel, with particular reference to continuous casting. *Metall. Trans. B* **1982**, *13*, 259–266. [CrossRef]

6. Kim, K.H.; Yeo, T.J.; Oh, K.H.; Lee, D.N. Effect of Carbon and Sulfur in Continuously Cast Strand on Longitudinal Surface Cracks. *ISIJ Int.* **1996**, *36*, 284–289. [CrossRef]
7. Won, Y.M.; Kim, K.H.; Yeo, T.J.; Oh, K.H. Effect of Cooling Rate on ZST, LIT and ZDT of Carbon Steels Near Melting Point. *ISIJ Int.* **2007**, *38*, 1093–1099. [CrossRef]
8. Won, Y.M.; Yeo, T.J.; Seol, D.J.; Oh, K.H. A new criterion for internal crack formation in continuously cast steels. *Metall. Mater. Trans. B* **2000**, *31*, 779–794. [CrossRef]
9. Yamanaka, A.; Nakajirna, K.; Okamura, K. Critical strain for internal crack formation in continuous casting. *Ironmak. Steelmak.* **1995**, *22*, 508–512.
10. Kobayashi, S.; Nagamichi, T.; Gunji, K. Numerical Analysis of Solute Redistribution during Solidification Accompanying δ/γ Transformation. *Trans. Iron Steel Inst. Jpn.* **1988**, *28*, 543–552. [CrossRef]
11. Ueshima, Y.; Mizoguchi, S.; Matsumiya, T.; Kajioka, H. Analysis of solute distribution in dendrites of carbon steel with δ/γ transformation during solidification. *Metall. Trans. B* **1986**, *17*, 845–859. [CrossRef]
12. Brody, H.D.; Flemings, M.C. Solute Redistribution in Dendritic Solidification. *Trans. Metall. Soc. Aime* **1966**, *236*, 615–624.
13. Voller, V.R.; Beckermann, C. A unified model of microsegregation and coarsening. *Metall. Mater. Trans. A* **1999**, *30*, 2183–2189. [CrossRef]
14. El-Bealy, M.; Thomas, B.G. Prediction of dendrite arm spacing for low alloy steel casting processes. *Metall. Mater. Trans. B* **1996**, *27*, 689–693. [CrossRef]
15. Won, Y.M.; Thomas, B.G. Simple model of microsegregation during solidification of steels. *Metall. Mater. Trans. A* **2001**, *32*, 1755–1767. [CrossRef]
16. Zhiqiang, H.; Kaike, C. Study on A Mathematical Model of Microsegregation in Continuous Cast Slab. *Acta Metall. Sin.* **2000**, *36*, 869–873.
17. Cornelissen, M.C.M. Mathematical Model for Solidification of Multicomponent Alloys. *Ironmak. Steelmak.* **1986**, *13*, 204–212.
18. Matsumiya, T.; Kajioka, H.; Mizoguchi, S.; Ueshima, Y.; Esaka, H. Mathematical analysis of segregations in continuously-cast slabs. *Trans. Iron Steel Inst. Jpn.* **1984**, *24*, 873–882. [CrossRef]
19. Yang, C.; Dong, H.; Hu, Z. Micro-mechanism of central damage formation during cross wedge rolling. *J. Mater. Process. Technol.* **2018**, *252*, 322–332. [CrossRef]
20. Zhou, X.; Shao, Z.; Tian, F.; Hopper, C.; Jiang, J. Microstructural effects on central crack formation in hot cross-wedge-rolled high-strength steel parts. *J. Mater. Sci.* **2020**, *55*, 9608–9622. [CrossRef]
21. Hiebler, H.; Zirngast, J.; Bernhard, C.; Wolf, M.M. Inner crack formation in continuous casting: Stress or strain criterion. In Proceedings of the 1994 Steelmaking Conference Proceedings, Chicago, IL, USA, 20–23 March 1994; pp. 405–416.
22. Mintz, B. The Influence of Composition on the Hot Ductility of Steels and to the Problem of Transverse Cracking. *ISIJ Int.* **1999**, *39*, 833–855. [CrossRef]

metals

MDPI

Article

Numerical Simulation of Macrosegregation Formation in a 2.45 ton Steel Ingot Using a Three-Phase Equiaxed Solidification Model

Tao Wang [1,2,3], Engang Wang [1,3,*], Yves Delannoy [4], Yves Fautrelle [2] and Olga Budenkova [2]

[1] Key Laboratory of Electromagnetic Processing of Materials (Ministry of Education), Northeastern University, Shenyang 110004, China; tao.wang1@grenoble-inp.fr
[2] University Grenoble Alpes, CNRS, Grenoble INP, SIMAP, F-38000 Grenoble, France; yves.fautrelle@grenoble-inp.fr (Y.F.); olga.budenkova@grenoble-inp.fr (O.B.)
[3] School of Metallurgy, Northeastern University, Shenyang 110004, China
[4] University Grenoble Alpes, CNRS, Grenoble INP, LEGI, F-38000 Grenoble, France; yves.delannoy@grenoble-inp.fr
* Correspondence: egwang@mail.neu.edu.cn; Tel./Fax: +86-24-8368-1739

Abstract: In the present work macrosegregation during solidification of a 2.45 ton steel ingot is simulated with a pure equiaxed model, which was tested previously via modeling of a benchmark experiment. While the columnar structure is not taken into account, a packed layer formed over inner walls of the mold at an early stage of solidification reproduces to some extent phenomena generally related to zones of columnar dendrites. Furthermore, it is demonstrated that interaction of free-floating equiaxed grains with ascending convective flow in the bulk liquid results in flow instabilities. This defines the irregular form of the negative segregation zone, the formation of which at the ingot bottom corresponds to experimental observation. Vertical channels reported in experimental measurements are reproduced in simulations. It is confirmed that intensification of ingot cooling may decrease segregation in the ingot.

Keywords: ingot; equiaxed grain; solidification; macrosegregation; surface cooling intensity

Citation: Wang, T.; Wang, E.; Delannoy, Y.; Fautrelle, Y.; Budenkova, O. Numerical Simulation of Macrosegregation Formation in a 2.45 ton Steel Ingot Using a Three-Phase Equiaxed Solidification Model. *Metals* **2021**, *11*, 262. https://doi.org/10.3390/met11020262

Academic Editor: Mohsen Eshraghi
Received: 21 December 2020
Accepted: 28 January 2021
Published: 4 February 2021

Publisher's Note: MDPI stays neutral with regard to jurisdictional claims in published maps and institutional affiliations.

1. Introduction

Manufacturing of large-size ingots is a fundamental process in industrial production of heavy machinery. The first thorough study of segregation in a large number of ingots ranging from 14 cwts. (765 kg) to 172 tons was presented in the first report of a special committee of the Iron and Steel Institute of Great Britain [1]. Apart from "the very thin extreme outer skin of true chill crystals," three zones were revealed in the ingots studied. The zone adjacent to the outer thin layer (zone 1) consisted of columnar grains directed inward, while the thickness of the zone was found to be dependent on casting conditions and steel composition. The second zone (zone 2) beyond zone 1, proceeding inward in a radial direction, was reported to be richer in segregates with an annular inner boundary "having roughly the form of a truncated cone or pyramid." In addition, A-shape segregates were documented for this zone. Furthermore, sulfur prints and etching revealed a central zone (zone 3) in which solid grains could be considered to be equiaxed or, as said in the report, "the crystals may cease to possess the hitherto well marked columnar form" [1]. Near the central axis, V-shape segregates were usually present: The lowest part of the central zone was defined as the purest, and the top of the ingot presented strong segregation.

Various laboratory-scale experiments were developed later in order to study the effect of solidification parameters on solid structure and segregation, and patterns similar to those reported for large-size ingots were found [2–4]. These experiments served for validation of solidification models, which were further used to explain the segregation phenomenon in ingots. Thus, the gravity-induced flow of liquid through the mushy zone and the remelting

of the solid phase were shown to be potentially responsible for the formation of centerline segregation, as well as of A-type and V-type segregates, depending on density variation due to liquid enrichment and on the variation and direction of the thermal gradient [5]. This analysis was then extended to multicomponent alloys [6]. State of the art regarding numerical simulations of segregation in ingots was thoroughly reviewed in 1999 [7] and 2009 [8]. Compact but detailed reviews were also provided for later periods [9,10] regarding both experimental and numerical studies aiming to reproduce segregation patterns observed in large-scale ingots. In this paper, we provide only a brief description of the limited number of numerical simulations conducted for large-size ingots with coupled equations, accounting for flow of the liquid phase, heat and mass transfer, and phase transition. In most of them, calculated values of segregation were compared with measurements performed in ingots. For example, multicomponent segregation was modeled for a 6.2 ton steel ingot and the distribution of carbon concentration obtained numerically was found to be qualitatively similar to that measured in axial and to transversal directions. However, negative segregation at the ingot bottom was clearly not obtained in simulations [11]. This discrepancy between numerical and experimental results was attributed to the eventual sedimentation of solid grains, which was not included in the model. Based on a volume-averaged formulation of a model that accounted for shrinkage, evolution of primary dendrite arm spacing and back-diffusion in the solid was used for the simulation of the solidification of a large steel ingot [7]. Although the predicted two-dimensional distribution of the carbon concentration qualitatively reproduced macrosegregation in the ingot, it did not show A-segregates, which is explained by the coarse mesh used in the simulation. Again, the negative segregation cone was not reproduced as the settling of solid crystals was not taken into account in the modeling. However, in more recent works, numerical models with fixed solid phase were still employed when particular parameters of solidification processes were studied. For example, flow instabilities as a result of buoyancy-induced thermal and solutal effects were shown to form either A-shaped or V-shaped channels [12], i.e., a qualitative analysis performed earlier [5] was undertaken for a 3.3 ton ingot with a more rigorous numerical model. It was shown that V-oriented or A-oriented segregates may form without any remelting of the solid phase. In addition, weak segregation at the ingot bottom (segregation index ~4%) was demonstrated for the case when solutal convection strongly prevailed over thermal convection, counteracting the latter. Later, formation of a negative segregation cone at the ingot bottom was confirmed [13] with expansion coefficients equal to the corresponding ones in the reference [12]. However, segregation in the upper part of the ingot was different, a fact that again can be attributed to the coarser mesh used for the simulation. Another numerical study with fixed solid phase carried out for a 3.3 ton steel ingot demonstrated that macrosegregation can be alleviated by increasing the cooling intensity of the ingot [14]. To date, the fixed solid phase approach remains attractive for numerical studies of solidification of large-scale industrial ingots, as it greatly reduces modeling complexity.

However, according to references elsewhere [3], even prior to publishing the report in 1926 [1], the central ingot zone had been supposed to be formed from free-floating equiaxed grains. One of the first attempts to numerically study the effect of the sedimentation of grains on macrosegregation was made for a 4 ton ingot [15]. Simulations were conducted for different zones with a simplified system of equations, where only the vertical component of velocity with a pre-calculated value was taken in the zone with the sedimentation cone. Later, a theory developed on the basis of volume averaging (or statistical ensemble averaging) provided a system of equations able to account for the floating equiaxed dendrites. A detailed review of equiaxed model development can be found elsewhere [16]. However, although the formulation was available, its application required the definition of multiple parameters for auxiliary closure equations, and this is still the case. Nevertheless, the pure equiaxed solidification model was applied to the study of macrosegregation in the 3.3 ton steel ingot [8,17,18]. Combeau et al. [8] numerically studied three cases, which corresponded to the fixed solid phase, to free-floating equiaxed grains with a dendrite

structure, and to free-floating grains of globular shape. Similar to previous modeling for steel ingots [11], the initial temperature of the melt was equal to the liquidus temperature of the nominal composition of steel, but this time the growth kinetic was taken into account for the solid phase. Probably due to the latter, the predicted negative segregation at the ingot bottom was more pronounced than in previous results in the case of fixed solid grains [11]. Qualitatively, segregation distribution obtained with free-floating dendrites was quite similar to results with the fixed solid phase but had a more "diffused" character. Although both cases demonstrated A-type segregation bands, the formation of which was found sensitive to mesh, a zone with positive segregation observed in the real ingot was only partially reproduced with free-floating grains. When the dendritic structure of grains was ignored, the negative segregation in the ingot was seriously overestimated. The same type of study was carried out with a slightly different formulation for momentum equation for the solid phase and a different drag force between the solid and liquid phases [17]. In addition, formation of the shrinkage cavity was considered in one of three cases studied. Results were quite similar to those obtained by Combeau et al. [8]. In the work of Nguyen et al. [18], a time-splitting technique was implemented in a model constructed using the finite element method (FEM) and applied to modeling of segregation in a 3.3 ton steel ingot accounting for different types of floating solid grains [8]. However, the study was focused on numerical treatment of the problem using FEM.

Finally, it should be mentioned that soon after pure equiaxed models started being used, three-phase columnar and equiaxed models [19–22], as well as models with an even greater number of phases [23], began to be exploited. Although these models allow some insight into the origin of various zones that form in the ingot [1], it must be accepted that these simulations are very sensitive to the choice made for closure relations and numerical parameters. On the other hand, application of pure equiaxed models with regard to large ingots was studied only for a very limited combination of parameters. In our previous paper, we presented a three-phase equiaxed solidification model that accounted for the growth of equiaxed grains, their motion, and the formation of macrosegregation [24]. In the model, a specific approach to the calculation of solute diffusion length under convective flow was applied. This model was then validated through numerical simulation for benchmark solidification of a Sn–10 wt.%Pb alloy in the AFRODITE setup [25]. In this study, we present the numerical simulation for the solidification of a 2.45 ton steel ingot to study the role of equiaxed grain transportation in the formation of global segregation. The effect of surface cooling intensity on grain growth, melt flow, and macrosegregation is also investigated.

2. Experiment Introduction

Numerical simulation was used to predict macrosegregation in a 2.45 ton steel ingot (Fe–0.45 wt.%C), which corresponded to a reported cast experiment [1]. The ingot was cast in a chill mold with the inner shape of a square-based pyramid, as schematically illustrated in Figure 1a. For the current simulation, only the ingot was considered, without the surrounding multi-layer mold, and a 2D axisymmetric geometry was used to approximate the three-dimensional shape of the ingot. The computational domain and mesh are presented in Figure 1b. Most of the mesh cells had a general size of 5 mm × 5 mm, but the cells near the cooling boundary were refined to 1 mm × 5 mm to allow a more precise calculation of the thermal gradient, the dynamic boundary layer, and the related transportation processes. At the beginning of simulation, the hot metal in the mold was assumed to be still and to have a uniform temperature of 1769 K, i.e., overheated by ~0.1 K with respect to its nominal liquidus temperature. Cooling conditions were applied directly to the ingot surface and were written via convective heat exchange with coefficients, accounting for heat transfer through different construction elements. Similar to Li et al. [20], the ambient temperature was set to 373 K, and two different convective heat transfer coefficients were applied: $h_{sup} = 30$ W m^{-2} K^{-1} in the upper zone and $h_{inf} = 300$ W m^{-2} K^{-1} in the lower zone. The boundary and initial conditions are provided in Figure 1b.

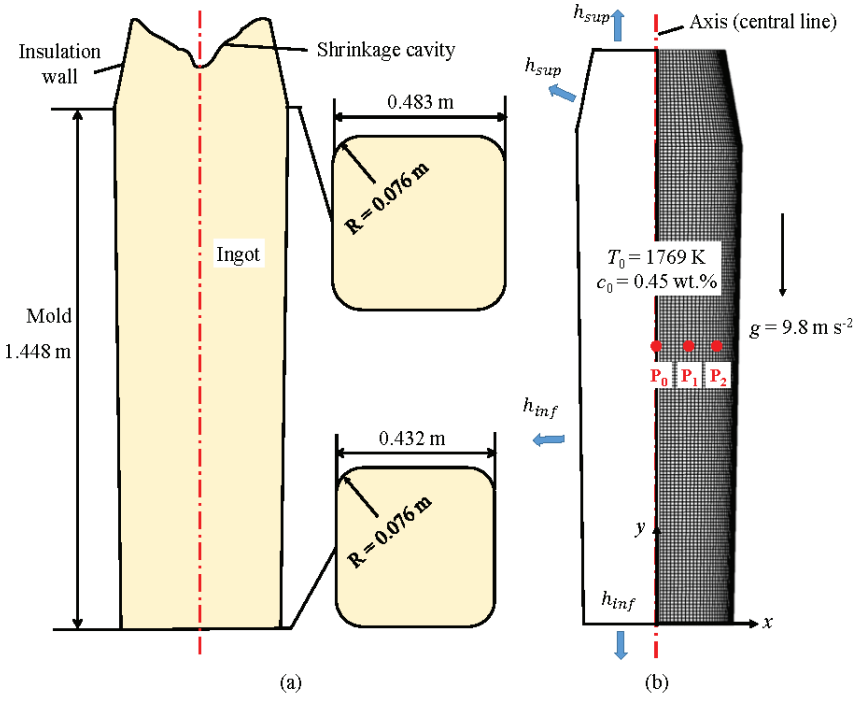

Figure 1. (**a**) Scheme of a 2.45 ton ingot with indication of sizes and (**b**) corresponding calculation domain. The initial conditions for the simulations are given, and two coefficients for convective heat exchange, h_{sup} and h_{inf}, are associated with the upper and lower parts of the ingot surface, respectively. The initial conditions for the simulations are $T_0 = 1769$ K, $c_0 = 0.45$ wt.%, and zero velocities in the liquid. The two coefficients for convective heat exchange, are h_{sup} and h_{inf}, with the upper and lower parts of the ingot surface defining the intensity of convective heat removal from the ingot as $h_{sup}(T - 373\ \mathrm{K})$ and $h_{inf}(T - 373\ \mathrm{K})$ for these parts, respectively. The indicated points P_0, P_1, and P_2 serve for the analysis of the calculation results.

3. Model Description

It is assumed that solidification occurs with equiaxed dendritic grains, which are allowed to float at the early stage of solidification and become immovable at the later stage. The model, described in detail elsewhere [25], combines multiphase flow, energy transportation, grain growth, and solute transportation with use of the volume average method. The key features and assumptions are enumerated below.

(1) Three phases are defined: the solid dendrite skeleton (*s*-phase); liquid within the imaginary surface (envelope), i.e., interdendritic liquid phase (*d*-phase); and extradendritic liquid phase (*l*-phase), as presented in Figure 2. The summation rule is satisfied for volume fractions associated with these phases: $f_s + f_d + f_l = 1$.

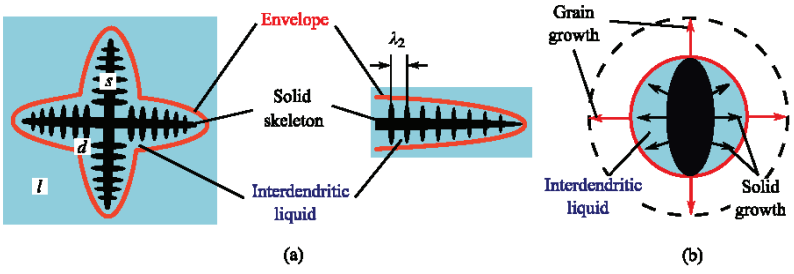

Figure 2. (**a**) Schematic figure for the dendritic structure and grain growth process, which consists of the expansion of the envelope (indicated by the red line), and (**b**) growth of the solid phase at the expense of the interdendritic liquid.

(2) Solidification is composed of the growth of the solid phase at the expense of the interdendritic liquid and expansion of the grain envelope, i.e., grain growth; see Figure 2. The former process is defined by the solute diffusive transportation rate, and grain growth rate is calculated using the Lipton–Glicksman–Kurz (LGK) model [26].

(3) When accounting for multiphase flow, only two moving phases are identified: the phase corresponding to the extradendritic liquid (l-phase) and the phase corresponding to the equiaxed grains (e-phase). The latter is actually composed of the united s-phase and the d-phase, where the volume fraction is defined as $f_e = f_s + f_d$. For free-floating grains, the momentum exchange coefficient between the liquid and grain phases is calculated using the Happel model [27]. When grains get packed, i.e., become immovable, permeability of the phase corresponding to grains is evaluated by the Kozeny–Carman equation.

(4) Grains to be packed should have at least one immovable neighbor to which they can attach. This immovable neighbor can be either a wall or an already packed region. Once the previous condition has been satisfied, the grain phase motion is set to zero once the phase fraction f_e reaches the packing limit value f_p^e.

(5) Nucleation is modeled with a source term for a grain number density of $n_{\max}$ per unit time in those cells of the mesh where local temperature drops below local liquidus temperature for the first time, or where local grain density is less than 1 m^{-3} and local temperature is lower than the liquidus temperature [8].

(6) In the conservation equations, all densities are constant and equal to the reference density, that is, $\rho_l = \rho_s = \rho_e = \rho_d = \rho_{ref}$. The reference density corresponds to the liquid density, with nominal solute concentration and initial temperature. In the buoyancy term, the solid phase inside the grain is assumed to have a larger density than the liquid phase. In addition, a constant difference between solid phase density and reference density is introduced. Liquid density is dependent on solute concentration and temperature, according to the Boussinesq approach, with the values of the thermal and solutal expansion coefficients (β_T and β_c) taken from elsewhere [8]. The momentum transport equations as well as turbulent model are gathered in Appendix A.

In simulation, the multiphase flow and macroscopic transportation of energy, solute, and grain number density are solved using ANSYS FLUENT® software (ANSYS Inc., Canonsburg, PA, USA), in which the modeling of the solidification at the micro scale is implemented with user-defined functions. To simplify comparison with the results in reference [20], maximal grain number density is set to $n_{\max} = 2 \times 10^9$ m^{-3}. The phase diagram data and properties of the Fe-C alloy are listed in Table 1.

Table 1. Thermodynamic and physical properties.

Property	Units	Quantity	References
Carbon content	wt.%	0.45	-
Melting point of pure iron	K	1805.15	[8]
Liquidus slope	$K\ (wt.\%)^{-1}$	−80.45	[8]
Equilibrium partition coefficient	1	0.314	[8]
Reference density	$kg\ m^{-3}$	7200	[28]
Solid–liquid density difference	$kg\ m^{-3}$	200	-
Specific heat	$J\ kg^{-1}\ K^{-1}$	725	[29]
Thermal conductivity	$W\ m^{-1}\ K^{-1}$	34	[8]
Latent heat	$J\ kg^{-1}$	2.72×10^5	[29]
Viscosity	$kg\ m^{-1}\ s^{-1}$	4.2×10^{-3}	[8]
Thermal expansion coefficient	K^{-1}	1.07×10^{-4}	[8]
Solutal expansion coefficient	$(wt.\%)^{-1}$	1.4×10^{-2}	[8]
Maximal grain number density	m^{-3}	2.0×10^9	[8]
Grain packing limit fraction	1	0.4	[8]
Secondary arm spacing	m	5.0×10^{-4}	[8]
Shape factor for tip growth	1	0.18	[30]
Sphericity	1	0.53	[30]
Liquid diffusion coefficient	$m^2\ s^{-1}$	2.0×10^{-8}	[8]
Gibbs–Thomson coefficient	$m^2\ s^{-1}$	1.9×10^{-7}	[31]

4. Results and Discussion

4.1. Nucleation and Grain Growth

According to the variation in the convective heat exchange coefficient along the ingot surface, the coldest zone formed at the bottom corner and the very first grains nucleated there when local temperature dropped below the liquidus temperature. Then nucleation extended over the bottom, sidewall, and top of the ingot, as presented in Figure 3a,b, via the distribution of the grain number density. Although redistribution of the grain number density due to grain sedimentation was observed near the top boundary (Figure 3a), after a while these grains were dispersed into bulk liquid (Figure 3b,c). The liquid near the chilled boundary and the nucleated grains moved downward, the former as a result of buoyancy due to the temperature difference, the latter due to drag force from the liquid and the imposed density difference between solid and liquid. Indeed, although the solid fraction was very small at 20 s and 50 s, after cooling started, the grains moved faster than liquid, as presented in Figure 4a,b. Due to strong cooling, the temperature near the ingot surface decreased rapidly and melt undercooling remained high, meaning that the grains descending along the wall grew quickly. Once grain volume fraction reached the packing limit value, the grains became attached to the wall or to the already packed layer and became immovable. At t = 20 s, a thin packed layer was mainly located near the bottom and lower sidewall, as seen in Figure 4a. Some grains descended to the bottom of the volume before being "captured" and may have accumulated there. However, the melt flow changed direction at the bottom of the ingot, moved toward the central axis, and rose to the middle region of the ingot. Consequently, some grains were dragged upward by the flow (Figure 3b), but with lower velocity (Figure 4b). It can be noted that the grain number density in the layer packed over the sidewall was slightly below the maximal value $n_{max} = 2 \times 10^9\ m^{-3}$, whereas at the ingot bottom and central axis this value could locally be as high as $6 \times 10^9\ m^{-3}$.

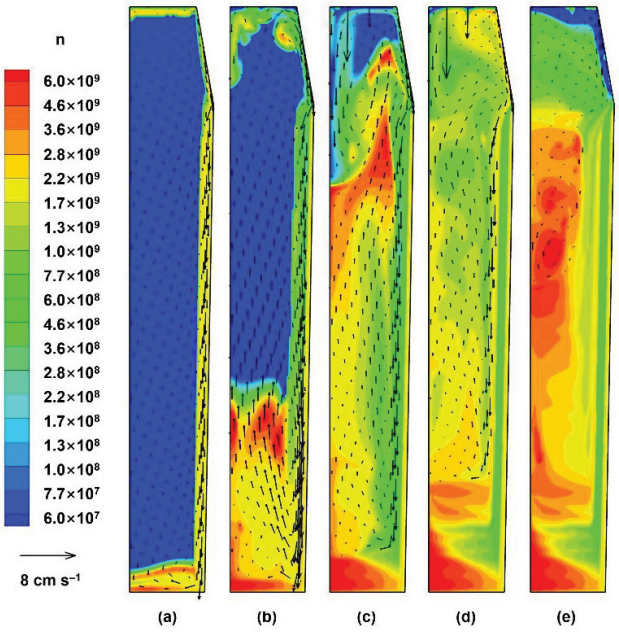

Figure 3. Grain number density distribution and velocity vectors of the grain phase at different times: (**a**) 20 s, (**b**) 50 s, (**c**) 100 s, (**d**) 200 s, and (**e**) 400 s. A logarithmic scale is used for the color map.

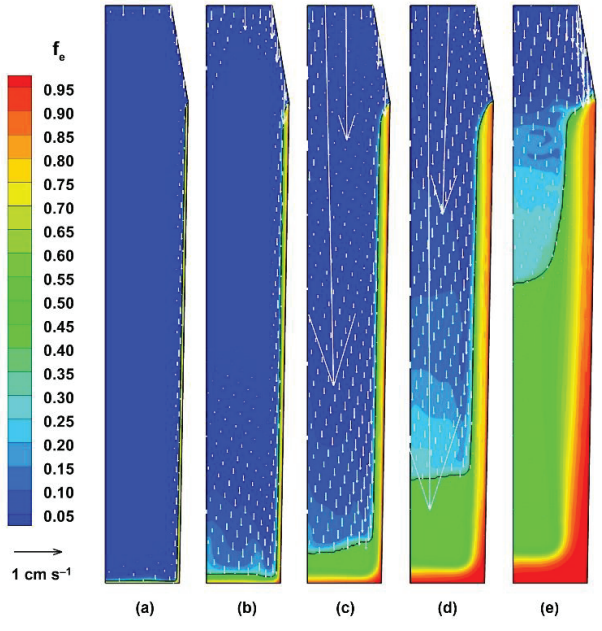

Figure 4. Grain phase fraction distribution and vectors of relative velocity between the *e*-phase and *l*-phase $\vec{u}_e - \vec{u}_l$, where the black line indicates the interface between packed and unpacked regions at different times: (**a**) 20 s, (**b**) 50 s, (**c**) 100 s, (**d**) 200 s, and (**e**) 400 s.

As the packing layer at the sidewall thickened, the temperature gradient and thermal buoyancy force at the solidification frontier decreased. The downward velocity of the liquid slowly decreased with time while the gravity force acting on the free-floating grains increased as they grew. At t = 100 s, the equiaxed grains ahead of the packed layer continuously descended to the bottom region, whereas the incoming flow from the upper region had virtually no nuclei or grains. In fact, the grain number density was low in these cells but remained above the 1 m^{-3} that prevents new nucleation there. Consequently, the grain number density in the region within 1 cm to 4 cm from the lateral surface was less than the mean value (Figure 3c). The lack of equiaxed grains in this region can explain why, in real ingots, the corresponding location is occupied by a columnar structure. At t = 100 s, a large grain number density was also observed in the upper region of the ingot, whereas the grain phase was mainly concentrated in the lower region (Figure 4c), indicating that a large number of small grains were dragged by the central upward flow. On the contrary, some larger equiaxed grains sedimented to the bottom since the buoyancy term related to their heavier mass prevailed over the upward drag force from the melt and piled up at the ingot center. This could be observed by grain number density at the ingot bottom, which was in the range of 3×10^9–6×10^9 m^{-3} (Figure 3c), and by the grain fraction distribution (Figure 4c).

As discussed below, solutal convection started to affect liquid phase flow after 100 s and supported the ascending melt flow near the central axis. At the same time, solid growth increased the mass of equiaxed grains, meaning that the grains in the upper region tended to fall down and continuously pile up toward the top of the ingot (Figures 3d and 4d). At t = 400 s, equiaxed grains had filled most of the volume in the chill mold. At a later stage, solidification slowed down as the heat transfer rate in the hot top region was much lower. Finally, at about t = 1000 s, the whole ingot was fully filled by packed grain, but solidification continued for a long time until the temperature dropped below the eutectic temperature of 1461.37 K [12]. However, we stopped the calculation at this stage because the grain distribution and macrosegregation would then barely change due to the very weak flow of residual liquid in the packed zone.

4.2. Macrosegregation Formation

Segregation in the ingot is characterized by the segregation index (SI), calculated as $SI = (c_{mix} - c_0)/c_0$, where the solute concentration for the solid and liquid mixture c_{mix} is calculated as the sum of the averaged concentration in the grain phase and extradendritic liquid weighted with corresponding volume fractions: $c_{mix} = f_e c_e + f_l c_l$. To understand the evolution of the segregation pattern presented in Figure 5, it should be borne in mind that solute is rejected at the interface between the solid phase and the interdendritic liquid and is transported to the extradendritic liquid according to the evolution of the fraction corresponding to the interdendritic liquid and by diffusion. In the model, the effect of convective flow on boundary layer thickness around the envelope surface is taken into account. Further distribution of the solute in the bulk is defined by the flow of extradenritic liquid, which is affected by thermal and solutal buoyancy force, as well as by grain motion.

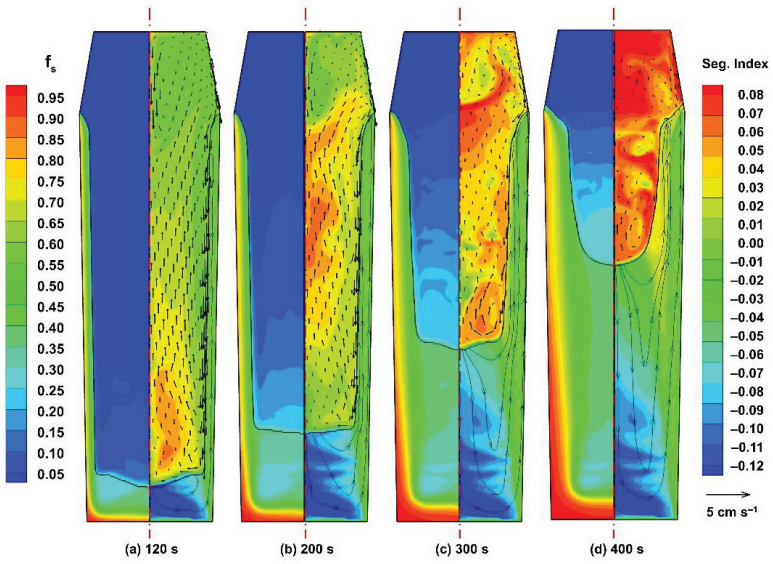

Figure 5. Solid phase fraction distribution (left half) and distribution of the solute concentration in the mixture overlapped by streamlines of fluid flow in the packed region and by velocity vectors of the liquid phase in the unpacked region (right half) at different times: (**a**) 120 s, (**b**) 200 s, (**c**) 300 s, and (**d**) 400 s. The black line indicates the interface between the packed and unpacked regions.

At the initial cooling stage, when both extradendritic liquid and grains descended along the wall, equiaxed grains grew but the solid fraction remained small. Consequently, little solute was rejected at this stage. The growth of the solid phase became noticeable inside the packed layer, mainly at the bottom, leading to the emergence of a "plume" near the central axis at 120 s, with an ascending flow as the extradendritic liquid enriched with carbon became lighter (Figure 5a). The upward flow inside the packed layer over the sidewall could probably be attributed to the pressure effect rather than to solutal buoyancy. However, to confirm this statement, additional parametric studies would be required. This flow was very weak since it occurred between grains whose fraction was within the range of 0.6–0.9, and provided strong resistance to the flow. The instantaneous segregation pattern presented at t = 200 s was defined by the redistribution of solute, which was continuously rejected by the solid phase growing in a lower ingot region, due to the upward flow of extrandendritic liquid. The latter was supported by solutal buoyancy but was counteracted by a drag force from descending grains (Figure 5b). Since the local value of solutal gravity was dependent on the solute distribution in the liquid and varied with time, it may have been balanced by the downward drag force or even conceded to the latter. This led to oscillation of the vertical component of velocity in the liquid in the central part of the ingot, resulting in negative segregation in the form of a "Christmas tree." Similarly, at a later stage (300 s and 400 s, Figure 5c,d, respectively), the clockwise vortex just above the packed layer was the result of upward solutal convection and the downward motion of grains. Incipient formation of vertical channels could be observed at t = 300 s (Figure 5c) at the edge of the packed layer, where the solid fraction increased (~0.3), whereas the extradendritic liquid flow still had a velocity in the order of several millimeters per second.

As mentioned above, we believed that the final segregation pattern could be evaluated at t = 1000 s (Figure 6c), since by that time the ingot was filled with packed grains with a fraction of more than 0.4 for most of the volume. Consequently, residual flow between the grains was negligibly small ($\sim 10^{-12}$ m s^{-1}) and practically did not affect distribution of the solute at the later solidification stage. As proof, it can be noted that the segregation

pattern at the bottom part of the ingot did not change between t = 400 s (Figure 5d, right) and t = 1000 s (Figure 6c, left), (note that the color scale is slightly different between the indicated figures), but changes occurred in the upper part of the ingot where grains were not yet packed at t = 400 s.

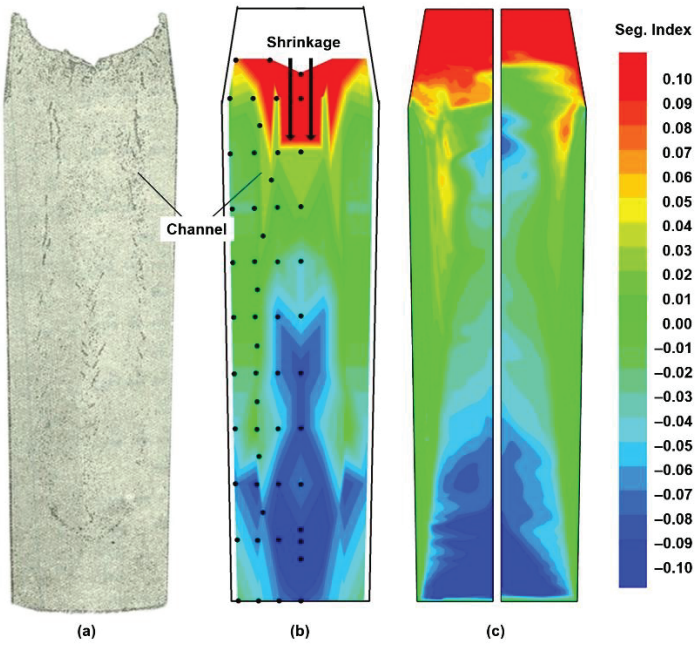

Figure 6. Comparison of the macrosegregation map between the experiment and the calculation: (**a**) sulfur print [1] (**b**) measured carbon segregation index [1], and (**c**) calculated carbon segregation index at t = 1000 s. Left: fine mesh. Right: coarse mesh.

Note that in Figure 6c, results obtained with two different grids with cell sizes of 5 mm × 5 mm and 10 mm × 10 mm are presented. Similar to previously reported studies, mesh size did not severely affect macrosegregation distribution. Rather, the difference related to mesoscale in terms of the number and location of the segregation channels at the upper part of the ingot and in the bottom zone of negative segregation. Thus, simulation with both grids showed vertical segregation channels (Figure 6c), the formation of which started at t = 300 s. However, with coarser mesh these channels were less pronounced and had a different configuration. It should be stressed that qualitatively similar vertical segregation lines were also observed in experiments near the columnar-equiaxed transition line (Figure 6b). The shape of the negative segregation zone obtained in the simulation was different than the reported one. In our opinion, this can be attributed mainly to the uncertainty of the boundary conditions that governed temperature distribution in the bottom corner of the ingot. Furthermore, the lack of measurements close to the ingot bottom did not really permit comparisons in the bottom vicinity. The discrepancy in height of the negative segregation zone between the experiments and the calculations probably indicates that interaction between ascending solutal flow and grain sedimentation was not extremely well reproduced. Yet again, this can be attributed to boundary conditions, since variation in cooling intensity clearly affected the height of that zone (Section 4.3). However, another option is the effect of shrinkage during solidification, which was not taken into account in the model and which could affect the flow of both phases when the solid fraction starts to develop. Moreover, an air gap may appear between the casting and the mold due to shrinkage, thereby increasing thermal resistance at the cooled wall and altering boundary

conditions. Finally, it is clearly shrinkage that affected segregation at the last solidification stage in the experiment and that defined solute distribution in the upper part of the ingot. Consequently, comparison was not really possible for this zone. We discuss the role of columnar dendrites in our conclusion.

A comparison of the segregation index along the central line between the calculation and the measurement (Figure 7) shows that the calculation accurately reproduced a general trend detectable in the measurements, i.e., negative segregation in the lower region and positive segregation in the upper region. Macrosegregation distribution along the central line predicted by the present model was compared with that carried out for the same-sized ingot with a three-phase mixed columnar-equiaxed model [20], in which equiaxed dendrites were considered globular. Similar to results reported elsewhere for 3.3 ton ingots [12,13], negative segregation at the centerline obtained with globular equiaxed grains was strongly overestimated [20], whereas results with the proposed description matched more accurately with the experiment.

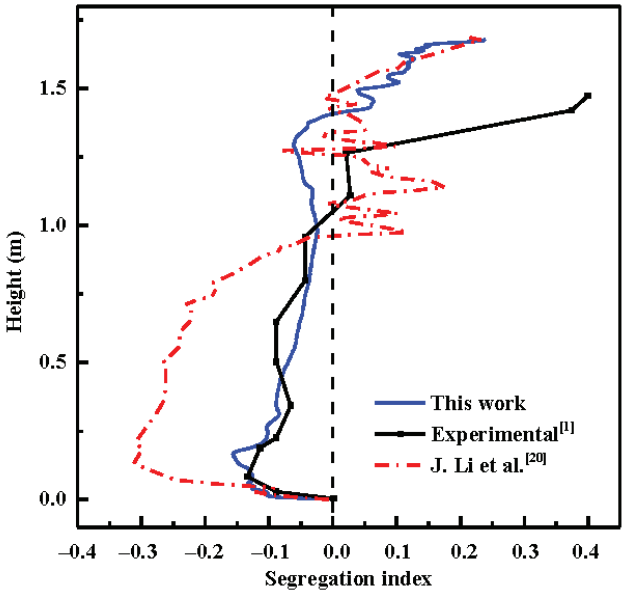

Figure 7. Comparison of the distribution of the segregation index along the central line of ingots between the calculation and the experimental measurement.

4.3. Effect of Mold Cooling Intensity

It has long been understood that an increase in ingot size favors macrosegregation formation. It has been demonstrated numerically that a special cooling procedure [22] or an increase in cooling rate [14] could alleviate macrosegregation. However, the effect of the cooling rate was studied with a fixed solid phase. In this section, we present a study aimed at verifying the effect of surface cooling intensity on final carbon macrosegregation with an equiaxed model. Initial conditions and ambient temperature remained the same as in the previous section, but the heat transfer coefficient h_{inf} was set to 100 W m^{-2} K^{-1}, 300 W m^{-2} K^{-1}, 600 W m^{-2} K^{-1}, and 1000 W m^{-2} K^{-1}. Although it is virtually impossible for the latter value of the heat transfer coefficient to be reached in industrial conditions, because this value was considered earlier [14] it is kept here as an illustration of a limiting case.

For all heat transfer coefficient values, the final distribution of the carbon concentration (Figure 8) presented positive segregation at the upper region of the ingot, which remained hot for a long time and was the last to solidify, and a negative cone near the ingot bottom.

However, as the value of h_{inf} increased, the volume of ingots with very low segregation, $-0.02 \leq \mathrm{SI} \leq 0.03$, also increased, whereas the height of the negative segregation cone at the bottom decreased. The positive segregation channels, discussed in Section 4.2, were also observed for higher values of the heat transfer coefficient (Figure 8c,d). However, their locations were transferred deeper into the ingot core, i.e., they moved closer to the axis of symmetry and farther from the top of the ingot.

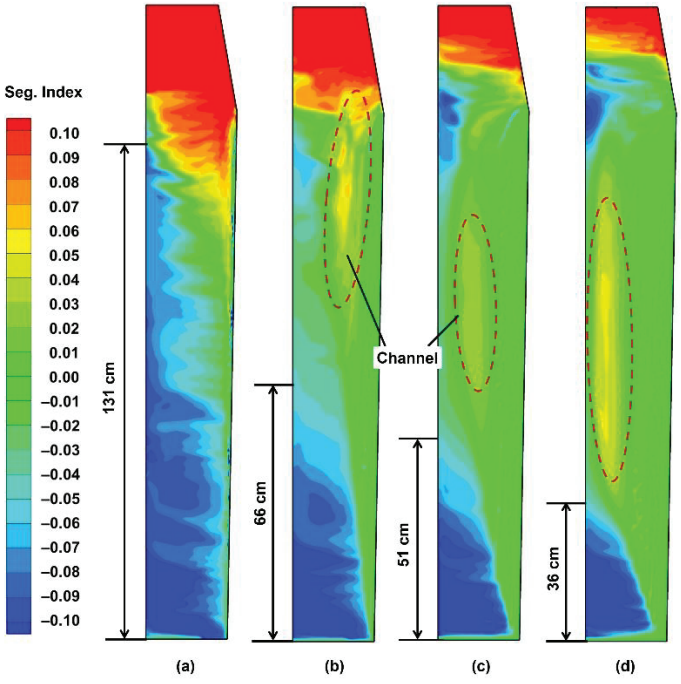

Figure 8. The final carbon segregation index profiles under different cooling intensities: (**a**) 100 W m^{-2} K^{-1}, (**b**) 300 W m^{-2} K^{-1}, (**c**) 600 W m^{-2} K^{-1}, and (**d**) 1000 W m^{-2} K^{-1}.

To explain the effect of the cooling rate at different solidification stages, it is appropriate to analyze fluid flow at characteristic points P_0 (0, 0.8), P_1 (0.1, 0.8), and P_2 (0.2, 0.8), the positions of which are indicated in Figure 1b. In Figure 9, a comparison of the evolution of the vertical component of liquid velocity over time at these points is presented for considered heat transfer coefficient values. Generally, the overall flow loop descended along the solidification front, which was parallel to the sidewall, and ascended in the ingot core, meaning that the vertical velocity had mainly a positive value at P_0 (Figure 9a) and mainly a negative value at P_2 (Figure 9c). When the grain phase was packed, liquid flow velocity approached zero due to large flow resistance from the fixed grain network. It is easy to observe that, at each point, the velocity obtained in the calculation with larger cooling coefficients reverted to zero at earlier stages.

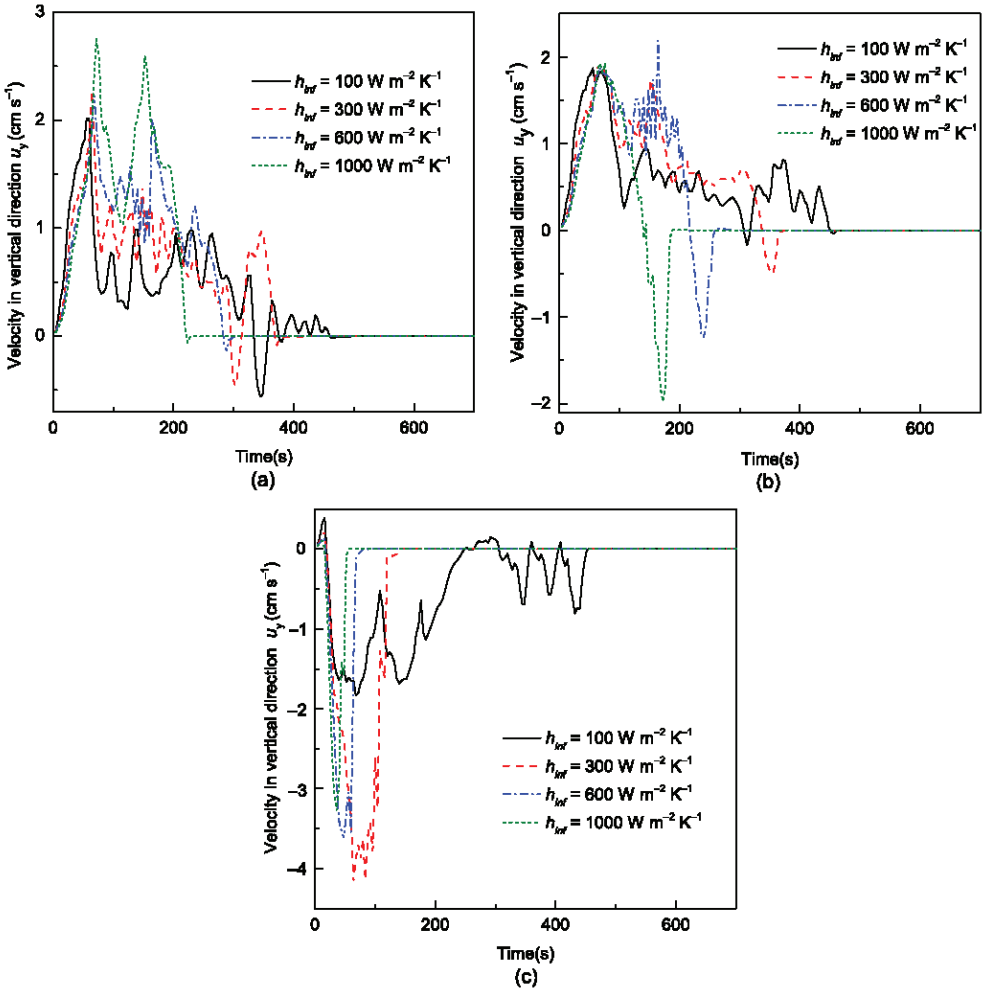

Figure 9. Variation in the vertical component of the liquid velocity at points P_0 (**a**), P_1 (**b**), and P_2 (**c**) during solidification for different values of the heat transfer coefficients.

The downward flow of liquid along the cooled sidewall intensified as the heat transfer coefficient increased. However it should be borne in mind that higher cooling rates promote earlier and faster growth of the solid phase, and this has a twofold effect. On the one hand, sedimentation of grains starts earlier everywhere in the volume and should be more intense. On the other hand, solute rejection at the solid–liquid interface also increases and contributes more intensively to the ascending flow. As already discussed above, the variation in the vertical component of velocity of extradendritic liquid near the axis and in the central part of the ingot is a result of competition between solutal upward convection and the downward drag effect from sedimenting grains.

Figure 9a shows that with stronger surface cooling, the upward flow rate at the central line monotonically increased with a maximal value of 2.27 cm s^{-1} for h_{inf} = 100 W m^{-2} K^{-1} versus 2.75 cm s^{-1} at t = 72 s for h_{inf} = 1000 W m^{-2} K^{-1}. That means that solutal buoyancy was stronger with a larger h_{inf} and that more grains, the solid fraction of which was still small, were transported by the central flow to the upper region under stronger cooling conditions. A decrease in velocity signified an increase in solid

fraction at point P_0, whereas, since the axial velocity remained positive, the downward drag force from the grains was not enough to reverse the liquid motion at the early stage of the process. Grains with a solid fraction descended, but "released" rejected solute that again helped intensify the upward solute convection. This process was repeated twice for $h_{inf} = 1000$ W m^{-2} K^{-1} with large variations in amplitude of axial velocity, and was stopped by the packed layer, which reached this height at ~200 s (Figure 10d). For smaller heat transfer coefficients, competition between growth of the solid fraction followed by descending grains and solutal convection gave rise to multiple flow oscillations that were finally also stopped due to grain packing. These oscillations gave an irregular form to the central zone of negative segregation.

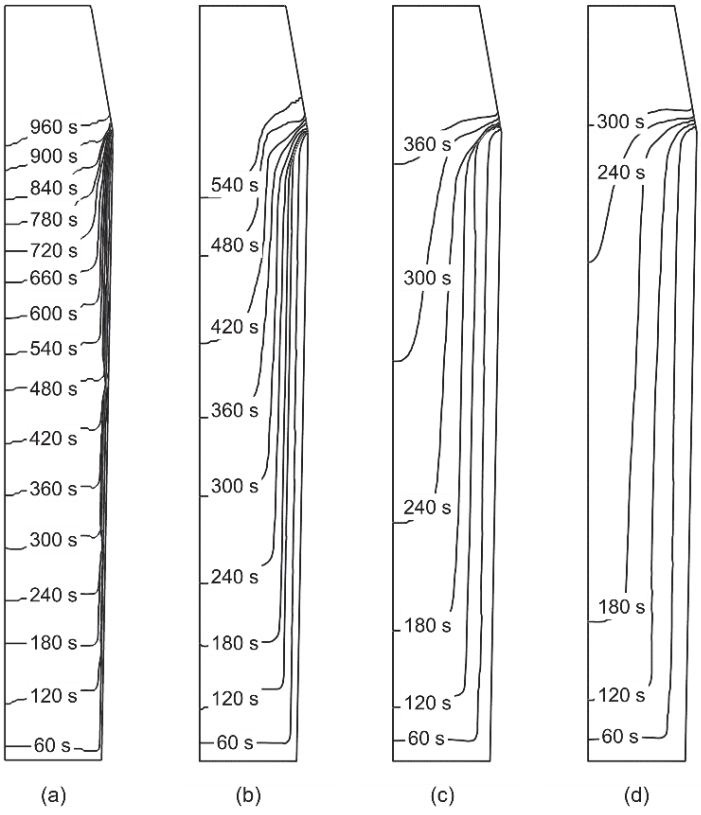

Figure 10. Packing line evolution at different heat transfer coefficients under different cooling intensities: (**a**) 100 W m^{-2} K^{-1}, (**b**) 300 W m^{-2} K^{-1}, (**c**) 600 W m^{-2} K^{-1}, and (**d**) 1000 W m^{-2} K^{-1}.

The results obtained at point P_2, 0.2 m from the central line and about 0.03 m from the ingot surface, are presented in Figure 9c. Here, the downward velocity value initially increased due to development of the flow field under the action of thermal buoyancy, before quickly reverting to zero when the packing layer reached that point. For the lowest value of the heat transfer coefficient, the process was different and was accompanied by flow oscillations that indicated flow instabilities similar to those described above. The effect of these instabilities on solute distribution in the ingot was also visible in Figure 8a as a variation in the segregation index near the ingot boundary. Finally, the flow behavior at point P_1, located 0.1 m from the central line (Figure 9b), presented a combination of effects described for point P_0 at the axis, which were followed by a change in flow direction to a descending one due to the sedimentation of the grains, the solid fraction of which was

sufficiently developed to counteract solutal convection. Yet with the lowest value of h_{inf}, velocity oscillations persisted until the packed layer was reached.

Finally, the evolution of the location of the zone edge (the packing line) for different cases is shown in Figure 10. The comparison was performed for periods of time, ranging from the beginning of cooling until the moment when the equiaxed grains piled up to the top of the mold. This took about 960 s, where $h_{inf} = 100$ W m^{-2} K^{-1}, 540 s where $h_{inf} = 300$ W m^{-2} K^{-1}, 360 s where $h_{inf} = 600$ W m^{-2} K^{-1}, and 300 s where $h_{inf} = 1000$ W m^{-2} K^{-1} for grains piling up the mold. After this, it took 500 more seconds for the equiaxed grains to fill the hot top region for each case. It should be noted that ingot solidification was still far from completion since the grains were packed at $f_e = 0.4$, whereas the solid fraction varied from 0.25 to 0.3.

5. Conclusions

A three-phase equiaxed solidification model was applied to study the formation of macrosegregation in a 2.45 ton industrial steel ingot. A comparison of the calculated macrosegregation with the reported measurements [1] showed their qualitative agreement despite uncertainties in boundary conditions and a rather sizeable simplification of physical phenomena in the model. Numerical results revealed flow instabilities related to competition between solutal and thermal buoyancy effects in the liquid, added to which was the gravity force acting on grains depending on the solid fraction. These instabilities led to an irregular form of the central zone with negative segregation perturbed by horizontal channels and the emergence of long vertical channels, also observed in experiments. However, V-type channels along the axis were not reproduced. The study of the effect of cooling intensity confirmed that stronger surface cooling relieves macrosegregation of ingots as flow is stabilized by faster development of the packed layer. Yet, in real industrial processes, improvement of cooling conditions is difficult because of the formation of an air gap between the solidifying ingot and the mold due to shrinkage. Therefore, more investigation is needed to improve the cooling conditions of chill molds.

One of the most important simplifications in the model is the absence of the shrinkage effect, which may alter the multiphase flow during the process once the solid phase starts to appear, and which is clearly responsible for the segregation pattern in the upper part of the ingot. The role of columnar growth, which is not taken into account in the model, is, however, less clear. Indeed, in simulation, a layer of packed grains along the cooled walls and bottom appeared quite quickly once the process began and somehow corresponded to columnar dendrites observed in various reported experiments [1,3,4,8,12] or calculations elsewhere [19,21].

Author Contributions: Conceptualization, E.W.; literature search, O.B. and T.W.; development of numerical code, T.W., Y.D. and Y.F.; calculation and production of figures, T.W.; data analysis, E.W., Y.D. and O.B.; mathematical description, Y.F.; original draft preparation, T.W. All authors have read and agreed to the published version of the manuscript.

Funding: This research was funded by the National Nature Science Foundation of China (Grant No. U1760206), the National Key R&D Program of China (Grant No. 2017YFE0107900), the Project of Introducing Talents of Discipline Innovation to Universities 2.0 (the 111 Project of China 2.0, No. BP0719037), and the ESA-MAP MICAST project contract 14347/01/NL/SH.

Institutional Review Board Statement: Not applicable.

Informed Consent Statement: Not applicable.

Data Availability Statement: No new data were created or analyzed in this study. Data sharing is not applicable to this article.

Conflicts of Interest: The authors declare no conflict of interest.

Appendix A

Equations for momentum conservation are required only for grain phase and for extradendritic liquid phase, and they are given with the Navier–Stokes equations coupled with a realizable $k_\varepsilon - \varepsilon$ turbulent model. Conditions for the grain packed region and unpacked region should be distinguished. If both phases can freely move, the momentum conservation equations are given by Equations (A1) and (A2) for the liquid and grain phases, respectively. If the grain phase becomes packed, the equation of motion for the grain phase reduces to $\vec{u}_e \equiv \vec{0}$ (instead of Equation (A2)) whereas the motion of the liquid is still described by Equation (A1).

$$\frac{\partial\left(f_l\rho_l\vec{u}_l\right)}{\partial t} + \nabla\left(f_l\rho_l\vec{u}_l\vec{u}_l\right) = -f_l\nabla P + \nabla\left[\left(\mu_l + \frac{\rho_l C_\mu k_\varepsilon^2}{\varepsilon}\right) f_l\left(\nabla\vec{u}_l + \left(\nabla\vec{u}_l\right)^T\right)\right] + \vec{F}_{Bl} + K_{le}\left(\vec{u}_e - \vec{u}_l\right) \quad \text{(A1)}$$

$$\frac{\partial\left(f_e\rho_e\vec{u}_e\right)}{\partial t} + \nabla\left(f_e\rho_e\vec{u}_e\vec{u}_e\right) = -f_e\nabla P + \nabla\left[\left(\mu_e + \frac{\rho_e C_\mu k_\varepsilon^2}{\varepsilon}\right) f_e\left(\nabla\vec{u}_e + \left(\nabla\vec{u}_e\right)^T\right)\right] + \vec{F}_{Be} + K_{le}\left(\vec{u}_l - \vec{u}_e\right) \quad \text{(A2)}$$

where $\vec{F}_{Bl}$ represents the bouyancy force, which is treated with the Boussinesque approximation for extradendritic liquid accounting for thermal and solutal expansion:

$$\vec{F}_{Bl} = f_l\rho_l\vec{g}\left[\beta_T\left(T_{ref}^b - T_l\right) + \beta_c\left(c_l^{ref} - c_l\right)\right] \quad \text{(A3)}$$

A similar term for the grain phase takes the Boussinesque approximation for interdendritic liquid and contains an additional term for the solid phase:

$$\vec{F}_{Be} = f_d\rho_l\vec{g}\left[\beta_T\left(T_{ref}^b - T_l\right) + \beta_c\left(c_l^{ref} - c_d\right)\right] + f_s\Delta\rho\vec{g} \quad \text{(A4)}$$

where c_l, c_d, and c_s are intrinsic solute concentrations associated with extradendritic liuid, interdendritic liquid, and solid phases, respectively, $\Delta\rho$ is the difference between solid phase density and reference density.

For the free-floating region, i.e., $f_e < f_p^e$, the momentum exchange coefficient between the liquid and grain phases K_{le} is calculated with the Happel model [27]. When $f_e \geq f_p^e$, the coefficient K_{le} is evaluated with the Kozeny–Carman equation:

$$K_{le} = \begin{cases} 18 f_l^2 f_e \frac{\mu_l}{d_e^2} \frac{2+4/3 f_e^{5/3}}{2-3f_e^{1/3}+3f_e^{5/3}-2f_e^2} & f_e < f_p^e \\ 150\mu_l f_e^2 / \left(d_k^2 f_l^3\right) & f_e \geq f_p^e \end{cases} \quad \text{(A5)}$$

The governing equations for k_ε and ε are given below.

$$\frac{\partial(\rho_m k_\varepsilon)}{\partial t} + \nabla\cdot\left(\rho_m\vec{u}_m k_\varepsilon\right) = \nabla\left[\left(\mu_m + \frac{\mu_{t,m}}{\sigma_k}\right)\nabla k_\varepsilon\right] + G_{k,m} - \rho_m\varepsilon \quad \text{(A6)}$$

$$\frac{\partial(\rho_m\varepsilon)}{\partial t} + \nabla\cdot\left(\rho_m\vec{u}_m\varepsilon\right) = \nabla\left[\left(\mu_m + \frac{\mu_{t,m}}{\sigma_\varepsilon}\right)\nabla\varepsilon\right] + \rho_m C_1 S\varepsilon - \rho_m C_2\frac{\varepsilon^2}{k_\varepsilon + \sqrt{\mu_{t,m}\varepsilon/\rho_m}} \quad \text{(A7)}$$

where index m is used for the mixture of l- and e-phases, whose properties are defined as $\rho_m = f_l\rho_l + f_e\rho_e$, $\mu_m = f_l\mu_l + f_e\mu_e$, $\vec{u}_m = \left(f_l\rho_l\vec{u}_l + f_e\rho_e\vec{u}_e\right)/\rho_m$. Closure relations and values for the constants used in Equations (A1)–(A7) are given in Table A1.

Table A1. Empirical constants and functions in the realizable $k_\varepsilon - \varepsilon$ model.

Parameters	Parameters
$G_{k,m} = 2\mu_t S^2$	$S = \sqrt{S_{ij}S_{ij}}$
$\mu_{t,m} = \rho_m C_\mu k_\varepsilon^2/\varepsilon$	$C_1 = max\ [0.43, \eta/(\eta+5)]$
$S_{ij} = 1/2\left(\partial u_j/\partial x_i + \partial u_i/\partial x_j\right)$	$C_\mu = 1/(4.04 + A_s k_\varepsilon U^*)/\varepsilon)$
$\eta = \sqrt{2}Sk_\varepsilon/\varepsilon$	$\varphi = \cos^{-1}\left(\sqrt{6}W\right)/3$
$A_s = \sqrt{6}\cos\varphi$	$\Omega_{ij} = 1/2\left(\partial u_j/\partial x_i - \partial u_i/\partial x_j\right)$
$U^* = \sqrt{S_{ij}S_{ij} + \widetilde{\Omega}_{ij}\widetilde{\Omega}_{ij}}$	$W = S_{ij}S_{jk}S_{ki}/S^3$
$C_2 = 1.9$	$A_0 = 4.4$
$\sigma_k = 1.0$	$\sigma_\varepsilon = 1.2$

References

1. Report on the heterogeneity of steel ingots. *J. Iron Steel Inst.* **1926**, *113*, 39–176.
2. Flemings, M.C. Directional Solidification and Composite Structures. In *Surfaces and Interfaces II*; Springer: Boston, MA, USA, 1968; pp. 313–352.
3. Fredriksson, H.; Hillert, M. On the formation of the central equiaxed zone in ingots. *Metall. Trans.* **1972**, *3*, 569–574. [CrossRef]
4. Fredriksson, H.; Nilsson, S.O. On the formation of macrosegregations in ingots. *Metall. Trans. B* **1978**, *9*, 111–120. [CrossRef]
5. Mehrabian, R.; Keane, M.A.; Flemings, M.C. Experiments on macrosegregation and freckle formation. *Metall. Trans.* **1970**, *1*, 3238–3241.
6. Fujii, T.; Poirier, D.R.; Flemings, M.C. Macrosegregation in a multicomponent low alloy steel. *Metall. Trans. B* **1979**, *10*, 331–339. [CrossRef]
7. Gu, J.P.; Beckermann, C. Simulation of convection and macrosegregation in a large steel ingot. *Metall. Mater. Trans. A Phys. Metall. Mater. Sci.* **1999**, *30*, 1357–1366. [CrossRef]
8. Combeau, H.; Založnik, M.; Hans, S.; Richy, P.E. Prediction of macrosegregation in steel ingots: Influence of the motion and the morphology of equiaxed grains. *Metall. Mater. Trans. B Process Metall. Mater. Process. Sci.* **2009**, *40*, 289–304. [CrossRef]
9. Pardeshi, R.; Voller, V.R.; Singh, A.K.; Dutta, P. An explicit-implicit time stepping scheme for solidification models. *Int. J. Heat Mass Transf.* **2008**, *51*, 3399–3409. [CrossRef]
10. Pickering, E.J. Macrosegregation in steel ingots: The applicability of modelling and characterisation techniques. *ISIJ Int.* **2013**, *53*, 935–949. [CrossRef]
11. Vannier, I.; Combeau, H.; Lesoult, G. Numerical model for prediction of the final segregation pattern of bearing steel ingots. *Mater. Sci. Eng. A* **1993**, *173*, 317–321. [CrossRef]
12. Založnik, M.; Combeau, H. Thermosolutal flow in steel ingots and the formation of mesosegregates. *Int. J. Therm. Sci.* **2010**, *49*, 1500–1509. [CrossRef]
13. Li, W.; Shen, H.; Zhang, X.; Liu, B. Modeling of species transport and macrosegregation in heavy steel ingots. *Metall. Mater. Trans. B Process Metall. Mater. Process. Sci.* **2014**, *45*, 464–471. [CrossRef]
14. Meng, Q.; Wang, F.; Li, C.; Li, M.; Zhang, J.; Cui, G. Numerical simulation of macrosegregation in water-cooled heavy flat ingot during solidification. *JOM* **2014**, *66*, 1166–1174. [CrossRef]
15. Chuang, Y.-K.; Schwerdtfeger, K. Equations for Calculating Sedimentation Segregation in Killed Steel. *Arch. Eisenhuttenwes.* **1975**, *46*, 303–310.
16. Beckermann, C.; Wang, C.Y. Multiphase/-scale modeling of alloy solidification. *Annu. Rev. Heat Transf.* **1995**, 115–198. [CrossRef]
17. Li, W.S.; Shen, H.F.; Liu, B.C. Numerical simulation of macrosegregation in steel ingots using a two-phase model. *Int. J. Miner. Metall. Mater.* **2012**, *19*, 787–794. [CrossRef]
18. Nguyen, T.T.M.; Gandin, C.A.; Combeau, H.; Založnik, M.; Bellet, M. Finite Element Multi-scale Modeling of Chemical Segregation in Steel Solidification Taking into Account the Transport of Equiaxed Grains. *Metall. Mater. Trans. A Phys. Metall. Mater. Sci.* **2018**, *49*, 1725–1748. [CrossRef]
19. Wu, M.; Nunner, G.; Ludwig, A.; Li, J.; Schumacher, P. Evaluation of a mixed columnar-equiaxed solidification model with laboratory castings. *IOP Conf. Ser. Mater. Sci. Eng.* **2012**, *27*, 012018. [CrossRef]
20. Li, J.; Wu, M.; Ludwig, A.; Kharicha, A. Simulation of macrosegregation in a 2.45-ton steel ingot using a three-phase mixed columnar-equiaxed model. *Int. J. Heat Mass Transf.* **2014**, *72*, 668–679. [CrossRef] [PubMed]
21. Leriche, N.; Combeau, H.; Gandin, C.A.; Založnik, M. Modelling of columnar-to-equiaxed and equiaxed-to- columnar transitions in ingots using a multiphase model. *IOP Conf. Ser. Mater. Sci. Eng.* **2015**, *84*, 1–8. [CrossRef]
22. Ge, H.; Ren, F.; Cai, D.; Hao, J.; Li, J.; Li, J. Gradual-cooling solidification approach to alleviate macrosegregation in large steel ingots. *J. Mater. Process. Technol.* **2018**, *262*, 232–238. [CrossRef]

23. Wu, M.; Ludwig, A.; Kharicha, A. A four phase model for the macrosegregation and shrinkage cavity during solidification of steel ingot. *Appl. Math. Model.* **2017**, *41*, 102–120. [CrossRef]
24. Wang, T.; Semenov, S.; Wang, E.; Delannoy, Y.; Fautrelle, Y.; Budenkova, O. Effect of Diffusion Length in Modeling of Equiaxed Dendritic Solidification under Buoyancy Flow in a Configuration of Hebditch-Hunt Experiment. *Metall. Mater. Trans. B* **2019**, *50*, 3039–3054. [CrossRef]
25. Wang, T.; Hachani, L.; Fautrelle, Y.; Delannoy, Y.; Wang, E.; Wang, X.; Budenkova, O. Numerical modeling of a benchmark experiment on equiaxed solidification of a Sn–Pb alloy with electromagnetic stirring and natural convection. *Int. J. Heat Mass Transf.* **2020**, *151*, 119414. [CrossRef]
26. Lipton, J.; Glicksman, M.E.; Kurz, W. Dendritic growth into undercooled alloy metals. *Mater. Sci. Eng.* **1984**, *65*, 57–63. [CrossRef]
27. Happel, J. Viscous flow in multiparticle systems: Slow motion of fluids relative to beds of spherical particles. *AIChE J.* **1958**, *4*, 197–201. [CrossRef]
28. Kubota, K.; Murakami, K.; Okamoto, T. Fluid flow and macrosegregation in cylindrical ingots. *Mater. Sci. Eng.* **1986**, *79*, 67–77. [CrossRef]
29. Sun, H.; Zhang, J. Study on the Macrosegregation Behavior for the Bloom Continuous Casting: Model Development and Validation. *Metall. Mater. Trans. B* **2014**, *45*, 1133–1149. [CrossRef]
30. Badillo, A.; Ceynar, D.; Beckermann, C. Growth of equiaxed dendritic crystals settling in an undercooled melt, Part 2: Internal solid fraction. *J. Cryst. Growth* **2007**, *309*, 216–224. [CrossRef]
31. Dou, K.; Yang, Z.; Liu, Q.; Huang, Y.; Dong, H. Influence of Secondary Cooling Mode on Solidification Structure and Macrosegregation Behavior for High-carbon Continuous Casting Bloom. *High Temp. Mater. Process.* **2017**, *36*, 741–753. [CrossRef]

metals

MDPI

Review

A Review of Large-Scale Simulations of Microstructural Evolution during Alloy Solidification

Nicholas Cusato [1], Seyed Amin Nabavizadeh [2] and Mohsen Eshraghi [1,*]

[1] Department of Mechanical Engineering, California State University, Los Angeles, 5151 State University Drive, Los Angeles, CA 90032, USA
[2] Department of Mechanical Engineering, The University of Akron, Auburn Science and Engineering Center 101, Akron, OH 44325, USA
* Correspondence: mohsen.eshraghi@calstatela.edu

Abstract: During the past two decades, researchers have shown interest in large-scale simulations to analyze alloy solidification. Advances in in situ X-ray observations of the microstructural evolution of dendrites have shown defects that can be very costly for manufacturers. These simulations provide the basis for understanding applied meso-/macro-scale phenomena with microscale details using various numerical schemes to simulate the morphology and solve for transport phenomena. Methods for simulating methodologies include cellular automaton, phase field, direct interface tracking, level set, dendritic needle networks, and Monte Carlo while finite element, finite difference, finite volume, and lattice Boltzmann methods are commonly used to solve for transport phenomena. In this paper, these methodologies are explored in detail with respect to simulating the dendritic microstructure evolution and other solidification-related features. The current research, from innovations in algorithms for scaling to parallel processing details, is presented with a focus on understanding complex real-world phenomena. Topics include large-scale simulations of features with and without convection, columnar to equiaxed transition, dendrite interactions, competitive growth, microsegregation, permeability, and applications such as additive manufacturing. This review provides the framework and methodologies for achieving scalability while highlighting the areas of focus that need more attention.

Keywords: solidification; microstructure; numerical modeling; large-scale simulation; dendrite growth

Citation: Cusato, N.; Nabavizadeh, S.A.; Eshraghi, M. A Review of Large-Scale Simulations of Microstructural Evolution during Alloy Solidification. *Metals* **2023**, *13*, 1169. https://doi.org/10.3390/met13071169

Academic Editors: Changming Fang and Chang Yong Jo

Received: 26 April 2023
Revised: 14 June 2023
Accepted: 15 June 2023
Published: 23 June 2023

1. Introduction

The research in the simulation of dendritic growth during alloy solidification used to be limited to small-scale, single dendrites that did not fully capture all of the physics behind solidification. The computation power and cost required for superior analysis have been the main hindrance for performing more complex, large-scale simulations. This article outlines the advances in both mathematical models and computational hardware/software that enable large-scale simulations of solidification microstructure.

While there is a significant amount of work on modeling solidification microstructure and dendrite growth including a few review papers from distinguished researchers [1,2], there has not been a review work on the large-scale modeling of solidification microstructure covering the various numerical techniques, computational methods, and examples of what has been accomplished thus far.

The goal of this review is to provide a comprehensive compilation of the most current research that has been conducted on large-scale simulations of solidification microstructure using advanced computing methods. Large-scale simulations of dendritic growth can greatly benefit manufacturing and materials engineers and scientists, offering a detailed understanding of microstructural evolution during solidification processes. Reducing the trial and error of the manufacturing process, the simulations save time, providing a greater understanding of the microstructure and defect formation. Many advances in in situ X-ray observations of solidification have identified areas that can benefit from the

large-scale realistic modeling of dendrites [3–10]. Lee and Hunt [11] first examined slabs of Al–Cu alloys for hydrogen pores in situ during directional solidification (DS). They discovered that as the growth speed of the dendrites increased, along with hydrogen content, the shape of the pores evolved into a "worm-hole-like" shape. Defects that form can be caused by numerous conditions such as gas bubbles, segregation, and tears as well as other factors that can be difficult to predict due to the rheological behavior of the mushy zone [12,13]. This cycle of casting and taking x-rays of the samples are both costly and time consuming. Therefore, a lot of research has been conducted to understand the physics behind these defects [14–21] and reproducing them using computer simulations. The initial simulations produced two-dimensional (2D) axisymmetric, branchless dendrite features that lacked the details needed to understand the issues that develop during the manufacturing processes. Therefore, there are three-dimensional (3D) aspects that are not captured by 2D simulations, which will be discussed in detail in later sections. However, 3D simulations require extensive computing power and algorithms to scale. Recent advances in the large-scale simulation of the solidification microstructure have produced some astonishing new discoveries [22]. This has been made possible thanks to developments in parallelization and supercomputing. State-of-the-art hardware and algorithm techniques have enabled researchers to produce computations that used to be seen as impossible. The ability to see high resolution in the formation of microstructures has never been more accessible. The size, spacing, and morphology of dendritic arms show a significant effect on the properties of the solidified materials [1].

Solidification modeling is a complex multiphysics problem including fluid flow, heat, and solute diffusion aspects. There is also a need to solve equations for phase change or track the interface to simulate the morphology. The morphology of the dendrites can be captured using cellular automaton (CA), phase field (PF), direct interface tracking (DIT), level set (LS), or dendritic needle networks (DNN) methods [21]. In terms of reproducing the physics, PF is one of the best methods to simulate dendrite growth accurately when compared to the front-tracking, boundary integral methods, and CA. However, depending on the aspect under consideration, each method has its own strengths and shortcomings. The majority of large-scale simulations of dendrite growth have used PF and CA methods. The transport phenomena, which consists of either heat transfer, diffusion, and fluid flow, can be solved using finite element (FE), finite difference (FD), finite volume (FV), or lattice Boltzmann (LB) methods. Scalability is accomplished using computational approaches that can take advantage of increasing the number of processing units. The selected numerical methods need to be scalable, making it easier to implement different parallelization techniques by using threads, message passing interface (MPI) [23–28], and compute unified device architecture (CUDA) [29–32], among other methods. Reducing the computational time is still a challenge for large-scale simulation. Therefore, many strategies have been developed over the years to address the computational time. Some researchers have focused on utilizing parallel computing algorithms to speed up the simulation while others have tried to optimize the meshing method and reduce the overall computational time by using the adaptive mesh refinement (AMR) strategy [33] or by applying different grid size and time step methods [34,35].

From a computational power point of view, technology is increasing toward Moore's law and the exascale era is already upon us [36–38]. Supercomputing has provided a small deviation from expectations, now known as the post-Moore era [39,40]. Now, the strategy to increase the ability to model dendritic solidification is finding limitations in mathematical models and algorithms. This limitation is partly associated with interpolation of the quantities around the interface of the dendrite where sharp gradients are present. By implementing an adaptive grid refinement model, the code's capability will be extended to a more accurate prediction of the interfacial region. In the AMR algorithm, finer grids are used for sharp gradient regions such as the solid–liquid interface, while the mesh coarsens in the rest of the computational domain. As a result, most computation time is spent solving the region occupied by the mushy zone. This method has been used by many

researchers separately or in combination with other parallelization methods to reduce the computational time [41–43]. Recently, parallel-GPU AMR has shown great promise in combining the effectiveness of the AMR scheme with the power of GPU computing [44–46]. This allows for high-speed simulations of purely diffusive dendrite growth.

These outstanding large-scale simulations have inspired many researchers to perform analysis on realistic grain growth. As an example, Miyoshi et al. [47] conducted a PF simulation study of ideal grain growth in an ultra-large-scale domain. Using a supercomputer, TSUBAME 2.5 at the Tokyo Institute of Technology, which consists of 1408 nodes, the team was able to investigate the number of sample grains that are necessary for repeatable results for grain size distributions. The largest domain consisted of 2560^3 grid points, which consisted of 3,125,00 initial grains. At this time and scale, it was the largest simulation performed by a factor of 10. This was an effective performance for observing and quantifying the steady-state growth behaviors. Another impressive simulation of large-scale was performed by Sakane et al. [48], who used a quantitative PF model to simulate a dilute binary alloy's (Al-3 wt.% Cu) grain growth under the influence of forced convection. A directional solidification condition was produced in a system with dimensions of $3.072 \times 3.078 \times 3.072$ mm^3. The computation of 1024^3 mesh points, during 60,000 steps, was completed using 128 GPUs within four hours. Their PF model could provide consistent results independent of the interface thickness. An LB model was coupled to simulate the melt flow.

The focus of this paper is to highlight important research on the large-scale simulation of dendritic growth and other microscale solidification features. We will discuss numerical methods as well as computational approaches used to produce large-scale simulations of the solidification microstructure. The actual domain size of these simulations depends on the physics considered and the features that are being simulated. The structure of this review will focus on the increasing complexity of features. Many case studies will be discussed in the following order: dendritic interactions and competitive growth; columnar to equiaxed transition (CET); solute transport and segregation; natural and forced convection; permeability. The details for each subject are outlined with respect to both the mathematical/computational models as well as the physical nature of the simulations.

2. Methods for Simulating the Morphology

The process of capturing the interface morphology in simulations can be accomplished with the CA, PF, DIT, or LS methods. Each method has its unique advantages and deficiencies. CA, which is relatively simple, stands alone from the others because of its local structure and will be discussed first. PF is probably the most powerful and will be analyzed with respect to some of the most notable case studies. Third, DIT will be discussed to feature the differences using a couple of research examples. Finally, the LS method will be reviewed, which is similar to DIT but requires knowledge about the temperature gradients at the interface. Dendrite needle network (DNN) and Monte Carlo (MC) methods will also be discussed. By simulating the morphology of dendrites, the complexity in geometry can be incorporated for the large-scale domain for manufacturing purposes.

2.1. Cellular Automation

CA is ideal for large-scale modeling simulations as its structure is considered local with respect to the objective domain. The ability to approach the morphology naturally, in a localized manner, allows for easy scalability on many processors. In the 1940s, the CA method was developed by John von Neumann using simple microscopic laws to model complex, macroscopic phenomena physically [49]. With a successful application in metallurgy, the CA method can accurately simulate processes such as grain growth, cracking, diffusion, or mechanical deformation. By superimposing a grid of cells on the area of interest, the evolution of these physical processes can be reproduced. State indices and variables are attributed to cells that evolve based on transition rules [50], outperforming the standard GPU implementations, making this effective for scalability as the interactions

of cells can be defined in three dimensions. Advantages over PF include being able to develop a spatial resolution by the order of magnitude of the smallest microstructure feature size [51]. CA is highly parallelizable, making it two orders of magnitude faster than alternative PF methods [52].

One of the largest strictly CA methodologies was recently performed by Zhang et al. (shown below in Figure 1) [53]. The study focused on the simulation of an Fe–C alloy during isothermal and directional solidification while using the CA model to simulate the CET. Using the CA model in combination with GPUs and MPI, the maximal speed-up ratio was measured to be 153.19. They were able to study the effects of increasing the cooling rate among other conditions, which promotes the occurrence of equiaxed dendrites ahead of the solidification front. The CA code was able to process 768^3 grids within 27.42 min for 8000 time steps. They were able to solve the problem of data race in the CA model by introducing an additional field variable with a modification to the capture rule. CA is regularly coupled with methods to solve for solute transport given its functional, elemental nature that allows it to be scaled [54–56]. The CA algorithm accounts for heterogeneous nucleation, the preferential growth directions, and growth kinetics of the dendrites [57]. Rafii-Tabar and Chirazi provide a comprehensive analysis of modeling solidification techniques in their review on multiscale modeling using CA and coupling techniques [58]. CA is often coupled with other methods such as FE and FD, which are described in later sections of this review in context to AM applications.

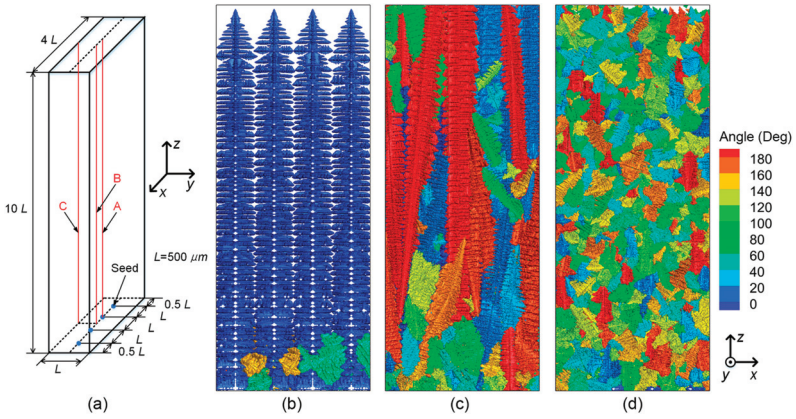

Figure 1. Directional solidification of the Fe-0.6 wt.% C alloy in a domain consisting of 400 × 100 × 1000 cells and a grid size of 5 μm, represented in (**a**) as a configuration of the computational domain at various nucleation angles and cooling rates: (**b**) 1 K/s, (**c**) 5 K/s, and (**d**) 10 K/s [53].

2.2. Phase Field

The PF method is a powerful and versatile tool to model microstructural dynamics [59,60]. Many phenomena can be represented using a simple set of differential equations [61]. Using continuous fields to describe the interfaces, the discontinuities of properties and boundary conditions are represented by a variation of one or more auxiliary field. These phase fields across a diffused interface are solved by integrating partial differential equations for the whole domain. Free-boundary problems with arbitrary complex interfaces are notoriously challenging [62].

Kobayashi [63] first brought the PF modeling of dendritic growth to the public's attention in 1993, showing a simple simulation for one component melt growth and showed its ability to solve the free-boundary problem. PF solves the time evolution equation of the PF variable, Ø. This was introduced to express the phase state (solid or liquid) of the material, in which the sharp interface is replaced by a diffuse interface. With a finite thickness, the PF variable has a smooth, but steep change. The versatility of the PF method allows for the simulation of the interface migration without tracking of the interface [64].

By simply solving an equation, PF can solve for the solid concentration, curvature of the interface energy, and capture the interface based on computational tracking. Kobayashi actually produced movies of grain growth simulation in 3D prior to 1990 [65], which inspired researchers to reproduce this method for larger scale domains.

PF is very computationally taxing, where the meshes for the interface require high density. AMR has been implemented on a large scale under certain conditions [66] such as 3D modeling [67–69] (but mostly 2D conditions due to limitations) as computational efficiency decreases as the volume fraction of the interface increases [70]. Therefore, parallel computational schemes are necessary for very large-scale simulations using a quantitative PF model. Shibuta et al. [71] utilized a supercomputer and PF to simulate the competitive growth of dendrite assemblages. They discussed convergence behavior that enabled the use of a large interface thickness. At the time (2011), it was the largest reported simulation of dendrite growth for a domain of 3.072 mm^3 for a total time of 100 s, using 768 GPUs on the supercomputer TSUBAME 2.0 (TSUBAME 2.5's predecessor). It is computationally oppositional to obtain a realistic looking microstructure and an extremely thin interface [72]. PF parameters are derived at a thin interface limit [73], which is competitively being pushed further.

Two years later, Takaki et al. [74] used the TSUBAME 2.0 for a very-large-scale 3D PF simulation of directional solidification of $3.072 \times 3.078 \times 3.072$ mm^3, which was equivalent to $4096 \times 4104 \times 4096$ meshes. This research produced interesting results (Figure 2), where unfavorably oriented dendrites and highly complicated interactions could be observed. As a result, controlling microstructures in terms of crystallographic structures has been considered for more complex structures. This is important as it expanded on both the domain size and complexity that was previously discussed by Shibuta et al. [71].

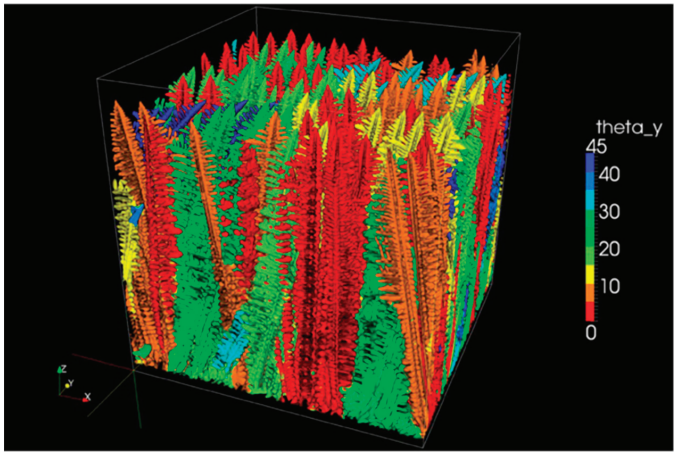

Figure 2. Simulation of competitive columnar dendrite growth by large-scale PF simulations where the inclination angle is indicated by color [74].

In order to simulate large-scale microstructures using PF models, the PF interface is required to be scaled up much larger than the physical interface to remove several artifacts that step from the thickness of the interface [75]. Using interpolation functions for average diffusivities and grand potentials of the bulk phases, the interface stretching is eliminated. The interface also faces (unrealistic) movement from the relaxation that can be countered by asymptotic analysis. Finally, artificial solute trapping can be mitigated by anti-trapping formulations [76]. These conditions need to be met to scale to higher resolutions while maintaining accuracy using PF methods. PF's advantage over the other methods lies within the field variables, which eliminate the need to identify and track the interface. Tourret et al. highlighted some of the most recent applications, perspectives, and challenges in PF modeling in the most recent review [60].

2.3. Direct-Interface-Tracking

DIT, a front tracking method, is a successful methodology for solving the energy equation as well as momentum and mass conservation equations. This requires treating the interface as incompressible. Since it requires the calculation of the temperature gradients at the interface in combination with the normal velocity and curvature of the interface, DIT is less powerful in comparison to the other techniques already mentioned [22].

Zhu et al. [77] used a quantitative virtual front tracking model, which is characterized by its mesh independency, to simulate 2D dendrite growth in the low Pèclet number regime. This means that the results converge to a finite value when the mesh size is refined. It has been observed that the mesh dependency is influenced by the methods of curvature and solid fraction calculations [78]. The simulated columnar dendrite evolution of an Al-4 wt.% Cu alloy was calculated in a domain of 600 × 1200 meshes on a single CPU in about 11 h of computational time. Figure 3 shows the evolution of the dendrites after 12 s when comparing the grain boundaries and solute map. The equilibrium composition was compared in good agreement to the LGK model.

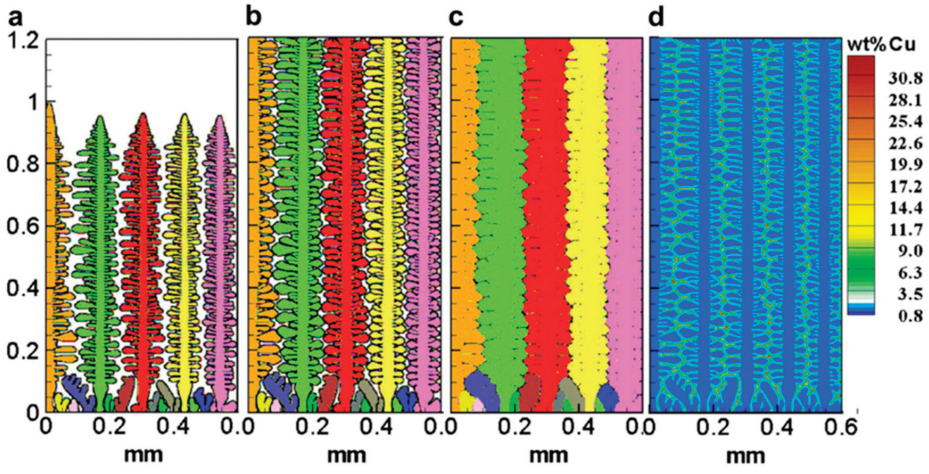

Figure 3. Evolution of directional solidification with the thermal gradient after (**a**) 2 s, (**b**) 3.2 s, (**c**,**d**) 12 s, (**a**–**c**) shows the grain boundaries and (**d**) solute map [77].

This process is considered with direct numerical simulations of flows with phase change. Tryggvason et al. [79] expanded on a multiphase flow model where different material properties in each phase were added at the phase boundaries. Juric et al. [80] used this method to observe complex dendritic structures such as liquid trapping, tip-splitting, side branching, and coarsening. This efficiently handles discontinuities in material properties between liquid and solid phases. DIT produces a method for simulating morphology that can be further defined based on tracking criteria. Front tracking explicitly provides the location of the interface at all times.

2.4. Level Set

Tracking the interface can be accomplished either explicitly or implicitly. Explicit tracking such as front tracking requires special care for topological changes [81]. Overcoming this is difficult in 3D; however, implicit representations such as LS or PF can handle these topological changes in a straightforward manner. LS represents the front as a level set of continuous functions. LS simulations are simple, which is an advantage, especially when computing the curvature. LS is similar to PF [82] as it also interchanges the interface with a field variable; however, it requires the knowledge of the direction in which the

solid front is advancing (along with its velocity and calculation of the normal vector from the interface) [83].

Tan et al. [84] utilized a LS simulation that combined the features of front-tracking and fixed-domain. A domain decomposition of eight domains was performed using the Cornell CTC supercomputer [85] for 5 h, while the 3D simulation of a single dendrite required 12 h with 16 nodes (each of the nodes consisted of two 2048 MHz CPUs). They were able to prove that the method provides accurate tracking of the interfaces, computation of the heat/mass/momentum transport avoiding boundary conditions, adaptive meshing, and the capability of multiple solid phases. The research involved a reasonable mesoscale value for a mesh width of 12.2 μm for the diffused interface for a full mesh of 1024 × 2048. In another study, Tan et al. [86] modeled multiple dendrite interaction with undercooling in the front using a LS method in a 3D domain. A solidification speed of 3000 μm/s and thermal gradient of 1400 K/cm was required for nucleation and is shown in the simulation below (Figure 4).

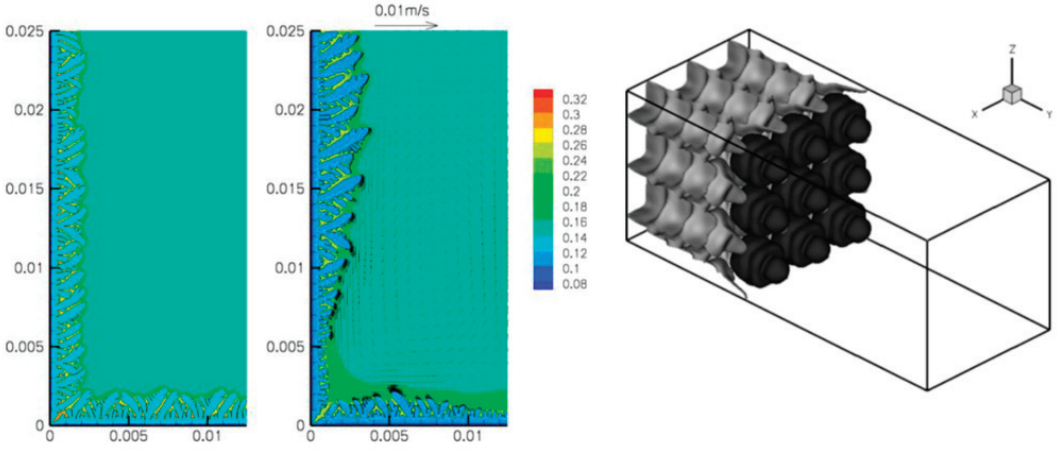

Figure 4. Solute concentration of Ta without (**left**) and with convection (**middle**) [84] and 3D crystal growth with front tracking and required undercooling for nucleation (**right**) [86].

The LS method is a helpful alternative to PF to avoid the asymptotic analysis needed for the PF method [62,87]. It is an extension of front tracking methods, where energy conservation issues derive from discretization errors. This is based on the direct application of temperature boundary conditions and the computation of heat fluxes, which was first addressed in Stefan problems [62], where the interface velocity is calculated from interpolation of the heat flux nodes near the interface. A LS method is useful for a direct calculation of the growth and shape of the solidification of dendrites without the need to apply the boundary condition explicitly at the freezing interface. Using a fixed FE grid, LS avoids the need for moving or adaptive gridding while providing an explicit and accurate tracking of the interface front [88]. Gibou et al. [89] provide a technical analysis of the LS methods and their applications in the computational review, which provides insight to adaptive Cartesian grids and parallel architectures.

2.5. Dendritic Needle Network

DNN is another novel method that is featured with respect to simulating the complex structure of dendrites. A mesoscale simulation resolution is needed for this, as each branch of the dendritic grain is considered a thin needle crystal, modeled as a network. PF and CA simulations are used to predict the dynamics of the individual branches for solidification or complex dendritic networks at a scale much larger than the diffusion length. Tourret and Karma [90] created a 2D multiscale model for DNN for both isothermal and directional

solidification that was validated through the comparison with analytic solutions. This DNN approach allows for investigations into the dynamics and stability of spatially extended dendritic arrays. The optimization of this model was proven to be four times faster than normal PF simulations. A 3D DNN simulation was scaled from 2D by defining the flux intensity factor (FIF), which is the strength of the concentration gradient at the tip of the needle. This is comparable to calculating the stress factor of a crack's tip, which is calculated using a contour integral and modeled as a parabolic tip. The main discrepancy for a 3D analysis is caused by Laplace's equation having no solution for a line terminating at a single point, which was accounted for by considering the solute flux intensity for a needle of finite thickness. The results were compared with the microscopy of a sample from NASA's microgravity solidification experiments, which showed a similar characteristic scale of the array spacing. Tourret and Karma [91] elaborated on this 3D DNN model using the same parameters with isothermal and directional solidification. An Al-7 wt.% Si alloy that was modeled in the previous microgravity experiment was analyzed with more scrutiny. They utilized a new 2D formulation for thick branches with paraboloidal tips. The comparison of the 3D simulations to samples from the CET in the Solidification Processing Project (CETSOL) [92] is shown in Figure 5. The simulation results of DNN, featured in white, followed a similar primary dendritic spacing to the markers of the samples featured in purple. This research provided a basis for quantitatively predicting the full 3D microstructure spacing of individual branches, which determine the mechanical strength of the structure.

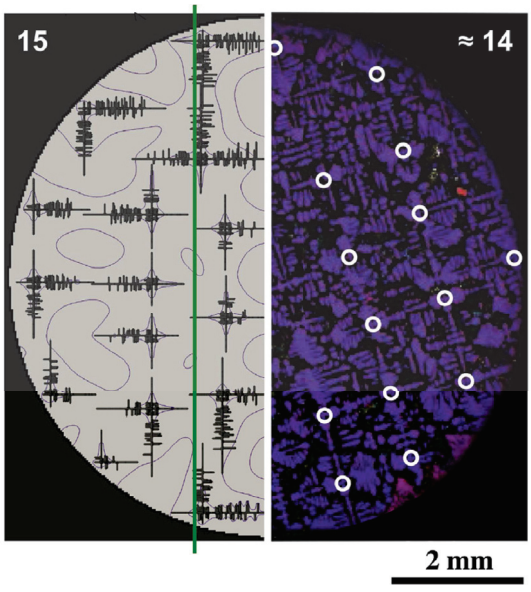

Figure 5. Cross-section microstructure comparison of the DNN simulation (**left**) to the polished microgravity sample (**right**) [91].

Tourret et al. [93] expanded on the DNN research by focusing on the isothermal growth of an equiaxed grain in a supersaturated liquid in 3D. Using PF, needle-based, and envelope-based approaches, benchmarks for an undercooled isothermal equiaxed growth were used to compare steady-state growth predictions. The theoretical Ivantsov solution provided the Péclet number that formed the basis of comparison, scaled with respect to the tip radius and velocity. The comparison of the model types is shown in Figure 6. While the lack of truncation radius bounding was apparent in the shapes, the coarseness of the dendrites caused the velocity to decrease due to the effect of the boundaries.

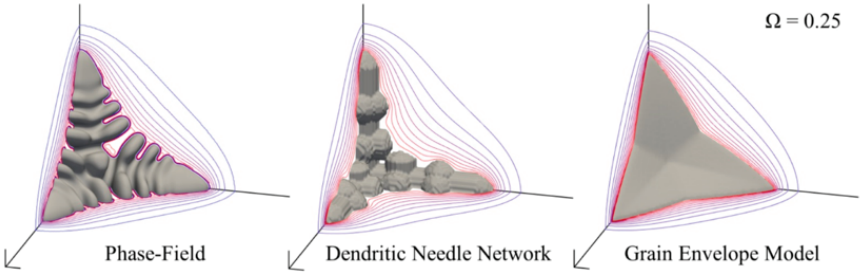

Figure 6. Comparison of model simulation types: PF (**left**), DNN (**middle**), and envelope (**right**) using a solute super-saturation (Ω) of 0.25 [93].

Nonetheless, this illustrates the effectiveness of DNN and grain envelope models (GEM) at reproducing PF results with reasonable accuracy. This comparison of models features an operational compromise between resolution and computational efficiency. While accuracy is important for large-scale simulations, multiscale models enable predictions of primary dendritic spacings, similar to industrial casting processes [94].

In context with PF, DNN solves a broad range of phenomena, where strong assumptions are made for the mesoscale models. Normally, these models do not account for the detailed evolution of the solid/liquid interface. DNN's representation of the dendritic structure as an array of needles allows for both steady-state and transient growth regimes to be described while accounting for the diffusive interactions between them. This bridges the PF approach with coarse grained stochastic models. Multiscale DNN allows for convective effects to be more effectively studied. Most recently, Isensee and Tourret [95] compared the oscillatory growth behavior to X-ray in situ imaging, identifying the fundamental mechanisms in which the gravity-induced buoyancy alters the dynamics of the crystal growth. DNN is a helpful approach for scaling simulations of morphology; however, in order to predict realistic microstructural evolution, incorporating fluid flow is crucial.

To compare the simulation methods that were just described, it is essential to produce simulations of a similar nature. However, as not many simulations have been created for this purpose, an analysis of the most outstanding simulations discussed in the above sections will serve as the basis for comparison (Table 1).

Table 1. Comparison of the simulation techniques.

	CA [53]	**PF [74]**	**LS [84]**	**DIT [77]**
Hardware	4 NVIDIA RTX 2080 Ti GPUs	TSUBAME 2.0	CTC supercomputer	single CPU
Compute time	27.42 min	288 h	5 h	11 h
Domain size (mm)	5 × 2 × 0.5	3.072 × 3.078 × 3.072	12.5 × 25.0	1.2 × 0.6
Mesh size	768 × 768 × 768	4096 × 4101 × 4096	1024 × 2048	600 × 1200

Monte Carlo (MC) simulations have also been widely used in studying solidification and grain growth processes as they allow scientists to model and predict how microstructures/grains evolve over time [96,97]. The Monte Carlo method involves making random changes to the system and then deciding whether to accept or reject the change based on a probability that depends on the free energy of the system [98]. This deterministic method is used to simulate grain boundaries on a large-scale, which is featured in the section for additive manufacturing (AM).

3. Mathematical Methods for Solving Transport Phenomena

The complex physics associated with the solidification process requires solving a number of differential equations for heat transfer, diffusion, fluid flow, and phase transformations. The numerical methods for solving these equations often include finite element

(FE), finite difference (FD), finite volume (FV), and lattice Boltzmann (LB). The first three are compared with respect to each other due to the many similarities shared between them, while LB is featured separately. Solving the transport phenomena can be accomplished in either the mesoscale (FE, FD, FV) or microscale by using molecular dynamics (MD). Solving a large-scale problem is impossible using this MD method; however, LB bridges the gap between the two by not considering each particle's behavior in isolation, as per MD. LB uses a distribution function to represent the behavior properties of a collection of particles.

The conventional method for the mesoscale is usually divided into two approaches, continuous or discrete. Using the continuous approach, an infinitesimal control volume and the conservation of energy, mass, and momentum are used to obtain partial differential equations, which is difficult to solve with complex geometry, boundary conditions, and nonlinearity. This problem is solved by discretizing the domain into finite elements, grids, or volumes in a macroscopic scale. Physical properties such as temperature, pressure, and velocity are represented at nodal points or averaged or assumed linearly/bilinearly across a finite volume/nodal point [99].

3.1. Finite Element/Difference/Volume

Many scholars have used FE, FD, and FV methods to solve the governing partial differential equations. Time and space are structured in a grid, where a continuous field variable is approximated at discrete grid points [100]. When extending into higher volumes, the FV methodology enables conformation to an irregularly shaped grid compared to the FD method's cartesian grid. The FE method divides a domain into discrete units, which is distinguished by the connectivity between the nodes and is suited for irregular structures. The trade-off between resolution and computational speed is dependent on the methodology chosen.

The FE method is also used to solve the governing equations for solute transport. Feng et al. [101] used FE to implement a fluid flow model for a mesoscale simulation. Utilizing the Galerkin FE method [102], an elemental matrix was developed and solved using an open access program C++ library (IML++) to solve both systematic and nonsystematic linear systems [103]. These resources have been helpful in developing models for many uses such as quantitatively predicting the fluid flow behavior induced by solidification shrinkage. The resulting mesoscale simulations were measured for variations in permeability from the shrinkage (Figure 7). With an average grain size of 300 µm, the domain contained 8000 realistic grains. The methodology for scaling will be discussed in more detail in context with the dendrite interactions and competitive growth.

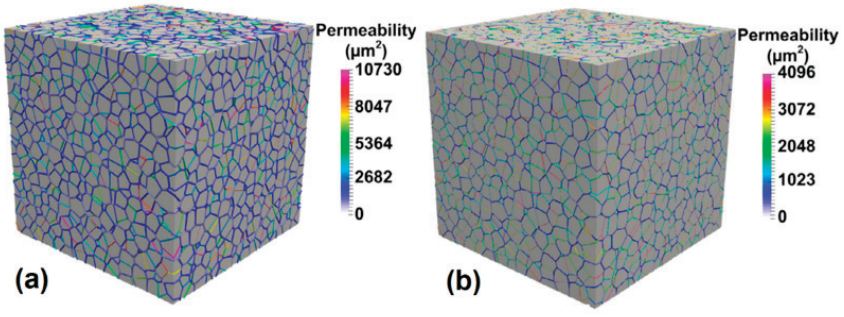

Figure 7. Variations in permeability (g) within a semisolid domain at (**a**) g = 0.70 and (**b**) g = 0.84 [101].

FV, on the other hand, is functionally designed to work in a 3D environment. Finite volume works as an integral scheme across an area, similar to FE, in which the chance for error is minimized. Integral schemes are computationally slower than differential schemes (FD), but this is dependent on the boundary conditions. FV is a conservative formulation that allows for a mesh to apply boundary conditions for a flow [94]. FV is

effective for coupling with CA, which was used to study artificial anisotropy [104]. Much effort has been made to simplify this process in mesoscale [105], for example, by creating a framework for FV [106] for casting processes (OpenCast) or integrating with sharp solid–liquid interfaces with the Eulerian–Lagrangian framework [107]. Navier–Stokes is unable to simply combine thermodynamics with the source term, therefore, FV is a common strategy for integrating these extra physics. LB, however, can naturally inject the complex physics of combining thermodynamics with the source term into the model for applications such as phase changes [101].

Despite their challenges, finite methods have provided useful integrations for modeling fluid flow with respect to meshing. Integration was applied as a moving mesh algorithm for quantitative PF equations by Karma et al. [108]. The sharp interface equations define the dendrite evolution in terms of the diffusion equation, which is expressed in a moving frame. Li et al. [109] expanded on the moving mesh framework for 3D multiphase flows. This adaptive grid method is useful for the disparity between the relatively small thickness and global length scale, which requires a locally refined grid inside the interface. This research has inspired others to utilize these methods for greater potential. Wang et al. [110] used these adaptive FE methods to measure the scalability of these domains. Comparing the tip velocities for undercooling cases, complex dendrites were studied for the potential to simulate more realistic physical problems (with a CPU that required about 60 h of time for 47,905 nodes). This numerical technique presents a framework for multicomponent (MC) alloys. The previously stated research has its limitations with respect to computation and time. FE has been used historically to model the transient thermal stresses and residual stresses from laser heat treatments [111]. With this context, it requires a higher degree of computation for realistic models. 3D finite element models provide a model for scalability [112–114] while other algorithms can enable multiscale complexity. Prakash et al. [115] provide a review on melting and solidification strategies in general purpose computational fluid dynamics software, which typically employs these types of methods.

3.2. Lattice Boltzmann

The LB method is a relatively newer approach for solving the solute transport and fluid flow. It is different from conventional modeling techniques as the system is modeled as a collection of particles moving on the discrete computational space's lattices. It is powerful for simulating both single and multiphase flows in complex geometries, which gives it an advantage over the conventional Navier–Stokes solvers [116–119]. It is very efficient in describing the fluid flow computationally [120] and can be coupled with different interface capturing methods. Interesting observations about the movement of dendrites can be made using large-scale LB models such as translation and rotation [121–124].

LB has been an important tool for our research on the large-scale simulation of dendritic solidification. Jelinek et al. [125] were able to visualize the flow of an Al-3 wt.% Cu alloy melt in 2D (Figure 8). The arrows represent the velocity vectors of the melt, while the contours represent temperature, where cooling occurs at the back and front as heat is applied at the sides. By incorporating the effects of melt convection, solute diffusion, and heat transfer, LB was able to be scaled using MPI and matched to CA using an identical mesh. LB's simple formulation is split into two steps: collision, which is completely local, and streaming, where MPI is used to transfer the distribution functions.

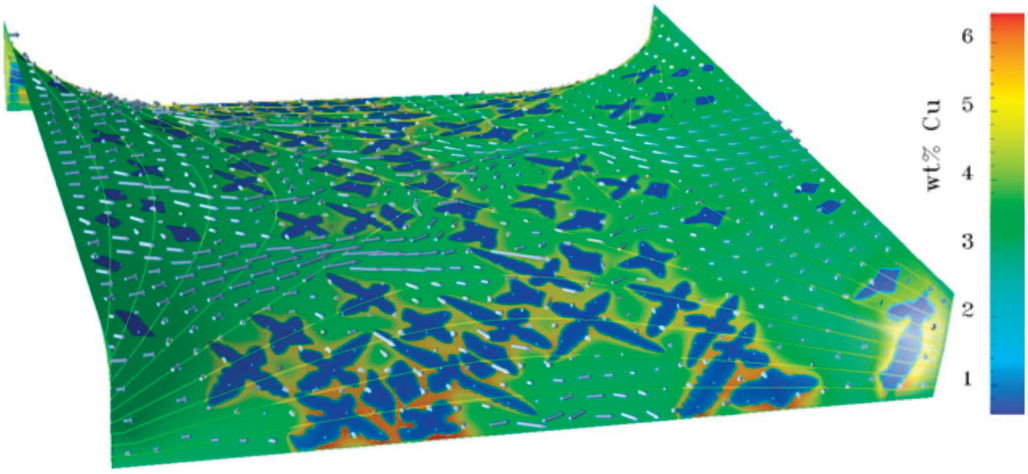

Figure 8. 2D simulation of flow melt around solidified dendrites, where colors represent solute concentration and contours represent temperature [125].

LB is very suitable for parallel processing, as this method does not rely on the assembly of a large global matrix, which makes CA a natural approach for coupling. However, LB has also been coupled with PF [121,126], where the equations of motion are solved for tracking the translational and rotational motion of the solid phase. Medvedev et al. [122] proposed a mesoscopic scheme to simulate dendritic solidification with both the motion and rotation of grains, which laid the framework for larger-scale simulations. This scheme was translated into 3D for multiple solid particles by Subhedar et al. [127], which optimized the diffuse interface-flow simulations. Software such as OPENPHASE [128] utilize PF and LB methods to combine dendrite growth simulations with fluid dynamics.

LB has advantages that are clear; computations are local and easy to handle in terms of complexity. It is efficient for parallelization while handling accuracy, numerical stability, and constitutive versatility. Therefore, the transport phenomena can be computed in a variety of use cases outside of fluid flow such as reaction systems, phase changes, material processing as well as heat transfer. Typically, simple simulations are performed using LB; however, with greater computation power, LB can be utilized for more than one use-case in a single simulation such as by studying phase change in combination with heat transfer. Ren et al. [129] verified this with experimental temperature profiles. They studied the influence of the dispositive position and relative position of the adjacent component and analyzed it with the metal droplet deposition method (MDDM) under heat conduction. LB was used to predict the heat transfer and phase change in the multi-layer deposition. Sakane et al. [130] used a domain decomposition method to simulate the free growth of an equiaxed dendrite in a domain of $2 \times 2 \times 6$ mm^3. This allowed for multiple-GPU parallelization, where the boundaries moved to divide the dendrite evenly.

When the heat transfer equation is solved in large-scale simulation for most metals, since thermal diffusivity is 100–1000 times larger than the solute diffusivity, the temporal resolution required for the solute diffusion equation is too fine for the energy equation [35]. If all the numerical models for simulating microstructure growth are explicit, then separate spatial scale and temporal scales for each physics can be employed to alleviate the problem and reduce the computational time. In other words, unique grid sizes and time steps can be used for different physics. The grid size and time steps are selected through the Courant–Friedrichs–Lewy condition [131] for each physics. However, the length scales should be fine enough to capture the secondary dendritic arm spacing (SDAS) and inter-dendritic flow for fluid flow and solidification growth features. This will result in a much coarser grid for fluid flow that reduces the overall computational cost [132]. This method

has been successfully applied by many researchers to reduce the computational time of large-scale simulation [34,35,132,133]. Recently, our group [133] studied the accuracy and computational efficiency of a multiple grid and time step scheme for a natural convection benchmark problem. We showed that through the appropriate selection of the grid and time step, computational savings up to tenfold could be obtained compared to when the same time step and grid size were used. The model was also accurate and only lost 9% accuracy for the worst case [133]. Chen et al. [134] presented a critical review on LB methods and applications that focused on solving multiphase problems.

4. Computational Approaches

In recent years, general-purpose computing on CPUs and GPUs with MPI and CUDA has been employed to speed up large-scale simulations of the solidification microstructure [135–141]. When MPI is used for parallelization, the computational domain is decomposed into finite subdomains in all directions. The information exchange between subdomains is carried through halo regions or ghost nodes. Based on the location of the subdomain, ghost nodes are either physical boundary conditions or contain neighbor subdomain boundary information. The ghost nodes are updated at each temporal iteration using MPI and the intercommunication between the subdomains [132]. The host program (CPU) divides the computational domain into thousands of thread blocks. Each thread block consists of a multiple of 32 threads. The kernel function is executed by the total number of threads in parallel in the device. It was shown that the computation time for a GPU with massive computation capacity and bandwidth is two orders of magnitude faster when compared with a serial CPU core [142].

Under certain conditions, CPUs are effective for simulations in comparison to GPUs. Sun et al. [143] characterized the accelerated performance quantitatively based on the total node points run on a single Intel Xeon E5-2699 v4 core and four NVIDIA GPUs. Figure 9 shows that at a lower number of nodes, the GPU efficiency was low. At 64^3 nodes, the speedup ratio was only 8.83, while the 640^3 case had a speedup of 155.29. The data communication between the devices was time consuming, while the calculation source of the GPU was largely unoccupied. The decline in speedups (1024^3 nodes = 152.30) is believed to be caused by the time used for output. Furthermore, the GPU efficiency increased as the number of nodes increased. With greater development, the acceleration in GPUs can be doubled by using shared memory [142], which is located at and shared by the same block.

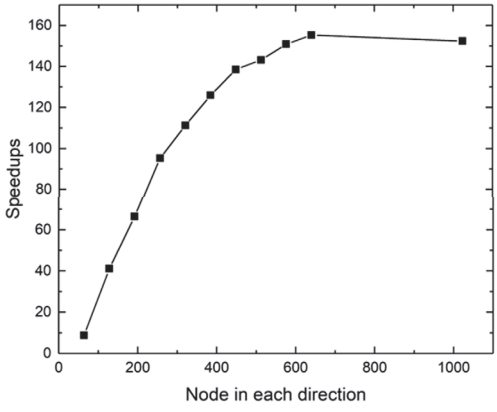

Figure 9. Speedups of single CPU core serial-programming vs. the multi-GPU parallel-programming efficiency [143].

Using multi-GPU cellular automata models, Wang et al. [144] simulated solidification structures in continuous casting blooms, which is known to be a computationally time-

consuming process. The model utilized a heterogeneous GPU-CA parallel algorithm to optimize the calculation parallelism and a multi-stream communication scheme to overlap computations and data transfers. They validated the model by the analytical LGK model and applied it to simulate the solidification structure. In comparison to single-core CPUs, the proposed model achieved speedups of 700× while maintaining similar calculation precision and producing results with minimal relative error.

The evolution of technology has given rise to a diversity in applications. Computer processing for large-scale simulations has been improved due to the number of processors. Supercomputers were the source of this amount of computation required, while CPUs were soon replaced by GPUs, which allowed for even faster calculations. Eventually, the bottlenecks for the speed were determined by the programming. Innovations in GPU technology such as NVLink, which allows for direct communication between GPUs, were assisted with toolkits such as NVIDIA's CUDA to program the GPUs directly. TSUBAME 3.0 (the most current of the series of supercomputers based at the Tokyo Institute of Technology) employs this technology, allowing four 20 GB/s data link per GPU for a total of 47.2 PFlop performance in half-precision [145]. MPI has shown effective use throughout trials, and the combination of techniques and optimizations has been proven to show significant success in GPU-rich supercomputers.

Jelinek et al. [125] produced a large-scale simulation for 2D dendritic growth, which was accomplished through MPI parallelization. Parallel programming utilizing this type of communication between the distributed-memory systems is the standard for large-scale simulations. The programming is approached using a single program, multiple data streams (SPMD) [146]. SPMD uses each processor, executing the same program on different data for MPI processes. Using a notion of rank to distinguish processes, the point-to-point communication is the fundamental primitive for sending and receiving. The scalability enabled this type of research to utilize Oak Ridge National Laboratory's Cray XT5 system (Kraken supercomputer) [147,148]. The dendrites were grown to a reasonable size in an "incubation region", then the results were stored to restart using the scalability of 41,472 of a total of 112,000 cores of the Kraken supercomputer. Figure 10 shows the final snapshot of the dendrite incubation domain, where the magnified portion shows the flow of the alloy melt between solidifying dendrites.

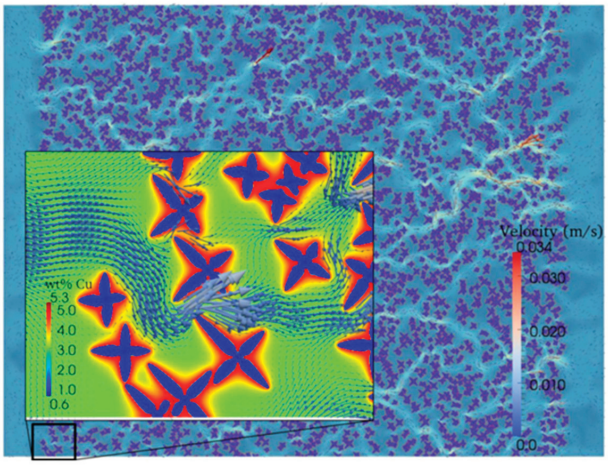

Figure 10. Large-scale domain of dendrite growth with enlarged composition analysis where the colors in the background and dendrites are represented as the solute concentration. Both the size and color of the arrows represent the magnitude of velocity [125].

The parallelization required for this amount of detail for such a large domain is only possible with a technique of spatial domain decomposition. This popular method of

splitting the spatial domain into equally-sized domains is specific to the number of cores used for the computation. The benefit of the CA-LB model is that only the subdomain boundary values need to be exchanged between the subdomains [125]. Implementing this in binary Hierarchical Data Format 5 (HDF5) yielded a high efficiency that resulted in a 50% reduction in the memory and computational time required, enabling high scalability.

Continuing this research, Eshraghi et al. [137] utilized the CA-LB model to simulate 3D dendrite growth in a macroscale domain of approximately 36 billion grid points (1 mm^3). The scale-up performance (strong scaling), where the number of processors was increased with the fixed domain size, was compared with the speed-up performance of a fixed processor load by scaling the domain size (weak scaling). Using this combination, the entire domain was filled with dendrites, as shown in Figure 11. The competition between the dendrites shows that the ones with orientations other than 90 degrees were blocked by the perpendicular dendrites.

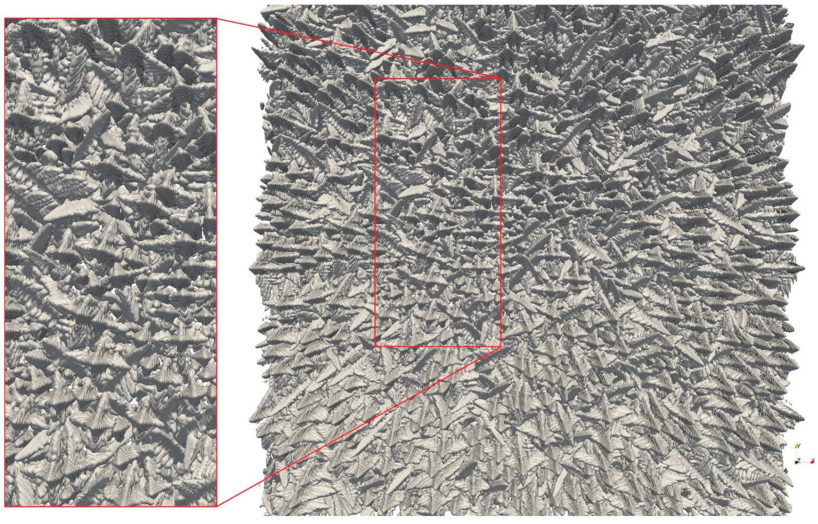

Figure 11. The 1-mm^3 domain of a 3D columnar dendritic microstructure simulated from 4000 initial seeds and approximately 36 billion grid points [137].

Shimokawambe et al. [135] were able to perform the first petascale PF simulation of dendrite growth that we know to date. The process was implemented locally on a single GPU using CUDA; then using 4000 GPUs, MPI was implemented, so host CPUs were used as a bridge for the data exchange. They used overlapping techniques to utilize both GPUs and CPUs to optimize the scalability, which were defined as Hybrid-YZ and Hybrid-Y. First, Hybrid-YZ exploited the data independency for array elements by dividing each subdomain into five regions, which were computed separately. The CPU cores were used to compute four y and z boundary regions, while the GPU was used to compute inside the region to produce halo regions. Hybrid-Y instead assigned only boundary regions in the y orientation of the boundary to CPUs [146]

Hybrid techniques for computational simulations have been the focus of research since modern high-performance computing (HPC) systems have been introduced to simulations. Yamanaka et al. [142] proved that GPU-accelerated PF simulation was faster than its CPU counterpart by two orders of magnitude. Heterogeneous computing has resulted in the development of many frameworks [149,150]. These many frameworks have been developed to enhance the computation and portability of these HPC techniques. "Multiphysics Object-Oriented Simulation Environment" (MOOSE) [151], FEniCS [152], "Portable, Extensible Toolkit for Scientific Computation" (PETSc) [153], Mesoscale Microstructural Simulation Project (MMSP) [154], and Structured Adaptive Mesh Refinement Application Infrastruc-

ture (SAMRAI) [155] are a few resources that have been built upon the models previously discussed. High performance interconnection networks [156] have also optimized research regarding many of the features described below.

5. Features and Applications

There are many unique use-cases for large-scale simulations of the solidification microstructure. The original focus of initial works was to provide a large macroscale domain for the direct numerical simulation of dendrites. The simulations grew in both dimensions and scale. Stochastic-based methods of modeling [54,55] have been used to produce larger simulation domains, but researchers had to develop special dynamic allocation techniques to minimize the computation costs for the large number of cells [57]. The trade-off between 2D and 3D is important for distinct use cases. A dendrite growing in a 3D domain versus a 2D domain in the presence of convection will experience less effect of flow on its growth and morphology, which is because of the obvious reason that the moving melt can flow around the dendrite arms in 3D. We studied the comparison of natural convection and forced convection on a single dendrite evolution in 2D and 3D using LB [157]. 3D dendrites grow faster than 2D, while secondary arms are more likely to form. Jegatheesan et al. [158] studied the effects of distributing nanoparticles in a buoyancy driven convection solidification by using an enthalpy-based method. When considering methods for convection, a reduction in volume from solidification (shrinkage driven flow) was not considered as it was studied only in 2D. However, adding a third dimension can improve the nanoparticle transport due to the enhanced diffusion, which is the result of the extra simulated room for the convection. This comparison serves as a helpful example of how observations in 2D can provide effective results. The simulation also highlighted the accumulation of nanoparticles at the grain boundaries while the presence of a large number of dendrites or even nanoparticles, with or without convection, could reduce the growth of a dendrite.

In a 3D space, competitive growth can be studied in detail, which cannot be expressed in 2D. When a dendrite enters the space of another, dendritic branches can block growth based on orientation. Sakane et al. [138] studied the dendrite interactions in the directional solidification of an Al–Cu binary alloy bicrystal using 512 GPUs with 1024^3 meshes. A PF-LB model was utilized with MPI to demonstrate that 3D phase field simulations could be performed within a reasonable computation time (12 h) while showing tertiary dendrite growth.

Another helpful comparison of 2D and 3D simulations of dendrite growth was accomplished by Sun et al. [143] by comparing the effectiveness of the MC PF model. In this case, a 2D simulation of Ti6Al4V was performed using Al and V solute simultaneously, which was a first of its kind. The results showed that the driving force and growth were magnified artificially in the pseudo-binary in comparison to the MC (ternary) PF model, violating the sharp interface (Figure 12). As a result of the benchmark comparisons, the MC PF model was scaled into a 3D model using a 512^3 nodal box with a capillary length of 0.840 μm. Using four Tesla K80 GPUs for a total of nearly 20 k cores, the resulting simulation showed that the inhibited growth of the shortest dendrite by diluted Al (V) was merged by its surrounding dendrites. This phenomenon has been studied experimentally in AM for the incremental arm spacing and coarsening of primary dendrites.

5.1. Dendrite Interactions and Competitive Growth

Dendritic growth is dependent on many factors that can generate many different phenomena. These effects need to be understood in detail to be able to predict the changes in the microstructure. Traditionally, the Walton and Chalmers competitive growth model [159] is utilized for the selection of growing multiple dendrites. Nickel-based superalloys have shown some astonishing growth phenomena [160–162] that cannot be simulated using the conventional model. First, this section will highlight the traditional model, then will expand on the phenomenon and other effects associated with competitive growth.

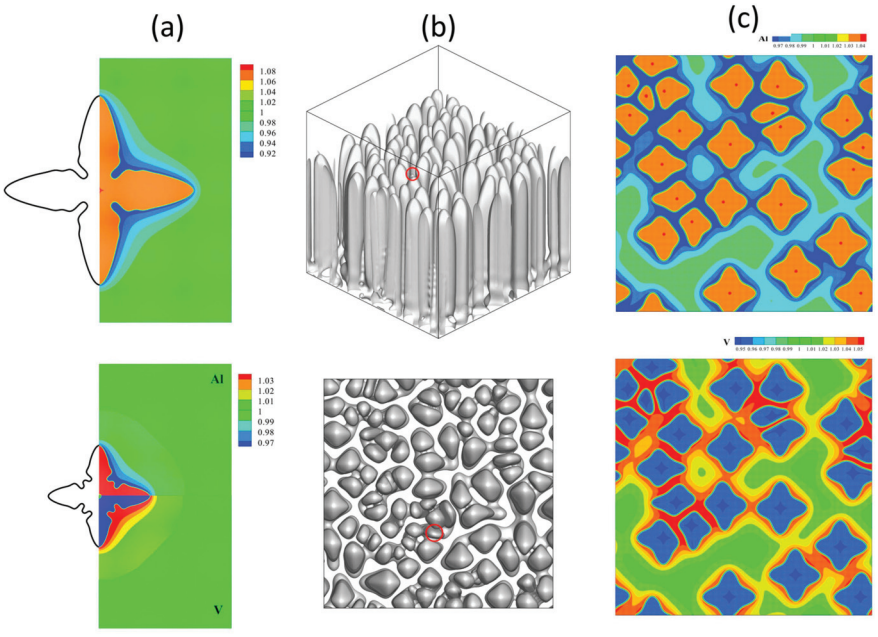

Figure 12. (**a**) Comparison of the pseudo-binary model (**top**) and MC model (**bottom**); (**b**) 3D simulation of 99 nucleation seeds for 3D view (**top**) and top view (**bottom**); (**c**) 2D evaluation of the solute concentration for Al (**top**) and V (**bottom**) solute [143].

In 2017, Yang et al. [163] used PF simulation to create a 3D dendrite growth in a nickel-based superalloy. The results were generated using a single NVIDIA GTX1080 GPU for a total of 774.292 GFLOPS (giga floating-point operations per second). From the dendrite arm spacing to inclination angles, the dendrite morphology evolution during this superalloy's casting can be understood to optimize the mechanical properties. The simulation was accomplished using a simplified approach by assuming the alloy as a pseudo-binary alloy, which was first popularized by Raghavan in 2012 [164]. PF has the capacity to simulate both isothermal and non-isothermal dendrite growth, which makes it versatile for applications such as asynchronous concurrent GPU computations. This allowed Yang et al. to show the interactions between the dendrites in an equiaxed multi-dendrite domain, which caused the dendrite arms to grow with a deviation from their initial crystal orientations [163]. As they fill the entire domain, the dendrites coarsen and coalesce, causing the melting of the secondary arms.

The comparison was accomplished using directional grain growth, allowing the height to be competitive. This illustrates that the growth is dependent on both the inclination angle and the position of the adjacent dendrites. This simulation showed how the favorably oriented (FO) dendrites outperformed the unfavorably oriented (UO) dendrites. This simulation was performed using an asynchronous concurrent algorithm to show that 774.29 GFLOPS were obtained in 512^3 computational grids on a single NVIDIA GTX1080 GPU. The growth of the dendrites obtained a height of 6.42 mm. However, in contrast to this study, the following study illustrates conditions where the opposite is true (UO outgrows FO).

Takaki et al. [165] published a study focused on simulating the competitive growth with converging grain boundaries in a large domain of 3.072×6.144 mm^2. The directional solidification of 3D dendrites was simulated to compare the effect of unfavorably oriented (UO) grain inclination angles. Using the Walton–Chalmers model [159], Takaki modeled a contrasting phenomenon where at the grain boundaries, the UO dendrites overgrew the

FO dendrites. This unusual overgrowth was more common when the thickness of the sample and the UO grain inclination angle were small. The secondary arms had higher growth at boundaries. Tertiary arm growth was enlarged at the convergence with the domain boundary.

Takaki used this competitive growth model for 3D analysis, where a collision of FO and UO grains occurred in the middle of the domain to form a straight GB. The FO and UO grains shared different properties, where the arrangements of the dendrites gradually became ordered [124]. The FO grains form a hexagonal arrangement, while the UO grain migrates in a lateral direction. This occurred as the UO dendrites penetrated deeper into the FO grains with respect to the reduction in the angle of orientation. This interaction was termed as "space-to-face interaction" [124]. Figure 13 shows the convergence of the differently oriented grains with respect to different degrees of orientation. This perspective from above the columnar dendrites shows that the UO dendrites with a lesser degree of orientation had a greater convergence, which is expected from previous competitive growth patterns.

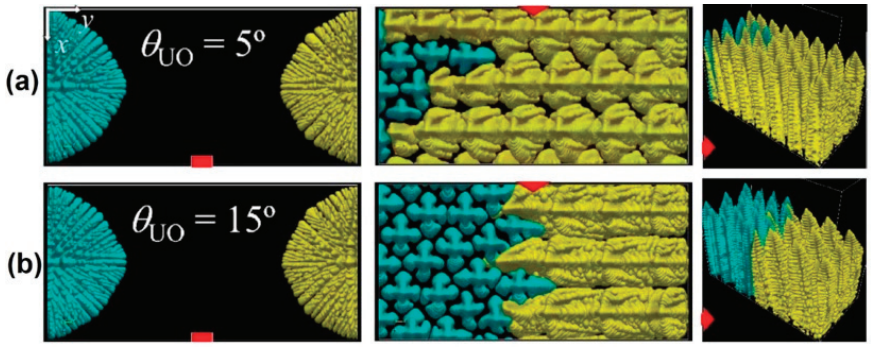

Figure 13. Dendrite interactions comparing different angles of UO dendrites of 5° (**a**) and 15° (**b**) at time 1.3 s (**left**) and 187.5 s (**middle** and **right**) (comparing both the top and 3D views, respectively) [165].

In large-scale grain growth, the Walton–Chalmers model is largely accepted as the general competitive-growth model for grain selection. In this model, FO grains block UO grains. In contrast, when analyzing primary arm spacing, Fourier transformation (FT), Voronoi decomposition, and minimum spacing tree have been employed to evaluate the arm arrays [57]. This has been the basis for new models to be developed for greater accuracy. Voronoi tessellation (VT) has been applied to approximate the morphology of equiaxed dendritic grains. The dendrites are formed from a mesoscale domain, where Voronoi grains are formed in the triangulation technique exemplified below (Figure 14) forming a polyhedral structure. These assumption models allow for complex model domains to be generated. For example, Feng et al. [101] simulated a 3D semi-solid microstructure using 1000 grains, where VT was used to approximate the final grain morphology to compare the volumetric inflow caused by shrinkage. Permeability will be discussed in more detail in a later section.

In order to evaluate the arrays, ordering, and spacing of primary arms, especially in 3D directional growth, different methods have been employed historically such as minimum spacing tree [166], Fourier transformation [167], Voronoi decomposition [168], and many others [169–172]. Using a modified Voronoi decomposition technique, where the small sides are removed from the Voronoi cells, the primary arm array was evaluated by Takaki et al. [173]. The hexagonal pattern showed typical-hepa defects that decreased with respect to time for tilted columnar dendrites in a computational domain of $1.152 \times 1.152 \times 0.768$ mm^3. These enabled predictions of the primary arm spacing, which is

crucial for the integrity of the material. This was ultimately possible through a convergence analysis of the tip undercooling of the dendrite/cell.

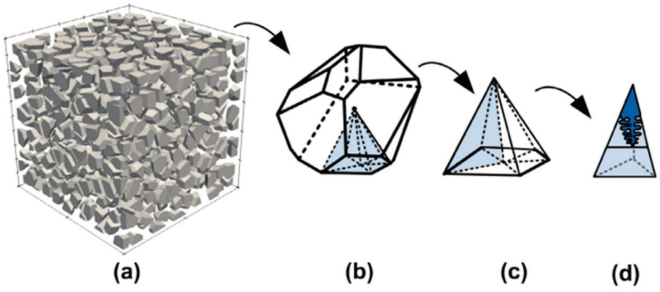

Figure 14. Voronoi grain from the mesoscale simulation: (**a**) 1000 grains in the mesoscale simulation; (**b**) consisting of single Voronoi grains; (**c**) which contain polyhedral structures; (**d**) tetrahedron schematic for equiaxed dendrite [101].

The ability to predict dendrite spacing is important for permeability research, as the fluid flow can only be researched under certain conditions. Porosity, which is an important type of defect that can form from casting, can be caused mostly by either shrinkage, where the volume changes upon solidification with a restricted feeding of the liquid, or the condensation of dissolved gases in the melt upon freezing. This has a strong negative effect on ductility and fatigue life, where internal pores create initiation sites for cracks and local stress concentrators [100]. As convergence occurs, permeability is another condition that requires a lot of research for the consideration of realistic predictions. Li et al. [174] produced a review article on Ti–6Al–4V solidification simulations for AM, where competitive growth is featured in context to different modeling techniques.

5.2. Columnar to Equiaxed Transition

In the context of design, columnar or equiaxed grains may be desired depending on the expected properties. The transition between columnar and equiaxed has been investigated for many years, where heterogeneous nuclei are commonly used to promote equiaxed grains. An example where equiaxed grains are preferred is for processes of the direct-chill casting of aluminum alloys [175]. However, its high angle grain boundaries can reduce creep rupture life. Therefore, it is important to control the grain structures using conditions such as high thermal gradients and low growth rates. We recently performed a 3D PF simulation of CET for an Inconel 718 alloy in a domain of $0.2 \times 0.1 \times 0.4$ mm^3. A CET solidification map was created to compare the growth rates and temperature gradients for the evolution of dendrites in equiaxed, columnar, and mixed regimes, as depicted in Figure 15. A model was developed to predict the primary dendrite arm spacing (PDAS) of columnar growth in a wide range of temperature gradients, solidification rates, and initial grain sizes. This novel approach is effective for optimizing process parameters for melting and solidification on a preexisting substrate such as in AM or welding applications.

Studies to determine the mechanisms behind CET have been a popular focus for research. Hunt [176] proposed an analytical model to predict CET based on the potential for equiaxed grains to nucleate ahead of the columnar front's undercooled region. The solid fraction was calculated using the truncated Scheil equation empirically to relate the cooling rate to the tip undercooling. Next, it was modified by Gäumann, Trivedi, and Kurz (GTK model) [177] to include the non-equilibrium effects of rapid solidification. Hunt's model shares the same relationship for CET based on key parameters of pulling velocity, thermal gradient, and composition.

The process of predicting the CET has been demonstrated by comparing 2D (10×30 mm^2) and 3D ($10 \times 30 \times 2$ mm^3) models using a stochastic model for alloy 718 [178]. CET begins

earlier in the 3D simulation because the grain growth is not confined in the third (z) direction, and there are more nucleation sites.

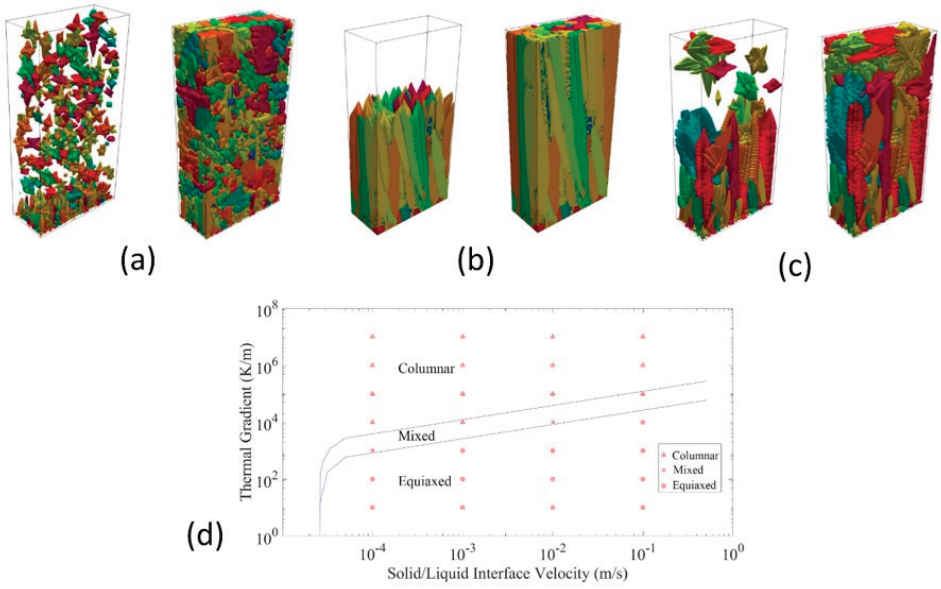

Figure 15. Evolution of (**a**) equiaxed, (**b**) columnar, (**c**) mixed dendrites, and (**d**) solidification map for the Inconel 718 alloy [126].

Dong et al. [179] showed a situation where equiaxed grains were placed ahead of the growth of the columnar front during solidification of Ni-based superalloys. This real-life situation results in casting defects such as stray grains or "tree rings" [180]. This was the precursor of the CET simulations, where it showed the gradual transition, realistic dendrites, and complex solute concentration profiles. The size of the domain was 2.5×4 mm^2 for a total of 500×800 cells in the domain. In another work, Dong et al. [176] focused on the solute interactions within the CET modeling. It was a unique finding that the solute interactions were strong in the secondary and tertiary arms, while a weak interaction between the solute and arms was observed in the columnar tips [1].

DNN provides a promise for describing the transient growth dynamics of higher order branches, which normally relies on strong assumptions. Geslin et al. [181] effectively simulated the CET in 2D, using DNN in a large domain with a 22.5×30 mm^2 size. Using a sharp interface model for directional solidification, they were able to observe complex phenomena such as "circular growth" (branchless growth), abrupt and progressive transitions with different grain structures. Therefore, when casting large samples in a crucible, the columnar front that progresses toward the inside of the sample is accurately simulated, where the slower solidification rates favor the nucleation of equiaxed grains [100]. Balasubramani et al. [182] reviewed the origin of equiaxed grains in solidification within the context of manufacturing treatments, which provides a greater understanding to the application of these simulations.

5.3. Solute Transport and Segregation

Solute transport is a phenomenon that is very flow dependent and can have effects on the development of the dendrites under well-defined thermal conditions. Effects on dendrite spacing and symmetry have been notably studied [183,184]. Wang et al. [55] were able to utilize a CA-FD model to simulate a controlled solute diffusion in the solidification of a binary alloy. Using a 2D model, they simulated a tertiary dendritic arm growth from a secondary dendrite arm, which was then blocked by another secondary dendrite. This

was helpful in predicting the primary dendrite arm spacing. The average primary arm spacing was found to be dependent on the current growing conditions and the way those conditions were reached.

These features for prediction models serve as a helpful analysis to develop a real-life understanding of the grain interactions. From interactions of both equiaxed and directional grain growth, the competition models show a clear understanding of the evolutional interactions. Even highlighting the transition between the two phases, comparing the mesoscale interactions on a microscale level requires a manageable distribution of resources. The prediction models for spacing utilize innovative techniques that provide a new understanding of competitive grain growth, even within the same primary arm. The features for this analysis have provided the foundation for more progress to be made with more complexity in dendritic evolution. Solute plumes are a resulting situation that occur in a directional solidification of Ga–In alloys. This solute-rich liquid that flies up is believed to be a crucial factor that causes, during solidification, a freckle defect [185]. Takaki et al. [186] studied the effects of natural convection in both 2D and 3D simulations. Performing a series of simulations where gravity was changed, they were able to show that as the gravity decreased in the negative region, primary arm spacing increased. Furthermore, the downward flow enhanced the growth of secondary arms, as unstable dendrite growth is caused by a large upward flow. Figure 16 shows the differences in the dendrite tips in 3D, while 2D shows the plume and freckle-like solidification defects forming. Using PF-LB simulations on TSUMBAME 2.5, they were able to simulate a domain of $0.384 \times 0.384 \times 1.536$ mm^3 with 95 h of computation time.

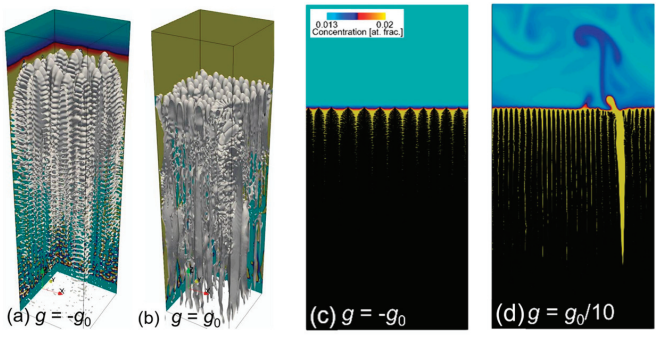

Figure 16. Dendrite morphologies and solute concentration distributions for 3D (**a**,**b**), and 2D (**c**,**d**) when comparing different forms of gravitational acceleration [186].

The flow influences both the solute transport variations and the upstream–downstream dendritic growth. The effects of convection can limit the downstream growth, while the upstream dendrites are promoted by the convection-induced anisotropy. The solute plumes are the result of gravity assisting in the direction of the dendrite growth. The presence of convection can change both the time- and length-scales, which can result in differences in the morphologies from the purely solute transport. Our team studied the buoyancy-induced flow during the directional solidification of 3D thin domains by comparing the Al–Cu and Pb–Sn alloy systems [187]. Sn is lighter than Pb, where more solute is rejected into the melt and its concentration around the interface increases. Upward buoyant force results from the decrease in the density of the liquid mixture around the interface. This large solute boundary layer that forms with a peak at the center is shown in Figure 17 and is also referred to as a chimney. This phenomenon has the potential to be stable during the solidification process, which carries the solute up, forming a recirculating flow. This can lead to decreased growth or remelting in this region during later stages of solidification and can form a freckle defect once completely solidified.

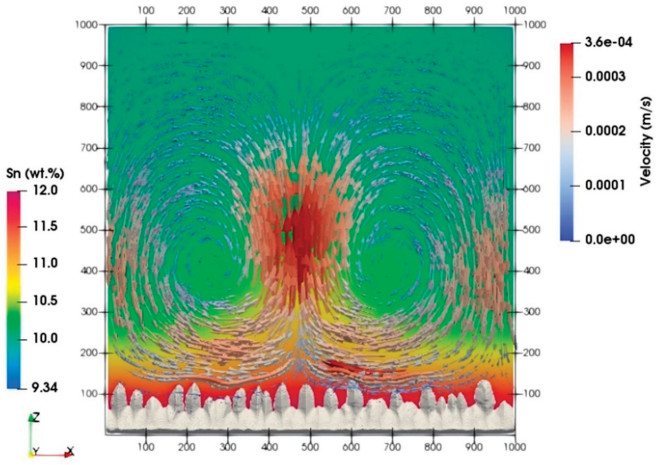

Figure 17. Chimney formation and the solute concentration field during the directional solidification of a Pb-10 wt.% Sn alloy [187].

Macrosegregation is the solute composition inhomogeneities at a macroscopic scale of a casting [188]. Heat treatment can remove these imperfections; however, spatial variations of mechanical properties can occur with respect to the nature, amount, and size of these defects. Gross compositional defects such as the formation of freckles or segregated chimneys is caused by macrosegregation. This is associated with the following causes: solidification shrinkage [189–192], natural and forced convection [193–195], grain movement [196], mushy deformation [195], and cavitation bubbles [197]. Fragmentation has been researched as an important phenomenon using large-scale simulations as it is responsible for grain refinement [198–201]. It is undesirable for certain manufacturing processes such as single crystal turbine blade casting [202] or AM of metastable β-Ti alloys [203,204]. Process parameters can define the formation of freckles that can be caused by remelting, where there is a sudden rise in temperature, deceleration of a growth front, or a change in flow conditions. Simulation is an effective method to study this capillary force driven process [59].

Kao et al. [132] developed a large-scale model to simulate freckle formation for the casting of Ga-25 wt.% In. Freckles form due to the remelting and fragmentation of dendrite arms by thermosolutal fluid flow, especially for alloys where the partitioned solute is lighter than the bulk fluid. Examples of such phenomena include Ni-based superalloy and Ga-25 wt.% In. The authors utilized the LB method for fluid flow and CA to simulate the solidification growth. The coupling between these two main equations is achieved by natural convection force and energy and solute transport equations at each node, so they utilized the MPI parallel algorithm to accelerate the large-scale simulation [205]. The formation of the freckles in the simulation is shown in Figure 18. The domain for the numerical model was a total of $32 \times 32 \times 0.16\ mm^3$, which is equivalent to 164 million cells.

Zang et al. [185] studied a comparison of forced and natural convection simulations in both equiaxed and columnar dendrite evolution. Understanding the effects on an Al–Cu alloy using PF-LB in an AMR algorithm, they were able to illustrate some unique phenomena. Dendritic fragmentation, angulation of dendrite arms, and splitting are dendritic growth behaviors that were the subjects of interest for the forced convection simulations, where the direction and intensity of the convection had a significant influence. Fragmentation occurred regardless of orientation for columnar dendrites, but was instead dependent on convection type.

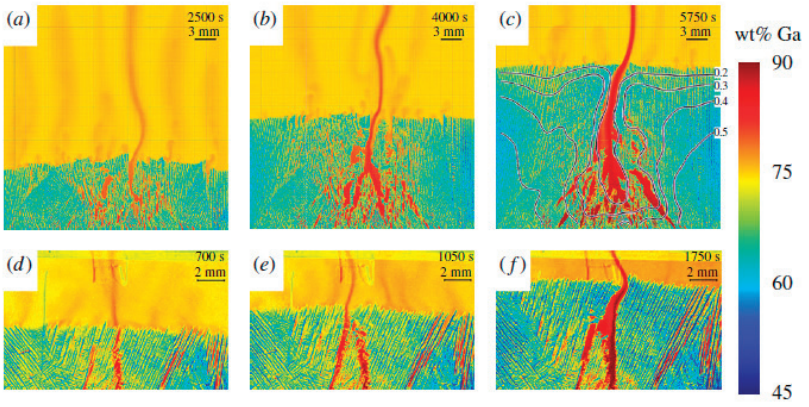

Figure 18. Freckle formation for the Ga-25 wt.% In binary alloy (**a**–**c**) simulation and (**d**–**f**) experimental results for G = 250 K/m in the vertical direction at different times [132].

Freckle formation, also known as channel segregation, is a unique byproduct of vacuum arc remelting (VAR). The solute is ejected upward and solidifies as freckles. Research has been conducted in understanding the segregation defects on the VAR process, simulating the ingot evolution under different arc distributions [206]. However, a lot of detail can be obtained by employing large-scale simulations of the microstructure, where solute transport is a driving factor. Hecht et al. [207] provided a review on multiphase solidification, where the effects of solute transport are mentioned in context to large-scale simulations.

5.4. Natural and Forced Convection

Forced convection has been a subject of interest for large-scale simulations as it has a lot of influence on solute distribution. Research has provided context for dendritic growth and compared the effects with and without convection. Another helpful comparison is between natural convection and forced convection. Convection was originally solved using NS solutions [208]. Simulations of dendrite growth with melt flow was first possible in the 1990s using PF [209–211], while being limited to 2D [42,212]. Early simulations of 3D were limited to a single dendrite [213], however, it is important to scale these algorithms for complex microstructures. Yuan et al. [214] studied the effects of dimensionality on dendritic growth simulations for convection by using a modified projection method of NS. When the 2D flow has a blockage from the primary dendrite arms, the 3D flow has the ability to wrap around the primaries. Therefore, it demonstrated that 3D simulations are necessary to correctly predict unconstrained solidification microstructures. Forced convection was studied by Jakhar et al. [215] in combination with thermal isotropy, where pressure fields were solved using the SIMPLER algorithm. The model was extended to multi-dendritic simulations with random distributions and orientations in order to study microstructural evolution. Takaki et al. [186] performed a large-scale PF and LB simulation ($0.384 \times 0.384 \times 1.536$ mm^3) to study the effects of natural convection during directional solidification. Comparing 2D and 3D, the effects of gravity were smaller for 3D, while the average primary arm spacing increased as gravity decreased, similar for both. Downward flow enhanced the growth of secondary arms, while upward flow, larger than a critical value, could produce plumes and freckle-like solidification defects. Using the TSUBAME 2.5 supercomputer, the computation took about 95 h for 1.5×10^6 computation steps in 3D.

Computational cost has been a limiting factor for research on convection, where LB is the most efficient for multi-GPU computation as the growth is able to be simulated with the solid motion, liquid flow, collision, and coalescence of multiple solids, and subsequent grain growth. However, much effort has been made to enhance this ability. Sakane et al. [216] created a 2D simulation for a large number of dendrites (350) utilizing PF and LB methods. Figure 19 shows the evolution of the solute concentration and flow

velocities, where a sedimentation path formed from the dendrites. Assuming inelastic collisions, the coalescence of the grains was observed. The nuclei generated at the top of the domain settled downward while growing equixially. The ability to scale performance was widely studied in this research, utilizing active parameter tracking (APT) [217,218]. Tracking the execution time with and without APT was compared to grains with and without motion, proving the efficiency of the model, where APT excels with convection. The parallel efficiency of the model showed that a simulation could be performed in a 64x larger domain with only twice the amount of time compared to a single GPU. The simulation was performed with 2048 × 2048 grid points and five grains per one GPU. APT algorithms were employed to simulate coalescence-free grain growth within a reasonable computation time [219].

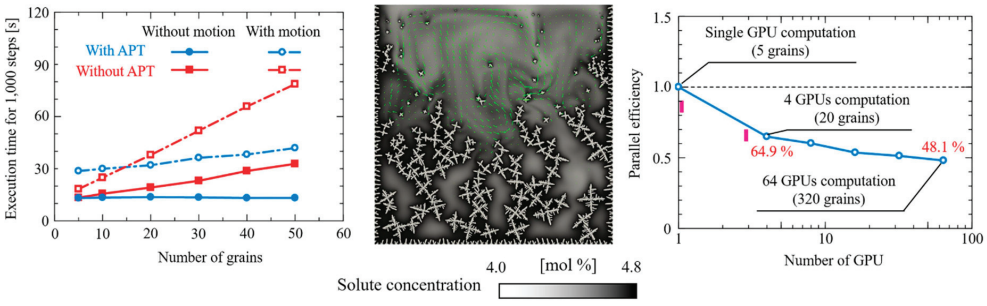

Figure 19. (**Left**) APT Efficiency comparison; (**middle**) evolution of solute concentration and flow velocities simulated by LB method; (**right**) parallelization efficiency with scaling GPUs [216].

Zhang et al. [220] combined the PF and LB with a parallel AMR algorithm for several studies of convection, both natural and forced, in 2D and 3D. They quantified the effect of both convection and undercooling by comparing the length ratio of dendrite arms. The investigation showed that as the undercooling decreased and the effect of convection increased, the length ratio had a peak value. This was due to the decrease in the crystal size compared to a higher undercooling. Second, the effect of gravity with a lateral force of convection was studied, where columnar dendrites grew anti-parallel to gravity. The accumulation of the solute from gravity stunted the growth; however, with the convection, the primary trunks of the dendrites showed a constant deflection angle until reaching a critical value. Sun et al. [221] used a 2D LB model to show that asymmetrical dendrites grew faster in an upstream direction, while slower downstream. Studies like this can help to optimize the solidification conditions for manufacturing by analyzing the effects of convection on dendrite growth.

5.5. Permeability

Permeability predictions have produced an effective method to analyze the distinct solidification conditions of the liquid flow through a mushy zone. Anisotropic porous media use Darcy's law, which is derived from the Navier–Stokes equation using an averaging procedure [222]. Interfacial stresses occur when the solid fraction is high enough for the solid to form a continuous structure. In a mesoscale domain, the solute distribution is limited by the permeability of the solidification structure, with consequences for grain refinement [223]. 3D interdendritic flow simulations have been performed using microtomography mappings to measure the permeability in Al–Cu [224]. However, the compromise between resolution and sample size is limited to the camera. Therefore, simulations have provided a solution with parallel programming, simulating both the morphology and the fluid flow. The complexity of the transport phenomena has resulted in interesting studies in large-scale such as cross-permeability [225], where experiments measuring permeability have a limitation of experimental volume fraction [226].

Permeability research has been characterized both numerically and experimentally. Permeability simulations have been validated in hypoeutectic aluminum alloys by Khajeh et al. [227], where the simulated microstructures for a dendritic network were modeled using the CA technique. 3D printing has been a helpful tool to perform experimental measurements from a simulated model. Most recently, Berger et al. [228] used a fused filament fabrication (FFF) technique to scale a PF model from 150 μm^3 to 5 cm^3 of an Al–Si–Mg alloy sample with a fraction solid varying from 0.61 up to 0.91.

Validation of these models requires more detail to ensure that the correct physics is being modeled [180]. Mitsuyama et al. [229] performed an analysis on the permeability of a large domain of 1.152 × 1.152 × 0.768 mm^3 using PF and LB, and approximated using the Kozeny–Caman (KC) equation [230], which is used most frequently to express permeability. Alternatively, the Poirier–Heinrich (PH) [231] equation can be used, but with uncertain accuracy due to its derivation from 2D simulations and experimental data [232]. Therefore, a lot of research has gone into validating these models. Such discrepancy has invoked studies based on different types of flow and growth patterns. In parallel flow, a solid fraction can change in dimensions with respect to the liquid that flows through the entire columnar dendrites, as shown in Figure 20. The simulations validated the use of a KC coefficient of $K_c = 3$ and the permeability tensor for this use case. Thus, the permeabilities in arbitrary directions for columnar solidification structures can be calculated without simulation. The main area of interest regards the specific interface areas and the temporal changes, described by the solid fraction.

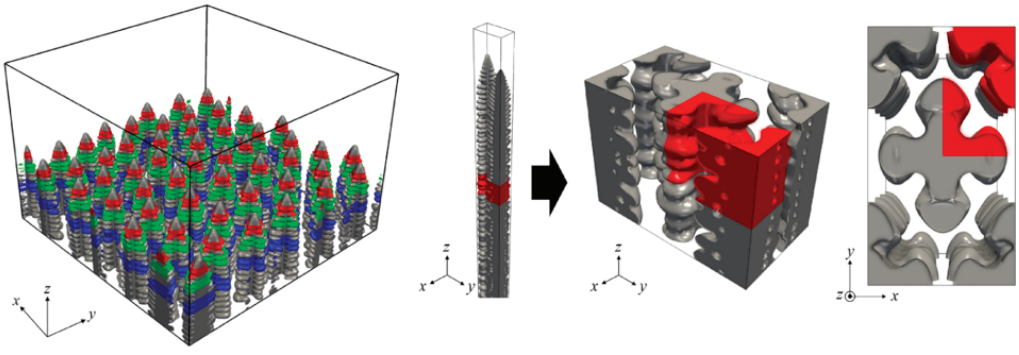

Figure 20. Domain of 1.152 × 1.152 × 0.768 mm^3 with 51 dendrites, extracting red part illustrates the arbitrary direction flow [229].

While approximation for equiaxed dendrites is effective, the KC equation is not as certain for directional solidification [233,234]. Takaki et al. [235] utilized a new permeability prediction method [209,225,232,236,237] using a parallel process of GPUs. They performed an analysis on permeability for columnar solidification structures with a periodic regular hexagonal array simulated using PF and LB. They were able to develop smooth variations in the qualities of solidification morphologies, where the permeability was shown to be independent of the array ordering of a consistent primary arm structure. This dimensionless permeability for a specific interface area can be attributed to the parallel GPU computing that performed this large-scale simulation. This reiterates the importance of large-scale simulation to study what is normally not possible with experiments.

5.6. Additive Manufacturing Applications

The study of AM is an important application of large-scale simulations where the solidification microstructure and related phenomena can significantly alter the material properties [238,239]. The porosity, propagation of cracks, or precipitation of second phases can have unique effects on the mechanical properties of the material. Many factors can

contribute to this, and this section elaborates on the different types of AM methods and studies that produce advances in our understanding of these processes. The molten pool is an interesting area of focus, where different dendrite morphologies can be obtained by controlling the thermal gradient and cooling rates. As an example, a FE-CA model was used by Yin et al. [240] to simulate dendritic growth in the molten pool of the laser engineered net shaping (LENS) process to study the laser moving speed, layer thickness, and substrate size. Comparing the simulations to experimental results is an effective measure for success. Yu et al. [241] researched a multigrid CA model to simulate these properties from an electron beam selective melting (EBSM) of a Ni-based superalloy, Inconel 718. Using the experimental data, the growth of tertiary dendrite arms was validated. This thermal-fluid model was compared to the experimental results of single-track scans, as shown in Figure 21. By studying how primary dendrite arms grow in the melt pool at the mesoscale, this research provided a promising approach for studying shrinkage porosity and the propagation of hot cracking.

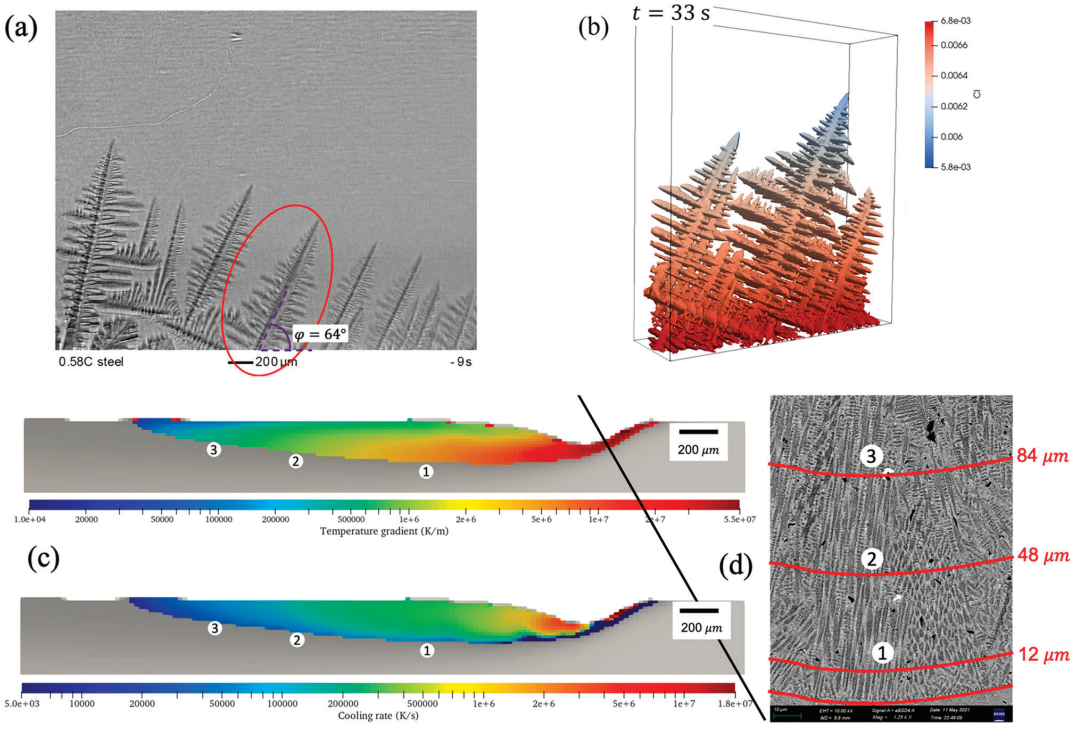

Figure 21. Comparison of the experimental (**a**) and simulated (**b**) microstructure by liquid solute concentration in the interfacial cells. (**c**) Simulated melt track showing temperature gradient (**top**) and cooling rate (**bottom**) compared with the experimental (**d**) solidified melting pool region, where numbers 1, 2, and 3 correspond to the parallel locations between simulation and experimental results [241].

The complexity of AM requires many components to efficiently model the processes. An interesting aspect of AM processes is the potential for location-specific microstructure control. Shi et al. [242] studied the effect of laser beam shaping on the morphology, size, and crystallographic texture for the laser powder bed fusion (L-PBF) of stainless steel. First, they used a process modeling code, ALE3D, for solving the continuity, momentum, and energy equations, which was developed at Lawrence Livermore National Laboratory using a hybrid finite element and finite volume formulation [243]. The output of the ALE3D

was the temperature field for all nodes through time. The transient temperature field was then imported to a simplified CA model to capture the grain structure. The ALE3D solver needed a coarser grid compared to the CA model. Therefore, the output temperature field from the ALE3D solver was projected on a finer CA mesh. They utilized the DREAM 3D software [244] and experimental measurements for the initial grain structure required in the CA model.

The properties of AM builds are highly dependent on the process parameters. Lian et al. [245] proposed a 3D CA-FV method to study the process parameters including laser scan speed and laser power to predict the grain structure for the single track directed energy deposition (DED) AM process of the Inconel 718 alloy. They also presented the grain growth for a multiple-layer deposition process with different raster patterns. The comparison of the 3D simulation results with electron backscattered diffraction (EBSD) and pole figure experimental results are shown in Figure 22. In their proposed method, the cellular automaton method, enriched with a grain nucleation scheme, was used to predict columnar, equiaxed, and mixed grains, while the FV method was used to solve heat transfer and thermocapillary flow.

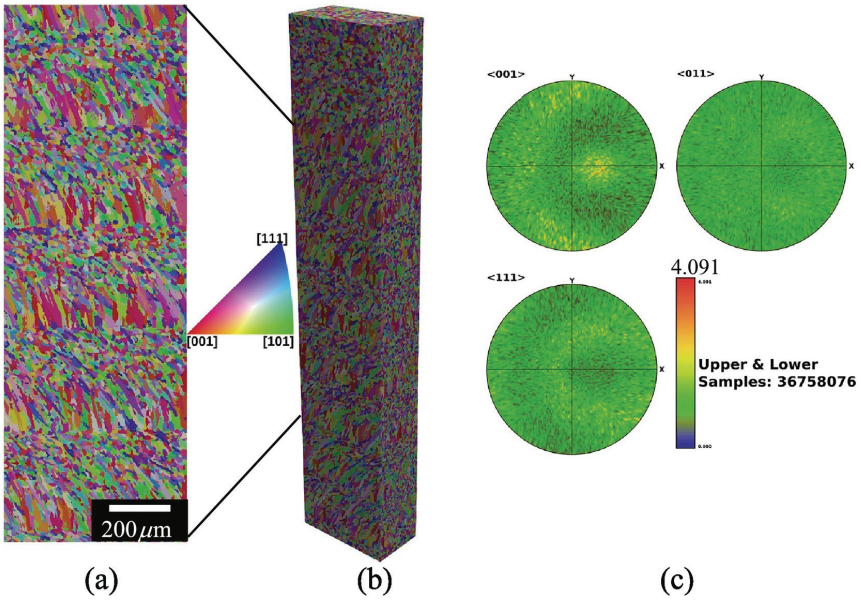

Figure 22. Simulation of the grain structure for multi-layer AM builds with a unidirectional raster pattern. (**a**) Midsection EBSD; (**b**) 3D grain structure; (**c**) 3D pole figure of these simulations [245].

L-PBF is the most popular process for manufacturing functional parts for different applications [138,157–159]. The simulation of L-PBF requires considering localized phenomena that are highly transient, making the simulation very complex. Marangoni convection in the melt pool, rapid solidification, topological depression of the melt, and thermal cycling are examples of such complex phenomena [242]. Elahi et al. [246] recently presented a computational framework for this type of simulation by using a combination of CALPHAD calculations for alloy properties, macroscale FE thermal simulations, and microscopic PF models for the melt pool solidification. They were able to calculate a billion grid points on a single cluster node of eight GPUs, providing insight into the grain texture selection with the details of dendrites for a realistic multiscale SLM simulation.

The large-scale simulations have enabled innovative melting strategies for AM such as localized melt-scanning to control the grain size and spacing of the primary dendrite arms. Raghavan et al. [247] produced predictions for grain sizing for a corresponding qualitative

texture plot. This process allows for a consistent solidification microstructure across the build. By comparing the experimental results with the simulations, context for the types of microstructures was validated with the types of melt strategies.

Kinetic Monte Carlo [248] has been used to simulate complex, non-traditional geometries, which are observed in AM processes. 3D grain structures have been simulated under diverse experimental conditions by Rogers et al. [249]. The open-source Stochastic Parallel Particle Kinetic Simulator (SPPARKS) distribution [250] was built to scale using MPI and a spatial-decomposition of the simulation domain. The 3D simulation below (Figure 23) was both quantitatively and qualitatively compared to the experimental results of AM processes such as LENS and L-PBF to study the temperature dependent grain boundary mobility and molten zones, respectively, which were both in good agreement.

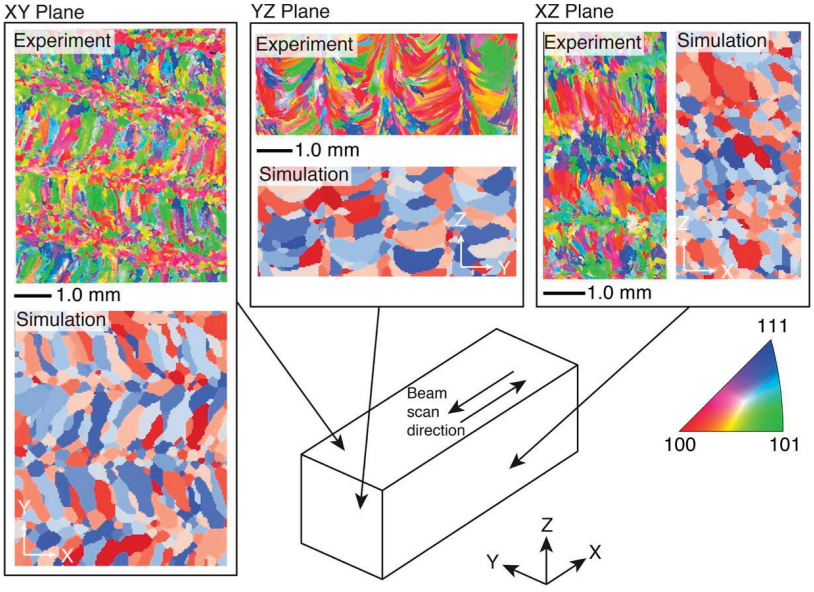

Figure 23. Simulated SPPARKS AM microstructures compared to the experimental scanning results of the 304L stainless steel deposited using LENS [249].

The research by Rogers et al. provides a comprehensive comparison of AM microstructure simulation methods such as CAFE [57,251], CA-LB [252], Monte Carlo [253,254], and empirical microstructure models [255]. In comparison, the CA models have a higher computation cost requirement. In addition, they are limited to a few passes of a heat source, which currently does not simulate solid-state grain evolution after solidification. On the other hand, Monte Carlo does not allow for the direct coupling of thermal and microstructural models or the incorporation of the material texture/anisotropy. However, Monte Carlo is open source in comparison, and utilizes idealized molten zones without the need to parameterize for specific material systems.

In their comparative study of phase field (PF) and cellular automaton (CA) computational models, Elahi et al. [256] sought to forecast the microstructure evolution during solidification in AM. The researchers discovered that PF simulations were superior in terms of accurately capturing microscopic features, whereas the CA simulations necessitated grid refinement to achieve a partial congruence with PF outcomes. Despite certain discrepancies, the average grain distributions drawn from various simulations demonstrated a satisfactory concurrence between the PF and CA models. However, the researchers identified differences between PF and CA in aspects such as transient growth regimes and the morphology of the solid–liquid interface. PF simulations depicted an initial period of

near-planar solidification, which then destabilized morphologically into cells or dendrites, an aspect overlooked in CA simulations. Additionally, the PF simulations accounted for the dynamics of side-branching post destabilization, leading to the removal of less favorably oriented grains, a phenomenon absent in CA simulations, which, in contrast, yielded smoother grain boundaries compared to those obtained from the PF simulations.

The potential for simulating AM is ever growing, as are the processing parameters. Because of AM's complex geometries, many novel techniques have been applied to determine the most optimal conditions. New simulation approaches are necessary to represent the performance and validate experiments.

6. Future Developments

The progression of large-scale simulations of the solidification microstructure has shown that the factors for realistic results are constantly improving. In prediction analysis, the complexity has grown with respect to technological advances. An interesting concept of utilizing machine learning for simulating grain growth has a lot more potential for future development. In 2017, Hu et al. [257] used a CA method, along with machine learning, to simulate the grain and pore growth in aluminum alloys. The back propagation neural network (BPNN) was used to create a correlation between the solidification parameters and pore growth; however, the domain was restricted to a size of 200 × 200 μm. Machine learning has the unique potential to assist in the modeling of dendritic features and has been implemented in the prediction of secondary arm spacing in aluminum alloys [258]. While deep learning has been used for the prediction of porosity defects in aluminum alloys [259], applications with simulations have been limited. Most recently, Hu et al. [260] used recurrent neural networks to accelerate PF predictions. By comparing different dimensionality-reduction methods such as linear (principal component analysis (PCA) [261]) and nonlinear embedding (isometric feature mapping (Isomap)) [262] and uniform manifold approximation and projection (UMAP) [263] techniques, the latent space can preserve the PF input parameters. The autocorrelation-based PCA proved to be the most efficient, while a computation speedup of 3x was able to be implemented using recurrent neural network (RNN) models with a fewer number of cells and a gating mechanism such as the gated recurrent unit (GRU) [264] or long short-term memory (LSTM) [265]. Figure 24 shows the implementation of the RNN model. Future development shows promise with the integration of mesoscale simulation systems.

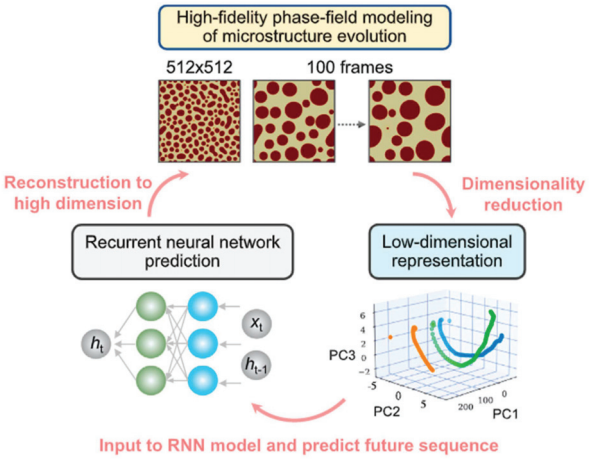

Figure 24. The RNN model to predict microstructural evolution in latent space for PF modeling [260].

Another potential area for higher development is the complexity of remelting in larger domains. The evolution of dendrite remelting consists of four stages, while the last

stage consists of fragmentation [266], which enables the further discretion of large-scale realistic simulations. An interesting phenomenon, where secondary arms remelt at the roots, detaching from the primary trunk, and moving toward unsolidified melt can be better understood in larger domains [267]. The combination of improved physics models and computational algorithms with thermodynamic databases would enable the calculation of multicomponent phase equilibria, allowing for more reliable simulations for real-world industrial applications.

7. Conclusions

The applications of simulating the evolution of the microstructure during solidification are as diverse as the observable features. The large-scale domain requires extensive computing power; therefore, a combination of hardware and numerical techniques are necessary to enable scaling. Employing the most efficient numerical methods together with communication techniques over a large number of processing units, the research into solidification simulations has resulted in innovative methodologies, enabling the investigation of various features during alloy solidification.

To enable efficient simulation of the solidification microstructure, various numerical methods have been developed to improve the simulation results over larger domains. Cellular automaton (CA), with its simplicity and computational efficiency, has been featured to simulate dendrite growth in large 2D and 3D domains. Phase field (PF), being the most popular, has been utilized to reproduce the physics more accurately. Although more computationally demanding compared to CA, PF has been used in the largest dendrite growth simulation to this date. Direct interface tracking (DIT) and level set (LS) methods are less popular for large-scale simulations. However, they provide a direct method to handle the sharp interface front, avoiding PF's asymptotic analysis, where techniques of adaptive mesh refinement (AMR) and parallelization have become a drawback in some situations. Scaling with a dendrite needle network (DNN) method allows for analytical and coarse-grained models to be used in combination, which can serve as a useful multiscale modeling technique.

Solving the transport phenomena is necessary for realistic simulations with a trade-off in complexity. Solving the differential equation can be integral to the performance of the simulation. While finite element, finite difference, and finite volume have been conventionally used to solve the heat transfer, diffusion, and fluid flow equations, the lattice Boltzmann method offers an alternative local method to reduce the computation cost, especially for the case of fluid flow. However, there are many trade-offs between the methods of simulating the transport phenomenon.

Many features were discussed in detail of increasing complexity. Competitive growth and dendrite interactions are better understood in large-scale simulations, which can result in a more realistic interpretation for columnar to equiaxed transition (CET). Simulating the solute transport can provide a deeper understanding of segregation, which can be greatly influenced by convection, both natural and forced. The mushy zone permeability is another area that can greatly benefit from large-scale parallel simulations. Additive manufacturing (AM) processes often involve complex physics, which can be influenced by processing parameters specific to the simulation, demanding higher computational power.

Several manufacturing and materials processing techniques can take advantage of the prediction capabilities offered by large-scale simulations of the solidification microstructure. The modeling approaches still have a lot of future improvements to innovate upon, with promising developments in machine learning and computing power.

Author Contributions: Conceptualization, N.C., S.A.N. and M.E.; methodology, N.C., S.A.N. and M.E.; investigation, N.C. and S.A.N.; writing—original draft preparation, N.C. and S.A.N.; writing—review and editing, M.E.; supervision, M.E.; project administration, M.E.; funding acquisition, M.E. All authors have read and agreed to the published version of the manuscript.

Funding: This work was partially supported by the National Science Foundation Award No. HRD-2112554 and the National Aeronautics and Space Administration (NASA) grant number 80NSSC20K0736.

Data Availability Statement: Data sharing is not applicable to this article.

Acknowledgments: N.C. was the recipient of a CREST-CATSUS fellowship, for which we are grateful. The authors also acknowledge California State University, Los Angeles and the University of Akron for their support.

Conflicts of Interest: The authors declare no conflict of interest.

References

1. Rappaz, M. Modeling and characterization of grain structures and defects in solidification. *Curr. Opin. Solid State Mater. Sci.* **2016**, *20*, 37–45. [CrossRef]
2. Asta, M.; Beckermann, C.; Karma, A.; Kurz, W.; Napolitano, R.; Plapp, M.; Purdy, G.; Rappaz, M.; Trivedi, R. Solidification microstructures and solid-state parallels: Recent developments, future directions. *Acta Mater.* **2009**, *57*, 941–971. [CrossRef]
3. Kurz, W.; Rappaz, M.; Trivedi, R. Progress in modelling solidification microstructures in metals and alloys. Part II: Dendrites from 2001 to 2018. *Int. Mater. Rev.* **2021**, *66*, 30–76. [CrossRef]
4. Liu, X.; Sun, Y.; Wang, Y.; Jia, S.; Wu, Y.; Peng, L.; Fan, J.; Li, Y.; Liu, J.; Li, A. The effect of cross-section geometry of castings on dendrite evolution in Mg Gd alloys by in situ X-ray radiography. *Mater. Charact.* **2022**, *186*, 111751. [CrossRef]
5. Feng, S.; Liotti, E.; Grant, P.S. X-ray Imaging of Alloy Solidification: Crystal Formation, Growth, Instability and Defects. *Materials* **2022**, *15*, 1319. [CrossRef]
6. Wang, Y.; Sun, Y.; Liu, X.; Wang, J.; Wei, M.; Wu, Y.; Peng, L. Recent progress in Mg alloys investigated via synchrotron radiation. *Mater. Sci. Technol.* **2022**, *38*, 131–142. [CrossRef]
7. Peng, Y.; Miao, K.; Sun, W.; Liu, C.; Wu, H.; Geng, L.; Fan, G. Recent Progress of Synchrotron X-Ray Imaging and Diffraction on the Solidification and Deformation Behavior of Metallic Materials. *Acta Met. Sin. (Engl. Lett.)* **2022**, *35*, 3–24. [CrossRef]
8. Feng, S.; Han, I.; Lui, A.; Vincent, R.; Ring, G.; Grant, P.S.; Liotti, E. Investigating Metal Solidification with X-ray Imaging. *Metals* **2022**, *12*, 395. [CrossRef]
9. Zhang, L.; Li, X.; Liu, Z.; Li, R.; Jiang, R.; Guan, S.; Liu, B. Scalable ultrasonic casting of large-scale 2219AA Al alloys: Experiment and simulation. *Mater. Today Commun.* **2021**, *27*, 102329. [CrossRef]
10. Liotti, E.; Lui, A.; Vincent, R.; Kumar, S.; Guo, Z.; Connolley, T.; Dolbnya, I.; Hart, M.; Arnberg, L.; Mathiesen, R.; et al. A synchrotron X-ray radiography study of dendrite fragmentation induced by a pulsed electromagnetic field in an Al–15Cu alloy. *Acta Mater.* **2014**, *70*, 228–239. [CrossRef]
11. Lee, P.D.; Hunt, J.D. Hydrogen Porosity In Directional Solidified Aluminum-Copper Alloys: In Situ Observation. *Acta Metall.* **1997**, *45*, 4155–4169. [CrossRef]
12. Dahle, A.; StJohn, D. Rheological behaviour of the mushy zone and its effect on the formation of casting defects during solidification. *Acta Mater.* **1998**, *47*, 31–41. [CrossRef]
13. Alexiades, V.; Cannon, J.R.; Cannon, V.A.A.J.R.; Visintin, A.; Epperson, J.F. Free Boundary Problems in Solidification of Alloys. *SIAM J. Math. Anal.* **1980**, *11*, 254–264. [CrossRef]
14. *Alloy Physics*; Wiley Online Library: Hoboken, NJ, USA, 2007. [CrossRef]
15. Aneesh, T.; Pawan, K.; Mohan, L.; Krishna, P.H.; Hotta, T.K.; Mohanty, C.P.; Gupta, M. Exploring Casting Defects of AA7075 Alloy in the Gravity Die Casting Simulation of an IC Engine Block. *Proc. Inst. Mech. Eng. Part E J. Process Mech. Eng.* **2022**, *236*, 1556–1565. [CrossRef]
16. Xiang, L.; Tao, J.Q.; Chen, Q.; Zhao, G.Z.; Zhang, F.Y.; Chai, S.X.; Xing, Z.H.; Li, M.; Yang, E.C.; Li, F. Mechanical Properties and Microstructure of Thin-Walled Al-Cu Alloy Casting. *Strength Mater.* **2022**, *54*, 302–308. [CrossRef]
17. Sertucha, J.; Lacaze, J. Casting Defects in Sand-Mold Cast Irons—An Illustrated Review with Emphasis on Spheroidal Graphite Cast Irons. *Metals* **2022**, *12*, 504. [CrossRef]
18. Gupta, R.D.; Sharma, N.; Khanna, R.; Sharma, S.; Dayal, S. A study of process optimization of carburetor die casting process. *Mater. Today Proc.* **2022**, *62*, 1420–1424. [CrossRef]
19. Li, Y.; Liu, J.; Huang, W.; Zhang, S. Microstructure related analysis of tensile and fatigue properties for sand casting aluminum alloy cylinder head. *Eng. Fail. Anal.* **2022**, *136*, 106210. [CrossRef]
20. Ali, R.; Zafar, M.; Manzoor, T.; Kim, W.Y.; Rashid, M.U.; Abbas, S.Z.; Zai, B.A.; Ali, M. Elimination of solidification shrinkage defects in the casting of aluminum alloy. *J. Mech. Sci. Technol.* **2022**, *36*, 2345–2353. [CrossRef]
21. Jolly, M.; Katgerman, L. Modelling of defects in aluminium cast products. *Prog. Mater. Sci.* **2022**, *123*, 100824. [CrossRef]
22. Srivatsan, T.S.; Sudarshan, T.S.; Manigandan, K. *Manufacturing Techniques for Materials: Engineering and Engineered*; CRC Press: Boca Raton, FL, USA, 2018. [CrossRef]
23. Gabriel, E.; Fagg, G.E.; Bosilca, G.; Angskun, T.; Dongarra, J.J.; Squyres, J.M.; Sahay, V.; Kambadur, P.; Barrett, B.; Lumsdaine, A.; et al. Open MPI: Goals, Concept, and Design of a Next Generation MPI Implementation. In *Recent Advances in Parallel Virtual Machine and Message Passing Interface*; Springer: Berlin/Heidelberg, Germany, 2004. [CrossRef]

24. Gropp, W.; Gropp, W.D.; Lusk, E.; Skjellum, A.; Lusk, A.D.F.E.E. Using MPI: Portable Parallel Programming with the Mes-Sage-Passing Interface. MIT Press: Cambridge, MA, USA, 1999; Volume 1.
25. MPICH. Available online: https://www.mpich.org/ (accessed on 15 May 2023).
26. Intel MPI Library. Available online: https://www.intel.com/content/www/us/en/developer/tools/oneapi/mpi-library.html#gs.46ggfe (accessed on 15 May 2023).
27. MVAPICH. Available online: https://mvapich.cse.ohio-state.edu/faq/ (accessed on 15 May 2023).
28. Open MPI. Available online: https://www.open-mpi.org// (accessed on 15 May 2023).
29. NVIDIA Developer. Available online: https://developer.nvidia.com/cuda-zone/ (accessed on 15 May 2023).
30. Cheng, J.; Grossman, M.; McKercher, T. *Professional CUDA C Programming*; John Wiley & Sons: Indianapolis, IN, USA, 2014.
31. Cook, S. *CUDA Programming: A Developer's Guide to Parallel Computing with GPUs*; Newnes: New South Wales, Australia, 2012.
32. Sanders, J.; Kandrot, E. *CUDA by Example: An Introduction to General-Purpose GPU Programming*; Addison-Wesley Professional: Boston, MA, USA, 2010.
33. Plewa, T.; Linde, T.; Weirs, V.G. Adaptive Mesh Refinement-Theory and Applications. In Proceedings of the Chicago Workshop on Adaptive Mesh Refinement Methods, Chicago, IL, USA, 3–5 September 2005. [CrossRef]
34. Dorari, E.; Eshraghi, M.; Felicelli, S.D. A multiple-grid-time-step lattice Boltzmann method for transport phenomena with dissimilar time scales: Application in dendritic solidification. *Appl. Math. Model.* **2018**, *62*, 580–594. [CrossRef]
35. Sakane, S.; Takaki, T.; Ohno, M.; Shibuta, Y.; Aoki, T. Acceleration of phase-field lattice Boltzmann simulation of dendrite growth with thermosolutal convection by the multi-GPUs parallel computation with multiple mesh and time step method. *Model. Simul. Mater. Sci. Eng.* **2019**, *27*, 054004. [CrossRef]
36. Schneider, D. The Exascale Era is Upon Us: The Frontier supercomputer may be the first to reach 1,000,000,000,000,000,000 operations per second. *IEEE Spectr.* **2022**, *59*, 34–35. [CrossRef]
37. Ji, H.; Daughton, W.; Jara-Almonte, J.; Le, A.; Stanier, A.; Yoo, J. Magnetic reconnection in the era of exascale computing and multiscale experiments. *Nat. Rev. Phys.* **2022**, *4*, 263–282. [CrossRef]
38. Zhang, N. Moore's Law is dead, long live Moore's Law. *arXiv* **2023**, arXiv:2205.15011. Available online: https://arxiv.org/ftp/arxiv/papers/2205/2205.15011.pdf (accessed on 15 May 2023).
39. Yanagimoto, J.; Banabic, D.; Banu, M.; Madej, L. Simulation of metal forming—Visualization of invisible phenomena in the digital era. *CIRP Ann.* **2022**, *71*, 599–622. [CrossRef]
40. Brasoveanu, A.; Moodie, M.; Agrawal, R. Textual evidence for the perfunctoriness of independent medical reviews. In Proceedings of the CEUR Workshop Proceedings, CEUR-WS, San Diego, CA, USA, 24 August 2020; pp. 1–9. [CrossRef]
41. Takaki, T.; Fukuoka, T.; Tomita, Y. Phase-field simulation during directional solidification of a binary alloy using adaptive finite element method. *J. Cryst. Growth* **2005**, *283*, 263–278. [CrossRef]
42. Chen, C.; Lan, C. Efficient adaptive three-dimensional phase field simulation of free dendritic growth under natural convection. *J. Cryst. Growth* **2010**, *312*, 1437–1442. [CrossRef]
43. Sahoo, S.; Chou, K. Phase-field simulation of microstructure evolution of Ti–6Al–4V in electron beam additive manufacturing process. *Addit. Manuf.* **2016**, *9*, 14–24. [CrossRef]
44. Watanabe, S.; Aoki, T. Large-scale flow simulations using lattice Boltzmann method with AMR following free-surface on multiple GPUs. *Comput. Phys. Commun.* **2021**, *264*, 107871. [CrossRef]
45. Sakane, S.; Aoki, T.; Takaki, T. Parallel GPU-accelerated adaptive mesh refinement on two-dimensional phase-field lattice Boltzmann simulation of dendrite growth. *Comput. Mater. Sci.* **2022**, *211*, 111507. [CrossRef]
46. Schive, H.-Y.; ZuHone, J.A.; Goldbaum, N.J.; Turk, M.J.; Gaspari, M.; Cheng, C.-Y. gamer-2: A GPU-accelerated adaptive mesh refinement—Accuracy, performance, and scalability. *Mon. Not. R. Astron. Soc.* **2018**, *481*, 4815–4840. [CrossRef]
47. Miyoshi, E.; Takaki, T.; Ohno, M.; Shibuta, Y.; Sakane, S.; Shimokawabe, T.; Aoki, T. Ultra-large-scale phase-field simulation study of ideal grain growth. *Npj Comput. Mater.* **2017**, *3*, 25. [CrossRef]
48. Sakane, S.; Takaki, T.; Rojas, R.; Ohno, M.; Shibuta, Y.; Shimokawabe, T.; Aoki, T. Multi-GPUs parallel computation of dendrite growth in forced convection using the phase-field-lattice Boltzmann model. *J. Cryst. Growth* **2017**, *474*, 154–159. [CrossRef]
49. Apel, M.; Spatschek, R.; Roters, F.; Larsson, H.; Gandin, C.-A.; Guillemot, G.; Podmaniczky, F.; Gránásy, L.; Schmitz, G.J.; Chen, Q. Microstructure Modeling. In *Handbook of Software Solutions for ICME*; Wiley Online Library: Hoboken, NJ, USA, 2016; pp. 269–323. [CrossRef]
50. Cagigas-Muñiz, D.; Diaz-Del-Rio, F.; Sevillano-Ramos, J.L.; Guisado-Lizar, J.-L. Efficient simulation execution of cellular automata on GPU. *Simul. Model. Pract. Theory* **2022**, *118*, 102519. [CrossRef]
51. Dorari, E. Modeling Dendritic Solidification Under Melt Convection Using Lattice Boltzmann and Cellular Automaton Methods. Ph.D. Thesis, The University of Akron, Akron, OH, USA, 2017.
52. Wesner, E.; Choudhury, A.; August, A.; Berghoff, M.; Nestler, B. A phase-field study of large-scale dendrite fragmentation in Al–Cu. *J. Cryst. Growth* **2012**, *359*, 107–121. [CrossRef]
53. Zhang, Y.; Zhou, J.; Yin, Y.; Shen, X.; Ji, X. Multi-GPU implementation of a cellular automaton model for dendritic growth of binary alloy. *J. Mater. Res. Technol.* **2021**, *14*, 1862–1872. [CrossRef]
54. Gandin, C.-A.; Rappaz, M. A coupled finite element-cellular automaton model for the prediction of dendritic grain structures in solidification processes. *Acta Metall. Mater.* **1994**, *42*, 2233–2246. [CrossRef]

55. Wang, W.; Lee, P.; McLean, M. A model of solidification microstructures in nickel-based superalloys: Predicting primary dendrite spacing selection. *Acta Mater.* **2003**, *51*, 2971–2987. [CrossRef]
56. Saad, A.; Gandin, C.-A.; Bellet, M.; Shevchenko, N.; Eckert, S. Simulation of Channel Segregation During Directional Solidification of In—75 wt pct Ga. Qualitative Comparison with In Situ Observations. *Metall. Mater. Trans. A* **2015**, *46*, 4886–4897. [CrossRef]
57. Gandin, C.A.; Desbiolles, J.L.; Rappaz, M.; Thevoz, P. A three-dimensional cellular automation-finite element model for the prediction of solidification grain structures. *Metall. Mater. Trans. A* **1999**, *30*, 3153–3165. [CrossRef]
58. Rafii-Tabar, H. Multi-scale computational modelling of solidification phenomena. *Phys. Rep.* **2002**, *365*, 145–249. [CrossRef]
59. Moelans, N.; Blanpain, B.; Wollants, P. An introduction to phase-field modeling of microstructure evolution. *Calphad* **2008**, *32*, 268–294. [CrossRef]
60. Tourret, D.; Liu, H.; Llorca, J. Phase-field modeling of microstructure evolution: Recent applications, perspectives and challenges. *Prog. Mater. Sci.* **2022**, *123*, 100810. [CrossRef]
61. Segurado, J.; Lebensohn, R.A.; Llorca, J. Computational Homogenization of Polycrystals. *Adv. Appl. Mech.* **2018**, *51*, 1–114. [CrossRef]
62. Chen, S.; Merriman, B.; Osher, S.; Smereka, P. A Simple Level Set Method for Solving Stefan Problems. *J. Comput. Phys.* **1997**, *135*, 8–29. [CrossRef]
63. Kobayashi, R. Modeling and numerical simulations of dendritic crystal growth. *Phys. D Nonlinear Phenom.* **1993**, *63*, 410–423. [CrossRef]
64. Takaki, T. Phase-field Modeling and Simulations of Dendrite Growth. *ISIJ Int.* **2014**, *54*, 437–444. [CrossRef]
65. Kobayashi, R. A Numerical Approach to Three-Dimensional Dendritic Solidification. *Exp. Math.* **1994**, *3*, 59–81. [CrossRef]
66. Provatas, N.; Goldenfeld, N.; Dantzig, J. Adaptive Mesh Refinement Computation of Solidification Microstructures Using Dynamic Data Structures. *J. Comput. Phys.* **1999**, *148*, 265–290. [CrossRef]
67. Chen, C.; Tsai, Y.; Lan, C. Adaptive phase field simulation of dendritic crystal growth in a forced flow: 2D vs. 3D morphologies. *Int. J. Heat Mass Transf.* **2009**, *52*, 1158–1166. [CrossRef]
68. Lu, Y.; Beckermann, C.; Ramirez, J. Three-dimensional phase-field simulations of the effect of convection on free dendritic growth. *J. Cryst. Growth* **2005**, *280*, 320–334. [CrossRef]
69. Jeong, J.-H.; Goldenfeld, N.; Dantzig, J.A. Phase field model for three-dimensional dendritic growth with fluid flow. *Phys. Rev. E* **2001**, *64*, 041602. [CrossRef] [PubMed]
70. Takaki, T.; Yamanaka, A.; Higa, Y.; Tomita, Y. Phase-field model during static recrystallization based on crystal-plasticity theory. *J. Comput. Mater. Des.* **2007**, *14*, 75–84. [CrossRef]
71. Shibuta, Y.; Ohno, M.; Takaki, T. Solidification in a Supercomputer: From Crystal Nuclei to Dendrite Assemblages. *JOM* **2015**, *67*, 1793–1804. [CrossRef]
72. Warren, J.; Boettinger, W. Prediction of dendritic growth and microsegregation patterns in a binary alloy using the phase-field method. *Acta Metall. Mater.* **1995**, *43*, 689–703. [CrossRef]
73. Suzuki, T.; Ode, M.; Kim, S.G.; Kim, W.T. Phase-field model of dendritic growth. *J. Cryst. Growth* **2001**, *237–239*, 125–131. [CrossRef]
74. Takaki, T.; Shimokawabe, T.; Ohno, M.; Yamanaka, A.; Aoki, T. Unexpected selection of growing dendrites by very-large-scale phase-field simulation. *J. Cryst. Growth* **2013**, *382*, 21–25. [CrossRef]
75. Choudhury, A.; Reuther, K.; Wesner, E.; August, A.; Nestler, B.; Rettenmayr, M. Comparison of phase-field and cellular automaton models for dendritic solidification in Al–Cu alloy. *Comput. Mater. Sci.* **2012**, *55*, 263–268. [CrossRef]
76. Echebarria, B.; Folch, R.; Karma, A.; Plapp, M. Quantitative phase-field model of alloy solidification. *Phys. Rev. E* **2004**, *70*, 061604. [CrossRef]
77. Zhu, M.; Stefanescu, D.M. Virtual front tracking model for the quantitative modeling of dendritic growth in solidification of alloys. *Acta Mater.* **2007**, *55*, 1741–1755. [CrossRef]
78. Beltran-Sanchez, L.; Stefanescu, D.M. A quantitative dendrite growth model and analysis of stability concepts. *Metall. Mater. Trans. A* **2004**, *35*, 2471–2485. [CrossRef]
79. Tryggvason, G.; Esmaeeli, A.; Al-Rawahi, N. Direct numerical simulations of flows with phase change. *Comput. Struct.* **2005**, *83*, 445–453. [CrossRef]
80. Juric, D.; Tryggvason, G. A Front-Tracking Method for Dendritic Solidification. *J. Comput. Phys.* **1996**, *123*, 127–148. [CrossRef]
81. Zhao, P.; Heinrich, J. Front-Tracking Finite Element Method for Dendritic Solidification. *J. Comput. Phys.* **2001**, *173*, 765–796. [CrossRef]
82. Kim, Y.-T.; Goldenfeld, N.; Dantzig, J. Computation of dendritic microstructures using a level set method. *Phys. Rev. E* **2000**, *62*, 2471–2474. [CrossRef]
83. Gibou, F.; Fedkiw, R.; Caflisch, R.; Osher, S. A Level Set Approach for the Numerical Simulation of Dendritic Growth. *J. Sci. Comput.* **2002**, *19*, 183–199. [CrossRef]
84. Tan, L.; Zabaras, N. A level set simulation of dendritic solidification of multi-component alloys. *J. Comput. Phys.* **2007**, *221*, 9–40. [CrossRef]
85. Corbit, M. The Cornell Theory Center. *IEEE Comput. Sci. Eng.* **1994**, *1*, 10–13. [CrossRef]
86. Tan, L.; Zabaras, N. Modeling the growth and interaction of multiple dendrites in solidification using a level set method. *J. Comput. Phys.* **2007**, *226*, 131–155. [CrossRef]

87. Osher, S.; Fedkiw, R. Level Set Methods and Dynamic Implicit Surfaces. *Appl. Mech. Rev.* **2004**, *57*, B15. [CrossRef]
88. Tan, L.; Zabaras, N. A level set simulation of dendritic solidification with combined features of front-tracking and fixed-domain methods. *J. Comput. Phys.* **2006**, *211*, 36–63. [CrossRef]
89. Gibou, F.; Fedkiw, R.; Osher, S. A review of level-set methods and some recent applications. *J. Comput. Phys.* **2018**, *353*, 82–109. [CrossRef]
90. Tourret, D.; Karma, A. Multiscale dendritic needle network model of alloy solidification. *Acta Mater.* **2013**, *61*, 6474–6491. [CrossRef]
91. Tourret, D.; Karma, A. Three-dimensional dendritic needle network model for alloy solidification. *Acta Mater.* **2016**, *120*, 240–254. [CrossRef]
92. Sturz, L.; Zimmermann, G.; Gandin, C.; Billia, B.; Magelinck, N.; Nguyen-Thi, H.; Browne, D.J.; Mirihanage, W.U.; Voss, D.; Beckermann, C.; et al. ISS-Experiments of Columnar-To-Equiaxed Transition in Solidification Processing. *Mater. Res. Microgravity* **2012**, *2012*, 56–62.
93. Tourret, D.; Sturz, L.; Viardin, A.; Založnik, M. Comparing mesoscopic models for dendritic growth. In *IOP Conference Series: Materials Science and Engineering*; IOP Publishing: Bristol, UK, 2020. [CrossRef]
94. Bellón, B.; Boukellal, A.; Isensee, T.; Wellborn, O.; Trumble, K.; Krane, M.; Titus, M.; Tourret, D.; Llorca, J. Multiscale prediction of microstructure length scales in metallic alloy casting. *Acta Mater.* **2021**, *207*, 116686. [CrossRef]
95. Isensee, T.; Tourret, D. Convective effects on columnar dendritic—A multiscale dendritic needle network study. *Acta Mater.* **2022**, *234*, 118035. [CrossRef]
96. Pal, P.; Abhishek, G.S.; Karagadde, S. A Monte Carlo approach to simulate dendritic microstructures during binary alloy solidification. *Model. Simul. Mater. Sci. Eng.* **2020**, *28*, 085001. [CrossRef]
97. Zhang, Z.; Ge, P.; Li, J.Y.; Ren, D.X.; Wu, T. Monte Carlo simulations of solidification and solid-state phase transformation during directed energy deposition additive manufacturing. *Prog. Addit. Manuf.* **2022**, *7*, 671–682. [CrossRef]
98. Zhang, Z.; Wu, Q.; Grujicic, M.; Wan, Z.Y. Monte Carlo simulation of grain growth and welding zones in friction stir welding of AA6082-T6. *J. Mater. Sci.* **2016**, *51*, 1882–1895. [CrossRef]
99. Mohamad, A.A. *Lattice Boltzmann Method Fundamentals and Engineering Applications with Computer Codes*, 2nd ed.; Springer Nature: Berlin/Heidelberg, Germany, 2019. [CrossRef]
100. Dantzig, J.A.; Rappaz, M. *Solidification Engineering Sciences Materials 2nd Edition Revised & Expanded*; EPFL Press: Lausanne, Switzerland, 2016.
101. Feng, Y.; Založnik, M.; Thomas, B.; Phillion, A. Meso-scale simulation of liquid feeding in an equiaxed dendritic mushy zone. *Materialia* **2020**, *9*, 100612. [CrossRef]
102. Thomée, V. *Galerkin Finite Element Methods for Parabolic Problems*; Springer: Berlin/Heidelberg, Germany, 2006. [CrossRef]
103. Dongarra, J.; Lumsdaine, A.; Pozo, R.; Remington, K. IML++ v. 1.2. In *Iterative Methods Library Reference Guide*; NIST Washington, National Institute of Standards and Technology: Gaithersburg, MD, USA, 1995.
104. Krane, M.J.M.; Johnson, D.R.; Raghavan, S. The development of a cellular automaton-finite volume model for dendritic growth. *Appl. Math. Model.* **2009**, *33*, 2234–2247. [CrossRef]
105. Zhang, X.; Zhao, J.; Jiang, H.; Zhu, M. A three-dimensional cellular automaton model for dendritic growth in multi-component alloys. *Acta Mater.* **2002**, *60*, 2249–2257. [CrossRef]
106. Shahane, S.; Aluru, N.; Ferreira, P.; Kapoor, S.G.; Vanka, S.P. Finite volume simulation framework for die casting with uncertainty quantification. *Appl. Math. Model.* **2019**, *74*, 132–150. [CrossRef]
107. Udaykumar, H.S.; Mittal, R.; Rampunggoon, P. Interface tracking finite volume method for complex solid-fluid interactions on fixed meshes. *Commun. Numer. Methods Eng.* **2002**, *18*, 89–97. [CrossRef]
108. Karma, A.; Rappel, W.-J. Quantitative phase-field modeling of dendritic growth in two and three dimensions. *Phys. Rev. E* **1998**, *57*, 4323–4349. [CrossRef]
109. Li, R.; Di, Y.; Tang, T. A General Moving Mesh Framework in 3D and its Application for Simulating the Mixture of Multi-Phase Flows. *Commun. Comput. Phys.* **2007**, *170*, 365–393.
110. Wang, H.; Li, R.; Tang, T. Efficient computation of dendritic growth with r-adaptive finite element methods. *J. Comput. Phys.* **2008**, *227*, 5984–6000. [CrossRef]
111. Farrahi, G.H. Finite element simulation of residual stresses in laser heating Application of Homotopy Analysis Method (HAM) in studying MEMS behavior. In Proceedings of the 7th Iranian Aerospace Society Conference, Tehran, Iran, 19–21 February 2008.
112. Yang, J.; Wang, F. 3D finite element temperature field modelling for direct laser fabrication. *Int. J. Adv. Manuf. Technol.* **2009**, *43*, 1060–1068. [CrossRef]
113. Qin, Q.; Shang, S.; Wu, D.; Zang, Y. Comparative Analysis of Bulge Deformation between 2D and 3D Finite Element Models. *Adv. Mech. Eng.* **2014**, *2014*, 942719. [CrossRef]
114. Alexopoulou, V.E.; Papazoglou, E.L.; Karmiris-Obratański, P.; Markopoulos, A.P. 3D finite element modeling of selective laser melting for conduction, transition and keyhole modes. *J. Manuf. Process.* **2022**, *75*, 877–894. [CrossRef]
115. Prakash, S.A.; Hariharan, C.; Arivazhagan, R.; Sheeja, R.; Raj, V.A.A.; Velraj, R. Review on numerical algorithms for melting and solidification studies and their implementation in general purpose computational fluid dynamic software. *J. Energy Storage* **2021**, *36*, 102341. [CrossRef]
116. Varnik, F.; Raabe, D. Chaotic flows in microchannels: A lattice Boltzmann study. *Mol. Simul.* **2006**, *33*, 583–587. [CrossRef]

117. Varnik, F.; Dorner, D.; Raabe, D. Roughness-induced flow instability: A lattice Boltzmann study. *J. Fluid Mech.* **2007**, *573*, 191–209. [CrossRef]
118. Varnik, F.; Raabe, D. Scaling effects in microscale fluid flows at rough solid surfaces. *Model. Simul. Mater. Sci. Eng.* **2006**, *14*, 857–873. [CrossRef]
119. Gunstensen, A.K.; Rothman, D.H. Lattice-Boltzmann studies of immiscible two-phase flow through porous media. *J. Geophys. Res. Solid Earth* **1993**, *98*, 6431–6441. [CrossRef]
120. McNamara, G.R.; Zanetti, G. Use of the Boltzmann Equation to Simulate Lattice-Gas Automata. *Phys. Rev. Lett.* **1988**, *61*, 2332–2335. [CrossRef] [PubMed]
121. Rojas, R.; Takaki, T.; Ohno, M. A phase-field-lattice Boltzmann method for modeling motion and growth of a dendrite for binary alloy solidification in the presence of melt convection. *J. Comput. Phys.* **2015**, *298*, 29–40. [CrossRef]
122. Medvedev, D.; Varnik, F.; Steinbach, I. Simulating Mobile Dendrites in a Flow. *Procedia Comput. Sci.* **2013**, *18*, 2512–2520. [CrossRef]
123. Zhang, S.; Li, C.; Li, R. Cellular automata-lattice Boltzmann simulation of multi-dendrite motion under convection based on dynamic grid technology. *Mater. Today Commun.* **2022**, *31*, 103342. [CrossRef]
124. Takaki, T.; Rojas, R.; Ohno, M.; Shimokawabe, T.; Aoki, T. GPU phase-field lattice Boltzmann simulations of growth and motion of a binary alloy dendrite. In *IOP Conference Series: Materials Science and Engineering*; Institute of Physics Publishing: Bristol, UK, 2015. [CrossRef]
125. Jelinek, B.; Eshraghi, M.; Felicelli, S.; Peters, J.F. Large-scale parallel lattice Boltzmann–cellular automaton model of two-dimensional dendritic growth. *Comput. Phys. Commun.* **2014**, *185*, 939–947. [CrossRef]
126. Nabavizadeh, S.A.; Eshraghi, M.; Felicelli, S.D. Three-dimensional phase field modeling of columnar to equiaxed transition in directional solidification of Inconel 718 alloy. *J. Cryst. Growth* **2020**, *549*, 125879. [CrossRef]
127. Subhedar, A.; Steinbach, I.; Varnik, F. Modeling the flow in diffuse interface methods of solidification. *Phys. Rev. E* **2015**, *92*, 023303. [CrossRef] [PubMed]
128. Openphase. Available online: www.openphase.de (accessed on 15 May 2023).
129. Ren, Y.; Liu, Z.; Pang, Y.; Wang, X.; Xu, Y. Lattice Boltzmann simulation of phase change and heat transfer characteristics in the multi-layer deposition. *Appl. Math. Mech.* **2021**, *42*, 553–566. [CrossRef]
130. Sakane, S.; Aoki, T.; Takaki, T. Parallel-GPU AMR implementation for phase-field lattice Boltzmann simulation of a settling dendrite. *Comput. Mater. Sci.* **2022**, *211*, 111542. [CrossRef]
131. De Moura, C.A.; Kubrusly, C.S. *The Courant–Friedrichs–Lewy (Cfl) Condition*; Birkhäuser: Boston, MA, USA, 2013; Volume 10.
132. Kao, A.; Shevchenko, N.; Alexandrakis, M.; Krastins, I.; Eckert, S.; Pericleous, K. Thermal dependence of large-scale freckle defect formation. *Philos. Trans. R. Soc. A Math. Phys. Eng. Sci.* **2019**, *377*, 20180206. [CrossRef]
133. Nabavizadeh, S.A.; Eshraghi, M.; Felicelli, S.D.; Tewari, S.N.; Grugel, R.N. Effect of bubble-induced Marangoni convection on dendritic solidification. *Int. J. Multiph. Flow* **2019**, *116*, 137–152. [CrossRef]
134. Chen, L.; Kang, Q.; Mu, Y.; He, Y.-L.; Tao, W.-Q. A critical review of the pseudopotential multiphase lattice Boltzmann model: Methods and applications. *Int. J. Heat Mass Transf.* **2014**, *76*, 210–236. [CrossRef]
135. Shimokawabe, T.; Aoki, T.; Takaki, T.; Endo, T.; Yamanaka, A.; Maruyama, N.; Nukada, A.; Matsuoka, S. Peta-scale Phase-Field Simulation for DendriticSolidification on the TSUBAME 2.0 Supercomputer. In Proceedings of the 2011 International Conference for High Performance Computing, Networking, Storage and Analysis, Seattle, WA, USA, 12–18 November 2011. [CrossRef]
136. Seiz, M.; Kellner, M.; Nestler, B. Simulation of dendritic–eutectic growth with the phase-field method. *Acta Mater.* **2023**, *254*, 118965. [CrossRef]
137. Eshraghi, M.; Jelinek, B.; Felicelli, S.D. Large-Scale Three-Dimensional Simulation of Dendritic Solidification Using Lattice Boltzmann Method. *JOM* **2015**, *67*, 1786–1792. [CrossRef]
138. Sakane, S.; Takaki, T.; Ohno, M.; Shimokawabe, T.; Aoki, T. GPU-accelerated 3D phase-field simulations of dendrite competitive growth during directional solidification of binary alloy. In *IOP Conference Series: Materials Science and Engineering*; Institute of Physics Publishing: Bristol, UK, 2015. [CrossRef]
139. Kao, A.; Krastins, I.; Alexandrakis, M.; Shevchenko, N.; Eckert, S.; Pericleous, K. A Parallel Cellular Automata Lattice Boltzmann Method for Convection-Driven Solidification. *JOM* **2019**, *71*, 48–58. [CrossRef] [PubMed]
140. Takaki, T.; Rojas, R.; Sakane, S.; Ohno, M.; Shibuta, Y.; Shimokawabe, T.; Aoki, T. Phase-field-lattice Boltzmann studies for dendritic growth with natural convection. *J. Cryst. Growth* **2017**, *474*, 146–153. [CrossRef]
141. Nabavizadeh, S.A.; Eshraghi, M.; Felicelli, S.D.; Tewari, S.N.; Grugel, R.N. The Marangoni convection effects on directional dendritic solidification. *Heat Mass Transf.* **2020**, *56*, 1329–1341. [CrossRef]
142. Yamanaka, A.; Aoki, T.; Ogawa, S.; Takaki, T. GPU-accelerated phase-field simulation of dendritic solidification in a binary alloy. *J. Cryst. Growth* **2011**, *318*, 40–45. [CrossRef]
143. Sun, W.; Yan, R.; Zhang, Y.; Dong, H.; Jing, T. GPU-accelerated three-dimensional large-scale simulation of dendrite growth for Ti6Al4V alloy based on multi-component phase-field model. *Comput. Mater. Sci.* **2019**, *160*, 149–158. [CrossRef]
144. Wang, J.; Meng, H.; Yang, J.; Xie, Z. Multi-GPU accelerated cellular automaton model for simulating the solidification structure of continuous casting bloom. *J. Supercomput.* **2023**, *79*, 4870–4894. [CrossRef]

145. Overview of TSUBAME3.0, Green Cloud Supercomputer for Convergence of HPC, AI and Big-Data ChainerMN: Scalable Distributed Deep Learning Framework Creation of Chemical Structures Aimed for Drug Design, Facilitated by Efficient GPU Computing. Available online: https://www.titech.ac.jp/ (accessed on 15 May 2023).
146. Strout, M.; Kreaseck, B.; Hovland, P. Data-Flow Analysis for MPI Programs. In Proceedings of the 2006 International Conference on Parallel Processing (ICPP'06), Columbus, OH, USA, 14–18 August 2006; pp. 175–184. [CrossRef]
147. Supercomputing at ORNL. Available online: https://www.ornl.gov/directorate/ccsd/supercomputing-ornl (accessed on 15 May 2023).
148. Baer, T. Comparison of Scheduling Policies and Workloads on the NCCS and NICS XT4 Systems at Oak Ridge National Laboratory. Available online: https://www.osc.edu/ (accessed on 15 May 2023).
149. Witherden, F.; Vermeire, B.; Vincent, P. Heterogeneous computing on mixed unstructured grids with PyFR. *Comput. Fluids* **2015**, *120*, 173–186. [CrossRef]
150. Hötzer, J.; Reiter, A.; Hierl, H.; Steinmetz, P.; Selzer, M.; Nestler, B. The parallel multi-physics phase-field framework Pace3D. *J. Comput. Sci.* **2018**, *26*, 1–12. [CrossRef]
151. Icenhour, C.; Keniley, S.; DeChant, C.; Permann, C.; Lindsay, A.; Martineau, R.; Curreli, D.; Shannon, S. Multi-physics object oriented simulation environment (moose). In Proceedings of the Gaseous Electronics Conference 2018 co-located with the Division of Plasma Physics Conference 2018, Oregon Convention Center, Portland, OR, USA, 5–9 November 2018; Idaho National Lab (INL): Idaho Falls, ID, USA, 2018.
152. Alnæs, M.; Blechta, J.; Hake, J.; Johansson, A.; Kehlet, B.; Logg, A.; Richardson, C.; Ring, J.; Rognes, M.E.; Wells, G.N. The FEniCS Project Version 1.5. Available online: http://fenicsproject.org (accessed on 15 May 2023).
153. Balay, S.; Gropp, W.D.; McInnes, L.C.; Smith, B.F. Efficient Management of Parallelism in Object-Oriented Numerical Software Libraries. In *Modern Software Tools for Scientific Computing*; Birkhäuser: Boston, MA, USA, 1997; pp. 163–202. [CrossRef]
154. Gruber, J.; Keller, T.; Lewis, D. Mesoscale Microstructure Simulation Project (MMSP). Available online: https://github.com/mesoscale/mmsp (accessed on 15 May 2023).
155. Parashar, M.; Browne, J.C. Systems Engineering for High Performance Computing Software: The HDDA/DAGH Infrastructure for Implementation of Parallel Structured Adaptive Mesh. In *Structured Adaptive Mesh Refinement (SAMR) Grid Methods*; Springer: New York, NY, USA, 2000; pp. 1–18. [CrossRef]
156. Lu, P.-J.; Lai, M.-C.; Chang, J.-S. A Survey of High-Performance Interconnection Networks in High-Performance Computer Systems. *Electronics* **2022**, *11*, 1369. [CrossRef]
157. Eshraghi, M.; Hashemi, M.; Jelinek, B.; Felicelli, S.D. Three-Dimensional Lattice Boltzmann Modeling of Dendritic Solidification under Forced and Natural Convection. *Metals* **2017**, *7*, 474. [CrossRef]
158. Jegatheesan, M.; Bhattacharya, A. A model for predicting the effects of buoyancy driven convection on solidification of binary alloy with nanoparticles. *Int. J. Heat Mass Transf.* **2022**, *182*, 121916. [CrossRef]
159. Walton, D.; Chalmers, B. The origin of the preferred orientation in the columnar zone of ingots. *Trans. Am. Inst. Min. Metall. Eng.* **1959**, *215*, 447–457.
160. Zhou, Y.; Volek, A.; Green, N. Mechanism of competitive grain growth in directional solidification of a nickel-base superalloy. *Acta Mater.* **2008**, *56*, 2631–2637. [CrossRef]
161. D'Souza, N.; Ardakani, M.G.; Wägner, A.; Shollock, B.A.; McLean, M. Morphological aspects of competitive grain growth during directional solidification of a nickel-base superalloy, CMSX4. *J. Mater. Sci.* **2002**, *37*, 481–487. [CrossRef]
162. Wagner, A.; Shollock, B.; McLean, M. Grain structure development in directional solidification of nickel-base superalloys. *Mater. Sci. Eng. A* **2004**, *374*, 270–279. [CrossRef]
163. Yang, C.; Xu, Q.; Liu, B. GPU-accelerated three-dimensional phase-field simulation of dendrite growth in a nickel-based superalloy. *Comput. Mater. Sci.* **2017**, *136*, 133–143. [CrossRef]
164. Raghavan, S.; Singh, G.; Sondhi, S.; Srikanth, S. Construction of a pseudo-binary phase diagram for multi-component Ni-base superalloys. *Calphad* **2012**, *38*, 85–91. [CrossRef]
165. Takaki, T.; Sakane, S.; Ohno, M.; Shibuta, Y.; Shimokawabe, T.; Aoki, T. Large-scale Phase-field Studies of Three-dimensional Dendrite Competitive Growth at the Converging Grain Boundary during Directional Solidification of a Bicrystal Binary Alloy. *ISIJ Int.* **2016**, *56*, 1427–1435. [CrossRef]
166. Dussert, C.; Rasigni, G.; Palmari, J.; Llebaria, A. Minimal spanning tree: A new approach for studying order and disorder. *Phys. Rev. B* **1986**, *34*, 3528–3531. [CrossRef]
167. Tourret, D.; Mertens, J.C.E.; Lieberman, E.; Imhoff, S.D.; Gibbs, J.W.; Henderson, K.; Fezzaa, K.; Deriy, A.L.; Sun, T.; Lebensohn, R.; et al. From Solidification Processing to Microstructure to Mechanical Properties: A Multi-scale X-ray Study of an Al-Cu Alloy Sample. *Metall. Mater. Trans. A* **2017**, *48*, 5529–5546. [CrossRef]
168. Takaki, T.; Sakane, S.; Ohno, M.; Shibuta, Y.; Shimokawabe, T.; Aoki, T. Primary arm array during directional solidification of a single-crystal binary alloy: Large-scale phase-field study. *Acta Mater.* **2016**, *118*, 230–243. [CrossRef]
169. Hui, J.; Tiwari, R.; Wu, X.; Tewari, S.N.; Trivedi, R. Primary dendrite distribution and disorder during directional solidification of Pb-Sb alloys. *Metall. Mater. Trans. A* **2002**, *33*, 3499–3510. [CrossRef]
170. Tewari, S.N.; Weng, Y.-H.; Ding, G.L.; Trivedi, R. Cellular array morphology during directional solidification. *Metall. Mater. Trans. A* **2002**, *33*, 1229–1243. [CrossRef]

171. Strickland, J.; Nenchev, B.; Perry, S.; Tassenberg, K.; Gill, S.; Panwisawas, C.; Dong, H.; D'Souza, N.; Irwin, S. On the nature of hexagonality within the solidification structure of single crystal alloys: Mechanisms and applications. *Acta Mater.* **2020**, *200*, 417–431. [CrossRef]
172. Pandit, K.; Upadhyay, S.; Tewari, S. Effect of cross-section-change induced advective flow on the primary dendrite array morphology of hypoeutectic Pb-Sb alloys during directional solidification. *J. Cryst. Growth* **2018**, *502*, 19–29. [CrossRef]
173. Takaki, T.; Sakane, S.; Ohno, M.; Shibuta, Y.; Aoki, T. Phase-field study on an array of tilted columnar dendrites during the directional solidification of a binary alloy. *Comput. Mater. Sci.* **2022**, *203*, 111143. [CrossRef]
174. Li, J.; Zhou, X.; Brochu, M.; Provatas, N.; Zhao, Y.F. Solidification microstructure simulation of Ti-6Al-4V in metal additive manufacturing: A review. *Addit. Manuf.* **2020**, *31*, 100989. [CrossRef]
175. Dong, H.; Lee, P. Simulation of the columnar-to-equiaxed transition in directionally solidified Al–Cu alloys. *Acta Mater.* **2005**, *53*, 659–668. [CrossRef]
176. Hunt, J. Steady state columnar and equiaxed growth of dendrites and eutectic. *Mater. Sci. Eng.* **1984**, *65*, 75–83. [CrossRef]
177. Gäumann, M.; Trivedi, R.; Kurz, W. Nucleation ahead of the advancing interface in directional solidification. *Mater. Sci. Eng. A* **1997**, *226–228*, 763–769. [CrossRef]
178. Nastac, L. An Efficient 3D Stochastic Model for Predicting the Columnar-to-Equiaxed Transition in Alloy 718. In *IOP Conference Series: Materials Science and Engineering*; Institute of Physics Publishing: Bristol, UK, 2015. [CrossRef]
179. Dong, H.B.; Yang, X.L.; Lee, P.D.; Wang, W. Simulation of equiaxed growth ahead of an advancing columnar front in directionally solidified Ni-based superalloys. *J. Mater. Sci.* **2003**, *39*, 7207–7212. [CrossRef]
180. Xu, X.; Zhang, W.; Lee, P.D. Tree-Ring Formation during Vacuum Arc Remelting of INCONEL 718: Part II. Mathematical Modeling. *Metall. Mater. Trans. A* **2002**, *33*, 1805–1815. [CrossRef]
181. Geslin, P.-A.; Chen, C.-H.; Tabrizi, A.M.; Karma, A. Dendritic needle network modeling of the Columnar-to-Equiaxed transition. Part I: Two dimensional formulation and comparison with theory. *Acta Mater.* **2021**, *202*, 42–54. [CrossRef]
182. Balasubramani, N.; Venezuela, J.; StJohn, D.; Wang, G.; Dargusch, M. A review of the origin of equiaxed grains during solidification under mechanical stirring, vibration, electromagnetic, electric-current, and ultrasonic treatments. *J. Mater. Sci. Technol.* **2022**, *144*, 243–265. [CrossRef]
183. Meng, X.-N.; Cui, L.; Shi, Y.-H.; Zhu, M.-Y. A CA-LBM model for simulating dendrite growth with forced convection. *J. Iron Steel Res. Int.* **2021**, *28*, 997–1008. [CrossRef]
184. Vázquez-López, C.; Calderón, A.; Rodríguez, M.E.; Velasco, E.; Cano, S.; Colás, R.; Valtierra, S. Influence of dendrite arm spacing on the thermal conductivity of an aluminum-silicon casting alloy. *J. Mater. Res.* **2000**, *15*, 85–91. [CrossRef]
185. Zhang, A.; Du, J.; Guo, Z.; Wang, Q.; Xiong, S. A Phase-Field Lattice-Boltzmann Study on Dendritic Growth of Al-Cu Alloy Under Convection. *Metall. Mater. Trans. B* **2018**, *49*, 3603–3615. [CrossRef]
186. Takaki, T.; Sakane, S.; Ohno, M.; Shibuta, Y.; Aoki, T. Large–scale phase–field lattice Boltzmann study on the effects of natural convection on dendrite morphology formed during directional solidification of a binary alloy. *Comput. Mater. Sci.* **2020**, *171*, 109209. [CrossRef]
187. Dorari, E.; Eshraghi, M.; Felicelli, S.D. *Buoyancy Induced Flow and Dendritic Pattern Formation during Directional Solidification*, The University of Akron: Akron, OH, USA, *Unpublished*.
188. Hebditch, D.J.; Hunt, J.D. Observations of ingot macrosegregation on model systems. *Metall. Trans.* **1974**, *5*, 1557–1564. [CrossRef]
189. Ge, H.; Ren, F.; Li, J.; Han, X.; Xia, M.; Li, J. Four-Phase Dendritic Model for the Prediction of Macrosegregation, Shrinkage Cavity, and Porosity in a 55-Ton Ingot. *Metall. Mater. Trans. A* **2017**, *48*, 1139–1150. [CrossRef]
190. Samanta, D.; Zabaras, N. Numerical study of macrosegregation in Aluminum alloys solidifying on uneven surfaces. *Int. J. Heat Mass Transf.* **2005**, *48*, 4541–4556. [CrossRef]
191. Zhang, C.; Shahriari, D.; Loucif, A.; Melkonyan, H.; Jahazi, M. Influence of thermomechanical shrinkage on macrosegregation during solidification of a large-sized high-strength steel ingot. *Int. J. Adv. Manuf. Technol.* **2018**, *99*, 3035–3048. [CrossRef]
192. Ren, F.; Ge, H.; Cai, D.; Li, J.; Hu, Q.; Xia, M.; Li, J. Simulation of Macrosegregation and Shrinkage Cavity in an Al-4.5 Wt Pct Cu Ingot Using a Four-Phase Model. *Metall. Mater. Trans. A* **2018**, *49*, 6243–6254. [CrossRef]
193. Han, Z.; Lewis, R.; Liu, B. Modelling of the thermosolutal convection and macrosegregation in the solidification of an Fe-C binary alloy. *Int. J. Numer. Methods Heat Fluid Flow* **2007**, *17*, 313–321. [CrossRef]
194. Zhao, H.; Zhang, Z.; Bai, Y.; Li, B.; Gao, M. Numerical and Experimental Study on the Direct Chill Casting of Large-Scale AA2219 Billets via Annular Coupled Electromagnetic Field. *Materials* **2022**, *15*, 1802. [CrossRef]
195. Cao, Y.; Miao, Y.; Li, D.; Chen, Y.; Fu, P.; Liu, H.; Kang, X.; Liu, H.; Sun, C. On the Mechanism of Steel Homogenization via Rare Earth Addition: Experimental Characterization and Numerical Simulation. *Met. Mater. Trans. B* **2022**, *53*, 1858–1874. [CrossRef]
196. Wang, C.; Liu, Z.; Li, B. A three-phase volume-averaged solidification model considering the growth direction of columnar crystal axis. *Int. J. Heat Mass Transf.* **2022**, *194*, 122974. [CrossRef]
197. Wang, F.; Tzanakis, I.; Eskin, D.; Mi, J.; Connolley, T. In situ observation of ultrasonic cavitation-induced fragmentation of the primary crystals formed in Al alloys. *Ultrason. Sonochem.* **2017**, *39*, 66–76. [CrossRef]
198. Fowler, A.C. The Formation of Freckles in Binary Alloys. *IMA J. Appl. Math.* **1985**, *35*, 159–174. [CrossRef]
199. Felicelli, S.D.; Poirier, D.R.; Heinrich, J.C. Modeling freckle formation in three dimensions during solidification of multicomponent alloys. *Met. Mater. Trans. B* **1998**, *29*, 847–855. [CrossRef]

200. Zimmermann, G.; Pickmann, C.; Hamacher, M.; Schaberger-Zimmermann, E.; Neumann-Heyme, H.; Eckert, K.; Eckert, S. Fragmentation-driven grain refinement in directional solidification of AlCu10wt-% alloy at low pulling speeds. *Acta Mater.* **2017**, *126*, 236–250. [CrossRef]
201. Campanella, T.; Charbon, C.; Rappaz, M. Grain refinement induced by electromagnetic stirring: A dendrite fragmentation criterion. *Metall. Mater. Trans. A* **2004**, *35*, 3201–3210. [CrossRef]
202. Dai, H.; Gebelin, J.; Newell, M.; Reed, R.; D'Souza, N.; Brown, P.; Dong, H. Grain Selection during Solidification in Spiral Grain Selector. *Superalloys* **2008**, *2008*, 367–374. [CrossRef]
203. Ng, C.; Bermingham, M.; Yuan, L.; Dargusch, M. Towards β-fleck defect free additively manufactured titanium alloys by promoting the columnar to equiaxed transition and grain refinement. *Acta Mater.* **2022**, *224*, 117511. [CrossRef]
204. Ren, N.; Li, J.; Panwisawas, C.; Xia, M.; Dong, H.; Li, J. Insight into the sensitivities of freckles in the directional solidification of single-crystal turbine blades. *J. Manuf. Process.* **2022**, *77*, 219–228. [CrossRef]
205. Xing, H.; Dong, X.; Sun, D.; Han, Y. Anisotropic lattice Boltzmann-phase-field modeling of crystal growth with melt convection induced by solid-liquid density change. *J. Mater. Sci. Technol.* **2020**, *57*, 26–32. [CrossRef]
206. Cui, J.; Li, B.; Liu, Z.; Qi, F.; Xu, J.; Zhang, J. Comparative investigation on ingot evolution and product quality under different arc distributions during vacuum arc remelting process. *J. Mater. Res. Technol.* **2022**, *18*, 3991–4006. [CrossRef]
207. Hecht, U.; Gránásy, L.; Pusztai, T.; Böttger, B.; Apel, M.; Witusiewicz, V.; Ratke, L.; De Wilde, J.; Froyen, L.; Camel, D.; et al. Multiphase solidification in multicomponent alloys. *Mater. Sci. Eng. R Rep.* **2004**, *46*, 1–49. [CrossRef]
208. Ananth, R.; Gill, W.N. Dendritic growth in microgravity and forced convection. *J. Cryst. Growth* **1997**, *179*, 263–276. [CrossRef]
209. Diepers, H.-J.; Beckermann, C.; Steinbach, I. Simulation of convection and ripening in a binary alloy mush using the phase-field method. *Acta Mater.* **1999**, *47*, 3663–3678. [CrossRef]
210. Beckermann, C.; Diepers, H.-J.; Steinbach, I.; Karma, A.; Tong, X. Modeling Melt Convection in Phase-Field Simulations of Solidification. *J. Comput. Phys.* **1999**, *154*, 468–496. [CrossRef]
211. Tönhardt, R.; Amberg, G. Phase-field simulation of dendritic growth in a shear flow. *J. Cryst. Growth* **1998**, *194*, 406–425. [CrossRef]
212. Tönhardt, R.; Amberg, G. Simulation of natural convection effects on succinonitrile crystals. *Phys. Rev. E* **2000**, *62*, 828–836. [CrossRef]
213. Al-Rawahi, N.; Tryggvason, G. Numerical simulation of dendritic solidification with convection: Three-dimensional flow. *J. Comput. Phys.* **2004**, *194*, 677–696. [CrossRef]
214. Yuan, L.; Lee, P. Dendritic solidification under natural and forced convection in binary alloys: 2D versus 3D simulation. *Model. Simul. Mater. Sci. Eng.* **2010**, *18*, 055008. [CrossRef]
215. Jakhar, A.; Bhattacharya, A.; Rath, P.; Mahapatra, S.K. Combined Effect of Thermal Anisotropy and Forced Convection on the Growth of Binary Alloy Equiaxed Dendrites. *J. Therm. Sci. Eng. Appl.* **2019**, *11*, 051010. [CrossRef]
216. Sakane, S.; Takaki, T.; Ohno, M.; Shibuta, Y.; Aoki, T. Two-dimensional large-scale phase-field lattice Boltzmann simulation of polycrystalline equiaxed solidification with motion of a massive number of dendrites. *Comput. Mater. Sci.* **2020**, *178*, 109639. [CrossRef]
217. Kim, S.G.; Kim, D.I.; Kim, W.T.; Park, Y.B. Computer simulations of two-dimensional and three-dimensional ideal grain growth. *Phys. Rev. E* **2006**, *74*, 061605. [CrossRef]
218. Takaki, T.; Hirouchi, T.; Hisakuni, Y.; Yamanaka, A.; Tomita, Y. Multi-Phase-Field Model to Simulate Microstructure Evolutions during Dynamic Recrystallization. *Mater. Trans.* **2008**, *49*, 2559–2565. [CrossRef]
219. Ohno, M.; Tsuchiya, S.; Matsuura, K. Formation conditions of coarse columnar austenite grain structure in peritectic carbon steels by the discontinuous grain growth mechanism. *Acta Mater.* **2011**, *59*, 5700–5709. [CrossRef]
220. Zhang, A.; Meng, S.; Guo, Z.; Du, J.; Wang, Q.; Xiong, S. Dendritic Growth Under Natural and Forced Convection in Al-Cu Alloys: From Equiaxed to Columnar Dendrites and from 2D to 3D Phase-Field Simulations. *Met. Mater. Trans. B* **2019**, *50*, 1514–1526. [CrossRef]
221. Sun, D.; Zhu, M.; Pan, S.; Raabe, D. Lattice Boltzmann modeling of dendritic growth in a forced melt convection. *Acta Mater.* **2009**, *57*, 1755–1767. [CrossRef]
222. Neuman, S.P. Theoretical derivation of Darcy's law. *Acta Mech.* **1977**, *25*, 153–170. [CrossRef]
223. Campanella, T.; Charbon, C.; Rappaz, M. Influence of permeability on the grain refinement induced by forced convection in copper-base alloys. *Scr. Mater.* **2003**, *49*, 1029–1034. [CrossRef]
224. Bernard, D.; Nielsen, Ø.; Salvo, L.; Cloetens, P. Permeability assessment by 3D interdendritic flow simulations on microtomography mappings of Al–Cu alloys. *Mater. Sci. Eng. A* **2005**, *392*, 112–120. [CrossRef]
225. Böttger, B.; Haberstroh, C.; Giesselmann, N. Cross-Permeability of the Semisolid Region in Directional Solidification: A Combined Phase-Field and Lattice-Boltzmann Simulation Approach. *JOM* **2016**, *68*, 27–36. [CrossRef]
226. Bhat, M.S.; Poirier, D.R.; Heinrich, J.C. Permeability for cross flow through columnar-dendritic alloys. *Metall. Mater. Trans. B* **1995**, *26*, 1049–1056. [CrossRef]
227. Khajeh, E.; Maijer, D.M. Permeability of dual structured hypoeutectic aluminum alloys. *Acta Mater.* **2011**, *59*, 4511–4524. [CrossRef]
228. Berger, R.; Apel, M.; Laschet, G.; Jessen, W.; Schröder, W.; Wipperfürth, J.; Austermann, J.; Hopmann, C. Permeability Measurements of 3D Microstructures Generated by Phase Field Simulation of the Solidification of an Al-Si Alloy during Chill Casting. *Metals* **2021**, *11*, 1895. [CrossRef]

229. Mitsuyama, Y.; Takaki, T.; Sakane, S.; Shibuta, Y.; Ohno, M. Permeability tensor for columnar dendritic structures: Phase-field and lattice Boltzmann study. *Acta Mater.* **2020**, *188*, 282–287. [CrossRef]
230. White, H.J. Book Review: Flow of Gases Through Porous Media. P. C. Carman. New York, Academic Press, 1956. ix + 182 pages, illust. Price $6.00. *Text. Res. J.* **1959**, *29*, 98. [CrossRef]
231. Heinrich, J.C.; Poirier, D.R. Convection modeling in directional solidification. *Comptes Rendus Mec.* **2004**, *332*, 429–445. [CrossRef]
232. Natsume, Y.; Takahashi, D.; Kawashima, K.; Tanigawa, E.; Ohsasa, K. Quantitative Model to Determine Permeability for Columnar Dendritic Structures. *ISIJ Int.* **2013**, *53*, 838–847. [CrossRef]
233. Khajeh, E.; Maijer, D.M. Physical and numerical characterization of the near-eutectic permeability of aluminum–copper alloys. *Acta Mater.* **2010**, *58*, 6334–6344. [CrossRef]
234. Puncreobutr, C.; Phillion, A.; Fife, J.; Lee, P. Coupling in situ synchrotron X-ray tomographic microscopy and numerical simulation to quantify the influence of intermetallic formation on permeability in aluminium–silicon–copper alloys. *Acta Mater.* **2014**, *64*, 316–325. [CrossRef]
235. Takaki, T.; Sakane, S.; Ohno, M.; Shibuta, Y.; Aoki, T. Permeability prediction for flow normal to columnar solidification structures by large–scale simulations of phase–field and lattice Boltzmann methods. *Acta Mater.* **2019**, *164*, 237–249. [CrossRef]
236. Ludwig, A.; Kharicha, A.; Hölzl, C.; Domitner, J.; Wu, M.; Pusztai, T. 3D Lattice Boltzmann flow simulations through dendritic mushy zones. *Eng. Anal. Bound. Elem.* **2014**, *45*, 29–35. [CrossRef]
237. Brown, S.; Spittle, J.; Jarvis, D.; Walden-Bevan, R. Numerical determination of liquid flow permeabilities for equiaxed dendritic structures. *Acta Mater.* **2002**, *50*, 1559–1569. [CrossRef]
238. Kyogoku, H.; Ikeshoji, T.-T. A review of metal additive manufacturing technologies: Mechanism of defects formation and simulation of melting and solidification phenomena in laser powder bed fusion process. *Mech. Eng. Rev.* **2020**, *7*, 19–00182. [CrossRef]
239. Tan, J.H.K.; Sing, S.L.; Yeong, W.Y. Microstructure modelling for metallic additive manufacturing: A review. *Virtual Phys. Prototyp.* **2020**, *15*, 87–105. [CrossRef]
240. Yin, H.; Felicelli, S. Dendrite growth simulation during solidification in the LENS process. *Acta Mater.* **2010**, *58*, 1455–1465. [CrossRef]
241. Yu, Y.; Li, Y.; Lin, F.; Yan, W. A multi-grid Cellular Automaton model for simulating dendrite growth and its application in additive manufacturing. *Addit. Manuf.* **2021**, *47*, 102284. [CrossRef]
242. Shi, R.; Khairallah, S.A.; Roehling, T.T.; Heo, T.W.; McKeown, J.T.; Matthews, M.J. Microstructural control in metal laser powder bed fusion additive manufacturing using laser beam shaping strategy. *Acta Mater.* **2020**, *184*, 284–305. [CrossRef]
243. Noble, C.R.; Anderson, A.T.; Barton, N.R.; Bramwell, J.A.; Capps, A.; Chang, M.H.; Chou, J.J.; Dawson, D.M.; Diana, E.R.; Dunn, T.A.; et al. *ALE3D: An Arbitrary Lagrangian-Eulerian Multi-Physics Code*; Lawrence Livermore National Lab.(LLNL): Livermore, CA, USA, 2017. [CrossRef]
244. Groeber, M.A.; Jackson, M.A. DREAM. 3D: A Digital RepresentationEnvironment for the Analysis ofMicrostructure in 3D. *Integr. Mater. Manuf. Innov.* **2014**, *3*, 5. [CrossRef]
245. Lian, Y.; Gan, Z.; Yu, C.; Kats, D.; Liu, W.K.; Wagner, G.J. A cellular automaton finite volume method for microstructure evolution during additive manufacturing. *Mater. Des.* **2019**, *169*, 107672. [CrossRef]
246. Elahi, S.; Tavakoli, R.; Boukellal, A.; Isensee, T.; Romero, I.; Tourret, D. Multiscale simulation of powder-bed fusion processing of metallic alloys. *Comput. Mater. Sci.* **2022**, *209*, 111383. [CrossRef]
247. Raghavan, N.; Simunovic, S.; Dehoff, R.; Plotkowski, A.; Turner, J.; Kirka, M.; Babu, S. Localized melt-scan strategy for site specific control of grain size and primary dendrite arm spacing in electron beam additive manufacturing. *Acta Mater.* **2017**, *140*, 375–387. [CrossRef]
248. Holm, E.A.; Battaile, C.C. The computer simulation of microstructural evolution. *JOM* **2001**, *53*, 20–23. [CrossRef]
249. Rodgers, T.M.; Madison, J.D.; Tikare, V. Simulation of metal additive manufacturing microstructures using kinetic Monte Carlo. *Comput. Mater. Sci.* **2017**, *135*, 78–89. [CrossRef]
250. Sandia National Laboratories. SPPARKS Kinetic Monte Carlo Simulator. Available online: https://spparks.github.io/ (accessed on 16 May 2023).
251. Zinoviev, A.; Zinovieva, O.; Ploshikhin, V.; Romanova, V.; Balokhonov, R. Evolution of grain structure during laser additive manufacturing. Simulation by a cellular automata method. *Mater. Des.* **2016**, *106*, 321–329. [CrossRef]
252. Rai, A.; Markl, M.; Körner, C. A coupled Cellular Automaton–Lattice Boltzmann model for grain structure simulation during additive manufacturing. *Comput. Mater. Sci.* **2016**, *124*, 37–48. [CrossRef]
253. Rodgers, T.M.; Madison, J.D.; Tikare, V.; Maguire, M.C. Predicting Mesoscale Microstructural Evolution in Electron Beam Welding. *JOM* **2016**, *68*, 1419–1426. [CrossRef]
254. Popova, E.; Rodgers, T.M.; Gong, X.; Cecen, A.; Madison, J.D.; Kalidindi, S.R. Process-Structure Linkages Using a Data Science Approach: Application to Simulated Additive Manufacturing Data. *Integrating Mater. Manuf. Innov.* **2017**, *6*, 54–68. [CrossRef]
255. Irwin, J.; Reutzel, E.; Michaleris, P.; Keist, J.; Nassar, A.R. Predicting Microstructure from Thermal History During Additive Manufacturing for Ti-6Al-4V. *J. Manuf. Sci. Eng.* **2016**, *138*, 111007. [CrossRef]
256. Elahi, S.; Tavakoli, R.; Romero, I.; Tourret, D. Grain growth competition during melt pool solidification—Comparing phase-field and cellular automaton models. *Comput. Mater. Sci.* **2022**, *216*, 111882. [CrossRef]

257. Hu, Y.; Xie, J.; Liu, Z.; Ding, Q.; Zhu, W.; Zhang, J.; Zhang, W. CA method with machine learning for simulating the grain and pore growth of aluminum alloys. *Comput. Mater. Sci.* **2018**, *142*, 244–254. [CrossRef]
258. Dong, A.; Nastac, L. Prediction of Secondary Dendrite Arm Spacing in Al Alloys Using Machine Learning. *Met. Mater. Trans. B* **2021**, *52*, 2395–2403. [CrossRef]
259. Nikolić, F.; Štajduhar, I.; Čanađija, M. Casting Defects Detection in Aluminum Alloys Using Deep Learning: A Classification Approach. *Int. J. Met.* **2022**, *17*, 386–398. [CrossRef]
260. Hu, C.; Martin, S.; Dingreville, R. Accelerating phase-field predictions via recurrent neural networks learning the microstructure evolution in latent space. *Comput. Methods Appl. Mech. Eng.* **2022**, *397*, 115128. [CrossRef]
261. Abdi, H.; Williams, L.J. Principal component analysis. *Wiley Interdiscip. Rev. Comput. Stat.* **2010**, *2*, 433–459. [CrossRef]
262. Orsenigo, C.; Vercellis, C. An effective double-bounded tree-connected Isomap algorithm for microarray data classification. *Pattern Recognit. Lett.* **2012**, *33*, 9–16. [CrossRef]
263. McInnes, L.; Healy, J.; Melville, J. UMAP: Uniform Manifold Approximation and Projection for Dimension Reduction. *arXiv* **2018**, arXiv:1802.03426. [CrossRef]
264. Cho, K.; van Merriënboer, B.; Gulcehre, C.; Bahdanau, D.; Bougares, F.; Schwenk, H.; Bengio, Y. Learning Phrase Representations Using RNN Encoder-Decoder for Statistical Machine Translation. In Proceedings of the 2014 Conference on Empirical Methods in Natural Language Processing (EMNLP), Doha, Qatar, 25–29 October 2014.
265. Hochreiter, S.; Schmidhuber, J. Long short-term memory. *Neural Comput.* **1997**, *9*, 1735–1780. [CrossRef] [PubMed]
266. Ren, N.; Li, J.; Bogdan, N.; Xia, M.; Li, J. Simulation of dendritic remelting and fragmentation using coupled cellular automaton and Eulerian multiphase model. *Comput. Mater. Sci.* **2020**, *180*, 109714. [CrossRef]
267. Guo, Z.; Mi, J.; Xiong, S.; Grant, P.S. Phase Field Simulation of Binary Alloy Dendrite Growth Under Thermal- and Forced-Flow Fields: An Implementation of the Parallel–Multigrid Approach. *Met. Mater. Trans. B* **2013**, *44*, 924–937. [CrossRef]

MDPI
St. Alban-Anlage 66
4052 Basel
Switzerland
www.mdpi.com

Metals Editorial Office
E-mail: metals@mdpi.com
www.mdpi.com/journal/metals

Academic Open
Access Publishing

mdpi.com

ISBN 978-3-0365-8601-4